214
Topics in Current Chemistry

Springer

Berlin
Heidelberg
New York
Barcelona
Hong Kong
London
Milan
Paris
Singapore
Tokyo

Transition Metal and Rare Earth Compounds

Excited States, Transitions, Interactions II

Volume Editor: Hartmut Yersin

With contributions by
D. Donges, D. R. Gamelin, H. U. Güdel, M. J. Riley,
H. Yersin

Springer

The series *Topics in Current Chemistry* presents critical reviews of the present and future trends in modern chemical research. The scope of coverage includes all areas of chemical science including the interfaces with related disciplines such as biology, medicine and materials science. The goal of each thematic volume is to give the non-specialist reader, whether at the university or in industry, a comprehensive overview of an area where new insights are emerging that are of interest to a larger scientific audience.

As a rule, contributions are specially commissioned. The editors and publishers will, however, always be pleased to receive suggestions and supplementary information. Papers are accepted for *Topics in Current Chemistry* in English.

In references *Topics in Current Chemistry* is abbreviated Top. Curr. Chem. and is cited as a journal.

Springer WWW home page: http://www.springer.de
Visit the TCC home page at http:/link.springer.de/series/tcc/
or http://link.springer-ny.com/series/tcc/

ISSN 0340-1022
ISBN 3-540-67976-6
Springer-Verlag Berlin Heidelberg New York

Library of Congress Catalog Card Number 74-644622

Springer-Verlag Berlin Heidelberg New York
a member of BertelsmannSpringer Science+Business Media GmbH

Printed in Germany

Cover design: Friedhelm Steinen-Broo, Barcelona; MEDIO, Berlin
Typesetting: Fotosatz-Service Köhler GmbH, 97084 Würzburg

SPIN: 10719407 02/3020 ra – 5 4 3 2 1 0 – Printed on acid-free paper

Volume Editor

Prof. Dr. Hartmut Yersin
Institut für Physikalische und Theoretische Chemie
Universität Regensburg
Universitätsstraße 31
93053 Regensburg, Germany
E-mail: hartmut.yersin@chemie.uni-regensburg.de

Editorial Board

Prof. Dr. Armin de Meijere
Institut für Organische Chemie
der Georg-August-Universität
Tammannstraße 2
37077 Göttingen, Germany
E-mail: ameijer1@uni-goettingen.de

Prof. Dr. Horst Kessler
Institut für Organische Chemie
TU München
Lichtenbergstraße 4
85747 Garching, Germany
E-mail: kessler@ch.tum.de

Prof. Steven V. Ley
University Chemical Laboratory
Lensfield Road
Cambridge CB2 1EW, Great Britain
E-mail: svl1000@cus.cam.ac.uk

Prof. Dr. Joachim Thiem
Institut für Organische Chemie
Universität Hamburg
Martin-Luther-King-Platz 6
20146 Hamburg, Germany
E-mail: thiem@chemie.uni-hamburg.de

Prof. Dr. Fritz Vögtle
Kekulé-Institut für Organische Chemie
und Biochemie der Universität Bonn
Gerhard-Domagk-Straße 1
53121 Bonn, Germany
E-mail: voegtle@uni-bonn.de

Prof. Kendall N. Houk
Department of Chemistry and Biochemistry
University of California
405 Hilgard Avenue
Los Angeles, CA 90024-1589, USA
E-mail: houk@chem.ucla.edu

Prof. Jean-Marie Lehn
Institut de Chimie
Université de Strasbourg
1 rue Blaise Pascal, B.P.Z 296/R8
67008 Strasbourg Cedex, France
E-mail: lehn@chimie.u-strasbg.fr

Prof. Stuart L. Schreiber
Chemical Laboratories
Harvard University
12 Oxford Street
Cambridge, MA 02138-2902, USA
E-mail: sls@slsiris.harvard.edu

Prof. Barry M. Trost
Department of Chemistry
Stanford University
Stanford, CA 94305-5080, USA
E-mail: bmtrost@leland.stanford.edu

Prof. Hisashi Yamamoto
School of Engineering
Nagoya University
Chikusa, Nagoya 464-01, Japan
E-mail: j45988a@nucc.cc.nagoya-u.ac.jp

Topics in Current Chemistry
Now Also Available Electronically

For all customers with a standing order for Topics in Current Chemistry we offer the electronic form via LINK free of charge. Please contact your librarian who can receive a password for free access to the full articles by registration at:

http://link.springer.de/orders/index.htm

If you do not have a standing order you can nevertheless browse through the table of contents of the volumes and the abstracts of each article at:

http://link.springer.de/series/tcc

There you will also find information about the

- Editorial Board
- Aims and Scope
- Instructions for Authors

Preface

For a long time, the properties of transition metal and rare earth compounds have fascinated chemists and physicists from a scientific view-point. More recently, their enormous potential as new materials has also been explored. Applications in different fields have already been realized or are under current investigation, e.g. new laser materials, IR to visible upconversion materials, systems involving photoredox processes for solar energy conversion, new photovoltaic devices, chemical sensors, biosensors, electroluminescent devices (OLEDs) for flat panel display systems, supramolecular devices with wide-range definable photophysical properties, materials for energy harvesting, optical information and storage systems, etc. Metal complexes are also highly important in biology and medicine. Most of the applications mentioned are directly related to the properties of the electronic ground state and the lower-lying excited states. Metal complexes with organic ligands or organometallic compounds exhibit outstanding features as compared to purely organic molecules. For instance, metal compounds can often be prepared and applied in different oxidation states. Furthermore, various types of low-lying electronic excitations can be induced by a suitable choice of the metal center and/or the ligands, such as metal-centered (MC, e.g. d-d* or f-f* transitions), ligand-centered (LC, e.g. π-π^*), metal-to-ligand-charge transfer (MLCT, e.g. d-π^*), intra-ligand-charge-transfer (ILCT) transitions, etc. In particular, the orbitals involved in the resulting lowest excited states determine the photophysical and photochemical properties and thus the specific use of the compound. It is also of high interest that the lowest excited electronic states can be shifted over the large energy range from the U.V. to the I.R. by chemical variation of the ligands and/or the central metal ion. Moreover, these excited states have mostly spin-multiplicities different from those of the electronic ground states. Thus, in contrast to organic molecules, spin-orbit coupling (induced by the metal center) is of crucial importance, for example, for the splitting and the population and decay dynamics of these multiplets as well as for transition probabilities and radiative deactivation paths. In summary, transition metal and rare earth compounds can be prepared with photophysical properties that are over wide ranges user-definable.

In view of the fascinating potential of these compounds, it is of substantial interest to develop a deeper understanding of their photophysical properties. In this volume [1], leading scientists present modern research trends in comprehen-

---

[1] See also the preceding volumes, Electronic and Vibronic Spectra of Transition Metal Complexes I and II, edited by H. Yersin, Topics in Current Chemistry 171 (1994) and 191 (1997).

sive reviews which not only provide a deep insight into the specific subjects, but are also written in a style that enables researchers from related fields and graduate students to follow the interesting presentations. In particular, in the present volume Daniel R. Gamelin and Hans U. Güdel review upconversion processes in luminescent transition metal and rare earth systems. Mark J. Riley relates geometric and electronic properties of copper(II) compounds. Finally, Hartmut Yersin and Dirk Donges discuss on the basis of case studies photophysical properties of organometallic and related compounds and demonstrate how these properties can be tuned by chemical variation. In a companion volume (Topics in Current Chemistry 213), Kevin L. Bray presents effects that are observed under application of high pressure. Max Glasbeek introduces us to optically detected magnetic resonance (ODMR) techniques as applied to transition metal complexes and Arnd Vogler and Horst Kunkely give a summary concerning the diversity of excited states as found in various compounds.

I hope that the contributions in the present and in the companion volume demonstrate the attractiveness and the enormous potential of metal compounds and that a more detailed understanding of the photophysical properties will open pathways for new developments.

Regensburg, Germany Hartmut Yersin
November 2000

Contents

Contents of Volume 191

Electronic and Vibronic Spectra of Transition Metal Complexes II

Volume Editor: Hartmut Yersin

ISBN 3-540-62922-X

Contents of Volume 213

Transition Metal and Rare Earth Compounds

Excited States, Transitions, Interactions I

Volume Editor: Hartmut Yersin

ISBN 3-540-67986-3

Upconversion Processes in Transition Metal and Rare Earth Metal Systems

Daniel R. Gamelin*, Hans U. Güdel

Department of Chemistry and Biochemistry, University of Bern, Freiestrasse 3, 3000 Bern 9, Switzerland
E-mail: hans-ulrich.guedel@iac.unibe.ch

The design and characterization of new luminescent materials is an active area of research. Here we present several current topics in the area of upconversion by transition-metal and rare-earth-metal doped halide lattices. Following introduction to the necessary background material related to upconversion mechanisms and kinetics, a series of topics are discussed which illustrate some key areas of developing interest in the field. These include the use of unconventional experimental and theoretical techniques for gaining insight into upconversion processes in rare-earth-doped lattices (e.g., power-dependence measurements, two-color laser excitation schemes, and correlated crystal field calculations), as well as several specific examples of exciting and unusual upconversion behavior in both transition-metal and rare-earth-metal systems. Finally, we discuss the variety of interesting effects host-lattice variation can have on the upconversion processes of a dopant ion, ranging from multiphonon relaxation properties to exchange interactions.

Keywords: Upconversion, Luminescence, Transition metals, Rare-earth metals, Doped halide lattices

---

* Present address: Department of Chemistry, University of Washington, Seattle, WA 98195–1700

Topics in Current Chemistry, Vol. 214

1
Introduction

Luminescent materials play an important role in many technologies, including display screens, optical communication amplifiers, lamps, and solid-state lasers. To this end, a tremendous volume of fundamental research has been devoted to the design and characterization of new luminescent materials displaying novel photophysical effects. Among such application-oriented research, a great deal of attention has been given to the development of materials capable of generating short-wavelength radiation from long-wavelength pump sources. Second-harmonic generation (SHG) [1], simultaneous two-photon absorption (STPA) [2], and upconversion (UC) [3–6], illustrated in Fig. 1, are three well-established methods for performing this conversion. Briefly, SHG generates new frequencies through the weakly wavelength-dependent hyperpolarizability of a substance, and requires intense coherent excitation sources. STPA involves the excitation of luminescence from a real excited state at shorter wavelength than the excitation photons, and is achieved through a small but non-zero absorption cross section at the pump wavelength. Finally, upconversion generates shorter wavelength luminescence through sequential discrete absorption and/or energy-transfer steps involving real metastable excited states of the chromophore. Upconversion thus relies on the presence of multiple metastable excited states, and this leads to dramatically different photophysical properties relative to the former two methods.

In this article, we discuss several specific topics of current interest in the area of upconversion involving metal ions doped into well-known halide host lattices. Rather than attempting to provide a complete historical survey, the emphasis is on identifying developing areas of research. These range from experimental and calculational approaches for studying general upconversion processes to the investigation of new classes of upconversion materials. In the latter area, the principle strategies for obtaining new upconversion materials involve (1) variation of the host lattice and (2) variation of the dopant metal ions. Variation of the host lattice, for example, from one having high phonon energies (e.g., fluo-

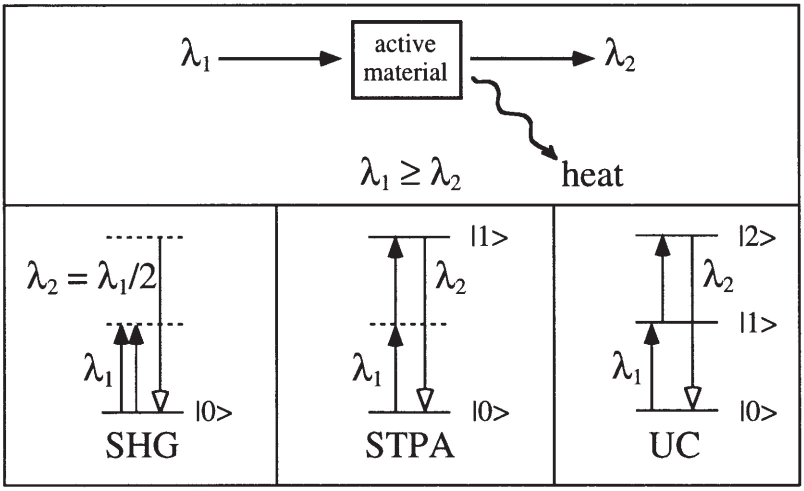

Fig. 1. Schematic representation of three common nonlinear processes that convert low-energy photon pump sources into higher-energy output: SHG = Second Harmonic Generation, STPA = Simultaneous Two-Photon Absorption, UC = Upconversion. Adapted from [17]

ride, oxide) to one having low phonon energies (e.g., chloride, bromide, iodide), can dramatically affect the competition between multiphonon and other radiative and nonradiative processes, and may lead to entirely different upconversion luminescence properties of a given ion. The use of host materials with specific optical or magnetic properties may also influence the upconversion properties of a dopant ion through sensitization or perturbation by exchange interactions. A change in metal ions can of course also have a dramatic effect. Here, we relate examples that emphasize the relatively unexplored upconversion properties of transition metals. When compared to the rare-earth ions, which by far dominate the upconversion literature, transition metals can be expected to show a number of differences in the relevant parameters that govern the upconversion dynamics. In particular, the larger radial extension of the d-orbitals than of the f-orbitals may lead to larger electron-phonon coupling strengths and a greater susceptibility to crystal-field and exchange perturbations. Finally, the design and study of new chromophores comprised of combinations of metal ions is emphasized. Here we present a few examples from our research with these new materials that show unusual upconversion properties attributable to exchange interactions between metal ions. In these examples, including rare-earth/rare-earth, rare-earth/transition-metal, and transition-metal/transition-metal ion pairs, exchange interactions are found to be particularly important when the ions are situated in close proximity to one another by the geometric constraints of the host material. The options available in the choice of hosts and codopant combinations can cover a very broad range of possibilities, leaving much to the imagination and creativity of the researcher, and illustrating the ability to use well-founded chemical principles to design and construct upconversion materials displaying exciting new photophysical properties.

2
Excited-State Decay

The minimum prerequisite for generation of upconversion luminescence by any material is the presence of at least two metastable excited states. In order for upconversion to be efficient, these states must have lifetimes sufficiently long for ions to participate in either luminescence or other photophysical processes with reasonably high probabilities, as opposed to relaxing through nonradiative multiphonon pathways. The observed decay of an excited state in the simplest case scenario, as probed for example by monitoring its luminescence intensity I, behaves as an exponential:

$$I(t) = I(0)\ \mathrm{e}^{-k_{\mathrm{tot}}t} \tag{1}$$

where the observed decay rate constant, k_{tot}, derives from the sum of all contributing radiative (rad) and nonradiative (nr) decay processes:

$$k_{\mathrm{tot}} = k_{\mathrm{rad}} + k_{\mathrm{nr}} = \tau_{\mathrm{obs}}^{-1} \tag{2}$$

Among the possible nonradiative processes, multiphonon relaxation generally makes the greatest contribution to k_{tot}. Multiphonon relaxation is most easily illustrated within the framework of the single configurational coordinate (SCC) model [7, 8]. This model assumes that the vibrational wavefunction overlap integrals responsible for multiphonon relaxation can be approximated by the interactions between the donor (excited) and acceptor (e.g., ground state) potential surfaces along one single effective nuclear coordinate, Q_{eff}. In cases where excited-state nuclear distortions are small, assuming harmonic potentials, identical ground- and excited-state force constants, and identical normal-coordinate descriptions, the SCC model describes the $T = 0$ K multiphonon decay rate constant as shown in Eq. (3):

$$k_{\mathrm{mp}}(0) \approx (C)\left(\frac{e^{-S}S^{p}}{p!}\right) \tag{3}$$

Here, $p = \Delta E_{0-0}/\nu_{\mathrm{eff}}$ is the dimensionless energy gap between the upper state and the closest lower-energy state in units of the effective vibrational energy, ν_{eff} (cm^{-1}). C is the electronic factor, and S is the Huang-Rhys dimensionless excited-state distortion parameter in units of vibrational quanta ν_{eff}. As shown in Eq. (2), k_{mp} is strongly dependent on p. Additionally, for a given reduced energy gap p, the introduction of even small excited-state distortions, S, can rapidly enhance the radiationless multiphonon relaxation rate such that this dominates the total 0 K relaxation. This model is easily extended to elevated temperatures, where substantial increases in k_{mp} may be observed [7, 8].

For the case of only one radiative decay channel, the radiative decay rate constant in Eq. (2) is described by Eq. (4) [9], where n is the index of refraction, the constant $\alpha = 1.5 \times 10^{4}$ s/m^{2}, and g denotes the degeneracy of the ground (a) or excited (b) state involved in the transition:

$$k_{\mathrm{rad}} = f \frac{g_{\mathrm{a}}}{g_{\mathrm{b}}} \frac{n[(n^2+2)/3]^2}{\alpha\lambda^2} \tag{4}$$

The radiative rate constant is thus directly proportional to the oscillator strength, f, of the transition, and is influenced by both degeneracies and the transition wavelength.

The vast majority of luminescent systems have only one emitting excited state, typically the lowest excited state [10]. This is because nonradiative relaxation tends to be extremely rapid among excited states due to the presence of high-frequency vibrations (e.g., stretching vibrations involving protons), small inter-excited-state energy gaps, and sizable electron-phonon coupling strengths. This situation is contrasted by the behavior of the rare-earth metal ions in crystals or complexes. Due to the high shielding of their f electrons, rare-earth ions are characterized by an extreme insensitivity to their environment, in particular having very small electron-phonon coupling strengths, S, in their various f-f excited states. As a result, k_{mp} values can be quite small, and many rare earth excited states are found to luminesce if separated from the nearest lower excited state by only ca. 6 quanta of the highest frequency vibration. Rare-earth ions therefore often have a series of luminescent f-f excited states, a property which makes them suitable for use in upconversion materials.

Since the first observations of upconversion in the mid-1960s [11–14], hundreds of studies involving most of the lanthanide and many actinide ions have been reported [3–5]. In many cases, efficient two-, three-, or four-quantum upconversion is observed. Recent milestones include the development of several all-solid-state rare-earth upconversion lasers operable at room temperature [6, 15], and the demonstration of a viable three-dimensional imaging technique based on rare-earth upconversion [16]. More recently, several transition-metal materials have also been shown to display interesting upconversion properties [17]. In these transition-metal systems a greater range of ground and excited state properties is observed, including stronger electron-phonon coupling strengths in some cases, and this may lead to new, unprecedented upconversion properties (Sects. 11 and 12).

3

The Building Blocks of Upconversion: Absorption and Energy Transfer

A wide variety of upconversion mechanisms have been proposed and observed. The majority of these involve some combination of absorption and nonradiative energy-transfer (ET) steps. Absorption may come in two basic forms. Ground-state absorption (GSA, Fig. 2a) results in promotion of an ion from its ground state to an excited state. Excited-state absorption (ESA, Fig. 2b) involves absorption of a photon by an excited ion, and results in promotion of that ion to a higher excited state.

The simplest upconversion mechanism possible is therefore that of GSA followed by ESA (GSA/ESA). GSA/ESA upconversion is inherently a single-chromophore effect, and as a consequence this mechanism is relatively insensitive to

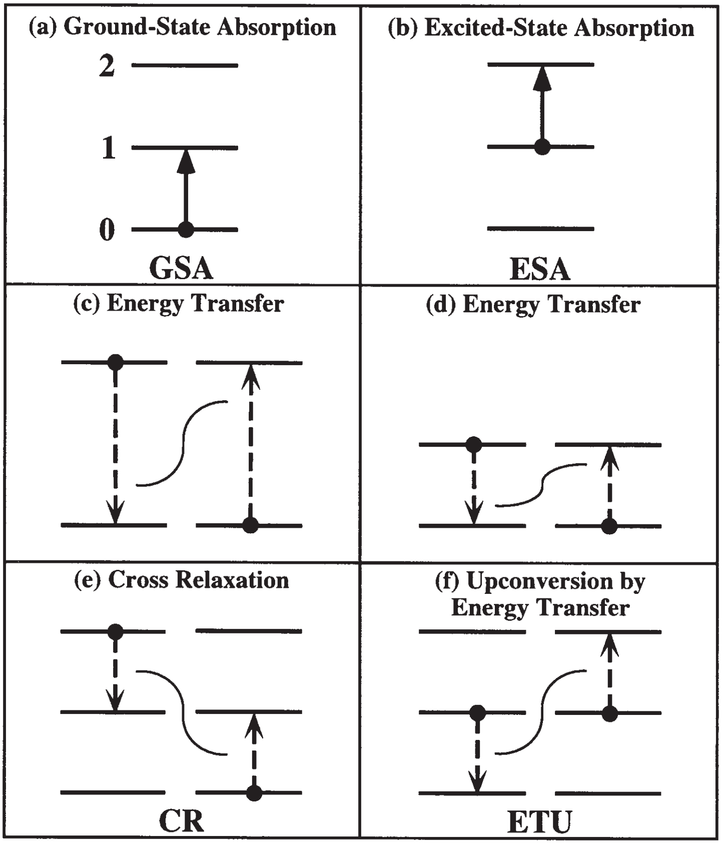

Fig. 2a–f. The basic building blocks of upconversion, and related processes. *Solid arrows* indicate radiative processes, and *dashed arrows* indicate nonradiative processes

concentration of the upconversion ion. For absorption over a sample length, l, that is short compared to the absorption length, the absorption pump rate $R_{a,b}$(ions/cm^{3}s) for a transition $a \rightarrow b$ is given by

$$R_{\mathrm{a,b}} = \frac{\lambda_{\mathrm{P}}}{hc\pi w_p^2} P\sigma_{\mathrm{a}} N_{\mathrm{a}} \tag{5}$$

where P(W/cm^2) is the incident pump power, λ_P is the pump wavelength, w_P is the pump radius, h is Planck's constant, c is the vacuum speed of light, σ_a is the absorption cross section from level a to level b, and N_a (ions/cm^3) is the population density of level a. In a three-level system, the rate constant for a GSA process between levels 0 and 1 is defined as $G = R_{0,1}/N_0$, and that for an ESA process between levels 1 and 2 is defined as $E = R_{1,2}/N_1$. For the GSA/ESA upconversion process to occur, both R_{GSA} ($R_{0,1}$) and R_{ESA} ($R_{1,2}$) must be nonzero. In the simple three-level scheme shown in Fig. 2a, b, at low pump rates, the population of level 1, N_1, is proportional to the rate, $R_{0,1}$, and hence

$$N_1 \propto P\sigma_0 N_0 \tag{6a}$$

Likewise, in Fig. 2b,

$$N_2 \propto P\sigma_1 N_1 \tag{6b}$$

For the concatenated GSA/ESA upconversion process, it follows that

$$N_2 \propto P^2 \sigma_0 \sigma_1 N_0 \tag{6c}$$

When a single excitation beam is used, photons of the same energy must be capable of inducing both excitation steps, and this places a restriction on the wavelengths at which this mechanism is effective (see Sect. 6). The expressions at Eq. (6a–c) are valid in the limit of low pump powers. For discussion of the analogous properties under high pump power conditions, see Sect. 5.

Energy transfer may take a variety of forms. ET among like levels of like ions is the basis for the common phenomenon of energy migration (Fig. 2c, d). A similar process between unlike ions may lead to energy trapping or sensitization effects. ET among unlike levels may result in cross relaxation (CR), by which an ion is partially deactivated through ET to a ground-state neighbor, resulting in two ions in lower excited levels (Fig. 2e). The reverse of cross-relaxation is also possible, in which a low-lying neighbor sacrificially donates its excitation energy to a neighboring excited ion, which is then promoted to a higher excited state. This process is referred to as energy-transfer upconversion, or ETU (Fig. 2f). A very common upconversion mechanism involves this type of ETU following initial excitation of two ions by GSA, and is referred to as GSA/ETU. Since ET processes are substantially slower ($<\sim 10^9$ s^{-1}) than the intramanifold relaxation that leads to relaxed excited states ($\sim 10^{12}$ s^{-1}), ETU always proceeds from relaxed excited states. Since two photons are required to generate two excited ions, under low-power conditions, the upconversion excitation spectrum will thus reflect the *square* of the GSA spectrum:

$$\begin{aligned} N_2 &\propto N_1^2 \\ &\propto P^2 \sigma_0^2 N_0^2 \end{aligned} \tag{7}$$

Note that ETU, like all ET processes, is inherently a pairwise or multicenter effect, and is therefore very strongly dependent upon ion concentration. Whereas GSA/ESA mechanisms often dominate upconversion processes in low-doped samples, upconversion in highly-doped samples is very often dominated by ET processes, in particular GSA/ETU.

The dependence of ETU on concentration results directly from the strong dependence of the ET rate constant on the interionic distance, R_{DA}, between the donor (D) and acceptor (A) centers. The ET kinetics obey Fermi's golden rule and are described within the Condon approximation as

$$w_{\mathrm{ET}} = \frac{4\pi^2}{h} V^2 (FC) \rho \tag{8}$$

where the electronic factor, V^2, is the square of the electronic-coupling matrix element, $V = |\langle D, A^* | H_{DA} | D^*, A \rangle|$ and ρ is the density of acceptor states. The Franck-Condon factor, $FC = |\langle \chi_{DA^*} | \chi_{D^*A} \rangle|^2$, reflects the nuclear reorganization associated with the ET process and is usually described by the spectral overlap integral $FC = \int g_D(\nu) g_A(\nu) d\nu$, i.e., the integrated overlap of the normalized donor emission and acceptor absorption spectral features, $g(\nu)$. In the case of exchange-induced electronic coupling, and in the simplest limiting scenario of isotropic direct exchange, the electronic factor in Eq. (8) is generally approximated as in Eq. (9a) [18]:

$$|\langle D, A^* | H_{DA} | D^*, A \rangle|^2 = J_0^2 \exp[-2 R_{DA}/r_0] \tag{9a}$$

where J_0 has units of energy and r_0 is the Bohr effective radius, which is on the order of 0.3 Å for lanthanide ions [19]. In the case of electric multipole-electric multipole ET, Eq. (8) can be reformulated as in Eq. (9b) [19], where the electronic factor is expressed in terms of the oscillator strengths, f, of the $D^* \rightarrow D$ and $A \rightarrow A^*$ electronic transitions, and is dependent on R_{DA}^{-k}:

$$w_{ET} = \frac{(\text{constant})}{\nu^2 n^4 R_{DA}^k} f_D f_A \int g_D(\nu) g_A(\nu) d\nu \tag{9b}$$

The superscript $k = 6, 8$, and 10 for electric dipole-dipole, dipole-quadrupole, and quadrupole-quadrupole contributions, respectively [20]. Because of the dependence of w_{ET} in Eq. (8) on $\exp[-2 R_{DA}/r_0]$ in the case of exchange, and on R_{DA}^{-k} in the case of multipole-multipole interactions, ET processes are very concentration dependent. At low dopant concentration levels ($<0.1\%$) in homogeneously-doped crystals, where R_{DA} is large, w_{ET} will approach zero leaving GSA/ESA as the only viable upconversion mechanism.

Two general methods for differentiating between GSA/ESA and GSA/ETU mechanisms are illustrated experimentally for the case of 1% Er^{3+}:$RbGd_2Br_7$ NIR → VIS upconversion in Figs. 3 and 4 [21]. Er^{3+} has a $4f^{11}$ electronic configuration and a $^4I_{15/2}$ ground state. When excited to the $^4I_{11/2}$ multiplet with NIR photons at approximately 10,200 cm^{-1}, this sample shows emission from the $^4F_{7/2}$ higher excited state, which lies ca. 20,400 cm^{-1} above the ground state.

The lower part of Fig. 3 shows the 15 K absorption spectrum of 1% Er^{3+}:$RbGd_2Br_7$ in the $^4I_{11/2}$ region of the NIR. The upper part of Fig. 3 shows a 20 K cw upconversion excitation spectrum collected with laser excitation in this same energy region while monitoring the upconverted $^4F_{7/2}$ luminescence. While the lowest energy peaks, between 10,160 cm^{-1} and 10,200 cm^{-1}, resemble those of the absorption spectrum, additional intensity (shaded features) is observed at higher energy which deviates from the GSA spectrum. The horizontal arrows indicate the energy ranges of the $^4I_{15/2} \rightarrow {}^4I_{11/2}$ GSA and $^4I_{11/2} \rightarrow {}^4F_{7/2}$ ESA transitions, determined from the full GSA spectrum [21]. These brackets show that the GSA and ESA transitions are expected to occur in slightly different energy regions, with an overlapping region between 10,210 cm^{-1} and 10,250 cm^{-1}. The new intensity to higher energy in the upconversion excitation spectrum comes from $^4I_{11/2} \rightarrow {}^4F_{7/2}$ ESA transitions. Intensity excited below 10,200 cm^{-1} follows

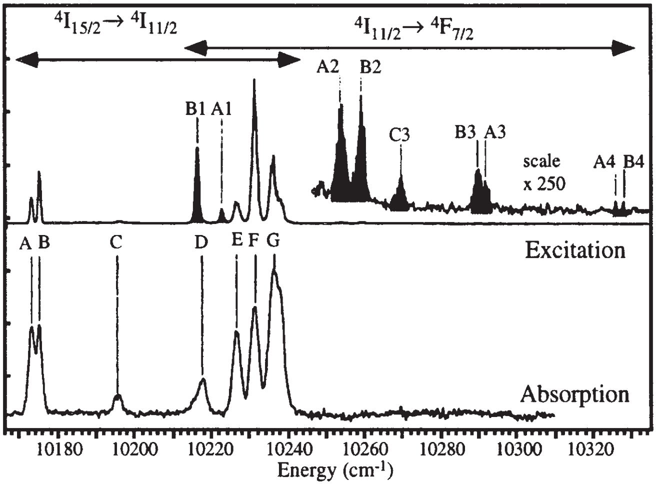

Fig. 3. 15 K absorption and 20 K pulsed upconversion excitation spectra in the region of the $^4I_{15/2} \rightarrow {}^4I_{11/2}$ transition of 1 % Er^{3+}: $RbGd_2Br_7$. The *shaded areas* indicate $^4I_{11/2} \rightarrow {}^4F_{7/2}$ ESA transitions. Note that the excitation spectrum above 10,245 cm^{-1} is scaled by a factor of 250 [21]

the GSA intensity pattern and likely derives from a GSA/ETU mechanism. The most intense upconversion excitation features are those in the middle of the excitation spectrum, where the GSA and ESA energy regions overlap. Excitation at these energies could result in GSA/ESA intensity or could contribute through a GSA/ETU mechanism.

The time profiles of the upconversion luminescence signals following pulsed excitation directly probe the upconversion mechanisms at these various excitation wavelengths. Figure 4a shows that 10 ns pulsed excitation of peak B3 at 10 K results in immediate luminescence from the $^4F_{7/2}$ state, which decays with a rate constant identical to that observed with direct $^4I_{15/2} \rightarrow {}^4F_{7/2}$ excitation (k_2 = 10,000 s^{-1}). This indicates that the $^4F_{7/2}$ state is populated within, and only within, the duration of the laser pulse, and thus implicates a GSA/ESA mechanism. This mechanism can only proceed while the sample is irradiated. Analogous measurements collected with excitation into peak A, shown in Fig. 4b, reveal a distinctly different behavior featuring a delayed maximum and a decay rate constant ($k_{\mathrm{UC\,decay}}$ = 380 s^{-1}) nearly two orders of magnitude smaller than that governing the natural decay of the $^4F_{7/2}$ excited state. The rise time of the upconversion signal in Fig. 4b ($k_{\mathrm{rise}} \approx$ 10,000 s^{-1}) correlates with the $^4F_{7/2}$ decay of Fig. 4a (k_2 = 10,000 s^{-1}). These results indicate that, in contrast with B3 excitation, $^4F_{7/2}$ population does not occur during the laser pulse but rather occurs subsequent to the laser pulse. This is a signature for a GSA/ETU mechanism. In GSA/ETU, upconversion may proceed as long as the intermediate $^4I_{11/2}$ population is nonzero. The upconversion luminescence signal can thus last longer than predicted by the natural decay rate of the emitting state, and in this case is observed to decay at a rate approximately twice that of the intermediate state, which decays with a constant of k_1 = 194 s^{-1}.

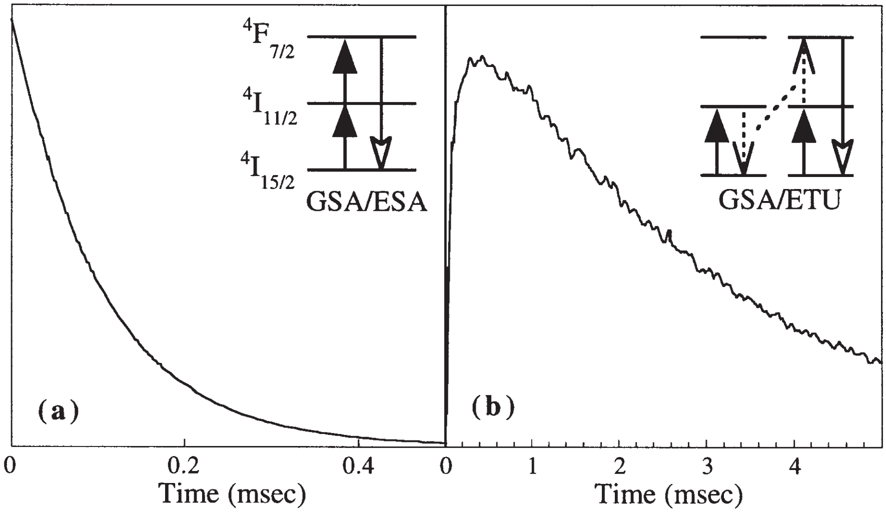

Fig. 4. 10 K time dependence of the $^4F_{7/2} \rightarrow {}^4I_{15/2}$ upconversion luminescence intensity of 1% Er^{3+}: $RbGd_2Br_7$ following 10 ns pulsed excitation into: **a** peak B3; **b** peak A in Fig. 3. The *insets* show the corresponding upconversion mechanisms of (a) GSA/ESA and (b) GSA/ETU. Adapted from [21]

As shown in Figs. 3 and 4, this combination of excitation scans and time dependence measurements can be used to determine the mechanism responsible for upconversion luminescence in a simple three-level system. By extension, the same approach can be used in studies of more complicated upconversion systems constructed from the basic mechanistic building blocks of absorption and energy transfer.

4
Rate Equation Models for Excited-State Dynamics

As illustrated by the discussion in Sects. 2 and 3 and the example in Figs. 3 and 4, the pertinent questions related to whether or not upconversion is observed are essentially kinetics questions: Does a system luminesce from higher excited states before undergoing interexcited-state relaxation? Can multiphoton excitation rates compete with interexcited-state relaxation rates? What is the rate-determining step in generating upconversion luminescence? Consequently, it is important to describe the kinetics of such a system in some detail. As with any chemical reaction, this is done by setting up a system of rate equations describing the concentrations of each of the relevant species, which in this case are the population densities, N_n, of the participating electronic states, n, and using rate constants to control the dynamic evolution of these populations. Figure 5 shows a model kinetic scheme describing a general three-level upconversion system similar to that observed experimentally in Fig. 3. This scheme contains contributions from all of the relevant rate parameters, including GSA (G) and ESA (E)

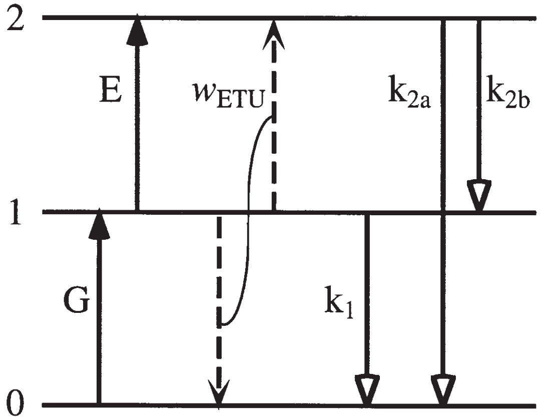

Fig. 5. Schematic illustration of the kinetic parameters described by the coupled rate equations of Eq. (10) for a three-level ensemble upconversion system. The *solid arrows* represent radiative processes and the *dashed arrows* represent nonradiative processes. G is the GSA rate constant, E is the ESA rate constant, w_{ETU} is the power-independent upconversion rate parameter, and k_n are linear decay rate constants

excitation rate constants (see Eq. 5), and the linear decay rate constants associated with each possible single-ion decay route (k_1, k_{2a}, and k_{2b}, where $k_2 = k_{2a} + k_{2b}$). In addition, the power-independent parameter describing the two-center ETU process is shown (w_{ETU}). Cross relaxation is not considered here, although it is easily accommodated in the rate equations. The time dependent population densities, dN_n/dt, of the three levels $n = 0, 1$, and 2, are then given by

$$\begin{aligned}\frac{dN_0}{dt} &= -\,\mathrm{G}N_0 + k_1N_1 + k_{2a}N_2 + w_{ETU}(N_1)^2\\ \frac{dN_1}{dt} &= \mathrm{G}N_0 - \mathrm{E}N_1 - k, N, + k_{2b}N_2 - 2w_{ETU}(N_1)^2\\ \frac{dN_2}{dt} &= \mathrm{E}N_1 - (k_{2a} + k_{2b})N_2 + w_{ETU}(N_1)^2\end{aligned} \tag{10}$$

At this level of description, this ensemble model assumes homogeneous doping and excitation densities such that the entire ensemble of ions can be described as having identical environments at all times, and the entire ensemble participates equally in the photodynamics of the system.

From these rate equations, a number of experimental observables can be simulated. Figure 6 shows the time-dependent upconversion decay curves calculated for a set of hypothetical three-level systems involving (a, b) pure ESA, (c, d) pure ETU, and (e, f) mixed ESA:ETU (40:60) rates under steady-state conditions, calculated to simulate the two experimental observables of decay following short pulses (a, c, e), as described above, and decay following long square-wave pulses during which the system has reached steady state (b, d, f).

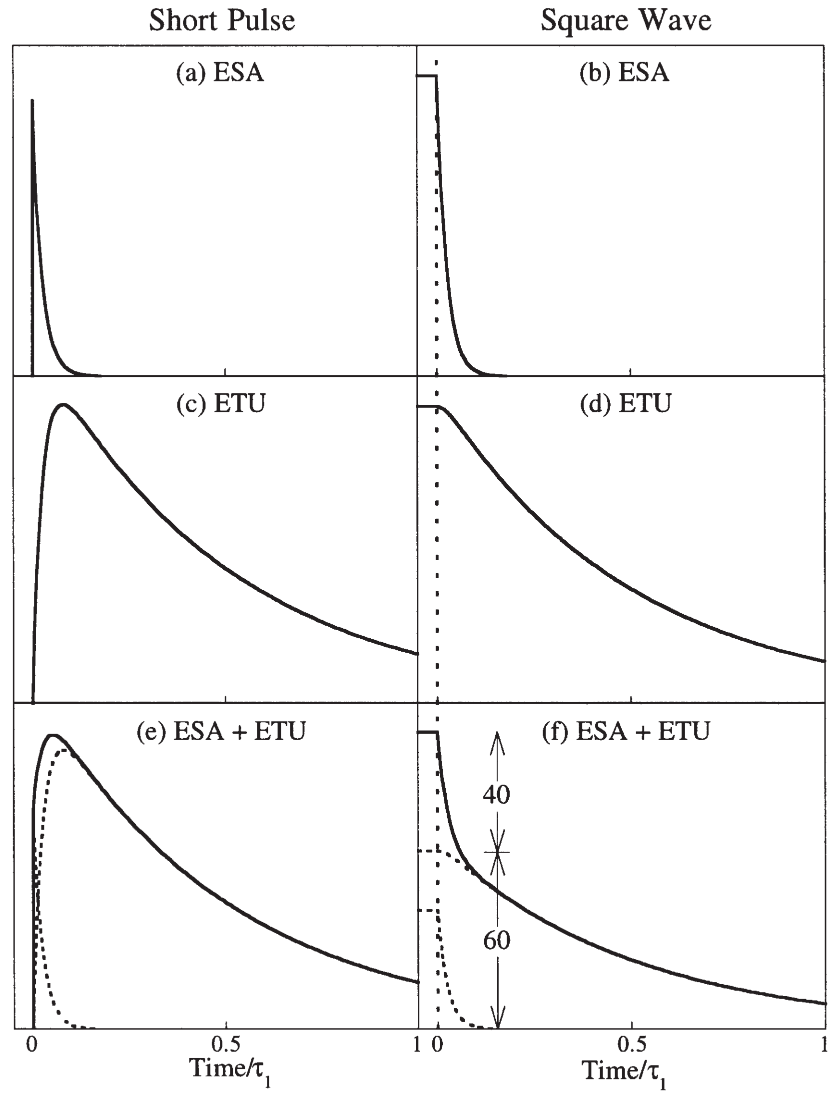

Fig. 6a–f. Time-dependent populations of level 2 in Fig. 5 calculated from Eq. (10) using the following parameters: Short pulse, at Time = 0: **a** $N_1 = 2$, $N_2 = 8\times10^{-20}$, $w_{\mathrm{ETU}} = 0$; **c** $N_1 = 2$, $N_2 = 0$, $w_{\mathrm{ETU}} = 7.5\times10^{-22}$; **e** $N_1 = 2$, $N_2 = 8\times10^{-20}$, $w_{\mathrm{ETU}} = 7.5\times10^{-22}$. Square wave, at Time <0 (excited steady state): **b** $G = 10^{-20}$, $E = 10^{-21}$, $N_1 = 2$, $N_2 = 8\times10^{-20}$, $w_{\mathrm{ETU}} = 0$; **d** $G = 10^{-20}$, $E = 0$, $N_1 = 2$, $N_2 = 1.2\times10^{-19}$, $w_{\mathrm{ETU}} = 7.5\times10^{-22}$; **f** $G = 10^{-20}$, $E = 10^{-21}$, $N_1 = 2$, $N_2 = 2\times10^{-19}$, $w_{\mathrm{ETU}} = 7.5\times10^{-22}$ ($E\,N_1 = 0.66\ w_{\mathrm{ETU}}\ N_1^2$). The *vertical dashed lines* in (b), (d), and (f) indicate the termination of the square laser pulse. For all curves, $k_1 = 1$, $k_{2a} = 20$, and $k_{2b} = 20$, $G = E = 0$ at time ≥ 0, and $N_0(0) = 2\times10^{20}$. (Units: $N_n = \mathrm{cm}^{-3}$, $G = E = k_n = \mathrm{s}^{-1}$, $w_{\mathrm{ETU}} = \mathrm{cm}^3\,\mathrm{s}^{-1}$). These parameters correspond to the small-upconversion limit and $k_2 \gg k_1$ in all cases. The parameters correspond to 100% GSA/ESA in (a) and (b), 100% GSA/ETU in (c) and (d). The parameters for (f) were chosen such that, under steady state conditions, 40% of N_2 derives from GSA/ESA and 60% from GSA/ETU, and the same parameters were then used for (e) at time = 0. The *dashed curves* in (e) and (f) show the contributions from ESA and ETU to the total intensity

The same parameters are used for each of the two simulation modes, and involve the usually encountered situation of $(k_{2a} + k_{2b}) > k_1$. The specific parameters used are listed in the figure caption. Importantly, all simulations reflect low-excitation-densities and low-upconversion rates, where the upconversion processes contribute in only a perturbative way to the intermediate-level populations and decay rates (i.e., $k_1 N_1 \gg E N_1$ or $2 w_{\mathrm{ETU}} N_1^2$). This corresponds to a power range that is experimentally easily accessible. As shall be described in Sect. 5, the use of higher pumping powers may in some cases lead to significant and interesting deviations from the behavior described in this section.

Figure 6a, b shows the results simulated for a case in which $\mathrm{E} \neq 0$ and $w_{\mathrm{ETU}} = 0$, i.e., only GSA/ESA is active. In both the pulsed and square-wave experiments, an immediate decay is predicted which is governed by the decay rate constant of the upper state, $k_2 = k_{2a} + k_{2b}$. These curves are analogous to that observed experimentally for $\mathrm{Er^{3+}}$:$\mathrm{RbGd_2Br_7}$ in Fig. 4a.

Figure 6c, d shows the results simulated for a case in which $w_{\mathrm{ETU}} \neq 0$ but $\mathrm{E} = 0$, i.e., only GSA/ETU is active. The pulsed experiment, Fig. 6c, shows the characteristic delayed maximum observed in Fig. 4b. When $\mathrm{E} = 0$, N_2 has a value of exactly zero at time zero, and so the rise of the upconversion transient truly begins at zero. Comparison to Fig. 6a, b shows that this rise derives from the decay rate constant of the upper state, $k_2 = k_{2a} + k_{2b}$. Since N_2 is proportional to N_1^2 in ETU (Eqs. 7 and 10), the decay of the transient N_2 population lasts substantially longer than the natural decay of the upper state, and has a rate constant exactly twice that of N_1 under these low-power conditions when all of the above assumptions are met. Figure 6d shows the corresponding data following a square pulse. The decay again proceeds with a rate constant exactly twice that of N_1 under the assumed conditions, with a small deviation at short times where k_2 is still consequential. Based on this comparison, it is clear that ESA and ETU mechanisms are readily distinguishable using either square-wave or pulsed excitation modes under these conditions (see below for $k_2 \leq k_1$).

Figure 6e, f show the experimentally relevant case in which a mixture of mechanisms occurs, i.e., $\mathrm{E} \neq 0$ and $w_{\mathrm{ETU}} \neq 0$. The parameters have been chosen such that under steady-state excitation conditions 40% of the upconversion is generated by GSA/ESA, and 60% by GSA/ETU. Panel e shows that following a short pulse the properties of both panels a and c can be identified. Specifically, a nonzero N_2 is observed at time = 0, but a delayed maximum and a long decay time are also observed. This provides a way to identify intensity involving both GSA/ESA and GSA/ETU contributions. This transient curve is triexponential, involving the decay of the GSA/ESA population, and the rise and decay of the GSA/ETU population (dashed lines). The analogous square-wave transient is shown in Fig. 6f. Termination of the square pulse leads to a simple biexponential decay curve, with a fast component corresponding to the natural decay rate of the upper state, and a slow component corresponding to twice the decay rate of the intermediate state (dashed lines). Again, a small deviation from pure biexponential behavior is observed at short times due to the effect of k_2. The relative contributions of each mechanism, in this case 40:60, can be determined from the decay curve as shown in Fig. 6f. This information can be introduced directly into Eq. (10) for data simulation.

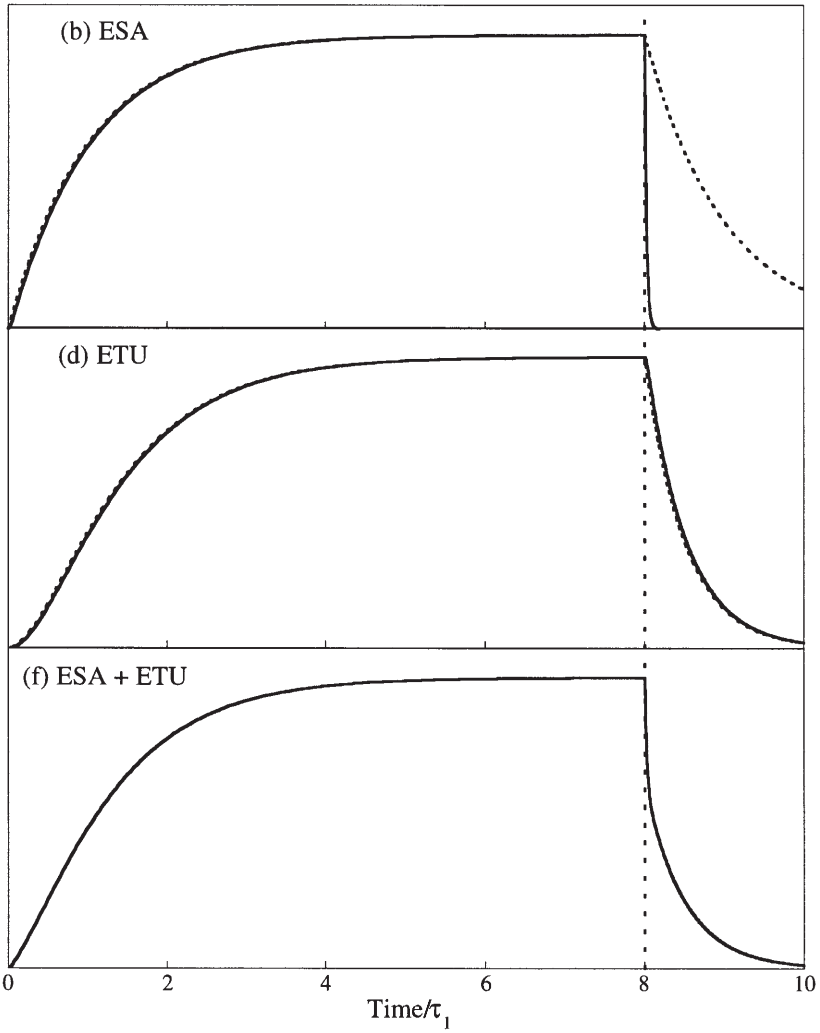

Fig. 7 b, d, f. Time-dependent populations of level 2 in Fig. 5 calculated from Eq. (10) using the same kinetic parameters as in Fig. 6b, d, f. The *vertical dashed lines* indicate the termination of the square laser pulse. The *dashed curves* show the evolution of (b) N_1 and (d) N_1^2, normalized for comparison

In addition to decay information, the square-wave experiment provides information relevant to the population of the intermediate state. Figure 7 shows the full square-wave upconversion responses calculated for the same three cases described in Fig. 6. The rise behavior of all three curves is similar, each occurring on the same time scale as the rise of the intermediate population. The rise of N_2 in Fig. 7b, the ESA case, is in fact nearly superimposable with the corresponding rise of N_1 upon introduction of the laser beam at time zero, shown as a dashed line. This direct correspondence derives from the linear dependence of N_2 on N_1 in Eq. (6) and in the $\mathrm{E}N_1$ term of Eq. (10). Only a small intensity deviation is observed between the normalized N_2 and N_1 rise curves in the short time domain, corresponding to the effects of k_2 in Eq. (10). In contrast, the rise of N_2 in Fig. 7 d, ETU, shows a delayed increase. This slow rise is approximately quadratic at short times, and this curve is nearly superimposable with the normalized *squared* N_1 response curve (dashed line) in both the rise and the decay. This relationship derives from the dependence in Eqs. (7) and (10) of N_2 on N_1^2 in the case of ETU. The mixed curve in Fig. 7 f shows properties of both b and d.

The condition specifying that the intermediate lifetime is substantially longer than that of the upper state is met in most cases, but not in all. This is because higher-excited states by definition have more radiative decay pathways and emit at shorter wavelengths, and both factors contribute to increasing their total radiative decay rate constants (see Eqs. 2 and 4). Upper states are also generally more susceptible to nonradiative cross-relaxation deactivation through channels not available to lower-energy states. Nevertheless, upconversion processes involving short-lived intermediates with longer-lived upper states are occasionally encountered. Many of the correlations described above are only applicable when k_1 is significantly smaller than k_2. As k_2 decreases and becomes comparable to or smaller than k_1, the information content of such experiments declines significantly. The analogous curves calculated for short-pulse excitation using a ratio of $k_2 = k_1/40$ show the following: while the pure GSA/ETU and GSA/ESA curves are still distinguishable by a delayed maximum in the former, the case of 40% ESA:60% ETU is essentially indistinguishable from that of the pure ESA. In the limit of $k_2 \ll k_1$, the upconversion rise time is correlated with the lifetime of the intermediate level, and the decay time with that of the upper level. The situation is even less informative for the square-wave experiment, where a negligible deviation is discernible between all three curves, occurring at the shortest time only.

To determine fully the kinetic parameters governing upconversion using Eq. (10) it is imperative to know the laser-induced excitation densities, N_1 and N_2, in steady state, or $N_1(0)$ and $N_2(0)$ in time-dependent studies. These parameters may be determined from careful measurement of the physical properties of the sample, the excitation configuration, and the experimentally absorbed power. These numbers are not easily reliably determined, however, and they are therefore more commonly estimated or taken as experimental unknowns in the use of these equations for simulations. The difficulty with which absolute excitation densities are determined is one of the practical limitations of this rate equation model.

A second commonly invoked kinetic model for ETU processes is the so-called Dimer Model [22, 23], in which pairs are treated as distinct isolated entities. Such scenarios are often encountered when trivalent rare-earth metal ions are substituted into divalent host lattices of the $\mathrm{CsNiCl_3}$ type. In these hosts, only small concentrations of $\mathrm{M^{3+}}$ ions can typically be incorporated, and it has been shown that more than 90% of all ions are introduced as ($\mathrm{M^{3+}}$ – vacancy – $\mathrm{M^{3+}}$) pairs to satisfy charge compensation requirements [24, 25]. The ions are thus introduced as isolated pairs. In this model, three excitation populations are considered. The first, N_1, refers to singly-excited dimers, i.e., those having only one ion excited to level 1. This population is assumed to behave as in Eq. (1), with $k_{tot} = k_1$. The second population, N_d, refers to dimers where both ions are excited to level 1. This population decays with a rate constant $k_d = 2k_1$, since deexcitation of either ion in the pair reduces N_d. The third population, N_2, derives from ETU involving the population N_d, and refers to dimers having one ion in level 2 and one ion in the ground state. The population N_2 decays with the rate constant k_2. The rate equations relevant to upconversion immediately following a short pulse in this model are given in Eq. (11) [22, 23]:

$$\begin{aligned}\frac{dN_d}{dt} &= -w'_{ETU}N_d - 2k_1N_d \\ \frac{dN_2}{dt} &= w'_{ETU}N_d - k_2N_2\end{aligned} \tag{11}$$

Note that the power-independent rate constant w'_{ETU} (s^{-1}) does not have the same units as w_{ETU} (s^{-1} cm^{-3}) in Eq. (10). Immediately following a short excitation pulse, the luminescence dynamics behave as described by Eq. (12) [22, 23]:

$$\begin{aligned}N_d &\propto e^{-(w'_{ETU}+2k_1)t} \\ N_2 &\propto e^{-(w'_{ETU}+2k_1)t} - e^{-k_2t}\end{aligned} \tag{12}$$

As with the ensemble model rate equations in Eq. (10), when $k_2 \gg k_1$ the upconverted population decays with a rate constant of twice that of the single ion, k_1, with modification due to the ETU rate constant, w'_{ETU}, when the latter is significant. A rise corresponding to the upper-state decay rate constant k_2 is observed. Again, when $k_2 \ll k_1$, k_2 dominates the upconversion decay, and the rise is determined by $2k_1 + w'_{ETU}$. k_1 is generally determined experimentally from the intermediate level downconversion by assuming that the observed signal is from singly-excited dimers and monomeric sites only [22, 23]. Input of this value for k_1 into Eq. (12) allows a value of w'_{ETU} to be determined directly from the upconversion decay profile. Importantly, no experimental determination of absolute population densities is required to obtain an absolute ETU rate constant, w'_{ETU}, in this model. As shall be seen in Sect. 8, this model also provides a conceptual advantage over the ensemble model of Eq. (10) even for describing ETU in isotropically-doped samples, since even in this case ETU occurs only within the innermost shells having the closest ion-ion separations.

5
Upconversion Power Dependence

The energy- and time-dependence of an upconversion process are extremely useful for identification of the upconversion mechanism. A third variable parameter that has received relatively little attention is the excitation power. It is often stated in the literature that two-photon excitation processes such as upconversion must follow a quadratic power dependence, or more generally, that the intensity of an n-photon excitation process will scale with P^n. This statement is only true, however, under certain experimental conditions. For example, the double-log power-dependence data in Fig. 8 were collected for the two-, three-, and four-photon excitations of Er^{3+}: $Cs_3Lu_2Cl_9$ using 6500 cm^{-1} (1.54 μm) NIR excitation as illustrated in Fig. 8a [26]. Data for 1% and 100% Er^{3+} concentrations are shown in Fig. 8b and c, respectively. The energy level scheme (a) for Er^{3+} shows that a series of excited states are energetically accessible through the sequential GSA and ESA of 6500 cm^{-1} photons, with ETU events also possible in some steps. In the 1% sample (Fig. 8b), both GSA/ESA and GSA/ETU mechanisms are found to be active. At the lowest power, the various excited-state populations all show power dependencies roughly proportional to P^n, with slopes of 1.8, 2.6, and 3.6 observed for the 2, 3, and 4-photon upconversion processes, respectively. Increasing the power in the 1% sample leads to a significant reduction of all three slopes (Fig. 8b). In the 100% sample (Fig. 8c), GSA/ETU dominates, and at the lowest experimental power, the power-dependence shows slopes comparable to those attained at high powers in the 1% sample. At the highest power in the 100% sample, these slopes are reduced to only 0.8, 0.8, and 1.0. These data thus reveal that this power dependence is itself power dependent.

To understand the origin of such behavior, we consider the power dependence of the rate equations presented in Eq. (10) [26–28]. Since the 100% sample in Fig. 8c shows pure GSA/ETU behavior, we consider the power dependence of

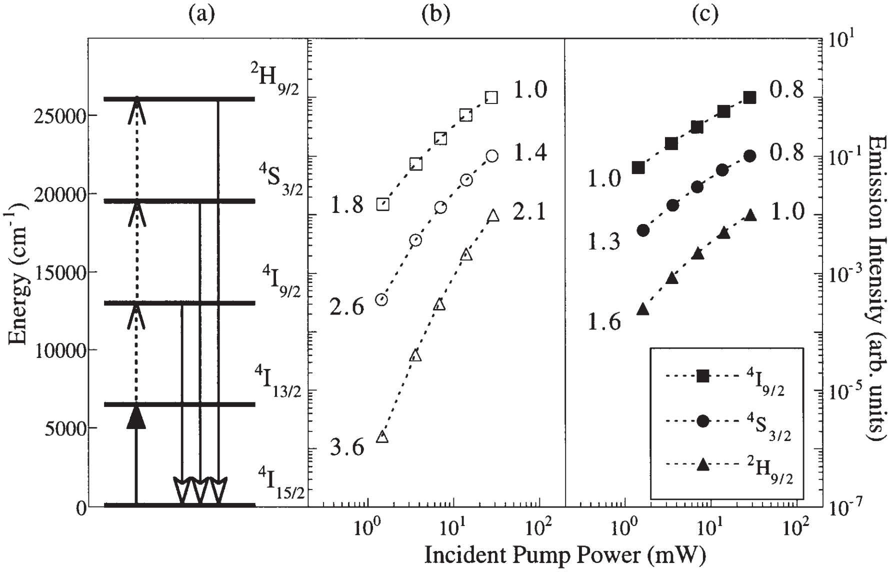

Fig. 8. **a** Multiphoton pumping scheme for Er^{3+} excited with 6500 cm^{-1} photons. **b, c** Measured emission intensities from the $^4I_{9/2}$ (2-photon), $^4S_{3/2}$ (3-photon), and $^2H_{9/2}$ (4-photon excitation) levels in (b) 1% Er^{3+}:$Cs_3Lu_2Cl_9$ and (c) $Cs_3Er_2Cl_9$ vs pump power at 6500 cm^{-1} in double-logarithmic representation. The numbers denote the slopes at low and high pump powers. Adapted from [26, 27]

this mechanism first, and return to that of the GSA/ESA mechanism afterwards. At low powers, $k_1N_1 \gg 2w_{\mathrm{ETU}}N_1{}^2$, and upconversion is a minor kinetic perturbation. The dominant depopulation channel of level 1 is via linear decay, k_1. Approximating the population of level 0 as a constant, Eq. (10) simplifies to

$$\begin{aligned} \frac{dN_1}{dt} &= \mathrm{G}N_0 - k_1N_1 \\ \frac{dN_2}{dt} &= -(k_{2a}+k_{2b})N_2 + w_{\mathrm{ETU}}(N_1)^2 \end{aligned} \tag{13}$$

Under steady-state conditions,

$$N_1 = \frac{1}{k_1}(\mathrm{G}N_0) \propto P^1 \tag{14}$$

and

$$N_2 = \frac{w_{\mathrm{ETU}}}{k_1^2(k_{2a}+k_{2b})}(\mathrm{G}N_0)^2 \propto P^2 \tag{15}$$

Thus, under low-power excitation conditions, the GSA/ETU intensity has the quadratic power dependence commonly discussed in the literature.

As the excitation power is increased, the upconversion rate $w_{\mathrm{ETU}}N_1^2$ increases much more rapidly than does k_1N_1, and above a certain power the high-power limiting condition of $k_1N_1 \ll 2w_{\mathrm{ETU}}N_1^2$ may be reached. At this power, upconversion is so rapid that it has become the dominant depopulation mechanism for the intermediate level. Inserting this limiting condition into Eq. 10 yields

$$\begin{aligned} \frac{dN_1}{dt} &= \mathrm{G}N_0 - 2w_{\mathrm{ETU}}(N_1)^2 + k_{2b}N_2 \\ \frac{dN_2}{dt} &= -(k_{2a}+k_{2b})N_2 + w_{\mathrm{ETU}}(N_1)^2 \end{aligned} \tag{16}$$

Under steady-state conditions,

$$N_1 = \left[\frac{(k_{2a}+k_{2b})}{w_{\mathrm{ETU}}(2k_{2a}+k_{2b})}(\mathrm{G}N_0)\right]^{1/2} \propto P^{1/2} \tag{17}$$

and

$$N_2 = \frac{1}{2k_{2a}+k_{2b}}(\mathrm{G}N_0) \propto P^1 \tag{18}$$

Thus, under high-power excitation conditions the GSA/ETU intensity no longer shows a quadratic power dependence, but rather increases with a linear dependence on power. The intermediate level population increases as the square root of the power. Note that although this behavior resembles a saturation effect, it does not derive from depletion of the ground-state population due to high excitation rates, but is indeed a property of the intermediate level branching kinetics. For comparison, Fig. 9a shows the power dependence of N_1 and N_2 in a double-logarithmic representation calculated for a GSA/ETU process using Eq. (10), where the dashed lines have the limiting slopes for low- and high-power excitation derived in Eqs. (13–18). Since the level populations are coupled in Eq. (10), the behavior of the lower level affects that of the upper level. In particular, the relationship $N_2 \propto N_1^2$ ensures that the N_2 curve is proportional to the square of the N_1 curve at all points. The slopes of the two curves at any given power are determined by the branching ratio between linear downconversion, $k_1 N_1$, and upconversion, $2 w_{\mathrm{ETU}} N_1^2$, rates at that power (or k_1 and $2 w_{\mathrm{ETU}} N_1$ rate constants). The log of this branching ratio is plotted in Fig. 9b as a function of the log of the excitation power. As seen from comparison of Fig. 9a and 9b, the derivative of the double-log power dependence curve is changing most rapidly when $k_1 = 2 w_{\mathrm{ETU}} N_1$, i.e., at the point M in Fig. 9b. The full curves in Fig. 9a are, for practical purposes, indistinguishable from their limiting asymptotes at $k_1 > \sim 50 (2 w_{\mathrm{ETU}} N_1)$ and $50\, k_1 < \sim 2 w_{\mathrm{ETU}} N_1$ (dashed curves).

Similar treatment of three-level GSA/ESA upconversion, assuming $k_2 = k_{2a}$, yields Eqs. (19–22).

Low-power limit:

$$N_1 = \frac{\mathrm{G} N_0}{k_1} \propto P^1 \tag{19}$$

$$N_2 = \frac{\mathrm{GE} N_0}{k_1 k_2} \propto P^2 \tag{20}$$

High-power limit:

$$N_1 = \frac{\mathrm{G} N_0}{\mathrm{E}} \propto P^0 \tag{21}$$

$$N_2 = \frac{\mathrm{G} N_0}{k_2} \propto P^1 \tag{22}$$

Thus, whereas GSA/ESA upconversion luminescence under low-power conditions shows the anticipated quadratic power dependence, that observed under high-power excitation conditions is expected to show only a linear dependence on pump power, exactly as in the GSA/ETU case (Eqs. 15 and 18). The intermediate-level population in a GSA/ESA system, however, remarkably becomes independent of changes in power at high powers when $k_2 = k_{2a}$ (Eq. 21), in contrast with the high-power $P^{1/2}$ behavior of the intermediate-level population in the GSA/ETU mechanism (Eq. 17). When $k_2 = k_{2b}$ in a GSA/ESA process the high power behaviors are identical to the low power behaviors described by Eqs. (19) and (20).

All of the cases treated in this section have been for the simplest three-level upconversion systems, under both GSA/ETU and GSA/ESA two-photon excitation conditions. For higher order multiphoton excitation processes, a number of

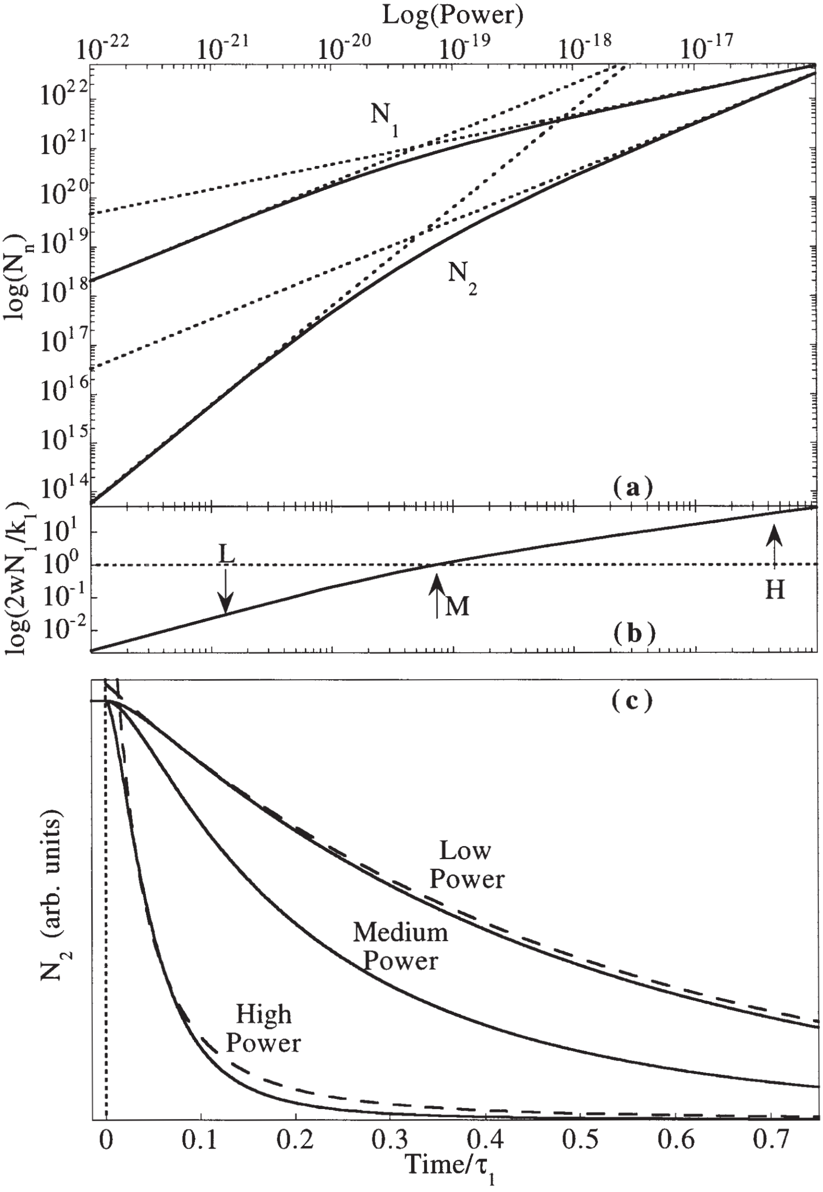

Fig. 9. **a** Double-logarithmic power dependence of the population densities, N_1 and N_2, of levels 1 and 2 in Fig. 5 calculated from Eq. (10) using the same parameters as in Fig. 6c, where power is taken as G. The *dashed lines* are the limiting slopes from Eqs. (14) and (15). **b** Double-logarithmic power dependence of the level 1 depopulation rate ratio between ETU (rate = $2w_{\mathrm{ETU}}N_1^2$) and linear downconversion (rate = k_1N_1). The *horizontal dashed line* indicates equal rates for the two. **c** Time-evolution of N_2 following termination of a cw beam at $t = 0$ for the high, medium, and low powers indicated in (b), plotted on linear axes. The *dashed lines* are the limiting behaviors from Eqs. (22) and (24)

scenarios can exist involving different combinations of relaxation pathways or ESA and ETU steps. Analytical solutions describing the power dependence asymptotes for the simplest of these are listed in Table 1 [27].

The time-dependent evolution of the level populations may also be dependent upon power. As described in Sect. 4, the GSA/ESA mechanism yields level populations that decay with their natural decay rate in the absence of excitation power. The N_1 and N_2 decay curves in the pure GSA/ESA limit are therefore independent of excitation power. This is not true for the GSA/ETU mechanism, which continues to function after termination of the excitation source. All of the time-dependence curves discussed in Sect. 4 were calculated using Eq. (10) under low-power conditions. In this limit, when $k_2 > k_1$, the kinetics inherent to level 1 are rate determining and the decay behaviors for the two metastable populations determined from integration of Eq. (13) are given by

$$N_1(t) \propto e^{-k_1 t} \tag{23}$$

and

$$N_2(t) \propto e^{-2k_1 t} \tag{24}$$

The decay rate constants of both N_1 and N_2 are independent of excitation power or N_1 excitation density under these low-power excitation conditions, and the upconversion decay rate constant of N_2 equals $2k_1$. This analytical limiting decay curve is plotted in Fig. 9c as the low-power dashed line, and compares very well to the numerical solution of Eq. (10) obtained for $k_1/2w_{\mathrm{ETU}}N_1 = 37$ (low power in Fig. 9b).

Under high-power conditions, where $2w_{\mathrm{ETU}}N_1 \gg k_1$, the decay curves take the form

$$N_1(t) \propto (N_1(0)\, w_{\mathrm{ETU}}\, t + 1)^{-1} \tag{25}$$

and

$$N_2(t) \propto (N_1(0)\, w_{\mathrm{ETU}}\, t + 1)^{-2} \tag{26}$$

Table 1. Double-logarithmic slopes of the steady-state excited-state population densities, N_i, of levels $i = 1 \ldots n$ and luminescences from these states for n-photon excitation. The investigated limits are: 1. small upconversion or 2. large upconversion by A) ETU or B) ESA, and decay predominantly i) into the next lower-lying state or ii) by luminescence to the ground state. Adapted from [27]

Influence of upconversion	Upconversion mechanism	Predominant decay route	Power dependence	From level
1. Small	ETU or ESA	Next lower state or ground state	$N_i \propto P^i$	$i = 1 \ldots n$
2. Large	A) ETU	i) Next lower state	$N_i \propto P^{i/n}$	$i = 1 \ldots n$
		ii) Ground state	$N_i \propto P^{1/2}$ $N_n \propto P^1$	$i = 1 \ldots n-1$
	B) ESA	i) Next lower state	$N_i \propto P^i$	$i = 1 \ldots n$
		ii) Ground state	$N_i \propto P^0$ $N_n \propto P^1$	$i = 1 \ldots n-1$

In contrast with the low-power expressions in Eqs. (23) and (24), Eqs. (25) and (26) are not exponential functions of time. In this limit, the N_1 and N_2 decay curves are both dependent upon excitation power, which is linearly proportional to $N_1(0)$. Note that the ratio of $2\,w_{\mathrm{ETU}}N_1/k_1$ changes with time in the absence of an excitation beam, so any analytical solution will only be approximate and only applicable to the short-time dynamics. Nevertheless, the comparison between the N_2 decay curve approximated by Eq. (26), included as a dashed line in Fig. 9 c, and the high-power decay curve calculated numerically from Eq. (10), shown as a solid line in Fig. 9 c, is satisfactory. Relative to the low-power decay curves, the key features of both high-power decay curves shown in Fig. 9 c can be summarized as (a) a more rapid decay time and (b) a nonexponential decay curvature. Equally important is the observation that the high-power decay behavior described by Eqs. (25) and (26) can be related to the power-independent ETU parameter w_{ETU}. Careful determination of $N_1(0)$ thus allows determination of w_{ETU} from time dependence data in such GSA/ETU systems [29–31].

Several examples of power-dependent upconversion behavior similar to that calculated in Fig. 9 have been identified experimentally [27]. Returning to the experimental example of Er^{3+}:$Cs_3Lu_2Cl_9$ introduced above [26], at low powers and low concentration in Fig. 8b, upconversion is inefficient and the slopes are seen to approach the P^n low-power limit for each excited state. As the power is increased in the 1% sample, the upconversion becomes competitive with downconversion and the slopes of all three upconversion luminescences decrease in a correlated way. At the highest accessible powers, upconversion and downconversion rates in this sample are comparable in magnitude. By raising concentrations, both absorption and ETU rates become significantly larger and the higher absorbed power region may be probed. Pulsed experiments show that GSA/ETU mechanisms dominate for all upconversion luminescence features in the 100% sample [26]. Increasing the power in the 100% sample results in slopes approaching the theoretical limit of 0.5 for $n = 2$ and 3, and 1.0 for $n = 4$ in the sequential ETU scenario described by case 2 A ii of Table 1. At the highest experimental powers and concentrations, the main depletion mechanism for all but the highest excited state is therefore ETU, not linear decay. This is a remarkable result given the number of quanta involved in this upconversion process, and indicates that this is an extremely efficient four-photon excitation scheme.

Measurements on other systems confirm the generality of this approach [27]. Deviations from the expected or calculated results are also observed in ETU systems, however, and appear to result from the breakdown of the assumptions inherent to the ensemble model rate equations presented in Eq. (10) [28]. Such breakdowns arise whenever dopant ions do not all have homogeneous environments, either geometrically or in excitation density. In a statistically-doped sample, a broad range of interionic separations may exist, and consequently a correspondingly large range of w_{ETU} values may also be operative. Ions having nearby neighbors will have the largest w_{ETU} values and will show competitive upconversion kinetics at lower powers. Other more isolated ions will always behave as in the low-power regime (i.e., $k_1 \gg 2\,w_{\mathrm{ETU}}N_1$). Since the former dominate the observed upconversion signals while the latter dominate the observed downconversion signals, power-dependence measurements of the two do not always track one another as predicted by Eq. (10) and shown in Fig. 9a [28, 32].

In summary, power dependence measurements can provide insight into the relative magnitudes of upconversion vs linear decay rates under real experimental conditions. Efficient upconversion systems will show deviations from the commonly asserted P^n power dependence, as upconversion shifts from being a kinetic perturbation in the low-power regime to being the dominant process affecting intermediate-level kinetics in the high-power regime.

6
Two-Color Excitation Experiments

In an experiment involving GSA/ESA excitation with a laser, both GSA and ESA steps must be accessible with the same photon energy. The use of two excitation sources, i.e., a two-color experiment, allows the efficiencies of the GSA and ESA steps to be optimized independently, which may lead to a substantial gain in overall upconversion performance if these two steps have maximum absorption cross sections at different wavelengths. By tuning the two wavelengths λ_0 and λ_1 independently, the absorption cross sections σ_0 and σ_1 of Eq. (6) can be maximized for each transition so that N_2 is maximized. This is illustrated experimentally in Fig. 10 for the case of ~0.1% Er^{3+}:$LaCl_3$ [33]. Exciting the $^4I_{15/2} \rightarrow {}^4I_{11/2}$ absorption feature at ca. 10,200 cm^{-1} yields $^4F_{7/2}$ GSA/ESA upconversion luminescence at ca. 20,400 cm^{-1}, as shown in Fig. 10a. The 78 K one-color upconversion excitation scan in this region, shown in Fig. 10b, has one dominant peak at 10,239.4 cm^{-1} with several small peaks to either side. Time-dependence studies show that this intense feature is due solely to GSA/ESA upconversion. Two two-color excitation scans are also shown in Fig. 10b. These were collected using a fixed excitation beam at the energy of the arrow, while scanning a second laser beam across the relevant energy region and probing the upconversion luminescence intensity. The spectrum marked "ESE" shows the upconversion excitation scan obtained with the fixed laser exciting into the highest-intensity GSA feature. This is an excited-state excitation spectrum (ESE), and probes the $^4I_{11/2} \rightarrow {}^4F_{7/2}$ ESA transitions. The ESE intensities are directly proportional to the ESA cross sections, σ_1, at the various excitation energies. The lowest-energy ESE feature is seen to correspond with the intense peak of the one-color excitation scan. The spectrum marked "GSE" was obtained while exciting into the most intense ESA peak (arrow) and monitoring the upconversion luminescence as a function of the second laser energy. The resulting spectrum closely resembles the $^4I_{15/2} \rightarrow {}^4I_{11/2}$ GSA spectrum obtained by conventional absorption techniques, and has intensities proportional to the GSA cross sections, σ_0, at the various excitation energies. The highest-energy feature of the GSE spectrum corresponds in energy with the intense feature of the one-color excitation scan.

Since $N_2 \propto \sigma_0\sigma_1$ (Eq. 6), intensity in the one-color upconversion excitation spectrum derives from the regions of overlap between the GSE and ESE spectra. From inspection of the data in Fig. 10 it is clear that the maximum of the one-color excitation scan results from the direct spectral overlap of two weak GSA and ESA features at 10,239.1 cm^{-1} and 10,240.0 cm^{-1}, respectively. The maximum

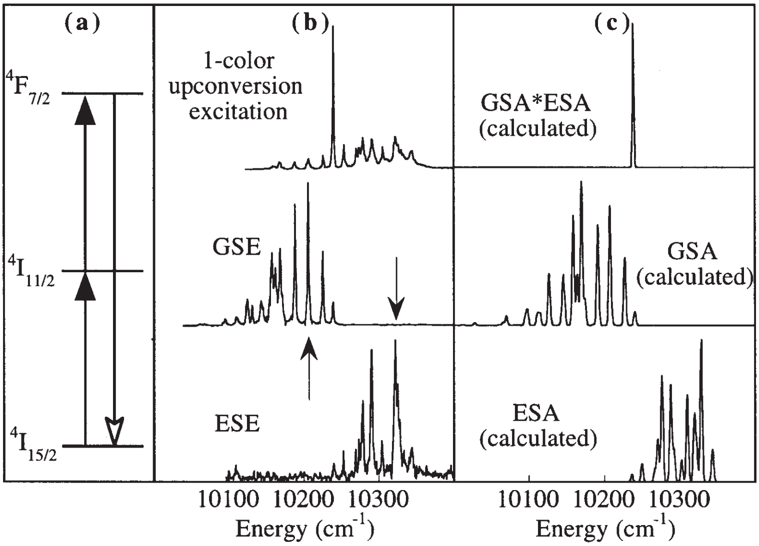

Fig. 10. **a** Two-photon upconversion excitation and luminescence scheme in Er^{3+}:$LaCl_3$. **b** One- and two-color upconversion excitation spectra of the $^4F_{7/2}$ luminescence in <1% Er^{3+}:$LaCl_3$ at 78 K. The excitation was σ polarized (E||a). The *upper trace* shows the one-color excitation scan, while the two *lower traces* show the two-color excitation scans obtained with one excitation energy fixed at the *arrow*. The spectra were not corrected for the decrease in laser power towards lower energies. **c** The *lower two traces* show the calculated intensity distributions for the GSA ($^4I_{15/2} \rightarrow {}^4I_{11/2}$) and ESA ($^4I_{11/2} \rightarrow {}^4F_{7/2}$) excitations at 78 K assuming Boltzmann distributions in both initial multiplets. The *upper trace* is the product of the calculated GSA and ESA traces, showing the maximum one-color overlap at the same energy as observed experimentally in (b). All spectra in (b) and (c) have been normalized to their highest intensity feature. Adapted from [33, 40]

two-color intensity, obtained with excitation simultaneously at the two arrows, is roughly two orders of magnitude greater than that of the one-color experiment. The sideband intensities observed in the one-color excitation spectrum (Fig. 10b) may derive from weak vibronic sideband absorption intensity or from a weak ETU mechanism as described in Sect. 3.

Two-color excitation can thus provide orders of magnitude intensity gains for GSA/ESA upconversion processes through the optimization of both σ_0 and σ_1. For practical applications such as lasing or imaging, this can lead to superior performance [6]. Two-color upconversion excitation methods have been applied in other cases to generate efficient upconversion where little or none was observed under one-color conditions, or to advance mechanistic studies.

7
Calculation of Rare-Earth Excited-State Absorption Properties

In view of the advantages inherent in the use of two-color excitation schemes, and the experimental difficulties associated with their implementation, it would be advantageous to be able to predict the ESA spectrum of a rare earth ion with enough precision to facilitate the design of such experiments. In the ideal case, calculations would allow prediction of when such an excitation scheme would be beneficial, and at which two wavelengths and with which polarization excitation should occur. Because of the narrow widths of f-f transitions in rare earth ions, this is an extremely challenging task.

Two semiempirical approaches are commonly applied in calculating the energies and intensities of f-f transitions in rare earth ions. The most common is the so-called Judd-Ofelt method. At this level of theory, the total oscillator strength for an f-f transition between $|SLJ\rangle$ and $|S'L'J'\rangle$ multiplets is given by Eq. (27) [34, 35]:

$$f = \frac{8\pi^2 m\nu}{3h} \frac{\chi}{2J+1} \sum_{k=2,4,6} \Omega_{(k)} |\langle SLJ || U^k || S'L'J' \rangle|^2 \tag{27}$$

where χ represents the local field corrections for electric/magnetic dipole absorption/emission processes and is simply related to the index of refraction of the sample. The reduced matrix elements of the tensor operator U^k are expressed in terms of Coulombic (F_2, F_4, and F_6) and spin-orbit (ζ) interactions. The empirical Judd-Ofelt parameters, $\Omega_{(k)}$, are obtained by least-squares fitting of Eq. (27) to experimental absorption intensity data. The experimental data should represent full multiplet-to-multiplet transition intensities, and this is generally approximated by using data from a room-temperature GSA spectrum as input. From a set of $\Omega_{(k)}$ values determined in this way, any intermultiplet transition oscillator strength may then be calculated. The Judd-Ofelt approach has proven to be extremely valuable in a number of studies involving evaluation of ESA and stimulated emission cross sections. This method is limited by its inability to provide any insight into the intensities of transitions between individual crystal-field (CF) levels of the multiplets. Clearly, the sharpness of the ESA features seen in Fig. 10b, the inequitable distribution of intensities among CF-CF peaks, and the sharpness of the laser excitation source all collaborate to mandate the use of a higher level of theory.

The energies of each of the $(2J+1)$ crystal-field levels within a multiplet may be calculated by diagonalization of the full $|SLJM_J\rangle$ matrix of a semiempirical effective Hamiltonian, $\hat{H}$, when this is expanded to include both CF and CCF terms as in Eq. (28) [36, 37]:

$$\hat{H} = \hat{H}_a + \hat{H}_{cf} + \hat{H}_{ccf} \tag{28}$$

where $\hat{H}_a$ refers to the atomic parameters, and includes all isotropic free-ion and crystal-field terms of the full Hamiltonian. Approximately 80–90% of the total $\hat{H}_a$ contribution arises from first-order Coulombic electron-electron and spin-orbit interactions within the 4f orbitals. Due to the high accuracy required of these calculations before they can be useful experimentally, however, this is not sufficient, and several higher order electrostatic and spin-orbit terms must be included in order to reproduce the experimental observables. $\hat{H}_{cf}$ and $\hat{H}_{ccf}$ represent the anisotropic components of the crystal-field interactions, consisting of one- and two-electron interaction operators, respectively. As with the Judd-Ofelt approach, parameter values of $\hat{H}$ are obtained from a least-squares fitting routine to a set of experimental energies in order to obtain high-quality wavefunction descriptions as output. From such wavefunctions, the energies of unobserved transitions may be calculated. The crystal-field eigenvectors from the energy-level calculations are also used to calculate both electric and magnetic dipole contributions to transition intensities with the use of phenomenological intensity parameters again obtained from fitting of experimental data to describe the odd-parity crystal field and electric dipole radiation field interactions with the 4f electrons [38, 39]. These crystal field calculations provide much more detailed descriptions of the properties of specific CF wavefunctions, and approach the type of predictive quality required above.

Crystal field calculations for $Er^{3+}:LaCl_3$ involving all the terms in Eq. (28) and 21 parameters were fitted to 73 experimental energies in exact C_{3h} symmetry, resulting in an rms standard deviation of 9.0 cm^{-1}, from which information pertinent to the two-color excitation data shown in Fig. 10 was calculated [40]. The relevant results are shown in Fig. 10c for comparison to the experimental results of Fig. 10b. The calculation reproduces the GSE and ESE spectra very well, and consequently also the dominant peak in the one-color upconversion excitation spectrum obtained from the product of these two. Note that these calculations do not provide information relating to the weaker vibronic GSA/ESA or GSA/ETU upconversion intensities observed experimentally in Fig. 10b. Based on these results, the prospect of calculating the information necessary to predict or even optimize a two-color excitation experiment appears promising. It is also apparent, however, that such an objective is extremely susceptible to small errors in calculated energies and/or intensities in an absolute sense. While the calculations in this case reproduce the experimental one-color excitation pattern, for example, they would predict a different combination of excitation energies for the maximum two-color upconversion intensity than is observed experimentally. The calculation also provides only integrated intensities for each of the CF-CF transitions, so bandshapes have to be approximated since monochromatic absorption cross sections are important for laser excitation. It is difficult to predict accurately the phonon-induced broadening generally observed in higher CF excitations of a given multiplet, and these need to be approximated based on the available data for the given system. With bandwidths varying by factors of 2 or more across a multiplet in the absorption spectrum, such approximations can lead to significant differences between the real and calculated monochromatic upconversion efficiencies.

Finally, the ability to calculate accurate spectral properties in a semi-empirical way relies on the quality of the data and assignments entered into the fitting routine. While such parameters may be relatively unambiguous in well-defined high-symmetry dopant sites such as $Er^{3+}:LaCl_3$, for which polarized spectroscopy is of great assistance, the application to lower-symmetry systems rapidly becomes more tenuous. Analogous calculations on the similar system $Er^{3+}:Cs_3Lu_2Cl_9$ using 23 parameters and 111 assigned transition energies yielded an rms standard deviation of 18.0 cm^{-1}, or twice that of $Er^{3+}:LaCl_3$, despite similar input size and quality [41]. The quality of the resulting wavefunctions in this case was insufficient for calculation of relative CF-CF absorption intensities and energies. This failure is attributed to the very small low-symmetry distortions that cause the real site symmetry to be C_3, rather than the idealized C_{3v} point group used in the calculations. This deviation leads to relaxation of the C_{3v} selection rules and introduces ambiguity into the assignment of the observed CF levels. It is likely that misassigned CF levels contribute to the inferior wavefunctions in this case.

8

Nearest-Neighbor Dominance in Cooperative Luminescence

Cooperative luminescence is the microscopic reverse of simultaneous pair excitation, and in Yb^{3+} involves the emission of a green photon following NIR $^2F_{7/2} \rightarrow {}^2F_{5/2}$ excitation by the simultaneous relaxation of two excited ions to the ground state. In general, cooperative upconversion systems can be treated by the same rate equations as those given in Eq. (10), where now E = G, $k_{2b} = 2k_1$, and the cooperative luminescence rate constant is $k_{\mathrm{coop}} = k_{2a}$. Under low-power conditions, where $G \ll k_1$ and $N_2 \ll N_1$, the steady-state cooperative luminescence rates in the limit of a purely radiative system are described by Eqs. (29) and (30):

$$I_{\mathrm{NIR}} \propto k_1 N_1 + 2k_1 N_2 \tag{29}$$

and

$$I_{\mathrm{coop}} \propto k_{\mathrm{coop}} N_2 \approx \frac{k_{\mathrm{coop}} G N_1}{2k_1} \tag{30}$$

The relative rates are thus approximately [42, 43]

$$\frac{I_{\mathrm{coop}}}{I_{\mathrm{NIR}}} \approx \frac{k_{\mathrm{coop}} N_2}{k_1 N_1} \approx \frac{k_{\mathrm{coop}} G}{2k_1^2} \tag{31}$$

At large interionic distances, the magnitude of k_{coop} is governed by interionic multipole-multipole interactions. In closely separated pairs of ions, k_{coop} may be enhanced by exchange interactions. In Yb^{3+}-doped solids, it has been shown that both quadrupole-dipole ($k_{\mathrm{coop}} \propto R^{-8}$) and forced-dipole-dipole ($k_{\mathrm{coop}} \propto R^{-6}$) interactions may contribute significantly to k_{coop}, with the two being equal in magnitude at $R \approx 8$ Å [42–44]. In the Yb^{3+}-doped glass Yb^{3+}:SrY_2F_8, calculations estimate a superexchange interaction between two fluoride-bridged Yb^{3+} ions separated by 7.5 Å to be an order of magnitude greater than the multipole-multipole interactions between these two ions [44]. Such exchange interactions are also strongly dependent upon R, and $k_{\mathrm{coop}} \propto \exp[-2R/r_0]$ in the limit of isotropic direct exchange (Eq. 9a). As with nonradiative ET rate constants, k_{coop} thus greatly benefits from short ion-ion separations and, conversely, experiments that probe cooperative or ET phenomena selectively probe the subset of ions having appropriately substituted nearest neighbor sites.

This general conclusion is beautifully illustrated by the example of 10% Yb^{3+}:RbY_2Br_7. In this host lattice, Yb^{3+} may occupy one of two crystallographically distinct substitution sites [45], A and B, as indicated in Fig. 11a, inset. These two sites have slightly different geometries, and consequently Yb^{3+} ions in each may be distinguished from one another spectroscopically. The presence of two sites shows up as two peaks of approximately equal intensity in the 10 K absorption spectrum of the $^2F_{7/2}(0) \rightarrow {}^2F_{5/2}(0')$ electronic origin, shown in Fig. 11a [46]. 0 and 0′ refer to the lowest crystal-field levels of the ground and excited states, respectively. These two peaks are separated by only 11 cm^{-1}, but their narrow bandwidth (fwhm ≈ 3 cm^{-1}) allows them to be distinguished in high-resolution experiments. Figure 11b shows the 10 K $^2F_{5/2}(0') \rightarrow {}^2F_{7/2}(0)$ NIR luminescence spectra of this same sample obtained with excitation into the higher energy $^2F_{7/2}(0) \rightarrow {}^2F_{5/2}(2')$ absorption peaks of site A (solid) or site B (dashed). Luminescence from both crystallographic sites is observed with both excitation wavelengths, but with different intensity ratios depending upon which site is being excited. This indicates that part of the excitation energy is transferred between sites A and B. The calculated intensity ratio based on 10 K Boltzmann statistics is approximately 1:4.75, while the observed intensity ratios for the two spectra are 1:2.2 and 1:6.4. This indicates that a kinetic barrier to intersite ET prevents the excitation density from being fully thermalized under these experimental conditions. The cooperative luminescence spectra in the $^2F_{5/2}(0')^2F_{5/2}(0') \rightarrow {}^2F_{7/2}(0)^2F_{7/2}(0)$ region, obtained under identical excitation conditions, are shown in Fig. 11c, where the energy axis is compressed by a factor of two to allow direct comparison with Fig. 11a, b. The cooperative luminescence spectra show a dramatic third peak at an energy of $A^*B^* \rightarrow AB$ (i.e., $^2F_{5/2}(0'_A)^2F_{5/2}(0'_B) \rightarrow {}^2F_{7/2}(0_A)^2F_{7/2}(0_B)$), with two weak peaks at energies $A^*A^* \rightarrow AA$ and $B^*B^* \rightarrow BB$. The integrated intensity pattern averaged over both excitation wavelengths is approximately 1:17:1.

The relative cooperative luminescence intensities observed in Fig. 11c are directly attributable to the importance of R in determining the magnitude of k_{coop} (see Eqs. 30 and 31). As shown by the repeating structural unit in Fig. 11a (inset), there exist two types of nearest-neighbor pairs, both of which are AB pairs. R for the two shortest AB pairs (1 @ $R_{AB} \approx 4.05$ Å and 2 @ $R_{AB} \approx 4.53$ Å) are thus much smaller than the shortest AA or BB pair distances (2 @ $R_{AA/BB} = 7.27$ Å and 2 @ $R_{AA/BB} = 7.38$ Å). Since all intimate dimer pairs in the RbY_2Br_7 lattice are AB hetero pairs, the strong R dependencies of both the exchange and multipole-multipole cooperative intensity mechanisms greatly bias this system in favor of AB pair cooperative luminescence. This bias is clearly observed experimentally in Fig. 11c, even though only approximately 2 out of 14 ions are paired in this way in 10% Yb^{3+}:RbY_2Br_7. It is instructive to note that the intensity ratio predicted in the absence of any R dependence would be 1:2:1. The intensity ratio predicted from an isotropic direct exchange model (i.e., $k_{coop} \propto \exp[-2R/r_0]$, $r_0 = 0.3$ Å, Eq. 9a), calculated using the crystallographic distances of the first 24 ($R \leq 9.5$ Å) dopant sites around a central atom of each type, is $1:10^9:1$. Essentially, all of the total cooperative luminescence intensity derived from the exchange mechanism is thus attributable to the two nearest-neighbor AB ion pairs (92% from $R_{AB} = 4.05$ Å and 8% from 2 @ $R_{AB} = 4.53$ Å). Likewise, the multipole-multipole mechanism yields a 1:36:1 intensity ratio using the same 24 dopant sites and the parameters governing eq-ed and ed-ed interaction

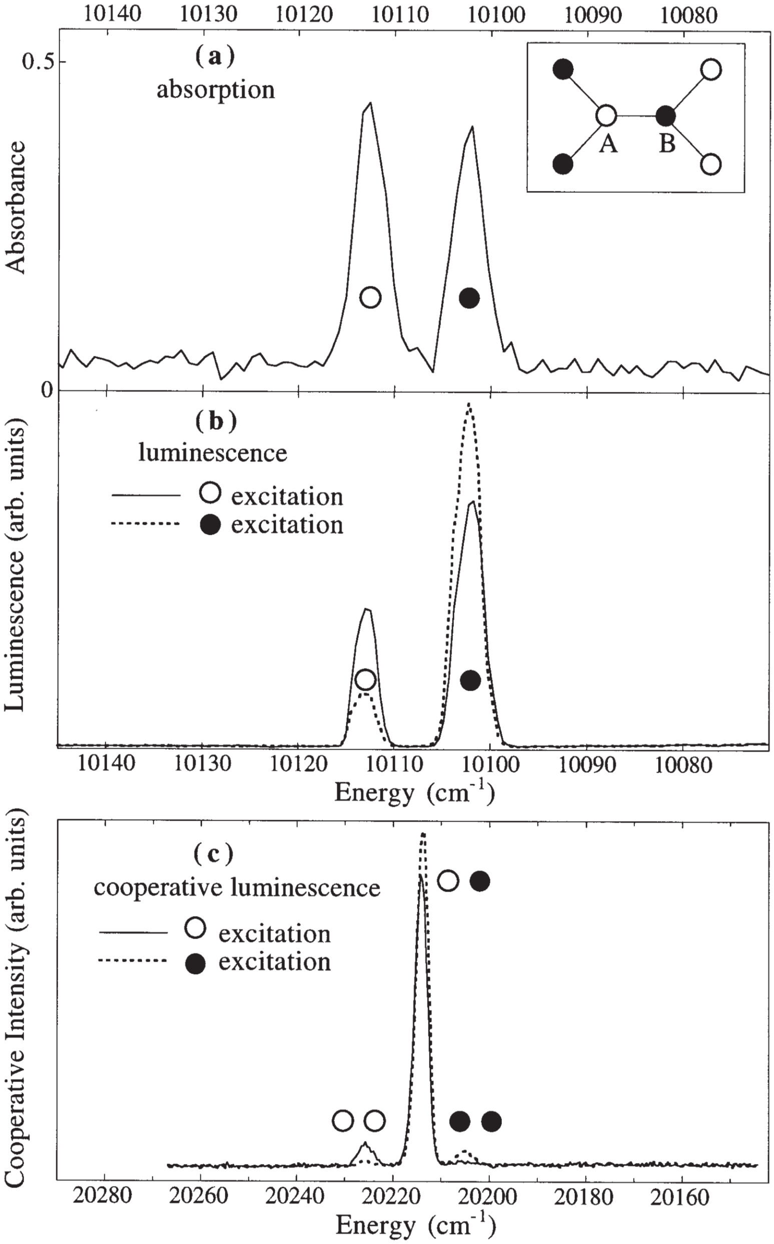

Fig. 11 a–c. 10 K spectra of 10% Yb^{3+}:RbY_2Br_7 in the $^2F_{7/2}(0) \leftrightarrow {}^2F_{5/2}(0')$ energy region: **a** absorption; **b** downconversion luminescence; **c** cooperative luminescence at twice the energy (note the different x axis). 0 and 0′ refer to the lowest-energy crystal field levels of the ground and excited states, respectively. The inset in (a) shows a subunit of the repeating sheet structure, indicating the presence of two alternating crystallographically-inequivalent dopant sites, referred to here as sites A (○) and B (●). The same symbols are used to label the observed spectral features strengths for Yb^{3+} presented in [43]. From this calculation, around 92% of the total cooperative intensity resulting from such multipole-multipole perturbations is attributable to the two nearest-neighbor AB ion pairs. While vastly more sophisticated theoretical methods have been developed to account for the inherent anisotropies of both exchange and multipole-multipole interaction mechanisms [18, 47], and to include consideration of other indirect exchange mechanisms (e.g., superexchange) [44], these simple models clearly illustrate the fact that both intensity mechanisms strongly favor observation of nearest-neighbor dimer pairs in cooperative luminescence experiments. The beauty of this 10% $Yb^{3+}:RbY_2Br_7$ system lies in its provision of two inequivalent Yb^{3+} sites. Even without any modeling the dominance of nearest-neighbor interactions in inducing cooperative luminescence is evident from Fig. 11.

The fact that the bulk cooperative luminescence spectrum can be related to microscopic pairwise interactions at all in this homogeneously-doped sample provides a very important insight into the workings of such processes. This result clearly illustrates and generalizes a most basic assertion of the shell model for energy transfer in isotropically-doped solids [48], namely, that pair effects such as energy transfer, ETU, or cooperative luminescence are dominated by nearest neighbor interactions, even at low concentrations. In contrast, measurements sensitive to single ion effects, such as absorption, probe the behavior of the bulk sample. Manifestations of such differences are observed experimentally, for example, in simultaneous measurements of the ETU (pair) and downconversion (monomer) time or power dependence analogous to that described in Sects. 4 and 5 using low dopant levels.

9

Photon Avalanche

One area where power-dependence measurements have been extensively used is in the description of photon avalanche upconversion systems. Photon avalanches have been observed in a number of rare-earth or transition-metal doped upconversion systems [6, 49–51]. Several room-temperature upconversion lasers have been made which take advantage of this route for achieving efficient population inversion [6, 15]. The term photon avalanche refers to an upconversion mechanism different from those of GSA/ESA and GSA/ETU described above, but still comprised of the absorption and ET building blocks introduced in Sect. 3. In contrast with GSA/ESA and GSA/ETU, the photon avalanche distinguishes itself by relying on an indirect method of intermediate-level population arising from cross relaxation, rather than direct GSA. This is generally only possible when GSA is weak. The avalanche mechanism requires a high ESA probability, which in turn requires both high ESA cross sections and large intermediate-level populations. The prominent experimental features of a photon avalanche are:

1. Upconversion excitation features not present in the GSA spectrum (indicative of an ESA step in the mechanism, see Sect. 3)
2. Two regimes in the upconversion power dependence, with an extremely nonlinear intensity jump when pump powers rise above a certain critical threshold

3. A lengthening of the time needed to achieve steady state conditions when using powers near the critical threshold
4. A loss of transparency at the excitation wavelength when using high excitation powers

Tm^{3+} has been studied in a number of host lattices for its red-to-blue upconversion properties which persist up to room temperature. Detailed studies of the mechanism of this upconversion have shown that it often proceeds by a photon avalanche process. Figure 12a illustrates that upconversion excitation in these cases involves excitation at an energy that is not resonant with any GSA transition (dashed arrow), but that is resonant with an ESA transition (solid up arrow). The upconversion luminescence at ca. 20,800 cm^{-1} from the $^1G_4$ excited state is monitored. Figure 12c shows the power dependence of Tm^{3+}:LaF_3 20,830 cm^{-1} upconversion luminescence excited at 15,743 cm^{-1} (A) and 15,423 cm^{-1} (B) in a 1% doped crystal, and at 15,743 cm^{-1} (C) in a 0.5% doped

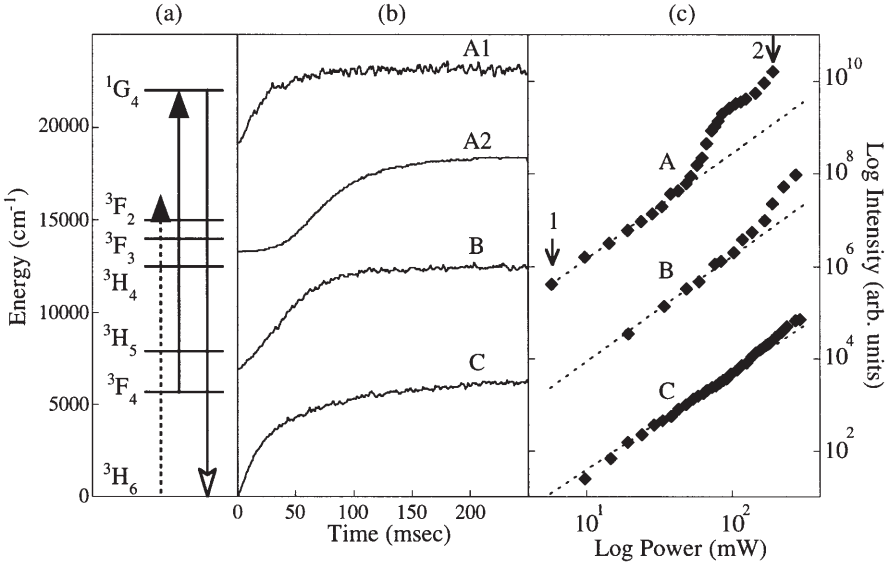

Fig. 12. **a** Energy-level scheme for Tm^{3+}:LaF_3 upconversion excitation (E||c) using ca. 15,750 cm^{-1} excitation to generate blue 20,830 cm^{-1} upconverted luminescence. The *dashed arrow* indicates nonresonant GSA, while the *solid up arrow* indicates intense resonant ESA. The *down arrow* indicates the upconversion luminescence. **b** Time-evolution of the 20,830 cm^{-1} upconversion luminescence following introduction of a cw laser beam at time = 0, plotted on linear axes. A1: 17,543 cm^{-1} excitation below the avalanche threshold in a 1% crystal. A2: same, with high power excitation above the avalanche threshold. B: same as A2, but with 15,423 cm^{-1} laser excitation. C: same as A2 but for a 0.5% Tm^{3+} doping level. Avalanche behavior is most evident in A2. **c** The dependence of upconverted luminescence on excitation power for three different experimental situations, shown in double-logarithmic representation. A: 15,743 cm^{-1} excitation, 1% doping. B: 15,423 cm^{-1} excitation, 1% doping. C: 15,743 cm^{-1} excitation, 0.5% doping. The *dotted lines* show a quadratic dependence on laser power. Avalanche behavior is most evident in A. Adapted from [52]

crystal, plotted on a double-logarithmic scale [52]. Low-power (10 mW) excitation leads to a quadratic power dependence with a slope of 2 in all cases (dashed lines). This low-power upconversion effectively proceeds by a weak GSA/ESA mechanism. As the power is raised in (A), a steep incline in the system response is observed at ca. 90 mW incident power, where a maximum slope of approximately 5 is observed, before the system levels out again to a slope of ca. 2 above 100 mW. Two regimes are thus clearly visible, with the connecting intensity jump between them being very pronounced. Figure 12b shows the temporal evolution of the $^1G_4$ emission after switching on a cw laser at 15,743 cm^{-1} with powers below (A1, ~6 mW) and above (A2, ~190 mW) the critical avalanche threshold as indicated in Fig. 12c. The response at 190 mW clearly shows a long induction period prior to steady state in the avalanche mechanism that is not present in the low-power GSA/ESA mechanism. Changing the excitation energy slightly to 15,423 cm^{-1} (B) alters the relative GSA and ESA cross sections and changes the avalanche power and time dependence. Similarly, changing the concentration (C) changes the avalanche properties (see below).

The sequence of events in a basic photon avalanche system are illustrated in Fig. 13. Step (a) shows an excitation energy that is not in resonance with any GSA transitions. This may lead to some non-zero excitation of level 1 through phonon-sideband absorption intensity, electronic Raman scattering, etc., but this excitation is very inefficient. In practice, step (a) is in every regard indistinguishable from GSA. As illustrated in step (b), an ion in level 1 may have a large ESA cross section at the same laser wavelength and may therefore be further excited to level 2, from which upconversion luminescence may be observed. Some of the level 2 population may also relax to level 1 through cross relaxation (step (c)). Population of level 1 by CR may also lead to ESA identical to that in step (b), and hence also to upconversion luminescence. At low pump powers, most ions in level 1 relax to level 0, and only a small fraction are involved in ESA. Low-power

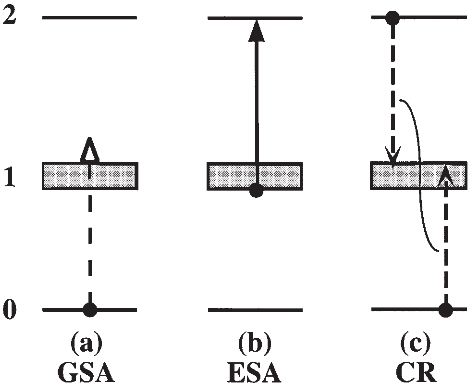

Fig. 13a–c. Schematic representation of the sequence of events in a simple three-level photon avalanche excitation mechanism: **a** nonresonant GSA to generate one ion in level 1; **b** resonant ESA to generate one ion in level 2; **c** nonradiative cross relaxation to generate two ions in level 1

upconversion therefore involves only steps (a) and (b), and is effectively an inefficient GSA/ESA upconversion excitation mechanism.

As the pump power increases, the population of level 2 increases with the square of the power, P^2, while that of level 1 increases linearly with power. At a certain power threshold, the population N_2 becomes large enough that its effect on N_1 through CR (step (c)) is no longer negligible. At high powers, the processes in steps (b) and (c) are no longer mere side processes, but become competitive with and even supersede the efficiency of step (a) in populating level 1. This shows up experimentally in the upconversion luminescence intensities, since the level 2 population, N_2, is related to $P\sigma_1 N_1$ (Eq. 6), and therefore reflects changes in N_1. The power at which the shift in mechanisms occurs is referred to as the avalanche threshold. At this threshold the system functions as an optical positive-feedback amplifier, with runaway ESA/CR populating level 1 autocatalytically. Since steps (b) and (c) populate level 1 in proportion to P, as does step (a), there need not be a great difference in the upconversion power dependence between the low- and high-power mechanisms. The mechanisms are different, however, and a step in quantum yield may be observed. The double-logarithmic power slope in the threshold region is therefore generally very steep (Fig. 12b (A)). Naturally, this step will only be observed if the upconversion quantum yield generated by the avalanche mechanism is greater than that generated by GSA/ESA. The weaker the GSA is, therefore, the more pronounced the step between the two regimes will be.

The kinetics associated with the photon avalanche have been explored for several systems using rate equations analogous to those presented in Eq. (10), now including additional terms to account for cross-relaxation events. In this context, the critical ESA pumping rate constant, E_c, at which the population of level 1 via CR occurs rapidly enough to lead to an avalanche, is given by Eq. (32) [53]:

$$E_c = k_1 \left[\frac{w_{CR} N_0 N_2 + k_2 N_2}{w_{CR} N_0 N_2 - k_{2a} N_2} \right] \tag{32}$$

where k_{2a} is the rate constant for relaxation from level 2 to the ground state (Fig. 5). As seen from this expression, if $w_{CR} N_0 N_2 > k_{2a} N_2$ then $E_c > 0$ and the avalanche occurs. If $w_{CR} N_0 N_2 < k_{2a} N_2$ then $E_c < 0$ and no avalanche is observed. Thus, a large cross relaxation rate, $w_{CR} N_0 N_2$, relative to the linear decay rate of the upper state, $k_2 N_2$, favors observation of a photon avalanche. Equation 32 also shows that systems with smaller intermediate decay rate constants, k_1, require lower powers to reach the avalanche regime.

At the avalanche threshold, the induction time required before steady state conditions are reached, t_c, defined by Eq. (33) [49], is at a maximum:

$$N_1(t) = N_1(\infty) \tanh\left(\frac{t}{t_c}\right) \tag{33}$$

For the usual photon avalanche conditions of small GSA (i.e., $G \approx 0$) and small k_1 [49],

$$t_c \propto c\sqrt{\frac{\sigma_1}{k_1\sigma_0}} \tag{34}$$

where c is a constant having units $s^{-1/2}$. Thus, a greater ratio of ESA/GSA oscillator strengths results in (a) a more pronounced transition between the two regimes in power-dependence measurements and (b) a longer induction period prior to reaching steady-state conditions in time-dependence measurements at the avalanche threshold power. Likewise, a longer intermediate lifetime, or smaller k_1, results in smaller required pump powers and a smaller induction period before reaching steady-state at the critical avalanche threshold power. Analogous relationships are also obtained for four-level or greater photon avalanche schemes [49].

Figure 12 also shows that the relative efficiencies of the two competing upconversion mechanisms in photon avalanche systems is dependent on both excitation wavelength and dopant concentration. In general, the wavelength dependence of the GSA step is small, since this step is nonresonant, but that of the ESA may be very large due to the sharp f-f excitation features. Small changes in excitation energy can therefore tune the ratio of GSA/ESA over a wide range, and hence tune the critical power and size of the step over a correspondingly wide range. Since cross relaxation plays an integral role in the avalanche mechanism, the critical parameters are sensitive to changes in concentration as well. This concentration dependence shows up both in the power dependence and in the time dependence. In the power dependence, lower concentrations require higher pump powers to achieve the same absorbed powers, in addition to potentially limiting the energy transfer cross relaxation rates by concentration effects. At high concentrations, other effects such as undesirable cross relaxation may quench the excited state populations, and an optimum concentration balancing these two effects generally exists.

Although rarely explored, the temperature dependence of an avalanche process is also of importance. In the analogous Tm^{3+} avalanche in the fluorozirconate glass 3% Tm^{3+}:BIGaZYTZr, for example, the value of P_c ($P_c \propto E_c/\sigma_1$, from Eq. 5) increases as the temperature is elevated, changing from 10 mW at 35 K to 80 mW at 300 K [54]. Similar behavior has been observed in other avalanche systems where investigated, including $Pr^{3+}:LaCl_3$ [55], $Tm^{3+}:Y_3Al_5O_{12}$ [6], and $Nd^{3+}:LiYF_4$ [56], all of which involve resonant or exothermic CR energetics. This behavior is generally attributable to ESA line broadening and redistribution of populations among Stark levels with increasing temperature, both of which lead to reduced ESA cross sections at higher temperatures. Higher pump powers are thus required at higher temperatures to achieve the same absorbed power, and consequently the avalanche threshold increases. In $Nd^{3+}:LiYF_4$, for example, the avalanche effect is only observed below 60 K, and is strongest at the lowest temperature investigated (6 K). The pump power threshold increases steadily with temperature, and a corresponding decrease in σ_1 over the same temperature increase has been measured ($\sigma_1 = 3.5 \pm 0.4 \times 10^{-20}$ cm^2 at 6 K and $1.7 \pm 0.2 \times 10^{-20}$ cm^2 at 55 K) [6, 56]. In cases where CR is endothermic, step (c) in Fig. 13 is thermally activated and another temperature dependence can be expected.

10
Optical Bistability

An extremely unusual power dependence has been observed in the cooperative upconversion luminescence of Yb^{3+}-doped $Cs_3Lu_2Br_9$ and related systems [57–61]. As illustrated by the 7.5 K power-dependence data in Fig. 14a, b, increasing the excitation power from the low-power excitation limit results in a sharp jump in both VIS and NIR luminescence intensities at a certain critical power. Reversing the direction of the power sweep also results in a sharp jump on the return path, but this jump occurs at a lower power than the forward jump, resulting in a hysteresis behavior with a distinct region of bistability. Monitoring the transmission of the laser beam shows that the absorption of the sample also increases and decreases at these same critical powers (Fig. 14a, inset) [62]. The properties of this jump are clearly dependent upon temperature, with smaller jumps observed at lower excitation powers as the temperature is elevated (Fig. 14).

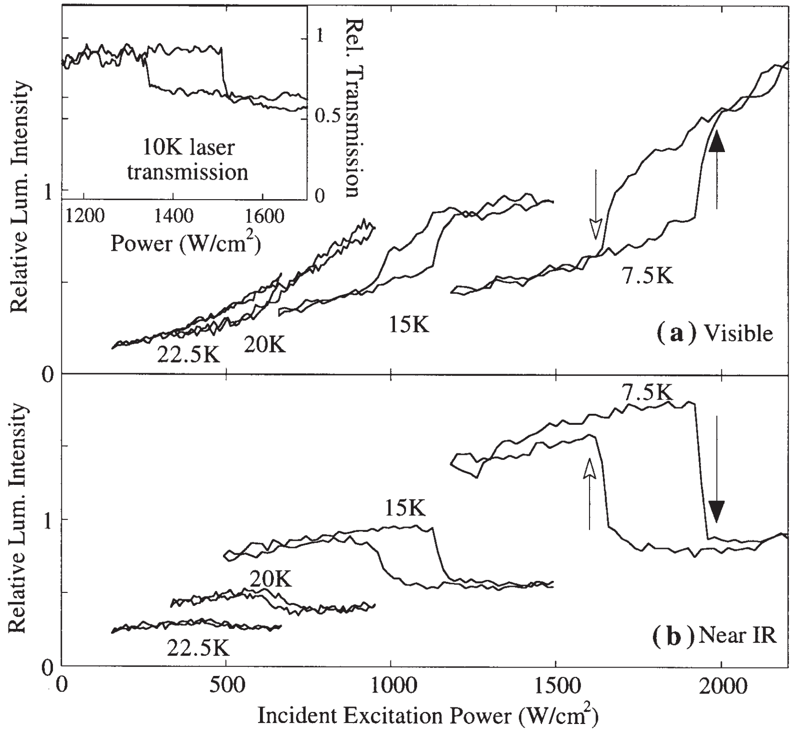

Fig. 14a, b. Power and temperature dependence of: **a** the visible cooperative luminescence; **b** the NIR downconversion luminescence in 10% $Yb^{3+}:Cs_3Lu_2Br_9$ excited at 10,591 cm^{-1}, plotted on linear axes. These data show distinct hystereses, the properties of which are temperature dependent. *Inset*: 10 K laser transmission, which also shows hysteresis behavior. Adapted from [62]

It has been proposed that this behavior results from the close interaction of two Yb^{3+} ions in these doubly-doped cofacial bioctahedral pairs [58–61], with only the closest-separated pairs contributing to the bistability behavior [61]. Indeed, the phenomenon is observed to be dependent upon Yb^{3+} doping levels [60], where increasing concentration reduces the incident power required to reach the hysteresis. Several concentrations have now been studied under identical conditions of wavelength, focal length, temperature, and sample thickness ranging from (100%) $Cs_3Yb_2Br_9$ to 1% Yb^{3+}:$Cs_3Lu_2Br_9$ [62]. Normalization of these data (not shown) for concentration by converting from incident power to *absorbed power* reveals that the phenomenon has the same power/temperature behavior for all concentrations within experimental error, despite the large range in Yb^{3+} concentration levels. Whereas in the 100% sample every Yb^{3+} has a close Yb^{3+} neighbor with which to form a dimer pair, statistical doping in the 10% sample provides only one Yb^{3+}-Yb^{3+} dimer for every 18 Yb^{3+} monomer dopant sites. As in 10% Yb^{3+}:RbY_2Br_7 (Sect. 8), the majority of the upconversion luminescence may arise from these low concentrations of nearest-neighbor ion pairs. The dominant contribution to the absorption and NIR luminescence, however, must come from isolated Yb^{3+} monomers at this 10% concentration. Since the bistability phenomenon is not restricted to the upconversion luminescence but is quantitatively similar for NIR transmission and luminescence, we now conclude that it must be a property of the entire ensemble of single Yb^{3+} ions [62].

The hysteresis power dependence is only observed within a specific narrow range of excitation wavelengths. Slight detuning outside of this range changes the shape of the power dependence from very sharp with a bistable region (Fig. 14a) to broad and S-shaped with no bistable region (Fig. 15a) [62]. The visible upconversion luminescence in the latter is reminiscent of the avalanche excitation data presented in Fig. 12c (A) and suggests a description of this effect as an avalanche process. This is strongly supported by time dependence measurements collected under these same conditions. Square-wave excitation at 36 mW, below the critical power, shows simple monoexponential rise and decay behaviors for both NIR and visible signals (Fig. 15b). Square-wave excitation at 82 mW, slightly above the critical power, shows a dramatically long induction period of several milliseconds before steady state is achieved, during which the visible luminescence gains intensity and the NIR luminescence loses intensity on the same time scale. The long induction period in Fig. 15b is analogous to the long induction period observed in the Tm^{3+} avalanche in Fig. 12b (A2), and shows a critical time over an order of magnitude larger than the natural Yb^{3+} $^2F_{5/2}$ decay time. This critical time is observed to be dependent upon the power used and lengthens as the critical power threshold of ca. 60 mW is approached [62]. As discussed in Sect. 9, these are characteristic features of the avalanche excitation mechanism.

As described in Sect. 9, photon avalanches are only observed in cases where $\sigma_1 \gg \sigma_0$. In treating this case as an avalanche, the following question arises: How does an ESA cross section become substantially greater than the GSA cross section in a cooperative luminescence system in which *by definition* the GSA and ESA steps are the same single-ion transition? The answer to this question is

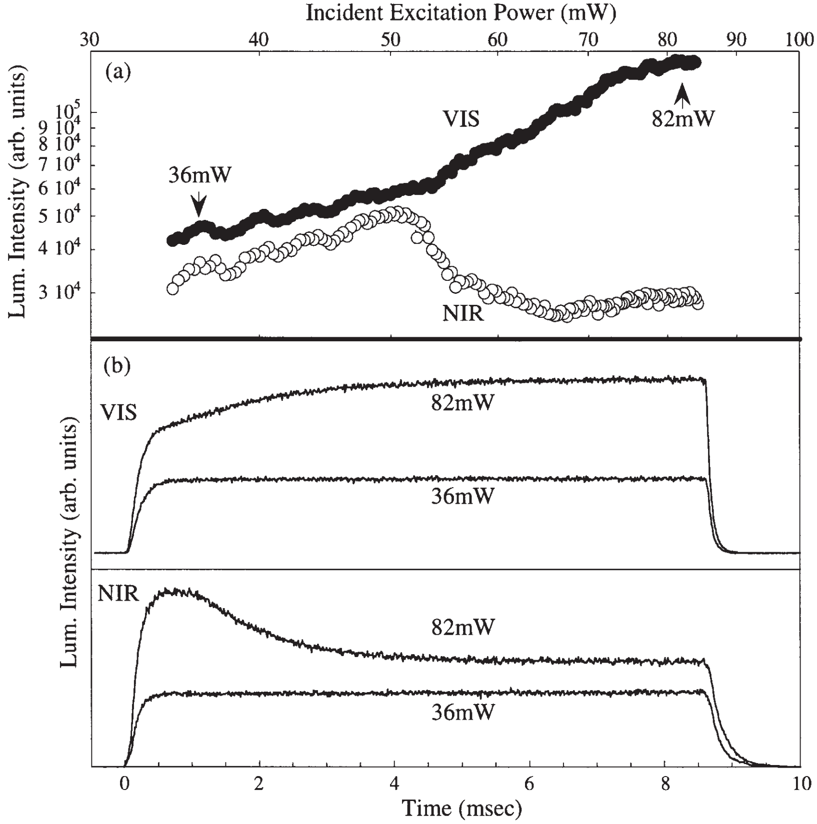

Fig. 15 a, b. 10 K power- and time-dependent luminescence data from 50% Yb^{3+}:$Cs_3Lu_2Br_9$ after slight detuning of the excitation energy to 10,590 cm^{-1}: **a** double-logarithmic power dependence of the visible and NIR luminescence signals, showing the typical avalanche behavior; **b** time dependence of the visible and NIR luminescence signals at the two powers indicated in (a). The 36 mW excitation is below the avalanche threshold and shows normal time dependence. The 82 mW excitation is above the critical avalanche threshold power and shows the delayed steady-state behavior characteristic of a photon avalanche. The time to reach steady state under these conditions is nearly two orders of magnitude longer than the decay period of the visible luminescence. Adapted from [62]

found in the temperature dependence of the absorption spectrum, shown in Fig. 16. Figure 16a shows the $^2F_{7/2} \rightarrow {}^2F_{5/2}$ Yb^{3+} absorption spectrum at two temperatures. In contrast with the generally observed behavior, the absorption cross sections of the $^2F_{7/2}(0) \rightarrow {}^2F_{5/2}(2')$ and $^2F_{5/2}(0')$ CF transitions increase significantly upon warming [62]. This is not the result of vibronic hot-band activity. It is only observed for these two electronic origins and apparently derives from thermally changing wavefunctions in the ground and/or excited states of these ions which begins even at the lowest temperatures measured. Variable-temperature neutron diffraction data show a structural change in this lattice type involving elongation along the trigonal (dimer) axis beginning at liquid helium tem-

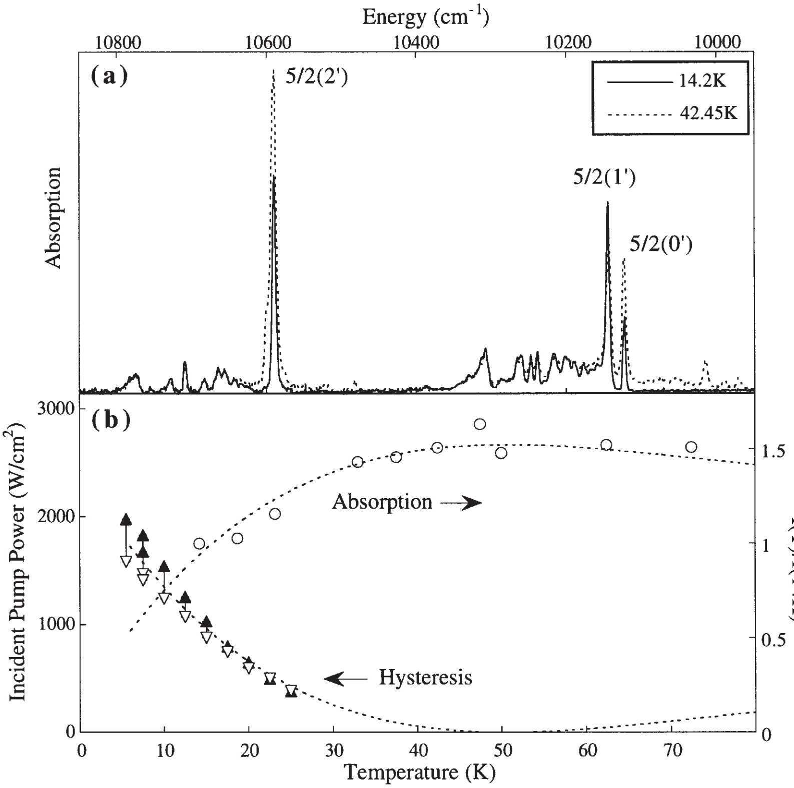

Fig. 16a, b. Temperature dependence of the absorption spectrum of 10% Yb^{3+}:$Cs_3Lu_2Br_9$: **a** comparison of the 14 K and 42 K absorption spectra. The intensities of the $^2F_{5/2}(2')$ and $^2F_{5/2}(0')$ features increase markedly, while those of the $^2F_{5/2}(1')$ and cold vibronic transitions stay the same or decrease slightly; **b** scatter plot of the normalized 10,591 cm^{-1} $^2F_{7/2}(0) \rightarrow$ $^2F_{5/2}(2')$ absorption cross section as a function of temperature, compared with the hysteresis data vs pump power for the same sample. The triangles indicate the widths of the power hystereses, which get larger as the temperature is lowered. The *dashed lines* in (b) are both obtained from the same arbitrary polynomial fit to the absorption data, which was inverted and superimposed on the hysteresis data as a guide to the eye. Adapted from [62]

peratures and continuing up to room temperature [63], and the observed increase in absorption cross sections may relate to this structural change. Plotting the absorption cross section at the excitation wavelength (10,591 cm^{-1}) vs temperature shows a continuous increase by ca. 50% between 10 K and 45 K, at which point band broadening and hot-band population effects cause the absorption cross section to turn over and decrease with increasing temperature. Similar behavior is observed in the absorption spectra of all concentrations, including that of a 1% doped sample where the statistical dimer concentration is effectively zero.

The variable temperature behavior of the absorption intensity is correlated with that of the hysteresis. In Fig. 16b, the hysteresis temperature dependence in

10% $Yb^{3+}:Cs_3Lu_2Br_9$ is compared with the absorption temperature dependence of the same sample. The triangles in the hysteresis data report the hysteresis widths at each temperature, which increase as the temperature is lowered. The dashed line is an arbitrary polynomial fit to the curvature of the absorption data to assist the eye. This same curve is inverted and superimposed on the hysteresis data. Figure 16b strongly suggests that the two phenomena are correlated. From these data, the temperature of 45 ± 5 K is identified as a critical temperature for both measurements. Above this temperature, the temperature and power dependencies are normal, and below this temperature both are unusual. Support for this correlation comes from the observation that both avalanche and bistability behavior are only observed with laser excitation into the 0′ and 2′ CF origins [62], and not into the 1′ or vibronic transitions, even though the latter have intensities between those of the former. From Fig. 16a, only these two origins show the unusual absorption temperature dependence to which this effect is attributed. Moreover, this unusual power dependence is observed only in the two host lattices where such variable-temperature absorption behavior is observed: Similar variable-temperature absorption data are also obtained for $Yb^{3+}:CsCdBr_3$, the only other lattice in which the hysteresis effect has been observed to date, but not for $Yb^{3+}:RbY_2Br_7$, $Yb^{3+}:Cs_2NaYBr_6$, or any of the analogous chloride lattices, which show no hysteresis behavior.

In describing this effect as an avalanche excitation mechanism, it is clear that the details of the process differ from those of the Photon Avalanche described in Sect. 9 since, being ultimately a single-ion effect, this mechanism does not involve runaway cross relaxation as an essential step, but is instead intimately related to temperature effects. Within the avalanche formalism, this mechanism is best described as a thermal avalanche, in which high excitation powers result in runaway sample heating rather than runaway cross relaxation. This mechanism is illustrated schematically in Fig. 17a. The dashed lines in Fig. 17a show the isothermal excitation behaviors for two internal sample temperatures, $T_{\mathrm{int,lower}}$ and $T_{\mathrm{int,upper}}$. The horizontal displacement between the two isotherms is related to their difference in temperature, $\Delta T_{\mathrm{int}} = T_{\mathrm{int,upper}} - T_{\mathrm{int,lower}}$. The pump rate $R_{0,1}$ for any given power P is greater at $T_{\mathrm{int,upper}}$ than at $T_{\mathrm{int,lower}}$ since $\partial\sigma/\partial T > 0$ (recall $R \propto P\sigma$, Eq. 5). Under real experimental conditions, the internal temperature of the sample is identical to the cryostat (external) temperature in the limit of low pumping powers. As with most excitation schemes, heat is deposited when the sample absorbs photons. At low pump powers on the $T_{\mathrm{int,lower}}$ isotherm in Fig. 16a, heat dissipation through the crystal to the helium bath is in steady-state equilibrium with heat deposition by the excitation beam, and the low-power steady-state sample temperature, $T_{\mathrm{int,lower}}$, is approximately constant at the cryostat temperature, T_{external}. Increasing the pump power in Fig. 17a, the system follows the $T_{\mathrm{int,lower}}$ isotherm until some critical power is reached at which the rate of sample heating exceeds the rate of sample cooling. Because $\partial\sigma/\partial T > 0$, exceeding this threshold triggers a self-reinforcing process of absorption/heating/absorption etc., which continues until a new steady state temperature, $T_{\mathrm{int,upper}}$, is achieved. The internal sample temperature has thus jumped from $T_{\mathrm{int,lower}}$ to $T_{\mathrm{int,upper}}$ at the critical power. Importantly, the critical threshold for switching back down to $T_{\mathrm{int,lower}}$ is obtained with less pump power than the

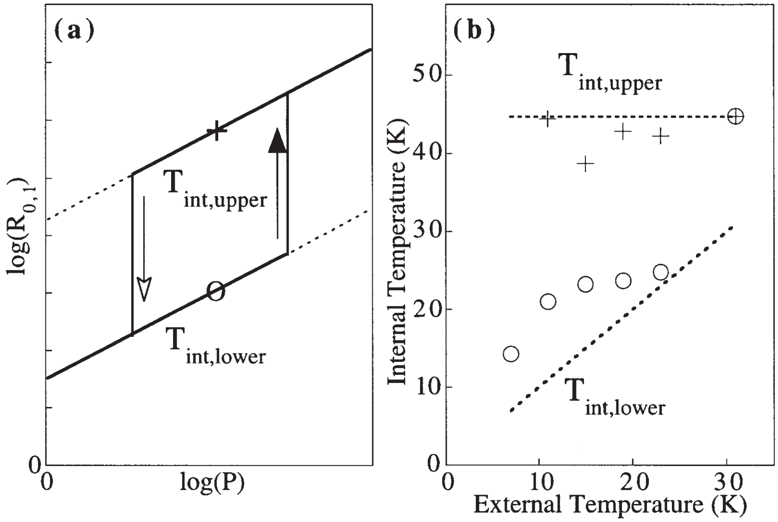

Fig. 17. **a** The effect of a laser-induced temperature change on excitation rate, $R_{0,1}$, in Yb^{3+}-doped $Cs_3Lu_2Br_9$ and related lattices. The *dashed lines* show hypothetical isothermal response curves for two internal temperatures, $T_{int} = T_{int,upper}$ and $T_{int} = T_{int,lower}$, in which the pump rates increase linearly with the pump powers in accordance with Eq. (5). Because $\sigma(T_{int,\,upper}) > \sigma(T_{int,\,lower})$, the $T_{int,\,upper}$ isotherm shows a greater pump rate for any given pump power. The *solid line* shows the response observed when a rapid jump in sample internal temperature is triggered by a change in the pump power. The critical pump power required to trigger this temperature jump is greater when $T_{int} = T_{int,lower}$ than when $T_{int} = T_{int,upper}$, since $\sigma(T_{int,upper}) > \sigma(T_{int,lower})$. The laser-induced temperature jump leads to a hysteresis with width proportional to the difference between $T_{int,upper}$ and $T_{int,lower}$. **b** Internal temperature measurements on the upper (+) and lower (○) branches in the bistable regions at various external temperatures, determined from the data in [59], assuming $T_{int,\,upper} = 45$ K. The temperature difference increases with decreasing $T_{external}$. The *dashed lines* in (b) show the two cases of $T_{int} = 45$ K and $T_{int} = T_{ext}$. Adapted from [62]

switching up threshold due to the higher absorption cross section at the higher internal temperature. As a consequence, when the power is reduced following the avalanche the sample temperature does not return to $T_{int,\,lower}$ immediately, but instead returns at a significantly lower power. This yields a bistable region in the power dependence, as illustrated in Fig. 17a.

The limiting value of $T_{int,upper}$ in Fig. 17a depends on the variable-temperature absorption properties of the sample at the excitation wavelength. As seen from the absorption data in Fig. 16b, $\partial\sigma/\partial T \approx 0$ when the temperature is ca. 45 K. During the avalanche cycle of absorption/heating/absorption etc., the sample's internal temperature can rise to ca. 45 K, but no further gain is introduced by increasing the internal temperature above 45 K, so the system equilibrates at this temperature. The value of $T_{int,\,upper}$ is thus an experimental constant, and is approximately independent of $T_{int,\,lower}$. This fact has been verified by internal temperature measurements using the intensity of a hot-band luminescence peak [57]. From such data it is possible to confirm that, under steady-state high-power (upper branch) conditions in the bistable region, $T_{int,\,upper}$ is always the same regardless of T_{external} (and $T_{\text{int, lower}}$), although its precise value is not well defined since the absolute oscillator strength of the hot-band luminescence feature probed is not known. Using the value of $T_{\text{int, upper}} = 45$ K estimated from the data in Fig. 16, the temperatures in Fig. 17b are determined. As seen in Fig. 17b, $T_{\text{int, lower}}$ essentially follows T_{external}, while $T_{\text{int,upper}}$ is essentially independent of T_{external}. ΔT increases as T_{external} is decreased, and this results in greater hysteresis widths at lower external temperatures (Fig. 14).

The sensitivity of the Yb^{3+} avalanche threshold to the exact excitation energy results from the fact that the absorption maximum shifts slightly with increasing temperature. A judicious choice of excitation energy allows optimization of the $\sigma(T_{\text{int, upper}})/\sigma(T_{\text{int, lower}})$ ratio and sharpens the avalanche step, analogous to the behavior observed in the Tm^{3+} avalanche data of Fig. 12.

In summary, the unusual luminescence power dependence observed in Yb^{3+}:$\text{Cs}_3\text{Lu}_2\text{Br}_9$ ultimately derives from the effect of power on the internal temperature of the sample, which when combined with a positive $\partial\sigma/\partial T$ leads to a unique avalanche and hysteresis phenomenon. From such a thermal model it is possible to reproduce the experimental power, temperature, concentration, and excitation-energy dependence of the Yb^{3+} optical bistability using only the experimental absorption temperature dependence data as input [62]. Such laser heating effects are generally not accounted for in power-dependence analyses, since in most cases, including the avalanche cases described in Sect. 9, absorption cross sections *decrease* with heating and may result in only a small flattening of the power dependence behavior. The power dependence of Yb^{3+}:$\text{Cs}_3\text{Lu}_2\text{Br}_9$ described here shows that the contribution of laser heating to the shape of a power dependence may be significant or even the dominant aspect of that power dependence when $\partial\sigma/\partial T > 0$.

11
Upconversion in Doped Transition Metal Ion Systems

Transition metals have been largely neglected as upconversion ions, but recent developments indicate that several such ions are also suitable for multiphoton excitation, and sometimes show properties different from those of the rare-earth ions, including the increased likelihood of encountering broad ligand-field-dependent excited-state features and strict spin selection rules [17]. $\text{Ni}^{2+}(3\text{d}^8)$, long studied for its laser potential in a variety of host lattices, was observed early on to show upper excited state emission due to ESA processes. This ESA is detrimental to the objective of laser action in such crystals [64]. $\text{Ti}^{2+}(3\text{d}^2)$ upconversion was also observed several years ago [65]. More recently, a systematic effort to discover new transition-metal upconversion systems, as well as to explore the properties of these two older systems, has been initiated. The three examples of $\text{Os}^{4+}(5\text{d}^4)$ [66, 67], $\text{Mo}^{3+}(4\text{d}^3)$ [32, 68], and $\text{Re}^{4+}(5\text{d}^3)$ [28, 68] have now been reported. In all of these systems, the same general building blocks as in rare earth doped systems are observed. The mechanisms of each are summarized in Table 2, along with key physical parameters that relate to their photophysics.

Table 2. Transition metal ions in doped halide lattices for which upconversion luminescence has been demonstrated, including relevant mechanistic and electronic-structural information. The lightest and heaviest lanthanides showing single-ion upconversion are also listed. Adapted from [17]

Ion	Electrons	Representative host	UC mechanism	ζ (crystal, cm^{-1})
Ti^{2+}	$3d^2$	$MgCl_2$	2-Color GSA/ESA	100
Ni^{2+}	$3d^8$	$CsCdCl_3$	GSA/ESA, Avalanche	620
Mo^{3+}	$4d^3$	Cs_2NaYCl_6	2-Color GSA/ESA	600
Re^{4+}	$5d^3$	Cs_2ZrCl_6	ETU	2300
Os^{4+}	$5d^4$	Cs_2ZrBr_6	GSA/ETU, GSA/ESA, Avalanche	2600
Pr^{3+}	$4f^2$	$LaCl_3$		749
Tm^{3+}	$4f^{12}$	$LaCl_3$		2638

Consider the comparison between the two d^3 ions, Mo^{3+} and Re^{4+}. Figure 18 presents the relevant portion of a Tanabe-Sugano energy-level diagram for octahedral d^3 ions. Luminescence is observed from both the first ($^2T_1/^2E$, NIR) and second ($^2T_2$, red) excited-state multiplets in both ions [69, 70]. In Mo^{3+}, excitation into the higher-energy, broader, and more intense $^4T_2$ and $^4T_1$ interconfigurational d-d transitions leads to rapid relaxation followed by red $^2T_2 \rightarrow {}^4A_2$ luminescence. $^2T_2$ luminescence is observed in both ions with NIR excitation [68]. The upconversion luminescence of 2.5% Re^{4+}:Cs_2ZrCl_6 is shown in Fig. 19a.

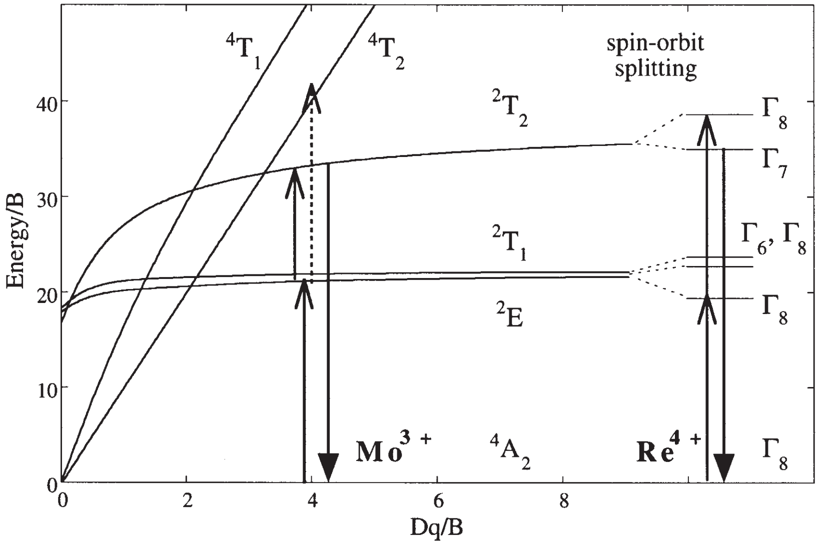

Fig. 18. d^3 Tanabe-Sugano energy-level diagram (using parameters from Mo^{3+}:C/B = 3.7, B = 487 [81]. *Up arrows* indicate two-photon excitation processes observed in Mo^{3+} and Re^{4+}. *Down arrows* indicate the upconversion luminescence used to monitor these processes. Adapted from [68]

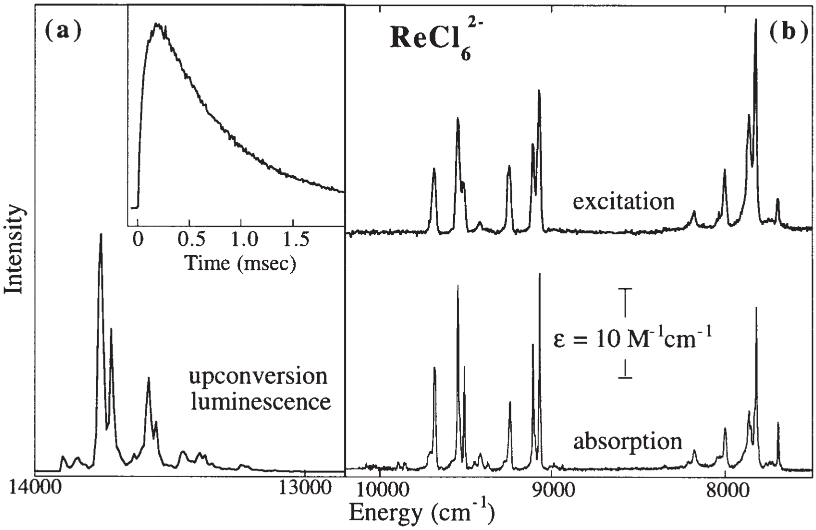

Fig. 19. **a** 15 K upconversion luminescence of 2.5% Re^{4+}:Cs_2ZrCl_6. *Inset*: 10 K time dependence of this luminescence following a 10-ns 9400 cm^{-1} excitation pulse to excite the $^2T_1/^2E$ manifold. **b** 15 K NIR upconversion excitation scan and 10 K NIR absorption spectrum. Note the discontinuous axis between (a) and (b). Adapted from [28, 68]

Figure 19b presents the $\Gamma_8(^4A_2) \rightarrow {}^2T_1/^2E$ absorption spectrum of 2.5% Re^{4+}:Cs_2ZrCl_6. A series of sharp transitions are observed that reflect the undistorted octahedral nature of these excited states. Excitation into these features produces the upconversion luminescence spectrum shown in Fig. 19a. The 10 K excitation scan of this luminescence is compared to the absorption spectrum in Fig. 19b. The upconversion excitation scan closely follows the absorption profile over the full energy range. This observation leads to the conclusion that at 10 K the dominant mechanism for upconversion in 2.5% Re^{4+}:Cs_2ZrCl_6 under these conditions is GSA/ETU. Time-dependent measurements confirm this conclusion (Fig. 19a, inset), showing the characteristic delayed maximum and a 10 K decay constant ($k_{dec} = 1400$ s^{-1}) approximately two times that of the $\Gamma_8(^2T_1)$ excited state ($k_1 = 505$ s^{-1}), as described in Sect. 4, and significantly smaller than that of the luminescent $\Gamma_7(^2T_2)$ state ($k_2 = 8475$ s^{-1}), which is responsible for the upconversion rise ($k_{rise} = 14285$ s^{-1}) [28].

Red luminescence is also observed in Mo^{3+}:Cs_2NaYX_6 (X = Cl, Br) with broadband NIR lamp excitation into the $^2E/^2T_1$ manifold of excited states (Fig. 20a) [32, 68]. The quadratic power dependence (inset, open circles) confirms that this luminescence derives from upconversion. The excited state energies in Mo^{3+}:Cs_2NaYCl_6 and Mo^{3+}:Cs_2NaYBr_6 (Fig. 18) result in favorable resonance of a first ($^4A_2 \rightarrow {}^2T_1/^2E$) and second ($^2T_1 \rightarrow {}^4T_2$) excitation step for either ESA or ETU, resulting in a plausible one-color upconversion pathway. In particular, the large expected bandwidth of the $^2T_1 \rightarrow {}^4T_2$ ESA transition results in a spectral overlap integral (Eq. 9) three times larger than that in Re^{4+}. One-color lamp excitation (Fig. 20b) under the same conditions as in Fig. 19, however, fails to yield

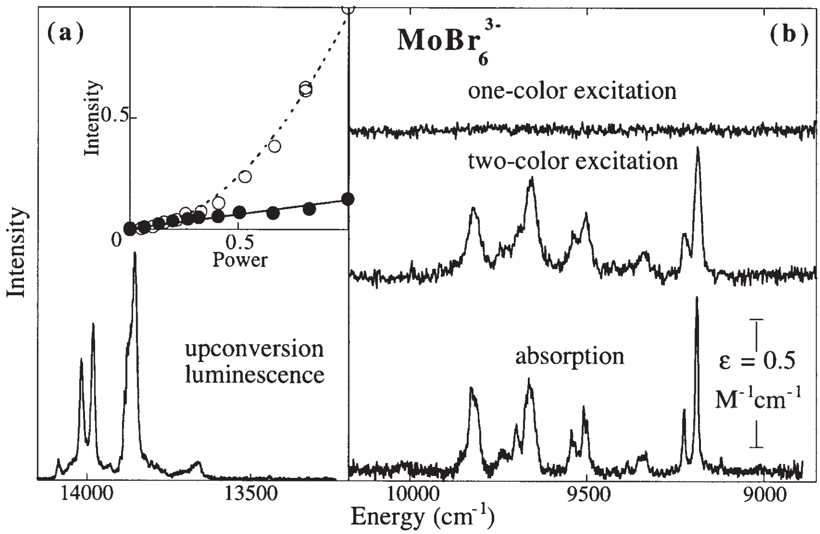

Fig. 20. **a** 15 K upconversion luminescence of 2.5% Mo^{3+}:Cs_2NaYBr_6. *Inset*: Upconversion intensity as a function of (○) total NIR excitation power (4 μW mm^{-2} max) and (●) 9065 cm^{-1} power for a fixed second-color power ($E_2 \leq 6060$ cm^{-1}), normalized at low powers. The *superimposed curves* show the predicted two-photon (- - -) and one-photon (——) behavior normalized at low powers. **b** 15 K NIR upconversion excitation scans with one-color (*top*) and with addition of a fixed second color ($E_2 \leq 6060$ cm^{-1}) (*middle*), compared to the 10 K NIR absorption spectrum in the same energy region (*bottom*). Note the discontinuous axis between (a) and (b). Adapted from [68]

any observable upconversion luminescence. Comparison to a Re^{4+} sample of the same concentration under the same conditions yields an experimental upper limit of ca. 10^{-3} relative upconversion efficiency in the Mo^{3+} sample. Mo^{3+} upconversion luminescence is, however, readily observed in a two-color experiment (Fig. 20b) in which the first color scans through the lowest energy GSA transitions while the sample is illuminated with a second color of lower energy, resonant with the intraconfigurational ESA transitions $^2T_1/^2E \rightarrow {}^2T_2$ (Fig. 18). The observed power dependence under these conditions (Fig. 20a, inset, full circles) is linear in each color. The dominant upconversion mechanism in Mo^{3+} is, therefore, two-color GSA/ESA, not one-color GSA/ETU as in Re^{4+}, despite favorable energetic resonance conditions for a one-color mechanism.

To understand these results, the ETU rates predicted for these two ions are compared. Their relative one-color ETU luminescence intensities, I_{ETU}, are directly related to the relative ETU rates obtained from Eq. (9). The magnitudes of the various factors are evaluated using the absorption and luminescence spectra of these species, and the greatest differences are found to derive from the oscillator strengths f_D and f_A; although spin-forbidden in both ions, f_D ($\Gamma_8(^4A_2) \rightarrow \Gamma_8(^2T_1/^2E)$) is ca. 10^2 times larger in Re^{4+} than in Mo^{3+} due to the greater spin-orbit coupling in Re^{4+} (Table 2), as this relaxes the spin selection rules for absorption. f_A is estimated to be ca. 10^3 times larger in Re^{4+}, where it relates to the spin-allowed $\Gamma_8(^2T_1/^2E) \rightarrow \Gamma_8(^2T_2)$ transition, than in Mo^{3+}, where it relates to the spin-forbidden $^2E \rightarrow {}^4T_2$ transition. The ratio of ETU intensities is therefore estimated to be $I_{Mo}/I_{Re} \approx 10^{-5}$, despite a DA spectral overlap integral that is approximately three times larger in Mo^{3+} than in Re^{4+} due to the broadband nature of the acceptor ($^4T_2$) absorption feature. This is consistent with the experimental upper limit for one-color excitation of $I_{Mo}/I_{Re} \leq 10^{-3}$. Introduction of a second color in Mo^{3+} excitation bypasses the spin restrictions of Eq. (9) by introducing direct $^2E \rightarrow {}^2T_2$ ESA, and renders the upconversion observable under these conditions.

Despite their similar electronic structures, upconversion processes in Mo^{3+} and Re^{4+} thus show dramatically different properties that can be related to differences in oscillator strengths due to spin selection rules. The observation of an energetically-resonant but spin-blocked upconversion pathway in Mo^{3+} differs from what is normally observed in rare earth upconversion materials. In the latter, spin-orbit coupling is usually so strong that spin selection rules are no longer relevant.

12
Host Lattice Contributions

Host properties are extremely influential in most upconversion processes. These influences can be used in advantageous ways, and four examples of very general routes to do so are described here as they apply to specific and unusual upconversion processes.

12.1
Phonon Properties

In the most basic of host-dopant interactions, host-dependent multiphonon effects can be used to tune the upconversion mechanism and/or the resulting luminescence energy of an ion. As an example, consider the four-photon excitation process described in Sect. 5 for the 1.54-μm excitation of Er^{3+} in $Cs_3Lu_2Cl_9$ and illustrated in Fig. 21a [26]. This upconversion mechanism involves the presence of a large standing population in the $^4I_{9/2}$ excited state to achieve efficient three- and four-quantum excitation. In $Cs_3Lu_2X_9$ lattices (X = Cl, Br, I), this upconversion benefits from long $^4I_{9/2}$ lifetimes (e.g., 9.8 ms in 1% Er^{3+}:$Cs_3Lu_2Cl_9$ at 295 K). This differs from the behavior commonly observed in fluoride and oxide lattices under similar excitation conditions, where the $^4I_{9/2}$ population rapidly relaxes to the $^4I_{11/2}$ state [71]. In these oxides and fluorides, upconversion may then proceed from the $^4I_{11/2}$ state by ETU to generate green $^4S_{3/2} \rightarrow {}^4I_{15/2}$ upconversion luminescence, but four 1.54-μm photons are still required to generate this luminescence. This is illustrated in Fig. 21b, and the key properties related to $^4I_{9/2}$ multiphonon relaxation in various host types summarized in Table 3.

Such differences in multiphonon relaxation rates are believed to be largely responsible for the strongly enhanced visible luminescence observed in low-

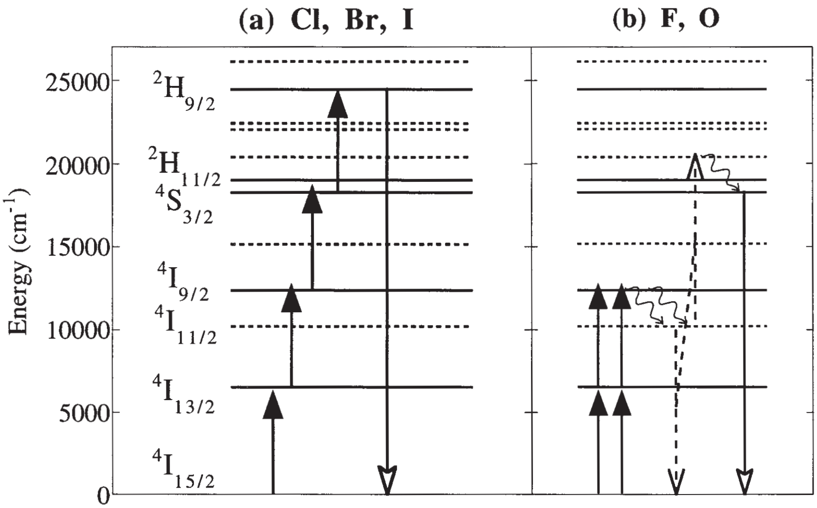

Fig. 21 a, b. Illustration of the 6500 cm^{-1}-excited Er^{3+} multiphoton upconversion processes commonly observed in low- vs high-phonon energy host lattices: **a** Cl, Br, I; **b** F, O, respectively. In the low-phonon-energy hosts, the absorption of four photons leads to luminescence from the $^2H_{9/2}$ state at 24,000 cm^{-1}. In the high-phonon-energy hosts, $^4I_{9/2}$ to $^4I_{11/2}$ multiphonon relaxation (*curly arrows*) is rapid and quenches this excitation pathway, resulting in predominantly 17,500 cm^{-1} $^4S_{3/2}$ luminescence following absorption of four photons. The kinetic parameters governing these processes are listed in Table 3

Table 3. Energetic parameters of oxide and halide lattices relating to upconversion involving the $^4I_{9/2}$ state of Er^{3+}, compiled from various literature sources. Δ (cm^{-1}) is the average Er^{3+} $^4I_{9/2}$–$^4I_{11/2}$ energy gap, ν_{max} (cm^{-1}) is the highest-energy lattice phonon energy, p is the reduced energy gap, k_{mp} is the estimated multiphonon-relaxation rate constant, k_{rad} is the estimated range of radiative rate constants, and $k_{tot} = k_{rad} + k_{mp}$. Adapted from [26]

	Δ (cm^{-1})	ν_{max} (cm^{-1})	p	k_{mp} (s^{-1})	k_{rad} (s^{-1})	k_{rad}/k_{tot}
Oxide	1894	600	3.1	1.25×10^6	200–1000	$<8 \times 10^{-4}$
Fluoride	2036	355	5.8	3.18×10^4	200–1000	$<3 \times 10^{-2}$
Chloride	2117	260	8.1	8×10^{-3}	200–1000	~1
Bromide	2135	172	12.3	2×10^{-8}	200–1000	~1
Iodide	2138	144	14.9	$<10^{-8}$	200–1000	~1

phonon-energy hosts (chloride, bromide, iodide) relative to that in high-phonon-energy hosts (fluoride, oxide). Thus, in addition to accessing luminescence transitions not available in the high-phonon analogs, low-phonon-energy hosts provide the opportunity to use fewer photons to achieve excitation of the same or even higher energy levels. In a more general sense, the phonon properties of host materials may be used to adjust the kinetic parameters relating to the excited-state photodynamics of a dopant ion, thereby tuning its upconversion properties [72].

12.2
Sensitization

In addition to its phonon properties, a host may be chosen for its optical properties. The most common optical contribution of a host is sensitization. Sensitized upconversion is well known, and indeed played a historically important role in the discovery of the upconversion phenomenon [3]. Because of its intense absorption features and fortuitously compatible energetics, Yb^{3+} is commonly used as a sensitizer of the $^4I_{11/2}$ level in Er^{3+}. Sensitization is an ET process involving two different ions, and so fits into that building block category. Host sensitization involves the use of pure sensitizer host materials. This plays the dual role of maximizing the optical density of the sample at the excitation wavelength and maximizing the probability that an acceptor ion will have a donor ion in close proximity (see Sect. 8). Using pure materials leads to maximum excitation delocalization, which increases the probability that the excitation will be transferred to a dopant ion.

Although well known, this principle is now being applied using new combinations of upconversion ions, in particular those involving transition metals. As an example, consider the effect of sensitization on upconversion in the Mo^{3+}-doped materials described in Sect. 11 [46]. The 10 K absorption spectrum of 5% Mo^{3+}:$Cs_2NaYbCl_6$, shown in Fig. 22, is dominated by several intense $^2F_{7/2} \rightarrow {}^2F_{5/2}$ Yb^{3+} features between 10,200 cm^{-1} and 11,000 cm^{-1}, with several weak Mo^{3+} $^4A_2 \rightarrow {}^2T_1/{}^2E$ features between ca. 9300 cm^{-1} and 10,200 cm^{-1}. The inherently long-lived Yb^{3+} excited-state provides an excellent energy match for ET to the ^2E state of Mo^{3+}, as illustrated in Fig. 22 (inset). The 10 K downconversion luminescence spectrum of this sample is also shown in Fig. 22. Following Yb^{3+} excitation, almost exclusively Mo^{3+} luminescence is observed. The Yb^{3+} luminescence is extremely weak, and has an integrated intensity of ca. 10^{-3} times that of Mo^{3+}. The 15 K lifetime of the Yb^{3+} excited state is concomitantly reduced. The $Yb^{3+} \rightarrow Mo^{3+}$ ET process is therefore essentially quantitative, even in this relatively dilute crystal, and results in a high population of the ^2E intermediate state.

Laser excitation into the Yb^{3+} absorption features leads to intense red upconversion luminescence from $^2T_2$ clearly visible by eye in this sample. Comparison of these data to the unsensitized Mo^{3+} data in Sect. 11 shows that sensitization may greatly facilitate the generation of upconversion luminescence for both physical and practical reasons. In Fig. 20, the low energy of the $^2E/^2T_1$ excited states precluded the use of a laser for excitation, and instead a lamp source was used with an average power of ca. 16 $\mu W/mm^2$ [68]. Sensitization by Yb^{3+} allows for excitation with a Ti: sapphire laser, where an average power of ca.160 mW/mm^2 was used, or 10^4 times more pump power. Since in the low power regime the upconversion is proportional to P^2, this implies ca. 10^8 more upconversion photons under this excitation scheme. If, in addition, an increase in excitation quantum yield due to the higher absorption cross section and nearly quantitative ET efficiency of Yb^{3+} sensitization occurs (Fig. 22), this may easily result in an increase in upconversion luminescence of more than 10 orders of magnitude between the two experiments.

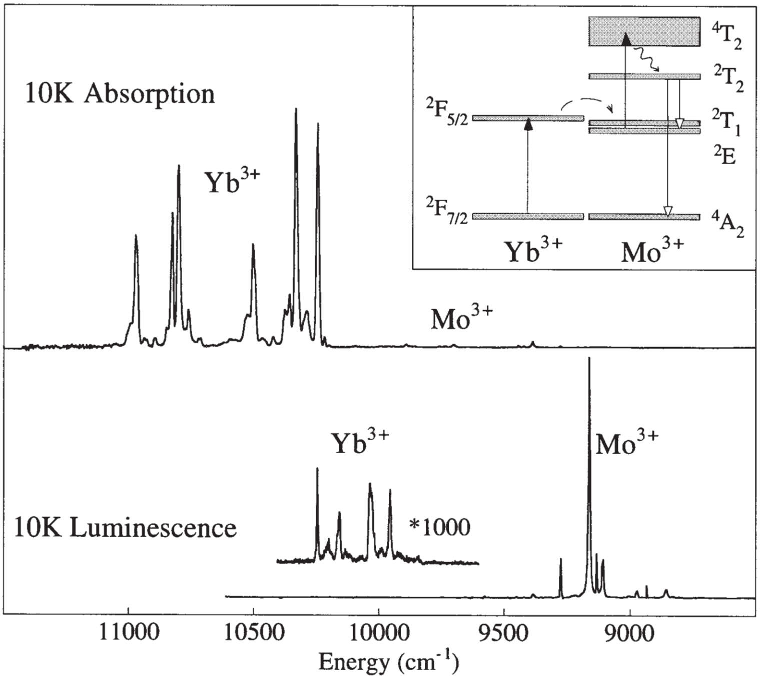

Fig. 22. 10 K absorption spectrum of 5% Mo^{3+}:$Cs_2NaYbCl_6$. The absorption features are labeled according to the chromophore, Yb^{3+} or Mo^{3+}. 10 K luminescence of this sample with 10,826 cm^{-1} Yb^{3+} excitation. This spectrum has been corrected for the instrument response. Note that the Yb^{3+} luminescence is magnified by a factor of 1000, showing nearly quantitative $Yb^{3+*} \rightarrow Mo^{3+}$ ET

12.3
Magnetic-Exchange Effects

Ni^{2+} has a $3d^8$ electronic configuration with a $^3A_2$ ground state. Upconversion in this ion has been reported in several hosts [64, 73]. This upconversion proceeds through a GSA/ESA mechanism, and at certain wavelengths shows photon avalanche behavior [74]. The upconversion excitation scheme for Ni^{2+}-doped $CsCdCl_3$ is shown in Fig. 23a, and involves a $^3A_2 \rightarrow {}^1E$ GSA step followed by nonradiative relaxation to the $^3T_2$ state. $^3T_2 \rightarrow {}^1A_1/{}^1T_2$ ESA then yields an ion in the luminescent $^1T_2$ upper excited state. In this host, both ESA and GSA steps involve spin-forbidden triplet-to-singlet excitations. As a result of the relatively small spin-orbit coupling parameter in Ni^{2+} ($\zeta \approx 620$ cm^{-1}, Table 2), these spin-forbidden transitions carry very low oscillator strengths, as seen in the 15 K absorption spectrum of 5% Ni^{2+}:$CsCdCl_3$ shown in Fig. 23b. The product of GSA and ESA absorption cross sections governing the two-photon excitation rate described in Eq. (6) is therefore very small.

Doping Ni^{2+} into a paramagnetic host results in a dramatic change in the optical properties of the system. Figure 23c shows the 15 K absorption spectrum of

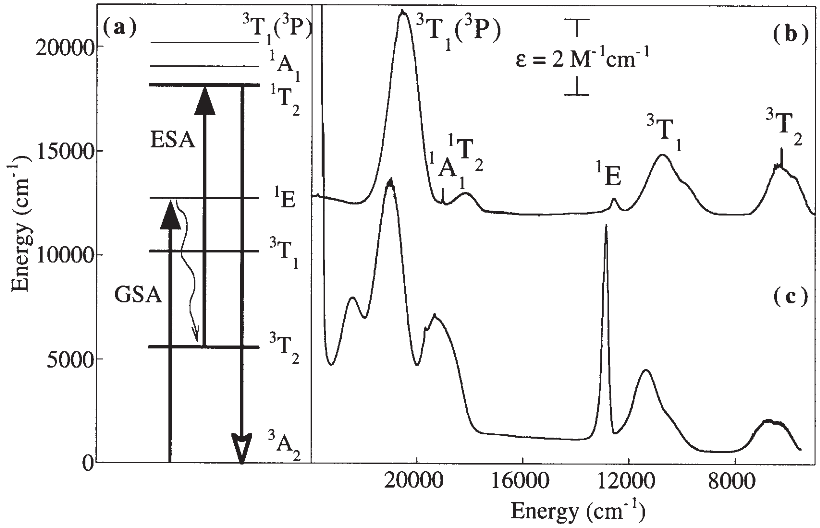

Fig. 23. **a** Two-photon GSA/ESA upconversion excitation mechanism in Ni^{2+}:$CsCdCl_3$. Both GSA and ESA transitions are spin forbidden triplet-to-singlet excitations with small cross sections. **b** 10 K absorption spectrum of 5% Ni^{2+}:$CsCdCl_3$. **c** 10 K absorption spectrum of 5% Ni^{2+}:$RbMnCl_3$. The $^3A_2 \rightarrow {}^1E$ oscillator strength has increased by an order of magnitude in (c) relative to (b). Adapted from [75]

5% Ni^{2+}:$RbMnCl_3$, where the $^3A_2 \rightarrow {}^1E$ absorption intensity is seen to be enhanced by a factor of ca. 20 [75]. Variable-temperature absorption experiments show that this feature is a hot band with intensity peaking at approximately 35 K. A similar enhancement is determined for the $^3T_2 \rightarrow {}^1T_2$ ESA cross section [75]. These absorption enhancements derive from exchange interactions between the Ni^{2+} ions and their neighboring Mn^{2+} ions [76]. Although many Mn^{2+} ions may participate in exchange interactions with each Ni^{2+} ion, the main observations can be explained by approximating this system to first-order as an exchange coupled Ni^{2+}-Mn^{2+} dimer. The exchange induced splittings in this dimer relevant to Fig. 23 are illustrated in Fig. 24. The dimer spin levels in the ground electronic state have total spins of $S_{\text{total}} = 3/2, 5/2$, and $7/2$. The Ni^{2+}-localized ^1E excited state has $S = 0$, and the $Ni^{2+}(^1E)-Mn^{2+}(^6A_1)$ dimer excited state therefore has only one spin level with $S_{\text{total}} = 5/2$. The Ni^{2+}–Mn^{2+} exchange interaction thus permits new spin to be allowed into this electronic excitation through the $^6\Gamma[Ni^{2+}(^3A_2)Mn^{2+}(^6A_1)] \rightarrow {}^6\Gamma[Ni^{2+}(^1E)Mn^{2+}(^6A_1)]$ dimer component. The intensity of this transition increases between 10 K and 35 K because the exchange-split ground-state manifold does not have the $S = 5/2$ level lowest in energy.

As it relates to upconversion, this Ni^{2+}–Mn^{2+} exchange interaction enhances both σ_0 for GSA and σ_1 for ESA in Eq. (6), since both relate to strongly spin-forbidden processes in the single ion, and both increase several fold upon interaction with Mn^{2+} [75]. The exchange interactions affect the spin-forbidden intensities most dramatically since these begin with little intensity and their descrip-

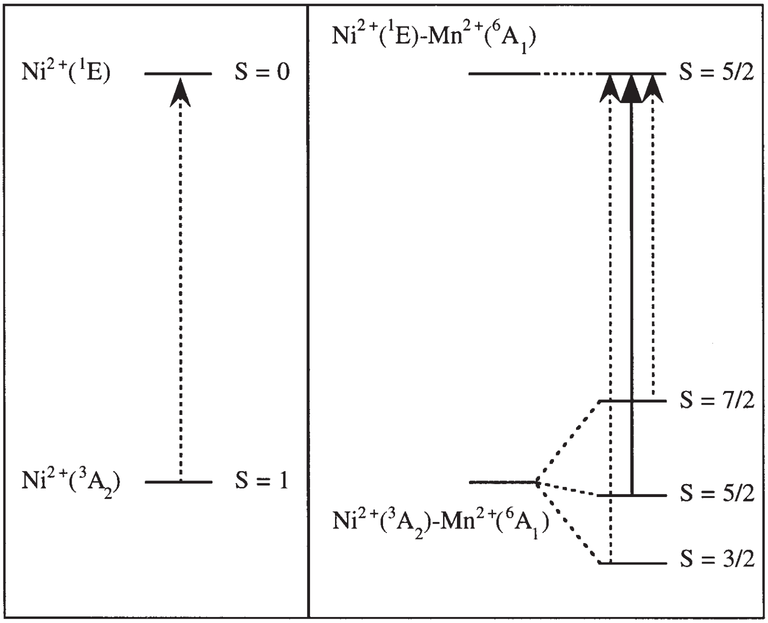

Fig. 24. Schematic illustration of the exchange mechanism for absorption intensity in a hypothetical Ni^{2+}–Mn^{2+} dimer subunit of Ni^{2+}:$RbMnCl_3$. *Left*: isolated Ni^{2+} ion, with the weak $^3A_2 \rightarrow {}^1E$ absorption cross section. *Right*: dimer splitting in the Ni^{2+}–Mn^{2+} exchange-coupled ground state. Exchange coupling introduces a spin-allowed dimer transition which is thermally activated and is more intense than the spin-forbidden dimer transitions

tion changes qualitatively from spin-forbidden to spin-allowed on going from the single ion to the dimer. Importantly, the lifetime of the $^3T_2$ intermediate state in the upconversion scheme of Fig. 23a is not significantly reduced ($k = 200\ s^{-1}$ in 5% Ni^{2+}:$RbMnCl_3$ compared to $k = 188\ s^{-1}$ in 1.5% Ni^{2+}:$CsCdCl_3$), since the exchange interactions do not significantly alter transitions which are already spin allowed in the single ion. Intense Ni^{2+} upconversion is observed in 5% Ni^{2+}:$RbMnCl_3$. The upconversion quantum yield is increased by approximately two orders of magnitude as a direct result of the increases in σ_0 and σ_1. This example demonstrates the rare use of the magnetic properties of a host material to influence the upconversion properties of a dopant ion, and its success suggests the possibility to regulate such upconversion processes through in situ magnetic perturbations.

12.4
Exchange-Induced Heterogeneous Ion Pair Upconversion

Host lattices may also contribute to upconversion in more direct ways. A dramatic example of this is in the exchange-induced upconversion phenomenon in 0.1% Yb^{3+}:$RbMnCl_3$ [77]. The lowest excited state of this host lattice is the Mn^{2+} ligand-field dependent spin-forbidden $^4T_1$ excited state with an origin at ca.

17,400 cm^{-1}. At temperatures below ca. 120 K, this lattice luminesces upon visible excitation and yields a characteristic broadband emission feature centered at about 15,700 cm^{-1} (see Fig. 25a).

Addition of Yb^{3+} to this host introduces new absorption features in the NIR that are readily assigned to Yb^{3+} $^2F_{7/2} \rightarrow {}^2F_{5/2}$ absorption. The Yb^{3+} excited state thus lies ca. 7000 cm^{-1} *lower* in energy than the lowest excited state of Mn^{2+}, excluding any possibility of direct $Yb^{3+} \rightarrow Mn^{2+}$ ET sensitization. Nevertheless, it is found that NIR excitation of Yb^{3+} at around 10,500 cm^{-1} leads to remarkably bright characteristic Mn^{2+} ($^4T_1 \rightarrow {}^6A_1$) upconverted luminescence at 15,700 cm^{-1}, as shown in Fig. 25a. One-color excitation scans between 10,000 cm^{-1} and 11,000 cm^{-1} of this upconversion luminescence show only the Yb^{3+} absorption features (Fig. 25c). Time dependence studies reveal that all Mn^{2+} excitation occurs within the 10 ns duration of a short laser pulse at 10,688 cm^{-1} (Fig. 25b), indicating a GSA/ESA process. These remarkable results are interpreted as indicating the presence of a relatively large direct Yb*Mn → YbMn* ESA cross section. This transition gains nonzero probability through the exchange interactions active between neighboring Mn^{2+} and Yb^{3+} ions in this lattice. Although the geometric details of these interactions are not yet known, several short ion-ion separations which could be conducive to exchange interactions involving dopant ions are possible in $RbMnCl_3$, the shortest of which are

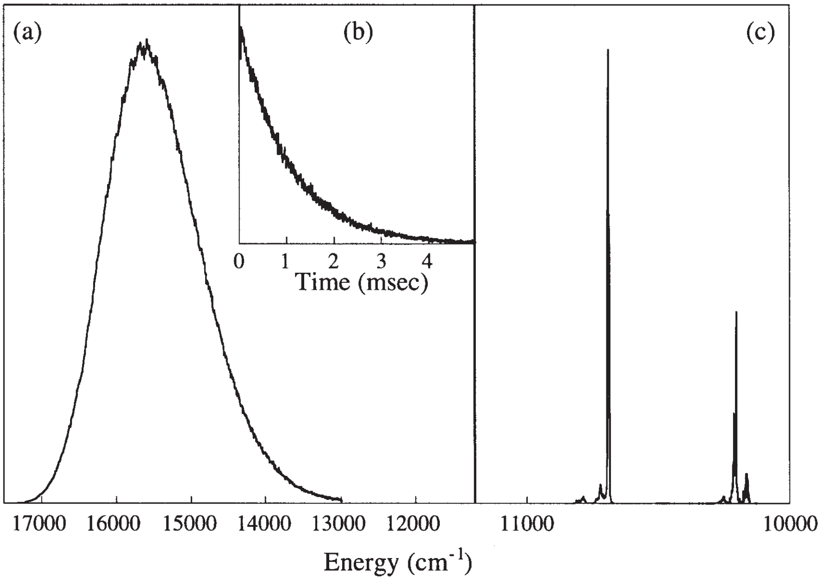

Fig. 25. **a** Upconversion luminescence in 0.1% Yb^{3+}:$RbMnCl_3$ obtained with NIR excitation into the $^2F_{7/2} \rightarrow {}^2F_{5/2}$ absorption feature of Yb^{3+} at 10,688 cm^{-1}. This broad luminescence spectrum is characteristic of the Mn^{2+} $^4T_1 \rightarrow {}^6A_1$ transition. **b** Decay of the Mn^{2+} $^4T_1 \rightarrow {}^6A_1$ upconversion luminescence following 10 ns pulsed excitation of Yb^{3+} at 10,688 cm^{-1}. **c** Upconversion excitation spectrum in the NIR. The only features observed are those of Yb^{3+} $^2F_{7/2} \rightarrow {}^2F_{5/2}$ absorption. Adapted from [77]

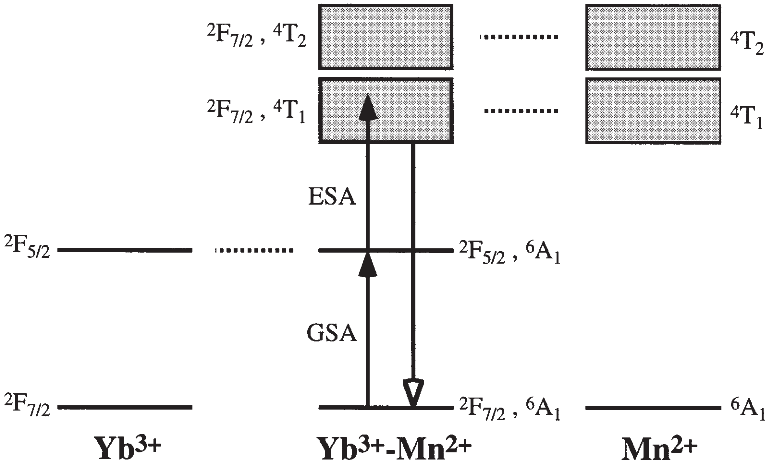

Fig. 26. Summary of the exchange-induced heterogeneous ion pair GSA/ESA upconversion process observed in 0.1% Yb^{3+} : $RbMnCl_3$. The $|^2F_{5/2}, {}^6A_1\rangle$ dimer level at ca. 10,000 cm^{-1} is predominantly localized on Yb^{3+} but has some Mn^{2+} character. Similarly, the $|^2F_{7/2}, {}^4T_1\rangle$ dimer level at ca. 17,400 cm^{-1} is predominantly localized on Mn^{2+} but has some Yb^{3+} character. A nonzero $|^2F_{5/2}, {}^6A_1\rangle \rightarrow |^2F_{7/2}, {}^4T_1\rangle$ ESA cross section results from this mixing

3.19 Å and 5.02 Å. The low oxidation state and d-type valence orbitals of Mn^{2+} result in large spatial extension of the unpaired Mn^{2+} electron density, which will enhance this effect relative to analogous situations involving two rare earth ions. These exchange interactions lead to a slight mixing of the Mn^{2+} and Yb^{3+} electronic wavefunctions, and in terms of a dimer picture result in a set of states as depicted in Fig. 26, center. In Fig. 26, center, the $|^2F_{5/2}, {}^6A_1\rangle$ pair state around 10,500 cm^{-1} is mainly localized on the Yb^{3+}, but it also has some Mn^{2+} character. Analogously, the $|^2F_{7/2},{}^4T_1\rangle$ and $|^2F_{7/2},{}^4T_2\rangle$ pair excited states are primarily localized on the Mn^{2+} ion but have some Yb^{3+} character. Within this dimer scheme, upconversion thus occurs by a GSA/ESA sequence in which the GSA step corresponds to the $|^2F_{7/2},{}^6A_1\rangle \rightarrow |^2F_{5/2},{}^6A_1>$ excitation and the ESA step corresponds to the $|^2F_{5/2},{}^6A_1\rangle \rightarrow |^2F_{7/2},{}^4T_1\rangle$ or $|^2F_{7/2},{}^4T_2\rangle$ excitation. This sequence is in very good agreement with the conclusion from the time dependence measurements that no energy transfer step is involved in the upconversion process. Studies are currently underway to determine the factors governing this upconversion in more detail.

This example illustrates a very interesting new upconversion process that is induced by exchange interactions between two active ions. The observed upconversion process is not consistent with the properties of either ion, but is truly a property of the new chromophore obtained with these exchange interactions. Analogous upconversion mechanisms are now imaginable for a variety of previously unexplored combinations of ions. These results will undoubtedly lead to the discovery of new upconversion materials involving ions previously thought unsuitable for upconversion.

13
Outlook

In this chapter we have focused on recent developments in the exploration of novel upconversion phenomena, ranging in scope from the discovery of new upconversion activators and mechanisms to the application of spectroscopy in providing detailed mechanistic information about a variety of unusual and exciting upconversion processes. The discovery of new upconversion ions, combinations of ions, and host materials are all areas of intense research. These areas will continue to provide interesting photophysical systems to study and potentially employ as luminescent materials.

The specific examples discussed in this chapter barely scratch the surface of the huge body of literature that has been published in the general area of upconversion since its discovery over three decades ago. Given this large body of literature, it is worth noting briefly a few salient omissions in the types of systems that have been studied. One general area that has only recently been approached in a systematic way is the use of transition metals as upconversion ions (see Sects. 11 and 12 and Table 2). These studies have introduced a number of new ions to the repertoire of available upconversion systems, and have also advanced our understanding of the fundamental photophysical properties of such ions. Given the many chemical differences between transition metal ions and their rare earth counterparts, some of which are illustrated in Sects. 11 and 12, the rich combination of photophysics and chemistry available in this area lends it great promise. In particular, the examples in Sects. 12.3 and 12.4 illustrate the very important role that exchange interactions can play in generating chromophores whose photophysical properties are more complex than simply the sum of their parts. As chemists, this opens the door to vast new possibilities in the design of such new luminescent materials.

A second, perhaps more general, omission involves the generation of upconversion in environments other than crystals and glasses. Discrete coordination complexes capable of upconversion, for example, could be used as luminescent probes in solution as many downconversion systems are currently employed, but would offer the unusual option of exciting to lower energy than the probed emission. The analogous use of simultaneous two-photon absorption as a bioanalytical tool has proven very successful recently [78]. The study of upconversion in discrete coordination complexes will undoubtedly provide new and unexpected results once such systems are systematically addressed. Given the huge body of literature dealing with the luminescent properties of transition-metal and rare-earth ions in solution, it is obvious that a major sacrifice in excited-state lifetimes must be accepted when working in solution, but also that the effects of solution can be limited somewhat by a judicious choice of encapsulating ligation [79, 80]. This area has to date remained wholly unexplored, and consequently stands as a challenge to innovative chemists and physicists alike.

Finally, the ability to regulate in situ the upconversion properties of an ion, or conversely to use upconversion as an in situ environmental probe, has not been demonstrated, although all of the key ingredients have been individually demonstrated. As described in Sect. 12, for example, different colors of Er^{3+} upconversion luminescence are observed depending on the vibrational properties of the environment. Likewise, Ni^{2+} may demonstrate two orders of magnitude enhancement in its upconversion intensity when involved in magnetic exchange interactions with a paramagnetic neighbor. As a transition metal ion, the energies of the Ni^{2+} excited states are also fairly susceptible to ligand-field perturbations, and these could be used to tune the two-photon excitation overlap as described in Sect. 6. Similarly, the set of transition metals listed in Table 2 all display rich redox or photo-redox chemistry, which could lead to their use as redox sensitive upconversion luminescent probes. Finally, as demonstrated in Sect. 8, cooperative luminescence, energy-transfer upconversion, and energy-transfer sensitization only proceed most efficiently when two excited ions are in close proximity to one another. This is the basis for the common employment of ET as a gauge of interchromophore distances, and upconversion luminescence could be imagined as an analogous probe of nearest-neighbor ion-ion interactions. All of these observations relate to aspects of environmental sensitivity that have yet to be explored in novel in situ upconversion schemes, and the future in this area is as unpredictable as it is full of possibility.

Acknowledgements. The authors thank the Swiss National Science Foundation for financial support, and Karl Krämer, Rafael Valiente, Oliver Wenger, and Markus Wermuth for helpful comments.

14
References

1. See for example: Bloembergen N (1962) Phys Rev 127:1918
2. See for example: McClain WM, Harris RA (1977) In: Lim EC (ed) Excited states. Academic Press, New York, vol III
3. Wright JC (1976) In: Fong FK (ed) Topics in applied physics: radiationless processes in molecules, condensed phases. Springer, Berlin Heidelberg New York, p 239
4. Kaplyanskii AA, Macfarlane RM (eds) (1987) Spectroscopy of solids containing rare-earth ions. North-Holland, Amsterdam, vol 21
5. Auzel FE (1973) Proc IEEE 61:758
6. Joubert MF (1999) Optical Materials 11:181
7. Reber C, Güdel HU (1990) J Lumin 47:7
8. Struck CW, Fonger WH (1975) J Lumin 10:1
9. Imbusch GF (1978) In: Lumb MD (ed) Luminescence spectroscopy. Academic Press, New York, p 1
10. Kasha M (1950) Discuss Faraday Soc 9:14
11. Ovsyankin VV, Feofilov PP (1966) JETP Lett 3:317
12. Ovsyankin VV, Feofilov PP (1966) JETP Lett 3:322
13. Auzel F (1966) C R Acad Sci Paris 263B:765
14. Auzel F (1966) C R Acad Sci Paris 263B:819
15. Lenth W, Macfarlane RM (1992) Optics & Photonics News 3:8
16. Downing E, Hesselink L, Ralston J, Macfarlane R (1996) Science 273:1185
17. Gamelin DR, Güdel HU (2000) Accounts of Chemical Research 33:235
18. Hadad CZ, Vásquez SO (1999) Phys Rev B 60:8586
19. Di Bartolo B (1968) Optical interactions in solids. Wiley, New York
20. In Eq. (9), n is the polarization-averaged index of refraction at energy $\nu(\mathrm{cm}^{-1})$
21. Riedener T, Güdel HU (1997) J Chem Phys 107:2169

22. Buisson R, Vial JC (1981) J Phys Lett 42:L115
23. Cockroft NJ, Jones GD, Nguyen DC (1992) Phys Rev B 45:5187
24. Henling LM, McPherson GL (1977) Phys Rev B 16:4756
25. McPherson GL, Henling LM (1977) Phys Rev B 16:1889
26. Lüthi SR, Pollnau M, Güdel HU, Hehlen MP (1999) Phys Rev B 60:162
27. Pollnau M, Gamelin DR, Lüthi SR, Güdel HU, Hehlen MP (2000) Phys Rev B 61:3337
28. Gamelin DR, Güdel HU (1999) Inorg Chem 38:5154
29. Diggle PC, Gehring KA, Macfarlane RM (1976) Solid State Communications 18:391
30. Guyot Y, Manna H, Rivoire JY, Moncorgé R, Garnier N, Descroix E, Bon M, Laporte P (1995) Phys Rev B 51:784
31. Pollnau M, Hardman PJ, Clarkson WA, Hanna DC (1998) Optics Communications 147:203
32. Gamelin DR, Güdel HU (2000) J Phys Chem B 104:10222
33. Krämer KW, Güdel HU, Schwartz RN (1998) Journal of Alloys, Compounds 275–277:191
34. Judd BR (1962) Phys Rev 127:750
35. Ofelt GF (1962) J Chem Phys 37:511
36. Richardson FS, Reid MF, Dallara JJ, Smith RD (1985) J Chem Phys 83:3813
37. Quagliano JR, Cockroft NJ, Gunde KE, Richardson FS (1996) J Chem Phys 105:9812
38. Reid MF, Richardson FS (1983) J Chem Phys 79:5735
39. Reid MF (1984) J Phys Chem 88:3579
40. Krämer KW, Güdel HU, Schwartz RN (1997) Phys Rev B 56:13,830
41. Lüthi SR, Güdel HU, Hehlen MP (1999) J Chem Phys 110:12,033
42. Kushida T (1973) J Phys Soc Japan 34:1318
43. Goldner Ph, Pellé F, Meichenin D, Auzel F (1997) J Lumin 71:137
44. Ovsyankin VV (1987) In: Kaplyanskii AA, Macfarlane RM (eds) Spectroscopy of solids containing rare earth ions. North-Holland, Amsterdam, vol 21, pp 343
45. Meyer G (1982) Prog Solid St Chem 14:141
46. Gamelin DR, Güdel HU (to be published)
47. Vásquez SO (1999) Phys Rev B 60:8575
48. Vásquez SO, Flint CD (1995) Chem Phys Lett 238:378
49. Guy S, Joubert MF, Jacquier B (1997) Phys Rev B 55:8240
50. Case WE, Koch ME, Kueny AW (1990) J Lumin 45:351
51. Chivian JS, Case WE, Eden DD (1979) Appl Phys Lett 35:124
52. Collings BC, Silversmith AJ (1994) J Lumin 62:271
53. Joubert MF, Guy S, Jacquier B (1993) Phys Rev B 48:10,031
54. Joubert MF, Guy S, Jacquier B, Linarés C (1995) J Appl Spectroscopy 62:716
55. Koch ME, Kueny AW, Case WE (1990) App Phys Lett 56:1083
56. Joubert MF, Guy S, Jacquier C, Linarés C (1994) Opt Mat 4:43
57. Hehlen MP, Güdel HU (1993) J Chem Phys 98:1768
58. Hehlen MP, Güdel HU, Shu Q, Rai J, Rand SC (1994) Phys Rev Lett 73:1103
59. Hehlen MP, Güdel HU, Shu Q, Rand SC (1996) J Chem Phys 104:1232
60. Lüthi SR, Hehlen MP, Riedener T, Güdel HU (1998) J Lumin 76/77:447
61. Hehlen MP, Kuditcher A, Rand SC, Lüthi SR (1999) Phys Rev Lett 82:3050
62. Gamelin DR, Lüthi SR, Güdel HU (2000) J Phys Chem B, in press
63. Dönni A, Fischer P, Furrer A, Cockcroft JK, Güdel HU (1991) J Solid State Chem 93 119
64. Moncorgé R, Benyattou T (1988) Phys Rev B 37:9186
65. Jacobsen SM, Güdel HU (1989) J Lumin 43:125
66. Wermuth M, Güdel HU (1998) Chem Phys Lett 281:81
67. Wermuth M, Güdel HU (1999) J Am Chem Soc 43:10,102
68. Gamelin DR, Güdel HU (1998) J Am Chem Soc 120:12,143
69. Flint CD, Paulusz AG (1981) Mol Phys 44:925
70. Flint CD, Paulusz AG (1981) Mol Phys 43:321
71. Ohwaki J, Wank Y (1994) Jpn J Appl Phys 33:L334
72. Riedener T, Krämer K, Güdel HU (1995) Inorg Chem 34:2745
73. Oetliker U, Riley MJ, Güdel HU (1995) J Lumin 63:63
74. Oetliker U, Riley MJ, May PS, Güdel HU (1991) Coord Chem Rev 111:125

75. Wenger OS, Gamelin DR, Güdel HU (2000) J Am Chem Soc 122:7408
76. Ferguson J, Guggenheim HJ, Tanabe Y (1965) Phys Rev Lett 14:737
77. Valiente R, Wenger OS, Güdel HU (2000) Chem Phys Lett 320:639
78. Shear JB (1999) Anal Chem 71:598
79. Werts MHV, Johannes WH, Geurts FAJ, Verhoeven JW (1997) Chem Phys Lett 276:196
80. Li M, Selvin PR (1995) J Am Chem Soc 117:8132
81. Stranger R, Moran G, Krausz E, Güdel HU, Furer N (1990) Mol Phys 69:11

Geometric and Electronic Information from the Spectroscopy of Six-Coordinate Copper(II) Compounds

Mark J. Riley

Department of Chemistry, The University of Queensland, St. Lucia, 4072, Australia
E-mail: riley@chemistry.uq.edu.au

The ground and excited state geometry of the six-coordinate copper(II) ion is examined in detail using the CuF_6^{4-} and $Cu(H_2O)_6^{2+}$ complexes as examples. A variety of spectroscopic techniques are used to illustrate the relations between the geometric and electronic properties of these complexes through the characterization of their potential energy surfaces.

Keywords: Copper(II) compounds, Jahn-Teller effect, Excited state geometries

Topics in Current Chemistry, Vol. 214

1
Introduction

There exists a large literature on the spectroscopic properties of copper(II) compounds. This is due to the simplicity of the d^9 electron configuration, the wide variety of stereochemistries that copper(II) compounds can adopt, and the fluxional geometric behavior that they sometimes exhibit [1]. The electronic and geometric properties of a molecule are inexorably linked and this is especially true with six-coordinate copper(II) compounds which are subject to a Jahn-Teller effect. However, the spectral-structural correlations that are sometimes drawn must often be viewed with caution as the information contained in a typical solution UV-Vis absorption spectrum of a copper(II) compound is limited.

Meaningful spectral-structural correlations can be obtained in a related series of compounds where detailed spectroscopic data is available. In the following sections two such series are examined; the six-coordinate CuF_6^{4-} and $Cu(H_2O)_6^{2+}$ ions doped as impurities in single crystal hosts. Using low temperature polarized optical spectroscopy and electron paramagnetic resonance, a very detailed picture can be drawn about the geometry of these ions in both their ground and excited electronic states. We then compare the spectroscopically determined structural data with that obtained from X-ray diffraction or EXAFS measurements.

2
Jahn-Teller Potential Energy Surfaces

In octahedral symmetry, the copper(II) ion has a ^2E electronic ground state due to the d^9 electron configuration with the unpaired electron in an e_g σ anti-bonding orbital. An exact octahedral geometry of six-coordinate copper(II) complexes is never realized due to a strong Jahn-Teller effect. The symmetry of the Jahn-Teller active vibration is e_g, the non-totally symmetric part of the symmetric square $[E_g \otimes E_g]$. For a $Cu(II)L_6$ complex, the two components of the degenerate e_g vibration are shown in Fig. 1 a [2].

Each component consists of changes in the Cu-L bond lengths and is therefore strongly coupled to the energy of the e_g σ anti-bonding orbitals. This results in the ground state electronic properties of $Cu(II)L_6$ complexes being largely determined by this $E \otimes e$ Jahn-Teller problem.

Any orthonormal linear combination of degenerate vibrational coordinates are also valid coordinates, although we shall see that the Q_θ, Q_ε pair given in Fig. 1 a is an especially suitable choice. A distortion along the Q_θ or Q_ε coordinates will result in the symmetry of the O_h complex being lowered to D_{4h} or D_{2h} respectively. Although group theory does not explicitly determine which component or combination of components the molecule will distort along, the epikernel principle [3] states that, in general, molecules will undergo the minimum symmetry reduction necessary to remove the degeneracy.

This implies that, in the absence of external perturbations such as asymmetric ligands or crystal packing forces, the Jahn-Teller distortion will be tetragonal (D_{4h}). This agrees with the vast majority of six-coordinate copper(II) com-

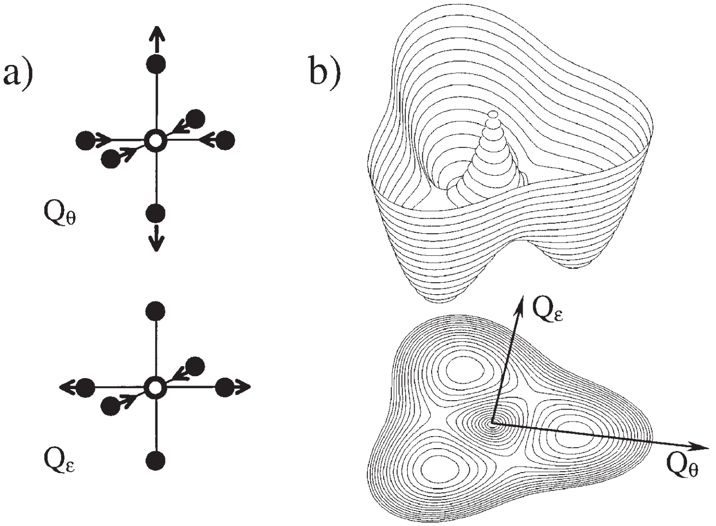

Fig. 1. **a** The two components (Q_θ, Q_ε) of the Jahn-Teller active e_g vibration of an Cu(II)L_6 octahedron. **b** The E ⊗ e Jahn-Teller potential energy surfaces with first and second order coupling terms

pounds where it is found that there are two axial bonds longer than the four equatorial bonds. This elongated rather than compressed geometry is understood to be a result of three competing factors [4]. The second order Jahn-Teller coupling will favor compression [5], while both the vibrational anharmonicity and the 3d-4s mixing will favor elongation [6]. This last mechanism is thought to dominate. The empty 4s orbital and the $3d_{z^2}$ orbital both transform as a_{1g} in D_{4h} point group, and the resulting symmetry allowed mixing causes the z^2 orbital to be depressed in energy. This results in the unpaired electron being in the x^2-y^2 orbital and the complex having an elongated geometry.

For an octahedral geometry there are three equivalent elongated distortions, where the elongated axis is directed along either x, y, or z axes. These equivalent directions result in the threefold symmetry of the two-dimensional potential energy surface as a function of Q_θ, Q_ε for the ground state of copper(II) as shown in Fig. 1b.

This two-dimensional potential energy surface is the lower energy solution obtained from the diagonalization of the potential energy operators in the E ⊗ e vibronic Hamiltonian acting within a ($|\theta>$, $|\varepsilon>$) electronic basis:

$$H = H_0 + H_{JT}$$

$$H_0 = [1/2\, h\nu\, (Q_\theta^2 + Q_\varepsilon^2) + K_3 Q_\theta (Q_\theta^2 - 3Q_\varepsilon^2)] \begin{pmatrix} 1 & 0 \\ 0 & 1 \end{pmatrix} \tag{1}$$

$$H_{JT} = A_1 \begin{pmatrix} Q_\theta & -Q_\varepsilon \\ -Q_\varepsilon & -Q_\theta \end{pmatrix} + A_2 \begin{pmatrix} (Q_\theta^2 - Q_\varepsilon^2) & 2Q_\theta Q_\varepsilon \\ 2Q_\theta Q_\varepsilon & -(Q_\theta^2 - Q_\varepsilon^2) \end{pmatrix}$$

The hν and K_3 parameters are the harmonic vibrational frequency and anharmonicity constant respectively of the vibrational Hamiltonian (H_0). The A_1 and A_2 parameters are the first-order and second-order Jahn Teller coupling constants respectively for the Jahn-Teller part of the Hamiltonian (H_{JT}).

In practice there are often low symmetry terms which influence the E ⊗ e Hamiltonian given above and these can be written as

$$H_{ST} = \begin{pmatrix} S_\theta & -S_\varepsilon \\ -S_\varepsilon & -S_\theta \end{pmatrix} \tag{2}$$

Here S_θ and S_ε are the tetragonal and orthorhombic components of the low symmetry field, sometimes called "strain terms." The signs of S_θ, S_ε are chosen to conform with the signs for the two coordinates Q_θ and Q_ε respectively. All parameters in Eqs. (1) and (2) can have units of energy if dimensionless units are used for Q_θ and Q_ε [2, 8].

When the strain terms are zero, the lower E ⊗ e surface is given by Fig. 1b. Here the energy and coordinate origin is where the upper and lower potential energy surfaces coincide at a conical intersection and the complex has O_h symmetry at this point. For A_1 and A_2 positive in Eq. (1) (appropriate to Cu(II)L_6 complexes), there are three minima on the surface at $\phi = 0$, 120, and 240° and three saddle points at $\phi = 60, 180$, and 300° which represent barriers for the interconversion between the minima. The often portrayed "Mexican hat" potential energy surface, in which only linear Jahn-Teller coupling terms are used, is inappropriate for the copper(II) ground state. The Mexican hat surface is a surface of revolution about the energy axis and therefore has no barriers or minima about an equi-energy trough. All experimental and theoretical studies suggest that the second-order and higher terms are important [4], resulting in the three equivalent minima separated by barriers as shown in Fig. 1.

We note that the full vibronic Hamiltonian of the E ⊗ e Jahn-Teller problem does not in itself result in a distorted molecule. The expectation values of the geometry using the vibronic wavefunctions remain octahedral. However, the form of the potential energy surface makes it very sensitive to external perturbations of the type given in Eq. (2). Any small perturbation is capable of localizing the wavefunctions at a particular minimum. In the solid state, the perturbations can be so large that they can substantially change the shape of the potential energy surfaces and the positions of the minima.

2.1
Ground State Properties of Cu(II)L_6 Complexes

The E ⊗ e warped Jahn-Teller potential energy surface shown in Fig. 1b is the dominant function in determining the ground state properties of Cu(II)L_6 complexes. The lower potential energy surface as a function of the angular coordinate, ϕ, is shown in Fig. 2.

The least energy pathway between the three minima is a Jahn-Teller pseudorotational motion passing over three barriers (or saddle points in the Q_θ, Q_ε space of Fig. 1b). Writing the vibronic Hamiltonian in Eq. (1) using polar coor-

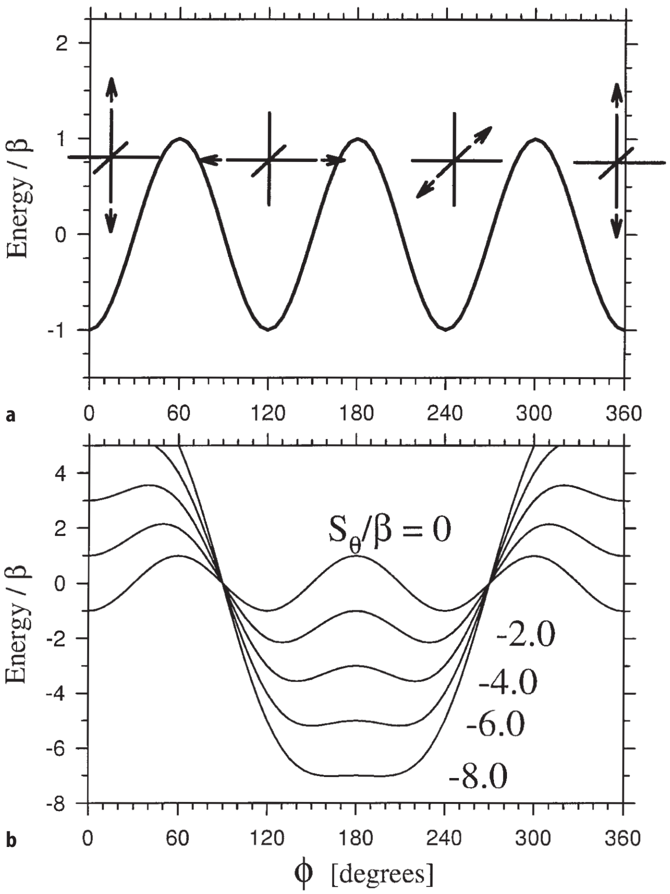

Fig. 2a, b. A circular cross-section of the lower E ⊗ e Jahn-Teller surface shown in Fig. 1: **a** without low symmetry terms – the three elongated octahedra correspond to the geometry at the three minima of the potential; **b** with various degree of S_θ such that a tetragonally compressed geometry is ultimately stabilized

dinates $Q_\theta = \rho\cos\phi$, $Q_\varepsilon = \rho\sin\phi$ one finds a functional form for Fig. 2 by taking a circular cross-section of the two-dimensional surface at $\rho = \rho_o = A_1/h\nu$:

$$V(\phi) = -\beta\cos(3\phi) \qquad \beta = (-K_3\rho_o^3 + A_2\rho_o^2) \tag{3}$$

This expression is obtained after using the similarity transformation on Eq. (1) that makes the first-order Jahn-Teller coupling (A_1) diagonal, and neglecting remaining coupling terms between the surfaces. These latter terms include the off-diagonal $A_2\rho^2\sin(3\phi)$ as well as kinetic energy terms, so Eq. (3) is only valid when A_1 is large.

Equation (3) gives an expression for the barrier heights (2β) in terms of the second-order coupling (A_2) and the vibrational anharmonicity (K_3). However, the least energetic pathway between the minima is far from circular as the value of ϱ for the saddle points is less than for the minima (see Fig. 1b). The barrier height given by $V(\phi)$ in Eq. (3) is then an overestimate.

An external strain applied to the vibronic Hamiltonian can be shown to be equivalent to a low symmetry distortion [7]. Within the approximation of the angular potential given by Eq. (3), the tetragonal (S_θ) and orthorhombic (S_ε) components of the strain modify the one-dimensional potential energy surface according to

$$V(\phi) = -\beta\cos(3\phi) - S_\theta\cos\phi - S_\varepsilon\sin\phi \tag{4}$$

Here the signs of the strain terms S_θ, S_ε are chosen to conform with the signs for the two coordinates Q_θ and Q_ε respectively. Consider a tetragonal perturbation initially ($S_\varepsilon = 0$). A positive value for S_θ will make one of the three minima ($\phi = 0$) lower than the other two in Fig. 2a. Unless the value of S_θ is very small, this stabilization of one minimum will make the molecule rigidly localized at an elongated geometry.

A negative value of S_θ will cause two minima to be lowered with respect to the third as shown in Fig. 2b. This will be true for $-S_\theta < 9\beta$, after which a single minimum at $\phi = 180°$ will exist [8]. The existence of two equivalent minima lower in energy than the third can lead to interesting temperature-dependent effects as outlined in Sect. 4.3. It should also be noted that the positions of the minima are moved from the elongated positions at $\phi = 120°, 240°$ to orthorhombic values that approach $\phi = 180°$ and merge into a single minimum when $-S_\theta = 9\beta$.

2.2
Excited State Properties of Cu(II)L$_6$ Complexes

The $^2T_{2g}$ excited multiplet of Cu(II)L$_6$ complexes can be coupled to both e_g and t_{2g} vibrations of the octahedron. The Jahn-Teller active e_g mode is the same as in the ground electronic state, whereas the t_{2g} mode of an octahedral complex corresponds to a trigonal distortion. Just as linear combinations of the e_g vibrational coordinates can be chosen to reproduce the three equivalent tetragonally elongated octahedra, linear combinations of the three components of the t_{2g} vibration can be chosen to reproduce the four equivalent trigonal distortions along the four C_3 axes of an octahedron. Apart from specific unusual values of the coupling constants [2] the $T \otimes (e_g \oplus t_{2g})$ potential energy surface will have either 3 tetragonal minima or 4 trigonal minima depending on the relative values of the coupling constants. It has been shown that the first-order coupling constant for coupling with e_g modes depends on the change of the e_π bonding parameter as a function of bond length, while the coupling with the t_{2g} modes depends on the absolute value of e_π [5]. Before we discuss the relative strengths, we note that spin-orbit coupling will split the $^2T_{2g}$ multiplet into Γ_7 and Γ_8 states of the O_h double point group. The Γ_7 state is nondegenerate while the Γ_8 state is subject to a $\Gamma_8 \otimes (e_g \oplus t_{2g})$ Jahn-Teller effect. By assuming a functional form for the variation of e_π with bond length, one can demonstrate that it is very unlikely that the minima of the Γ_8 surface are along the t_{2g} modes [9]. For a cubic system the Γ_8 excited state potential energy surface of Cu(II)L$_6$ complexes are expected to have three minima at positive tetragonally elongated geometry, with the same sign as the distortion in the ground electronic state but much less in magnitude.

3
Optical Spectroscopy

While six-coordinate copper(II) compounds will almost always adopt a tetragonally elongated geometry, if the complex is doped as an impurity into a crystal lattice which already has a particular site distortion, then it is possible to impose a different geometry onto the copper(II) complex. In this section we examine a series of fluoride hosts in which the metal site has a geometry that varies from an octahedron that is compressed through cubic to elongated. We can then examine the geometry of copper(II) complexes that results from the balance between the geometry it wishes to adopt intrinsically and the perturbation that the host lattice superimposes.

3.1
Magnetic Dipole and Vibronic Selection Rules

Copper(II) has the largest spin-orbit coupling constant of the first row transition metals and so one may expect large effects in the optical spectrum. However, this is not seen in practice as the optical spectra are usually very broad. This broadening is largely due to excited state displacements along both a_{1g} and e_g modes as discussed in Sect. 2.2 above. In favorable cases, however, one can directly see the spin-orbit splitting of states if sharp electronic origins appear through a magnetic dipole intensity mechanism.

Table 1 gives the orbital and spin-orbital selection rules appropriate for a D_{4h} copper(II) ion in a compressed and elongated environment. Here the Mulliken

Table 1. Vibronic and magnetic dipole selection rules for a centrosymmetric Cu(II) L_6 complex

O_h parent	Transition	Vibronic		Magnetic dipole	
		$E \perp z$	$E \parallel z$	$H \perp z$	$H \parallel z$
	Compressed geometry				
^2E_g	$^2A_{1g}\ (\Gamma_6) \rightarrow {}^2B_{1g}\ (\Gamma_7)$	✓ (✓)	✓ (✓)	× (✓)	× (×)
$^2T_{2g}$	$^2E_g\ (\Gamma_7)$	✓ (✓)	✓ (✓)	✓ (✓)	× (×)
	(Γ_6)	(✓)	(✓)	(✓)	(✓)
	$^2B_{2g}\ (\Gamma_7)$	✓ (✓)	× (✓)	× (✓)	× (×)
	Elongated geometry				
^2E_g	$^2B_{1g}\ (\Gamma_7) \rightarrow {}^2A_{1g}\ (\Gamma_6)$	✓ (✓)	✓ (✓)	× (✓)	× (×)
$^2T_{2g}$	$^2B_{2g}\ (\Gamma_7)$	✓ (✓)	✓ (✓)	× (✓)	✓ (✓)
	$^2E_g\ (\Gamma_7)$	(✓)	(✓)	✓ (✓)	× (✓)
	(Γ_6)	✓ (✓)	× (✓)	(✓)	(×)

✓ transition allowed, × transition forbidden.

notation is given for the pure orbital states and the Bethe (Γ) notation [10] for the spin-orbital states. The selection rules are given for both transitions between orbital states and transitions between spin-orbit states (in brackets).

It is found experimentally that the intensity of both the magnetic dipole and vibronically induced electric dipole allowed transitions are principally determined by the orbital character of the electronic states. That is, transitions that are forbidden in the orbital basis but allowed in the spin-orbit basis in Table 1, are likely to be weak.

For magnetic dipole intensity this may be understood by the following reasoning. The ground electronic state consists of relatively pure z^2 and $x^2 - y^2$ states for a compressed and elongated geometry respectively. In a compressed environment, only the transitions from z^2 ($m_l = 0$) to xz, yz ($m_l = \pm 1$) states are allowed. These transitions require a $\Delta m_l = \pm 1$ change in orbital angular momentum and so will be (x, y) polarized. In an elongated environment, however, the transitions from $x^2 - y^2$ to both xz, yz ($\Delta m_l = \pm 1$) and xy ($\Delta m_l = 0$) states are allowed in (x, y) and z polarizations respectively.

Figure 3 shows the 4 K spectrum of CuF_6^{4-} doped K_2ZnF_4 in the region of the $^2T_{2g}$ excited state multiplet to illustrate these points [11]. In this spectral region there are two orbital states ^2E_g and $^2B_{2g}$ or three spin-orbit states; the ^2E_g state splits into Γ_7, Γ_6, and the $^2B_{2g}$ state transforms as a Γ_7. There are three possible polarization directions for a uniaxial crystal with the unique axis c: α ($\mathbf{k} \| c$, $\mathbf{E} \perp c$, $\mathbf{H} \perp c$), σ ($\mathbf{k} \perp c$, $\mathbf{E} \perp c$, $\mathbf{H} \| c$), and π ($\mathbf{k} \perp c$, $\mathbf{E} \| c$, $\mathbf{H} \perp c$). Here **k** is the direction of light propagation and **E**(**H**) are the electric(magnetic) vectors perpendicular to **k** of the linearly polarized light. These three directions can identify the electric and magnetic dipole allowed transitions in the spectrum. Electric dipole allowed transitions have $\alpha = \sigma \neq \pi$ while magnetic dipole allowed transitions have $\alpha = \pi \neq \sigma$, as the equal polarisations $\alpha = \sigma$ and $\alpha = \pi$ have the same orientation of the electric and magnetic component of the polarized light respectively.

An examination of Fig. 3 reveals that there are three broad electric dipole allowed transitions and two sharper magnetic dipole allowed electronic origins. The sharp origins are largely absent in σ polarization indicating that these magnetic dipole allowed transitions are x,y polarized as predicted by the orbital selection rules as these origins are the split components of the ^2E_g orbital state. Of the broad electric dipole allowed transitions, the highest energy one is absent in π polarization ($E \| z$) indicating that it principally has $^2B_{2g}$ orbital character. Both these absences predicted by the orbital selection rules are relaxed on going to the spin-orbit selection rules (Table 1). However this relaxation is not observed experimentally (Fig. 3), indicating that the effect of spin-orbit coupling on the transition intensities in CuF_6^{4-} doped K_2ZnF_4 is small.

However, the effect of the spin-orbit coupling on the energy levels of this system is large as observed by the 1207 cm^{-1} splitting of the orbital ^2E_g state shown in Fig. 3. Where it can be observed, the splitting of the ^2E_g state is an accurate way to quantify the degree of the tetragonal distortion in the excited states of $Cu(II)L_6$ complexes. Figure 4 shows the energy levels of the $^2T_{2g}$ excited multiplet as a function of a tetragonal ligand field, Δ_t, and the spin-orbit coupling constant, λ.

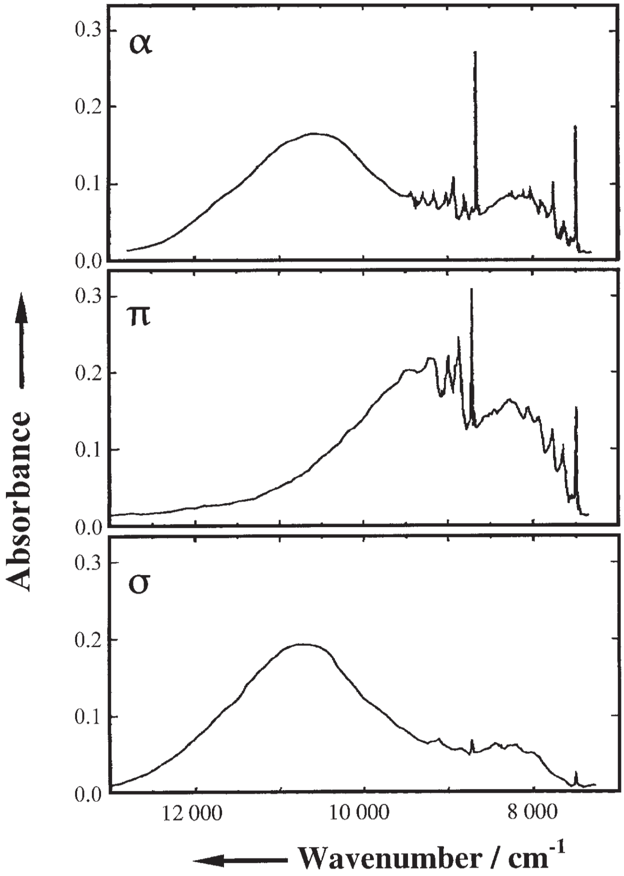

Fig. 3. Polarized absorption spectra of CuF_6^{4-} of 3% Cu(II) doped in K_2ZnF_4 at 4K [11]. The polarization directions α, σ, π are defined in the text

The energy separation of the magnetic dipole origins will depend on where the minima of the potential surfaces are located when a harmonic vibrational potential is added to the purely electronic levels shown in Fig. 4. However, to a good approximation, the components of the split ^2E_g will both have their minima at the same geometry and a semi-quantitative picture emerges. The $\Gamma_7 - \Gamma_6$ splitting of the ^2E_g state approaches λ for both strongly compressed and strongly elongated tetragonal ligand fields. As the strength of the tetragonal compression decreases, this splitting *increases* to a limiting value of $3/2\lambda$ as it approaches cubic symmetry. As the strength of a tetragonal elongation decreases, the splitting *decreases* to 0 as it approaches cubic symmetry.

The positive slope of the ^2E_g (Γ_7, Γ_6) split pair means that the excited state minima will tend to be at a compressed geometry. This means that Franck-Condon factors will make the observation of transitions to the ^2E_g (Γ_7, Γ_6) states difficult to observe from a tetragonally elongated ground state and they have not,

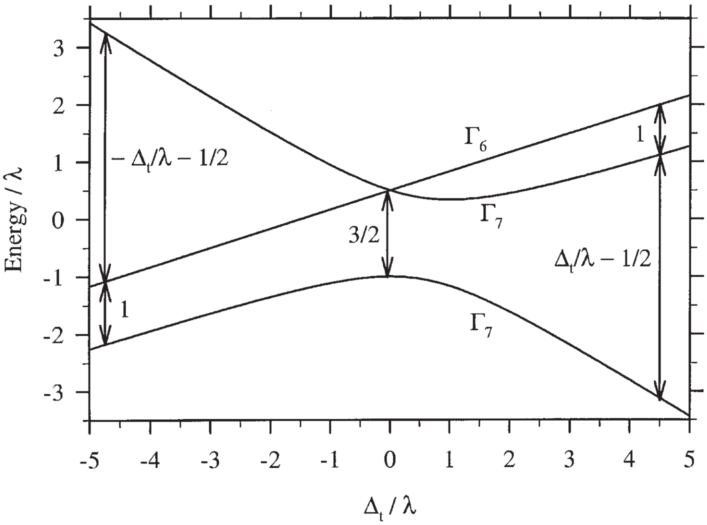

Fig. 4. The energy of the $^2T_{2g}$ multiplet as a function of the tetragonal field Δ_t and the spin-orbit coupling, λ. The negative and positive values of Δ_t/λ correspond to a tetragonal compression and elongation respectively. The energy separations indicated on the left and right hand sides of the figure are the limiting values

in fact, been experimentally observed for an elongated CuF_6^{4-} complex. The situation is quite different for the tetragonally compressed CuF_6^{4-} complex, where the splitting is observed to vary in the expected manner in cubic Cu(II)/$KZnF_3$ (1300 cm^{-1}) to the increasingly tetragonally compressed Cu(II)/K_2ZnF_4 (1207 cm^{-1}), $KCuAlF_6$ (1073 cm^{-1}), and Cu(II)/Ba_2ZnF_6 (1068 cm^{-1}) systems. The decrease in this splitting for increasing tetragonal compression agrees very well with the structural data of the host crystals [12].

In all these cases the CuF_6^{4-} ion adopts a true compressed geometry. In the absence of structural information about an impurity ion, it is important to verify the geometry using an independent technique such as EPR (Sect. 4). As discussed in Sect. 2.1, a tetragonal compression superimposed on the warped Jahn-Teller surface can often result in a double minima potential energy surface, each minimum corresponding to an elongated geometry.

3.2
Magnetic Circular Dichroism

The $g_{||}$ values of the ground and excited electronic states can be used to determine both the sign and the temperature dependence of the magnetic circular dichroism (MCD) of the magnetic dipole origins of copper(II) systems. For a tetragonal system the sign of $g_{||}$ is a meaningful quantity independent of any phase conventions for the wavefunctions [13]. The ground state $g_{||}$ value for copper(II) ions in either a tetragonally compressed or elongated environment is positive since it is determined by a small shift from the spin-only value due to the spin-orbit mixing of the $^2T_{2g}$ multiplet into the electronic ground state. The sign of the excited states, however, can be either positive or negative and accurate perturbation expressions for these have been found [14]. Figure 5 shows the $g_{||}$ values of the two components of the ^2E_g excited and the $^2A_{1g}(z^2)$ ground electronic states which can be used to interpret the MCD of Cu(II)/K_2ZnF_4.

The Kramers' doublets split in the applied axial magnetic field according to the values of $g_{||}$ as shown schematically in Fig. 5b. In the low temperature limit,

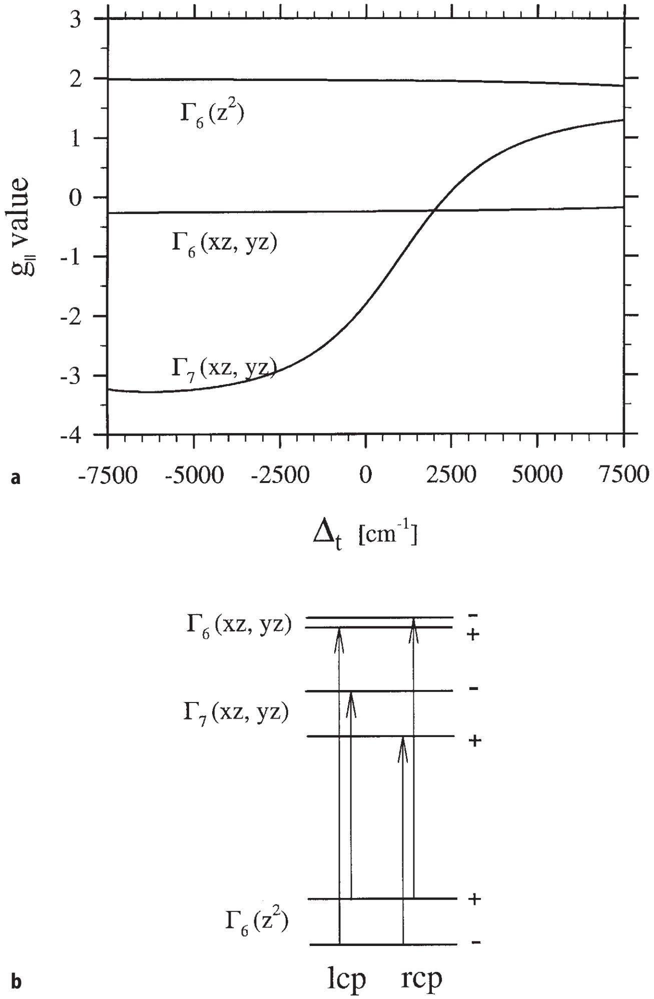

Fig. 5. **a** The calculated $g_{||}$ values for the Γ_6, Γ_7 (E_g) excited and $\Gamma_6(^2A_{1g})$ ground electronic states as a function of the tetragonal field Δ_t. The perturbation expressions of [13] have been used with the AOM parameters: $\Delta_o = 7000$ cm^{-1} and $\lambda = 0.85 \times 830$ cm^{-1}. **b** The allowed magnetic dipole transitions for circularly polarized light (k||c) in an applied magnetic field ||c for a tetragonally compressed Cu(II)L_6 complex

only the $m_s = -1/2$ component of the ground state Kramers' doublet will be populated and only $z^2(-) \rightarrow \Psi(+)$ transitions will be observed. The Γ_7, Γ_6 (D_{4h} double group) spin-orbit split components of the ^2E_g state absorb right and left circularly polarized light respectively. This results in the signs observed in the low temperature MCD spectrum shown in Fig. 6.

As the temperature is raised, population of the other component of the ground state Kramers' doublet leads to $z^2(+) \rightarrow \Psi(-)$ type transitions which will be of the opposite sign. The sign of $g_{||}$ of the Γ_7 state means that the $z^2(-) \rightarrow \Psi(+)$ and $z^2(+) \rightarrow \Psi(-)$ transitions will tend to cancel. The very small $g_{||}$ of the Γ_6 state means that a new MCD signal will develop to lower energy and opposite sign as the temperature is increased. The temperature dependence of the MCD spectrum shown in Fig. 6 displays this behavior and allows the tetragonal field to be quantified as $\Delta_t \sim 1900\ \mathrm{cm}^{-1}$ [11].

Similar arguments can be used to establish the excited state geometries of copper(II) doped into the cubic perovskite $KZnF_3$ [19]. The CuF_6^{4-} centers in this host can be shown by EPR experiments [15] to be localized at low temperature

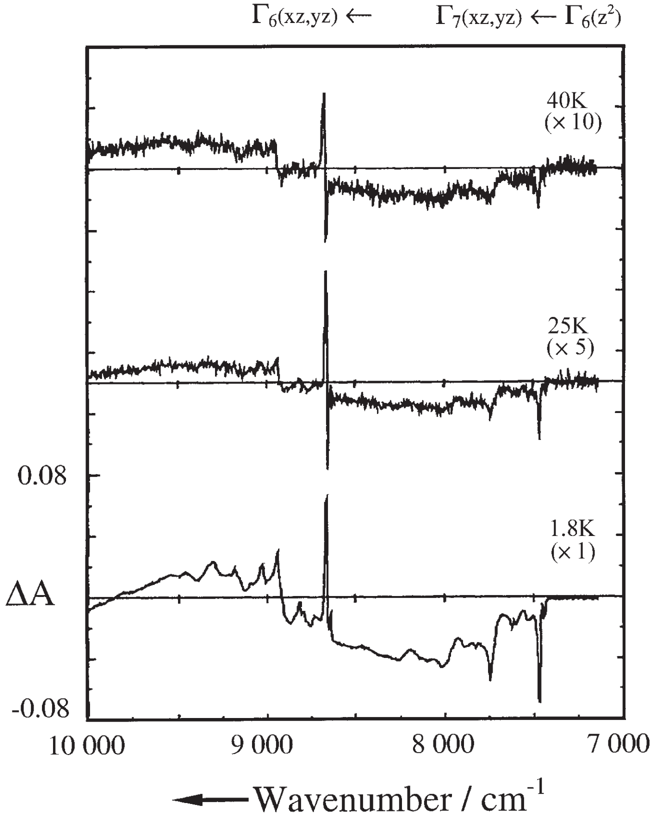

Fig. 6. The temperature dependence of the MCD spectrum of the magnetic dipole allowed $\Gamma_6(^2A_{1g}) \rightarrow \Gamma_6, \Gamma_7$ (E_g) transitions in Cu(II)/K_2ZnF_4 [11]. The applied field is 5 Tesla

in one of the three equivalent minima corresponding to a tetragonally elongated octahedron (Sect. 2.1). These elongated centers are randomly distributed along the x, y, z cubic axes. An MCD spectrum along a cubic axis is then a superposition of one axial and two transverse spectra. A careful analysis of the MCD spectrum of the sharp magnetic dipole allowed origins unambiguously establishes the excited state geometry of the zero phonon levels of the excited electronic states [19]. The $\Delta A/A$ quantity from the MCD is very useful in this regard as the intensity of both ΔA and A will be reduced equally by the vibrational overlap factors due to the relative displacement of ground and excited state potential energy surfaces. $\Delta A/A$, however, is independent of this as the vibronic reduction cancels. The sign and magnitude of the $\Delta A/A$ values can be compared with those calculated from ligand field theory [9] to establish the position of the minima in the excited state potential energy surfaces. The most informative cross-section of the multi-dimensional potential energy surfaces is along the Jahn-Teller mode Q_θ and for Cu(II)/$KZnF_3$ this information is summarized in Fig. 7. This is the simplest picture to explain the optical data. It is clear from the EPR however that the E_g ground state potential should more closely resemble Fig. 1b. That is, there will be a minimum at positive Q_θ and a higher energy saddle point at negative Q_θ. The $^2T_{2g}$ excited state would be expected to undergo a $T \otimes e$ Jahn-Teller effect (Sect. 2.2), but from Fig. 7 it can be concluded that this excited state Jahn-Teller effect is largely quenched by the spin-orbit coupling.

The spin orbit coupling splits the orbital $^2T_{2g}$ state into Γ_7 and Γ_8 states (O_h double group) separated by

$$E(\Gamma_8) - E(\Gamma_7) = 1/2\ \{[(\Delta_o + \lambda/2)^2 + 6\lambda'^2]^{1/2} - \Delta_o + 5/2\lambda\} \tag{5}$$

where Δ_o is the cubic ligand field, and λ' and λ the reduced spin orbit coupling ($\lambda = k\zeta$) in the e_g and t_{2g} orbitals respectively. The orbital reduction factors are found to be $k' = 0.85$ from EPR measurements and $k = 0.95$ from Eq. (5). This cubic anisotropy $k' < k$ reflects the different covalency in the metal-ligand bonds in the different electronic states. The covalency of the t_{2g} orbitals is expected to be small as they participate only in π bonding which is considerably weaker that the σ bonding formed by the e_g orbitals, and this is reflected in a smaller orbital reduction value. The Γ_7 excited electronic state shown in Fig. 7 is therefore exactly octahedral, while the Γ_8 state will be close to octahedral; the $\Gamma_8 \otimes e$ Jahn-Teller effect is expected to be very small. The octahedral Γ_7 state is interesting as it is the emitting state in the Cu(II)/$KZnF_3$ fluorescence.

3.3
Fluorescence

Fluorescence from a six-coordinate copper(II) complex is quite rare and it is easy to see why from the energy level diagram of Fig. 7. If the CuF_6^{4-} center is distorted from an octahedral geometry then the lowest level of the $^2T_{2g}$ multiplet comes very close in energy to the upper sheet of the $E \otimes e$ Jahn-Teller surface. For positive Q_θ in Fig. 7 this is the z^2 excited state, and will offer an efficient

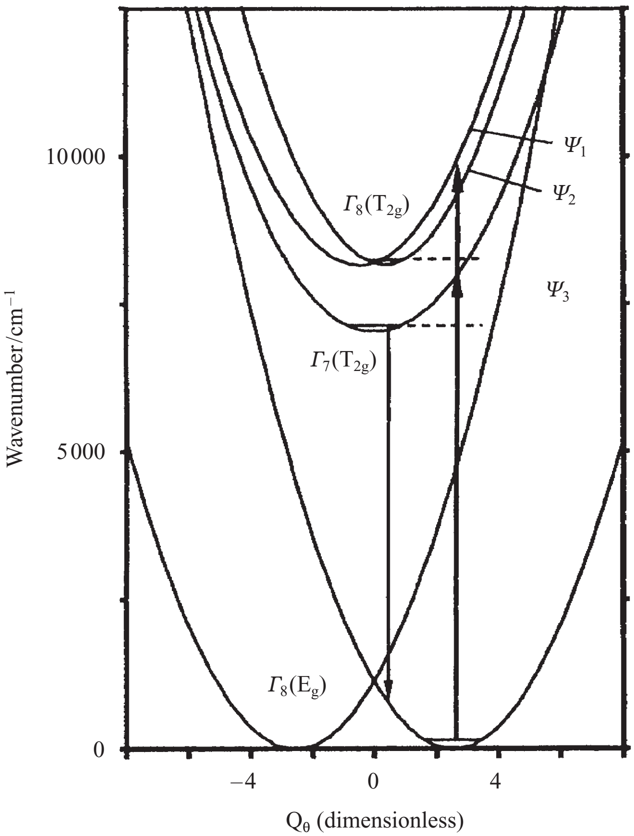

Fig. 7. The potential energy surfaces of the CuF_6^{4-} complex in $KZnF_3$ as a function of Q_θ, as determined by spectroscopic measurements [9]. The *vertical arrows* indicate Franck-Condon maxima in the absorption and fluorescence spectra, the *horizontal dotted lines* indicate observed zero phonon origins

pathway for radiationless deactivation. This is thought to be why fluorescence in $Cu(II)L_6$ complexes is so rarely observed: it requires a high symmetry so that a large energy gap exists between the emitting state and the upper surface of the $E \otimes e$ Jahn-Teller ground state.

To date CuF_6^{4-} fluorescence has only been observed for $Cu(II)/KZnF_3$ and $Cu(II)/K_2ZnF_4$ [16, 17]. These systems are favorable as they are doped rather than pure crystals, and are in cubic/slightly compressed sites, all of which will tend to minimize radiationless deactivation. The fluorescence spectrum confirms the general picture given by Fig. 7 [16].

4
Electron Paramagnetic Resonance

4.1
Static EPR

Electron paramagnetic resonance (EPR) is also a technique whereby the local structure of an impurity ion may be inferred by correlating the geometry with the experimentally determined electronic properties of the center. The third order expression for the g values can be written in terms of the Jahn-Teller angular coordinate ϕ as

$$\begin{aligned} g_x = g_e &+ 4u_x - 2(u_y^2 + u_z^2) - (u_x u_y - u_y u_z + u_z u_x) \\ &- [2u_x + (2u_z^2 - u_y^2) - (2u_x u_y + u_y u_z - u_z u_x)] \cos\phi \\ &+ \sqrt{3}\, [2u_x + u_y^2 - (u_y u_z + u_z u_x)] \sin\phi \\ u_x = k_x^2\zeta/E_{yz}&,\ u_y = k_y^2\zeta/E_{zx},\ u_z = k_z^2\zeta/E_{xy} \end{aligned} \tag{6}$$

The g_y and g_z are generated by the cyclic permutation of x, y, z, and ϕ, $\phi + 120°$, $\phi + 240°$ respectively. Here k_i and E_i are the orbital reduction parameters and the energy of each of the three components of the $^2T_{2g}$ multiplet and $g_e = 2.0023$ is the free electron g value.

Alternatively the 10 × 10 d^9 ligand field matrix can be diagonalized as a function of ϕ. The g-values can then be calculated from the lowest Kramers' doublet $\Psi^{\pm}$ using the magnetic dipole moment operator:

$$\begin{aligned} g_x &= 2 < \Psi^+ | k_x l_x + g_e s_x | \Psi^- > \\ g_y &= 2i < \Psi^+ | k_y l_y + g_e s_y | \Psi^- > \\ g_z &= 2 < \Psi^+ | k_z l_z + g_e s_z | \Psi^+ > \end{aligned} \tag{7}$$

For the present case where the geometry is restricted to Jahn-Teller coordinates, the symmetry is always D_{2h} or higher, and the matrix can be blocked into two 5 × 5 matrices which can be diagonalized separately.

Using experimentally determined g values of a rhombic CuL_6 complex with D_{2h} symmetry, ϕ can be determined. This value of ϕ is unique within a factor of 120°; other values are equivalent with the interchange of axes. The value of ϕ can then be related to the three independent bond lengths of the centrosymmetric complex:

$$\begin{aligned} \phi &= \arctan [Q_\varepsilon / Q_\theta] \\ Q_\theta &= 1/\sqrt{12}\, [-\Delta r_1 - \Delta r_2 + 2\Delta r_3 - \Delta r_4 - \Delta r_5 + 2\Delta r_6] \\ Q_\varepsilon &= 1/2\, [\Delta r_1 - \Delta r_2 + \Delta r_4 - \Delta r_5] \end{aligned} \tag{8}$$

Figure 8 shows the g values calculated using both the perturbation formula and the matrix diagonalization methods as a function of the Jahn-Teller angle ϕ. The angle $\phi = 0°$, with the phase of Q_θ given in Fig. 1a taken as positive, corresponds to an elongated octahedral geometry. Consequently the g-values are characteristic of an $x^2 - y^2$ type ground state with $g_{||} > g_{\perp}$. The value $\phi = 60°$ cor-

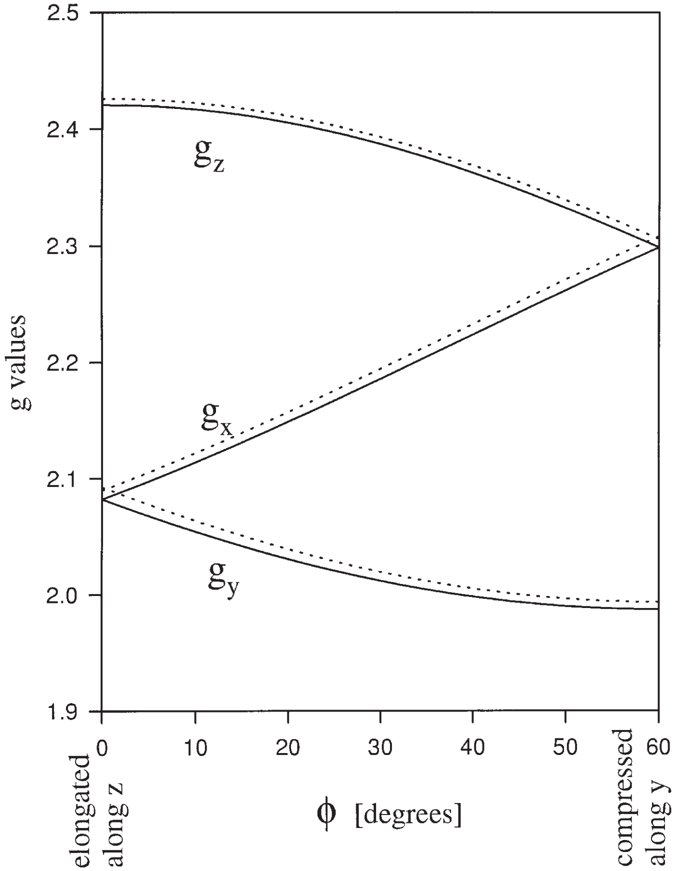

Fig. 8. The g-values of a CuL$_6$ complex as a function of the Jahn-Teller angle ϕ. The parameter values that have been used are $k_x = k_y = k_z = 0.8$, $E_{xy} = E_{yz} = E_{zx} = 10{,}000\ \mathrm{cm}^{-1}$, $\zeta = 830\ \mathrm{cm}^{-1}$. The *solid line* shows the results from applying Eq. (7) to the wavefunctions obtained from a matrix diagonalization while the *dotted line* is from the perturbation formula given in Eq. (6)

responds to a linear combination of Q_θ, Q_ε that gives a tetragonally compressed octahedral geometry:

$$Q = \frac{1}{2} Q_\theta + \frac{\sqrt{3}}{2} Q_\varepsilon \qquad (9)$$

$$= 1/\sqrt{12}\ [+\Delta r_1 - 2\Delta r_2 + \Delta r_3 + \Delta r_4 - 2\Delta r_5 + \Delta r_6]$$

The observation of $g_{||} \le 2 < g_\perp$ is then diagnostic of a compressed octahedral geometry. However, this can sometimes be obscured at room temperature due to the population of higher vibronic levels that become increasingly delocalized with the single potential energy minimum. The $g_{||} > g_\perp$ that is indicative of an elongated geometry can also be obscured in the room temperature EPR spectrum. In this case higher vibronic levels are populated, which are localized in different minima. These effects can be avoided by making measurements at low temperature. However, they are often interesting in their own right as they give additional information about the potential energy surface, not just the position of the lowest energy minimum. This will be discussed in the following sections.

4.2
d_{z^2} Type Ground States

A review of six-coordinate Cu(II) complexes with $g_{||} < g_{\perp}$ has emphasized the dangers of interpreting the EPR of samples which are not magnetically dilute [18]. In particular, elongated copper(II) octahedra can be arranged in an "antiferrodistortive" way which simulates a compressed octahedron. This arrangement of elongated octahedra is shown in Scheme 1, where the other pair of short bonds is perpendicular to the page.

As mentioned in the previous section, the $g_{||} < 2$ expected for a pure z^2 type electronic state is sometimes obscured by a small amount of x^2-y^2 type character. This is due to two factors. First, the $g_{||}$ shift is small ($\Delta g_{||} = -3u^2$ for an isotropic u in Eq. 6) for a pure z^2 electronic state and large ($\Delta g_{||} = 8u - 7u^2$) for a pure x^2-y^2 state. This means that a small admixture of x^2-y^2 character into the nominally pure z^2 ground electronic state will have a large effect on the resulting $g_{||}$ value. Second, as shown in Fig. 2b, if the host lattice imposes a minimum at a tetragonally compressed geometry, it is likely to be quite a shallow potential function about the $\phi = 180°$ minimum compared to the angular potential about a tetragonally elongated minimum. The shallow or soft potential then implies a large amplitude motion in this direction. The electronic part of the vibronic wavefunction is a function of ϕ given by

$$\Psi = \Psi(x^2 - y^2)\cos(\phi/2) + \Psi(z^2)\sin(\phi/2) \qquad (10)$$

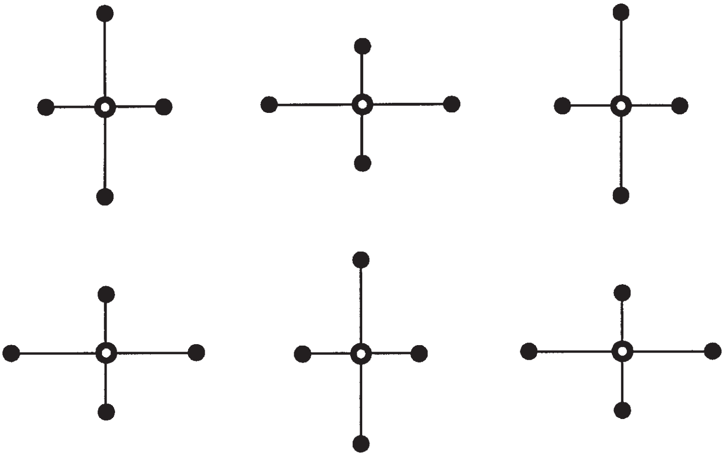

Scheme 1. Two-dimensional antiferrodistortive ordering in Cu(II) L_6 complexes

A static mixture of x^2-y^2 and z^2 electronic functions, as written in Eq. (10), implies a static orthorhombic geometry and will result in orthorhombic g values.

However, for a vibronic function vibrating about the $\phi = 180°$ single minimum, there will be a dynamic mixture of x^2-y^2 into the nominally pure z^2 ground state. The dynamic mixture can be calculated numerically [19] and results in the square of the above coefficients: $\langle \cos^2(\phi/2)\rangle \neq 0$, $\langle \sin^2(\phi/2)\rangle \neq 0$, and $\langle \sin(\phi/2)\cos(\phi/2)\rangle = 0$. That is, the fractional part of each component of the electronic states can be determined but the "cross-term" that would exist in a static wavefunction given by Eq. (10) is zero. Another way of picturing this is to consider the vibronic wavefunction extending to an equal degree on either side of $\phi = 180°$. The coefficient to x^2-y^2 in Eq. (10) changes sign at $\phi = 180°$. If one evaluates the cross-term as the molecule vibrates, then it will cancel. The g values can be evaluated using Eq. (6) by using the numerically calculated $\langle \cos^2(\phi/2)\rangle - \langle \sin^2(\phi/2)\rangle$ for $\cos\phi$ and setting $\sin\phi = 2\langle \sin(\phi/2)\cos(\phi/2)\rangle = 0$.

For tetragonal systems ($S_\varepsilon = 0$ in Eqs. 2 and4) the cross term $\sin\phi$ is always zero. One physical consequence of this is that Eq. (6) will always reduce to give the tetragonal g values:

$$\begin{aligned} g_{||} &= g_e + 4u - 5u^2 + 2[2u-u^2]\cos\phi \\ g_{\perp} &= g_e + 4u - 5u^2 - [2u-u^2]\cos\phi \end{aligned} \tag{11}$$

An isotropic u has been used for simplicity. Analogous tetragonal formula for anisotropic u values can be obtained from Eq. (6). Note that a pure x^2-y^2 or z^2 type ground electronic state will have the coefficients in Eq. (10) that result in $\cos\phi = 1$ and -1 respectively in Eq. (11). This will result in the $\Delta g_{||}$ shifts discussed previously.

For a cubic system ($S_\theta = S_\varepsilon = 0$), Eq. (6) is invalid as the ground state becomes a spin quartet (Γ_8) state rather than an isolated Kramers' doublet. The interested reader should consult Ham [7] for further discussion. It is noted that the higher energy vibronic singlets are Kramers' doublets so Eq. (6) will be valid for these levels if they are isolated from others. In these cases one will always find $\langle \sin(\phi/2)\rangle = \langle \cos(\phi/2)\rangle = 0.5$, giving $\cos\phi = 0$ and the isotropic g values

$$g_{iso} = g_e + 4u - 5u^2 \tag{12}$$

The numerically calculated $\cos\phi = \langle \cos^2(\phi/2)\rangle - \langle \sin^2(\phi/2)\rangle$ is equal to the Ham reduction factor "q" for the ground vibronic state in the case of linear coupling and no strain [7]. The original suggestion that the zero point motion within a single potential minimum can result in a small admixture of an electronic state that can have a large effect on the g values of copper(II) complexes was made by O'Brien [20].

4.3
Temperature Dependent EPR

EPR spectroscopy can show temperature dependent features for a number of reasons, one of which is due to a temperature dependent exchange coupling between different molecules that can average the resonance lines. In what follows we are concerned with the population of vibronic levels of a single molecule and assume that the transitions between these levels is fast, so that averaging of the Boltzmann distribution occurs. This means that the EPR spectrum of individually populated vibronic levels with differing electronic properties is not seen; rather, an average is seen. This situation occurs for copper(II) systems where the symmetry is low enough that the vibronic levels are separated by >50 cm^{-1}. Exceptions occur where the transition between close lying levels is slow; for example the $Cu(H_2O)_6^{2+}$ ion in $Zn(H_2O)_6(SiF_6)$ changes from tetragonal to isotropic at ~20 K [21]. This temperature dependence does not follow a Boltzmann average, but results from a temperature dependent exchange between the three elongated conformers of the molecule that are at similar energies and are separated by barriers.

The $Cu(H_2O)_6^{2+}$ ion has been the subject of many theoretical [22] and experimental [23, 24] studies as a classic Jahn-Teller ion. Tutton salts have the general formula $M^IM^{II}(H_2O)_6(SO_4)_2$ and offer many isomorphous structures of both pure copper(II) compounds and hosts for doping $Cu(H_2O)_6^{2+}$ impurities. Each divalent metal ion is on a centrosymmetric site with various amounts of orthorhombic distortion. The g values as a function of temperature are shown in Fig. 9a for the copper(II) ion doped into $M^I_2Zn(H_2O)_6(SO_4)_2$, $M^I = K^+, Rb^+, Cs^+$. The interpretation is as follows. The $Cu(H_2O)_6^{2+}$ ion will attempt to adopt the $E \otimes e$ Jahn-Teller potential energy surface with three equivalent minima at the preferred tetragonally elongated geometry. However, the orthorhombic site symmetry of the host crystal results in a large low symmetry perturbation of the $E \otimes e$ Jahn-Teller surface. The main perturbation is a large value of $-S_\theta$, which stabilizes two minima below a third as shown in Fig. 2b. In the present case there is also a non-zero S_ε, which will discriminate between the two lower minima.

At low temperature the molecules are in their lowest vibronic level, which is localized in the lowest energy minimum. This minimum is shifted from the $\phi = 120°$ exact tetragonal geometry so the resulting g values are slightly orthorhombic, but approximate the g values of a tetragonally elongated complex ($\sim g_\perp < \sim g_{||}$). As the temperature is increased, the population of a higher vibronic level localized in the other minimum ($\phi \sim 240°$) occurs. Whereas the first minimum corresponds to an approximate geometry with an elongation along the x molecular axis, the higher energy minimum corresponds to a geometry with an elongation along y. This closely approximates the swapping of x and y axes. This results in the lowest g value along z being temperature independent and the two higher energy g values being averaged.

There is much information that can be gained from the temperature dependent g values and this is summarized in the ground state potential energy schematics shown in Fig. 9b. The experimental data can be fitted to the vibronic energies and wavefunctions obtained from a parameterized Jahn-Teller surface with the low symmetry S_θ, S_ε terms [23]. The vibronic wavefunctions can be used to calculate the g values and the energy levels can be used to determine the Boltzmann average. Implicit in this approach are the assumptions:

1. That each vibronic level can be treated as an isolated Kramers' doublet (the applied magnetic field does not mix the levels).
2. There is fast averaging between vibronic levels.

Figure 9b shows a schematic cross-section of the full fitted surfaces. The trends in the experimental data that can be directly related to these potentials are:

1. At low temperature the g values become increasingly close to tetragonal, going down the series K^+, Rb^+, Cs^+. This is because $-S_\theta$ is also decreasing down the series. As discussed in Sect. 2.1, as $-S_\theta$ increases, the two minima at $\phi = 120°, 240°$ are gradually shifted to a single minimum at $\phi = 180°$. Therefore the K^+ host, with the largest $-S_\theta$, will have the largest shift from $\phi = 120°$ and the most orthorhombic g values at low temperature.
2. The temperature dependence of the g values decreases down the series K^+, Rb^+, Cs^+. This is due to an increase in the energy difference between the two

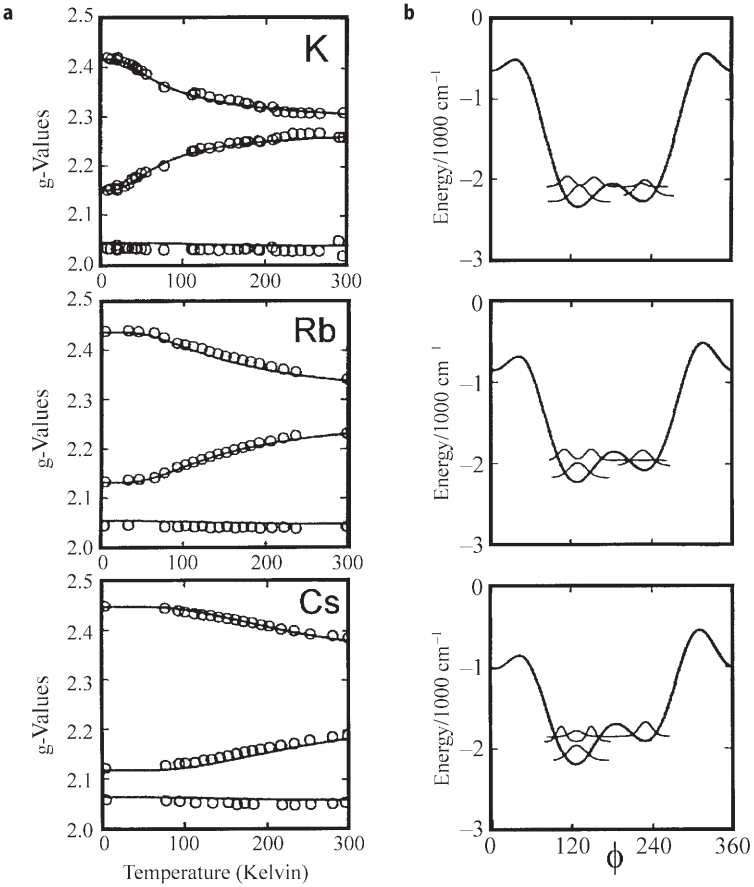

Fig. 9. The variation of the g-values with temperature for a number of copper(II) doped Tutton salts [23] with the general formula $A_2Zn(H_2O)_6(SO_4)_2$ where the cation A is: **a** K; **b** Rb, c) Cs

lowest minima, which in turn is determined by the orthorhombic component of the strain, S_ε. Both the tetragonal and the orthorhombic components of the low symmetry appear to decrease as the cation gets larger.

It was pointed out many years ago by Ham [7] that one of the interesting features of the Jahn-Teller effect in the solid state is that the high symmetry $E \otimes e$ potential energy surface is very susceptible to low symmetry perturbations. This has recently been realized in the lower symmetry environment of the $(ND_4)_2Cu(D_2O)_6(SO_4)_2$ Tutton salt [25]. The energy difference in the two lowest minima is quite small ($\sim 100\ cm^{-1}$) and a relatively small value of S_ε can reverse the energy order. The crystal packing, when the $Cu(D_2O)_6^{2+}$ ion has the geometry of the higher energy minimum, results in a slightly smaller cell volume. This means that an application of external hydrostatic pressure effectively changes S_ε and reverses the energies of the lowest two minima. A much larger geometry change is observed than one would see in applying pressure to a non-Jahn-Teller system and is an example of the amplification of a small perturbation that Ham has discussed [7].

5
Extended X-Ray Absorption Fine Structure

Extended X-ray Absorption Fine Structure (EXAFS) is the oscillating portion of an X-ray absorption spectrum that is a result of constructive and destructive interference of the outgoing wave of a photoelectron and the backscatter from the surrounding atoms [26]. EXAFS is a unique tool for structural determination, as it does not depend on long-range order. The measurement of a particular X-ray absorption edge means that it is element specific. In addition, modern X-ray sources from synchrotrons are intense enough to make measurements on dilute samples, for example on the impurities doped into host crystals.

The X-ray absorption process acts on a very fast timescale, essentially instantaneously with respect to molecular vibrations or thermal averaging between conformers. This is in contrast with diffraction techniques where data is collected over a period of hours and is an average of the whole crystal. Thus EXAFS is capable of probing the instantaneous local geometry of the absorbing species.

5.1
Examples

The $CuCl_6^{4-}$ ion in the 3-chloroanilinium salt: $(3\text{-}Cl\text{-}an)_8(CuCl_6)Cl_4$ was reported as being tetragonally compressed from an X-ray crystal structure [27]. However, the observed EXAFS spectrum of the Cu edge could only be modeled with an elongated structure [28]. The conclusion from the EXAFS study was that there was a dynamic disorder between two elongated structures that have their long axes orientated at 90° to each other. This is similar to the antiferrodistortive order discussed in Sect. 4.2, except that here it is due to the interconversion between two conformers of similar energy of the *same* molecule as shown in Scheme 2.

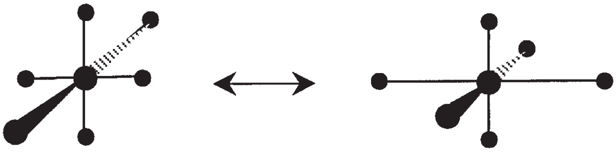

Scheme 2. Dynamic exchange between two of the minima on the ground state potential energy surface of a Cu(II)L_6 complex subject to a small axial compression

This conclusion was further supported by EPR results. A large mixture of x^2-y^2 character would be necessary to explain the large $g_{||}$ shift in this compound if it were compressed with a predominately z^2 ground state. However, such a large mixture would only arise from a soft angular potential that would also result in a large temperature dependence of the EPR. This is not observed, as the EPR is almost temperature independent down to 10 K. Below 10 K, orthorhombic g values result, indicating that the dynamic disorder has been frozen out at this temperature.

In common with the above example, copper(II) Tutton salts also show similar behavior as discussed in Sect. 4.3. Here however, there are orthorhombic g values over the temperature range 4–300 K, with the values changing from close to that expected for a tetragonal elongation to that of an "apparent" tetragonal compressed geometry. These systems are well understood [23] and are similar to the (3-Cl-an)$_8$(CuCl$_6$)Cl$_4$ example except that the energy of the two elongated conformers differ by energies of the order 100 cm^{-1}. This means that there is only a gradual change in g values as the upper level becomes thermally populated.

The thermal population of the upper level also causes the crystal structure to have bond lengths that are apparently temperature dependent. The actual bond lengths are not temperature dependent but the averaged values are. A plot of the three independent Cu-OH$_2$ bond lengths as a function of temperature, as determined by diffraction techniques, is shown as symbols in Fig. 10. The long and medium bonds appear to converge, but this is just an average of the long and medium bonds of the two conformers shown in Scheme 2. As a confirmation of these ideas we recently measured the EXAFS spectrum of $(ND_4)_2Cu(D_2O)_6(SO_4)_2$ over a temperature range 10–290 K [29]. The bond lengths obtained from the analysis of the spectra are shown as the solid lines in Fig. 10 and were found to be essentially temperature independent as expected for the actual bond lengths of the unaveraged conformers.

6
Future Directions

This short review has shown the type of detailed information on the ground and excited state geometry of six-coordinate copper(II) complexes that is possible using spectroscopic techniques. Often the use of more than one technique is desirable and can give complementary information. An exciting future direction

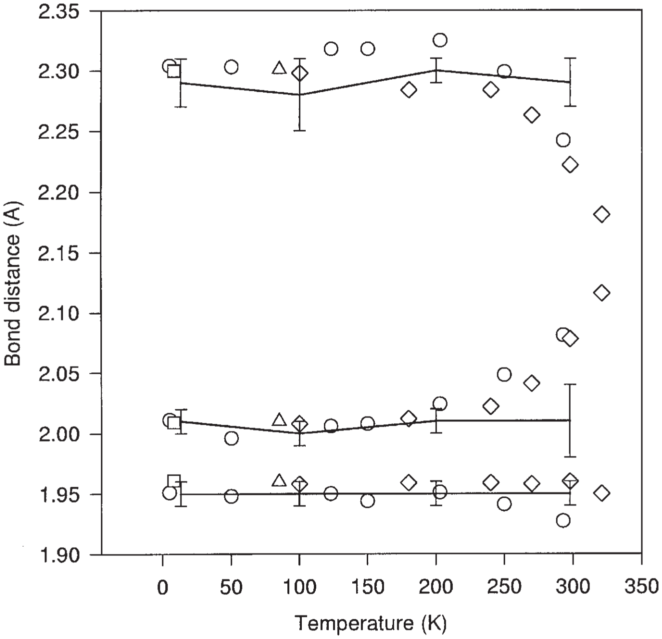

Fig. 10. The variation of the bond lengths of $(ND_4)_2Cu(D_2O)_6(SO_4)_2$ as a function of temperature. *Symbols* show data from X-ray and neutron diffraction experiments, while the *solid line* shows the results from EXAFS measurements

of these types of studies is the deliberate control over the geometry of such complexes. The recently demonstrated pressure induced switching of the elongated axis in a copper(II) Tutton salt [30] provides one example of this possibility.

7
References

1. Reinen D (1983) Comments Inorg Chem 2:247
2. Bersuker IB (1984) The Jahn-Teller effect and vibronic interactions in modern chemistry. Plenum Press, New York
3. Ceulemans A, Beyens D, Vanquickenbourne LG (1984) J Am Chem Soc 106:5824
4. Deeth RJ, Hitchman MA (1986) Inorg Chem 25:1225
5. Bacci M (1979) Chem Phys 40:237
6. Riley MJ (1998) Inorg Chim Acta 268:55
7. Ham FS (1972) In: Geschwind S (Ed) Electron paramagnetic resonance. Plenum Press, New York, chap 1
8. Reinen D, Krause S, Inorg Chem (1981) 20:2750
9. Dubicki L, Riley MJ, Krausz ER (1994) J Chem Phys 101:1930
10. Koster GF, Dimmock JO, Wheeler RG, Statz H (1963) Properties of the thirty-two point groups. MIT Press, Cambridge Mass
11. Riley MJ, Dubicki L, Moran G, Krausz ER, Yamada I (1990) Chem Phys 145:363
12. Finnie K, Dubicki L, Krausz ER, Riley MJ (1990) Inorg Chem 29:3908
13. Pryce MHL (1959) Phys Rev Lett 3:375

14. Riley MJ, Dubicki L, Moran G, Krausz ER, Yamada I (1990) Inorg Chem 29:1614
15. Bill H (private communication)
16. Dubicki L, Krausz ER, Riley MJ (1989) J Am Chem Soc 111:3453
17. Dubicki L, Krausz ER, Riley MJ, Yamada I (1989) Chem Phys Lett 157:315
18. Bertini I, Gatteschi D, Scozzafava A (1979) Coord Chem Rev 29:67
19. Riley MJ, Hitchman MA, Reinen D (1986) Chem Phys 102:11
20. O'Brien MCM (1964) Proc Roy Soc Lond Ser A 281:323
21. Bleaney B, Ingram DJE (1950) Proc Phys Soc Lond Ser A 63:408
22. Tachikawa H (1996) Chem Phys Lett 260:583
23. Riley MJ, Hitchman MA, Mohammed AW (1987) J Chem Phys 87:3766
24. Silver BL, Getz D (1974) J Chem Phys 61:638
25. Simmons CJ, Hitchman MA, Stratemeier H, Schultz AJ (1993) J Am Chem Soc 115:11,304
26. Zhang HH, Hedman B, Hodgson KO (1999) In: Solomon IE, Lever ABP (Eds) Inorganic electronic structure and spectroscopy, vol 1. Wiley, New York, chap 9
27. Tucker D, White PS, Trojan KL, Kirk ML, Hatfield WE (1991) Inorg Chem 30:823
28. Ellis PJ, Freeman HC, Hitchman MA, Reinen D, Wagner B (1994) Inorg Chem 33:1249
29. Masters VM, Riley MJ, Hitchman MA, (to be published)
30. Hitchman MA, Maaskant W, van der Plas J, Simmons CJ, Stratemeier H (1999) J Am Chem Soc 121:1488

Low-Lying Electronic States and Photophysical Properties of Organometallic Pd(II) and Pt(II) Compounds. Modern Research Trends Presented in Detailed Case Studies

Hartmut Yersin*, Dirk Donges+

Institut für Physikalische und Theoretische Chemie, Universität Regensburg,
93040 Regensburg, Germany
E-mail: Hartmut.Yersin@chemie.uni-regensburg.de

Two homologous organometallic compounds, $Pd(2\text{-thpy})_2$ and $Pt(2\text{-thpy})_2$ (with 2-thpy^-=2-(2-thienyl)-pyridinate, structure formulae in Fig. 1), are chosen for case studies of photophysical properties of the lowest excited states. The triplets of these two representative compounds are marked by differences of nearly two orders of magnitude in metal/MLCT (metal-to-ligand charge transfer) character. Determination of detailed photophysical properties of both compounds is possible, since highly resolved spectra are obtained when the compounds are dissolved in an n-octane matrix (Shpol'skii matrix), when the measurements are carried out at low temperature (typically at $T = 1.3$ K), and when modern techniques of laser spectroscopy are applied. In addition, methods of time-resolution and of microwave double-resonance, such as optically detected magnetic resonance (ODMR), microwave recovery, and phosphorescence microwave-double resonance (PMDR) are used. In particular, it is shown that with increasing metal character of the triplet, that is when $Pd(2\text{-thpy})_2$ is compared to $Pt(2\text{-thpy})_2$, many properties change characteristically and in part by orders of magnitude. For example, the following properties will be addressed: Transition probabilities, emission decay times, zero-field splittings (zfs), processes of spin-lattice relaxation (slr), intersystem crossing rates, intrastate relaxation rates, excited state binding properties as compared to those of the electronic ground state, anharmonicity effects, metal-mediated ligand-ligand coupling or spatial extensions of the excited state wavefunctions. Moreover, we focus on spin-selectivity in the vibrational satellite structures of the emission spectra as identified by the complementary methods of time-resolved emission and PMDR spectroscopy. We also discuss radiative deactivation processes, such as spin-vibronic Herzberg-Teller and Frank-Condon activities. Further, we specify sub-picosecond relaxation paths on the basis of micro-second time resolution by applying for the first time the method of time-resolved excitation spectroscopy to transition metal complexes. It is further demonstrated that the size of zero-field splitting of the triplet state can be used as an ordering parameter, that reflects the metal participation in the lowest triplet. Thus, one can relate $Pd(2\text{-thpy})_2$ and $Pt(2\text{-thpy})_2$ to a larger number of other compounds, such as $[Rh(bpy)_3]^{3+}$, $[Pt(bpy)_2]^{2+}$, $Pt(qol)_2$, $[Pt(mnt)_2]^{2-}$, $[Ru(bpy)_3]^{2+}$, $[Os(phen)_3]^{2+}$, $[Os(bpy)_3]^{2+}$, etc. (compare Fig. 1 and Table 11) and one obtains a series that demonstrates chemical tunability of photophysical properties. – For several specific subjects, we present the basic background information in order to make the paper more easily readable, also for non-specialists.

Keywords: Triplets in organometallic compounds, Chemical tunability, Spin-lattice relaxation, Excited state binding properties, Vibronic coupling, Spatial extensions of electronic states, ODMR results

---

* Author for correspondence; Home page: http://www.uni-regensburg.de/~hartmut.yersin/

+ Present address: D. Donges, Lambda Physik AG, Hans-Boeckler-Strasse 12, 37079 Göttingen, Germany

Topics in Current Chemistry, Vol. 214

1
Introduction

Organometallic or related complexes of the platinum metal group are highly attractive, since they are already or can potentially be used for very different kinds of new materials, such as for systems involving photo-redox processes for solar energy conversion [1–6], for photovoltaic devices [6–8], chemical synthesis [9], chemical sensors [10–12], biosensors [13], organometallic electroluminescent devices (OLEDs = organic light emitting devices) [14], and for energy harvesting [15–17], etc. The basic properties of all of these systems are strongly related to the characteristics of the low-lying excited electronic states and of the ground states, which should therefore be studied in detail.

Moreover, metal compounds with organic ligands are also of high scientific interest since they exhibit specific photophysical properties and effects which are not found in organic compounds or in transition metal complexes with metal-centered (MC) states. However, detailed studies of the electronic structures are only rare. Still, it is well known that many of the specific properties of organometallic and related compounds can be associated with the larger number of low-lying electronic states and with the importance of metal d-orbital character and the larger spin-orbit coupling effects as compared to organic compounds. Thus, a detailed investigation will reveal new and unexpected properties and will certainly provide a basis for future applications.

Interestingly, due to the large number of available compounds with different degrees of metal participation in the low-lying states one can introduce the concept of tunability of photophysical properties by chemical variation. Indeed, with respect to the metal character, it is possible to find an ordering parameter which allows one to classify the compounds discussed here in a well-defined sequence. This is due to the fact that very frequently the lowest excited states are triplets which split even at zero magnetic field into three substates. Recently, it has been shown that the value of this total zero-field splitting (zfs) is a valuable ordering parameter that measures the metal participation in the triplet wavefunctions [18–24]. The utility of this ordering is also reflected in a number of other photophysical properties, such as transition probabilities between the triplet substates and the ground state as well as emission decay times [18, 19, 21, 22], spatial extensions of the electronic states [22, 23], geometry changes due to excitation [18, 19, 21–23], size of deuteration-induced blue shift of the 0–0 transitions [19, 21–23, 25], etc. Figure 1 shows a sequence of complexes of the platinum-metal group. This series can in fact be viewed and applied in the sense of a chemical tunability, as employed in several recent investigations [21–24].

The lowest excited electronic states of the compounds shown in Fig. 1 have to be assigned to different types of frontier orbital transitions. (Compare also Ref. [26].) Thus, the low lying triplets of $[Rh(bpy)_3]^{3+}$and $[Pt(bpy)_2]^{2+}$are mainly characterized by ligand centered (LC) $^3\pi\pi^*$ states with small metal admixtures [19, 21–24, 27–34] and those of $[Ru(bpy)_3]^{2+}$, $[Os(bpy)_3]^{2+}$, and $[Os(phen)_3]^{2+}$ represent ^{3}MLCT (metal-to-ligand charge transfer) states. [3, 4, 18, 21–25, 33, 35–50] (In particular, see Ref. [22] in which many additional references are given.) The cyclometalated Pt(II)-compounds and $[Pt(mnt)_2]^{2-}$ have to be assigned to an intermediate situation with significant ^{3}LC/MLCT admixtures, though with quite different positions in the sequence given in Fig. 1 [18, 20, 22–24, 51–66], whereas the lowest excited states of the oxinate complexes, such as $Pd(qol)_2$, $Pt(qol)_2$, and $Pt(qtl)_2$, are characterized as ^{3}ILCT (intra-ligand charge transfer) states [67–75] with relatively small metal-d or MLCT admixtures [72–75]. Nevertheless, the ordering expressed by the sequence shown in Fig. 1 is still applicable.

It is aimed, in the present investigation, to focus on photophysical properties, which depend on the metal character and which can be "tuned" by changing the metal participation. The increase of metal character is particularly distinct when Pd(II) complexes are compared to the corresponding Pt(II) complexes. For example, the zero-field splitting of the lowest triplet – reflecting the metal character – increases by nearly a factor of a hundred, when $Pd(2\text{-}thpy)_2$ is compared to $Pt(2\text{-}thpy)_2$ (Fig. 1). This is due to the significantly greater MLCT ($d\pi^*$) admixtures to the lowest ^{3}LC ($\pi\pi^*$) states in the Pt(II) complex as compared to the Pd(II) complex.

A comparison of these two compounds is particularly attractive since very detailed investigations of photophysical properties have been carried out during the last decade. Thus, extensive information is available for a detailed *case study*. Interestingly, a number of important and more general photophysical effects can be elucidated. Moreover, this *case study* may also be viewed and extended in the sense of a chemical tunability according to the sequence shown in Fig. 1.

This review is organized as follows: In the short Sect. 2., we briefly present the matrix material (n-alkanes = Shpol'skii matrices), wherein the chromophores are experimentally investigated. The matrix plays a crucial role, because only by choosing a suitable chromophore-matrix system, is it possible to obtain the required detailed information. In Sects. 3 and 4 properties of the two compounds $Pd(2\text{-}thpy)_2$ and $Pt(2\text{-}thpy)_2$ are presented. Several interesting and new photophysical effects are discussed and emphasized by subsection titles. In Sect. 5, trends that are connected with an increase of metal character are outlined, and in Sect. 6, properties of $Pd(2\text{-}thpy)_2$ are compared to those of $Pt(2\text{-}thpy)_2$. Section 7 concludes the paper with an outlook to a larger number of transition metal complexes.

Several properties of the compounds can only be understood on the basis of specific theoretical models. For a better readability of this review, it seems

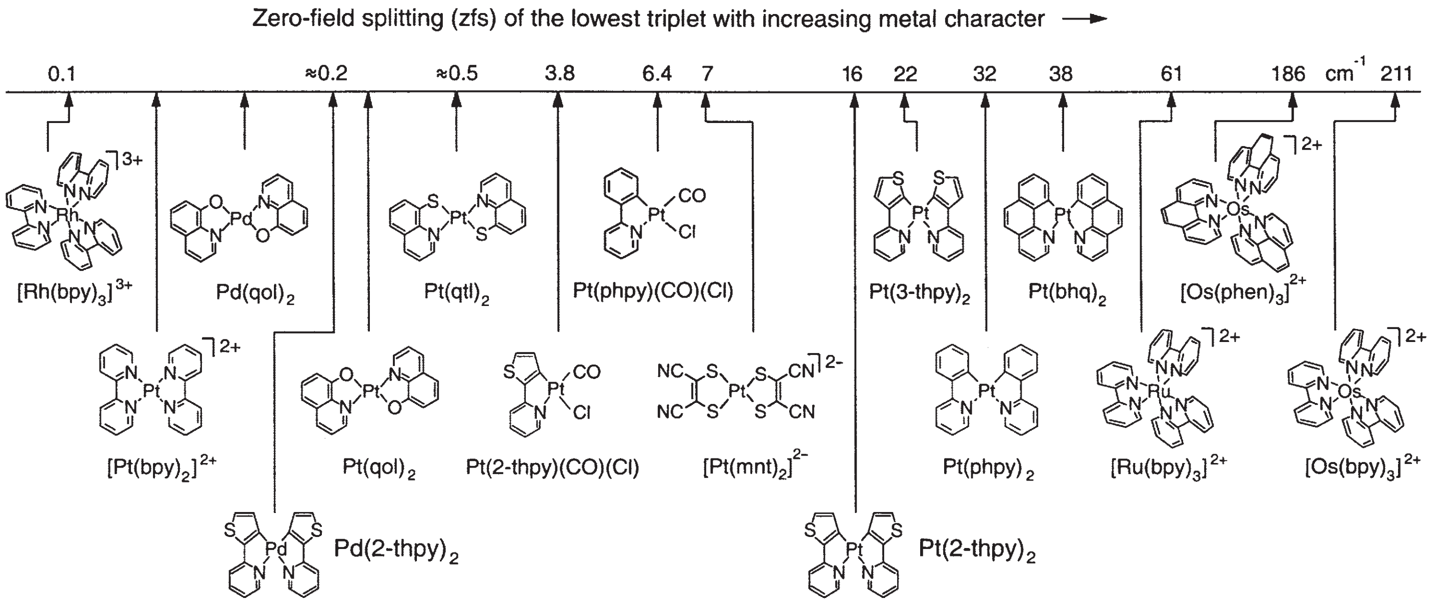

Fig. 1. The compounds are arranged according to an increasing total zero-field splitting (zfs) of the lowest excited triplet. This splitting reflects the size of metal participation (MLCT and/or d-orbital character) in the corresponding wavefunctions

to be useful to present also the corresponding basic background. This information is given in separate sections, where it is mainly needed. In particular, in Sects. 4.2.2 and 4.2.3 the basic information concerning Herzberg-Teller (HT) vibronic coupling and Franck-Condon (FC) activity is presented. In Sect. 4.2.6, the important processes of spin-lattice relaxation, such as *direct, Orbach*, and *Raman processes*, which govern the population dynamics in the system of the triplet substates are introduced. And in Sect. 4.2.10, we introduce fingerprints that are connected with localization and delocalization in the excited states, respectively.

2

Shpol'skii Matrices

For the interpretation of photophysical properties of molecules, it is extremely useful and often essential to have the information contained in highly resolved electronic spectra. In many cases, the highest obtainable resolution depends crucially on the matrix material. For example, it has been shown for several organic compounds (e.g. see the Refs. [76–80]) that by use of n-alkane matrices – the so-called Shpol'skii matrices [80] – one can, at low temperatures, obtain more than a hundred times better resolved spectra than in glass forming matrices. This technique has also been applied to porphyrins and phthalocyanines with metal centers [81–84] and recently, by Yersin et al., also to transition metal complexes [18, 23, 24, 56–65, 72–75]. The Shpol'skii technique is even applicable to compounds that are insoluble in n-alkanes if intermediate solvents are applied (e.g. see Refs. [23, 56–63]). Usually, Shpol'skii matrices are poly-crystalline at low temperatures. Under suitable conditions, the guest molecules substitute host (matrix) molecules and thus find a relatively inert matrix cage. Suitable conditions for an application of the Shpol'skii technique are given when the guest molecules are nearly planar, exhibit no or only a small dipole moment in the ground state and fit approximately to the size of the alkane host molecules. The doping concentration should be of the order of 10^{-5} to 10^{-4} mol l^{-1} to guarantee a well isolated doping situation. Nevertheless, one usually finds different chromophore sites (different guest-host cage structures) which depend, for a given chromophore and a given matrix material, on the cooling conditions and for a given chromophore but different n-alkanes, on the lengths of the alkane molecules used. (Structure data of several n-alkanes are given, for example, in the Refs. [85a, 85b, 86a, 86b].)

In a comparative study with Pt(2-thpy)$_2$ as the chromophore, for example, different n-alkanes (n-hexane, n-heptane, n-octane, n-nonane, and n-decane) have been applied. The various sites of Pt(2-thpy)$_2$ in these matrices are distributed over an energy range of about 400 cm^{-1} [59]. It has been found that n-octane is the most suitable material. In this matrix, one finds only one dominating site that carries about 98% of the emission intensity. Moreover, the (inhomogeneous) linewidth of the electronic origin line is as small as 2 to 3 cm^{-1} (fwhm). This result was obtained with a cooling rate of about 20 K per second [59]. For completeness, it should be mentioned that the occurrence of more than one dominating site does not represent a strong restriction for the optical investigations that are of interest here, because by site-selective excitation (or site-selective detection of emission), one can often select well-defined single-site spectra. Moreover, the inhomogeneous broadening effects can also often be reduced significantly by applying the methods of line-narrowing spectroscopy (e.g. see Ref. [87]).

Interestingly, the same n-octane matrix can equally be used successfully for Pt(2-thpy)$_2$ and Pd(2-thpy)$_2$.

3
Pd(2-thpy)$_2$

An introduction to the spectroscopic properties of Pd(2-thpy)$_2$ is given by presenting the room temperature absorption and the 80 K emission spectra of the dissolved complex (Fig. 2). The spectra are reproduced from Refs. [54] and [88], respectively. The various bands observed in the absorption spectrum are assigned to spin-allowed transitions from the singlet ground state to singlet excited states according the relatively high molar extinction coefficients. The most recent classifications are given by K. Pierloot, A. Ceulemans et al. [66] based on a CASPT2 ab initio method (complete active space additionally dealt with a second order perturbation approach [89]). These calculations were carried out within the approximation of a C_{2v} point group symmetry of the complex and by use of 12 active orbitals, but without including spin-orbit coupling. The accuracy of this method is assumed to be about two thousand cm^{-1}. The C_{2v} symmetry corresponds to a planar geometry of the chromophore, while there is an angle of $\approx 17°$ between the two ligands according to the gas phase calculations of Ref. [66]. Therefore, the optimum geometry of Pd(2-thpy)$_2$ in the gas phase has C_2 symmetry. (Compare also the discussion concerning the symme-

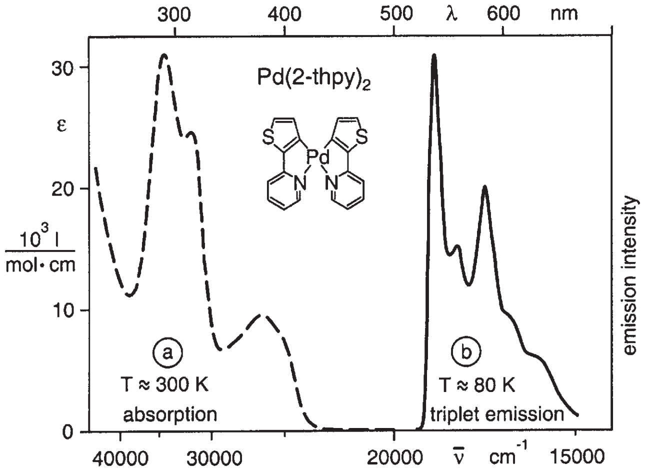

Fig. 2. (*a*) Absorption spectra of Pd(2-thpy)$_2$ dissolved in CH_2Cl_2, from Ref. [88]. (*b*) Emission spectrum of Pd(2-thpy)$_2$ dissolved in butyronitrile, from Ref. [54]

try of Pt(2-thpy)$_2$ in a Shpol'skii matrix in Sect. 4.2.1.) The two intense transitions seen in the absorption spectrum of Fig. 2a between ≈ 30,000 and 35,000 cm^{-1} are assigned to ^{1}LC states and thus confirm an earlier classification by M. Maestri et al. [54]. However, the calculations of Ref. [66] ascribe to the corresponding excited states considerable MLCT admixtures. In the energy region below 30,000 cm^{-1}, the absorption spectrum reveals one peak at 26,300 cm^{-1} and a shoulder near 25,000 cm^{-1}. These two features are assigned in Ref. [66] to the lowest singlets with relatively large MLCT character. Although some LC character is also present in these states, they may still be assigned to ^{1}MLCT states [66], (Compare also Ref. [54]). Within the approximation of the C_{2v} point group symmetry, these two states are classified as $^1A_1$ (shoulder near 25,000 cm^{-1}) and $^1B_1$ (peak at 26,300 cm^{-1}) representations (ground state $^1A_1$). The ^{1,3}dd* metal-centered (MC) states are expected to occur above ≈ 27,000 cm^{-1} [66]. However, due to the low transition probabilities corresponding to these states, the related absorption features would be hidden below the other much stronger transitions.

The structured emission found below about 18,900 cm^{-1} (Fig. 2b) is assigned to a triplet state due to the relatively long emission decay time of 280 µs at T = 80 K [54]. In this reference [54], the emitting triplet has been assigned to result from an admixture of LC and MLCT states. It will be shown below (Sects. 3.1.1, 5, and 6) that the MLCT contribution is still very small, as already indicated by the position of Pd(2-thpy)$_2$ in the sequence of compounds shown in Fig. 1. Interestingly, this latter assignment is also reproduced by the CASPT2 ab initio calculations [66]. However, these calculations predict the occurrence of two very close triplet states of $^3A_1$ and $^3B_2$ representation with $^3B_2$ lying less than 300 cm^{-1} above $^3A_1$. It should already be mentioned here that the highly resolved spectra discussed in Sect. 3.1.2 do not reveal the existence of two closely neighbored triplet states.

3.1

The Lowest Triplet State of Pd(2-thpy)$_2$

Figures. 3 and 4 show highly resolved phosphorescence and phosphorescence excitation spectra of Pd(2-thpy)$_2$ for the energy range of the lowest triplet state [56]. The compound is dissolved in an n-octane matrix (Shpol'skii matrix). Due to the specific chromophore-cage interaction, one obtains only one strongly dominating site. Interestingly, the situation is different for deuterated n-octane matrices. (Compare Sect. 3.1.6 and see also Table 4.)

The spectra shown in the Figs. 3 and 4 represent time-integrated low temperature (T ≤ 1.5 K) spectra. The smallest line width (fwhm) is ≈ 2 cm^{-1}. The enormous increase of resolution due to this technique becomes obvious, when the highly resolved emission spectrum is, for example, compared to the spectrum shown in Fig. 2b. The gain in resolution is connected with the application of the Shpol'skii matrix. On the other hand, the resolution that is obtained for Pd(2-thpy)$_2$ dissolved in butyronitrile just due to cooling down to T = 1.3 K is not significantly improved, as is demonstrated by the broad band spectrum depicted in Fig. 3b.

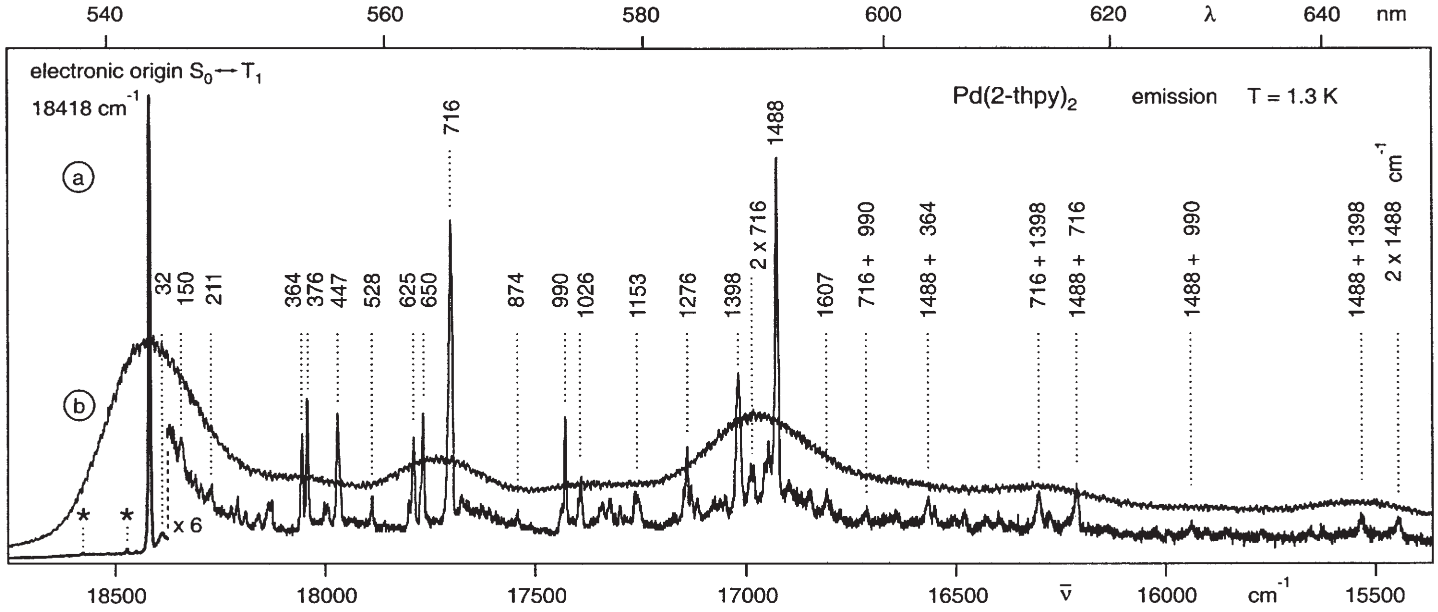

Fig. 3. Emission spectra of Pd(2-thpy)$_2$ (*a*) in an n-octane Shpol'skii matrix (line spectrum) and (*b*) in butyronitrile (broad band spectrum) at $T = 1.3$ K, $\lambda_{exc} = 337.1$ nm (N$_2$-Laser). The energies of the vibrational satellites are specified relative to the electronic origin at 18,418 cm^{-1}. The structures marked by *asterisks* on the high energy side of the electronic origin result from other sites and vanish with a site-selective excitation, e.g. at 19,113 cm^{-1} (18,418 cm^{-1} + 695 cm^{-1} vibrational satellite). Concentration of Pd(2-thpy)$_2 \approx 10^{-5}$ mol/l. Note: For a better comparison, the broad band spectrum is shifted by 200 cm^{-1} to lower energy. (Compare Ref. [56])

The highly resolved spectra reflect interesting and detailed information about the compound and allow us to specify a number of important properties, as will be discussed in the subsequent sections.

3.1.1
Electronic Origin(s)

The dominating peak at (18,418 ± 1) cm^{-1} lies within the limits of experimental error at the same energy in the emission and excitation spectra (Figs. 3 and 4). Therefore, this transition is assigned to the electronic origin, i.e. the 0–0-transition between the lowest triplet $\mathbf{T_1}$ and the ground state $\mathbf{S_0}$ (**0**). The assignment to the electronic origin is also substantiated by the fact that the vibrational energies determined from the resolved vibrational satellite structure only fit to the energy position of this peak at 18,418 cm^{-1} (see Sect. 3.1.2). The assignment of the emitting state as triplet has already been reported in Refs. [52, 54] and is based on the relatively long emission decay time at $T \approx 80$ K. This assignment is further evidenced by the occurrence of three emission decay components from the three triplet sublevels **I, II, III** at low temperature (Sect. 3.1.3), by the ODMR results (optically detected magnetic resonance) (Sect. 3.1.5), and by the splitting into three Zeeman components (next subsection).

3.1.1.1
Splitting into Zeeman Components

The observation of a splitting of the origin line at 18,418 cm^{-1} into three components under application of high magnetic fields represents a clear confirmation of the triplet nature of the corresponding state. This is demonstrated in Figs. 4b to 4e. Application of a magnetic field of B = 12 T leads to a total splitting of about 22 cm^{-1}, which corresponds to the g factor of the free electron of about two. This behavior is not unexpected because the total Zeeman splitting at B = 12 T is by a factor of about a hundred larger than the total zfs which lies in the order of 0.2 cm^{-1} (Sect. 3.1.5 and Refs. [61, 90]). This situation is therefore characteristic for the high-field limit, in which the triplet spins are no longer oriented relative to the molecular frame. Instead, at high field, the quantization axis is the direction of the external magnetic field (e.g. see Refs. [81, p. 560] and [91]). Due to this behavior, the splitting becomes largely symmetric even for statistically distributed Shpol'skii microcrystals (see Fig. 4e).

3.1.2
Vibrational Satellite Structures

Apart from the electronic origin lines, both the emission and excitation spectra (Figs. 3 and 4) exhibit rich structures, which are assigned to vibrational satellites that correspond to the $\mathbf{S_0} \leftrightarrow \mathbf{T_1}$ electronic origins. The analysis of these satellites provides some insight into properties of the electronic states involved and requires therefore a detailed study. Here, the discussion will be confined to time-integrated spectra, while later in Sects. 3.1.3 to 3.1.6, the results of time-dependent studies will also be reported. The latter investigations will provide an

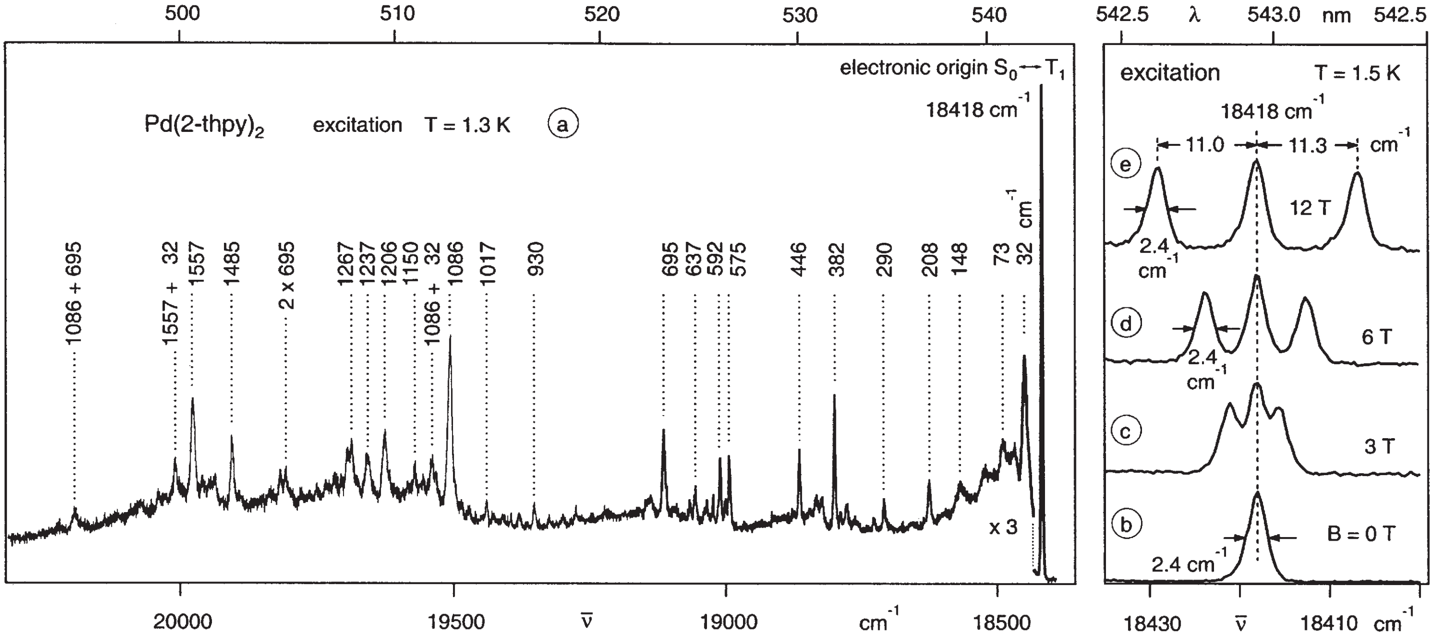

Fig. 4. Excitation spectra of Pd(2-thpy)$_2$ in n-octane (*a*) at T = 1.3 K and (*b*) to (*e*) at T=1.5 K, respectively. Concentration c = 10^{-5} mol l^{-1}. The emission is detected at $\bar{\nu}_{det}$ = 17,702 cm^{-1} (18,418 cm^{-1} – 716 cm^{-1} vibrational satellite). The excitation spectra (*b*) to (*e*) show the region of the electronic origin near 18,418 cm^{-1} on an enlarged scale. With application of high magnetic fields up to B = 12 T, the origin line at 18,418 cm^{-1} (0–0 transition) splits into three Zeeman lines. (Compare Refs. [56, 74])

insight into the vibrational satellite structures of *individual* triplet sublevels. These properties, however, are hidden in time-integrated spectra.

Vibrational energies of the ground state $\mathbf{S_0}$ and the excited state $\mathbf{T_1}$ can be determined from the emission and the excitation spectrum, respectively, relative to the electronic origin (0–0-transition) at 18,418 cm^{-1}. (Table 1) The satellites below about 100 cm^{-1} relative to this line exhibit normally significant lattice (matrix) vibrational character. The influence of the chromophore-cage interaction can even be important up to about 150 cm^{-1} (see Sect. 3.1.6 and Ref. [57]). In the energy range up to about 600 cm^{-1}, one usually finds metal-ligand (M-L) vibrations. In the same energy region, but up to about 1600 cm^{-1}, one observes fundamentals of internal ligand vibrations (compare [19, 21–23, 33, 34, 47, 48, 56–60, 72, 92]). A clear distinction between these different vibrational characters, in particular in the lower energy range is not yet possible for Pd(2-thpy)$_2$, as neither a normal coordinate analysis nor highly resolved spectra of per- and partially deuterated Pd(2-thpy)$_2$ compounds are available. For example, by use of this latter information, it was possible to distinguish between vibrational M-L and internal ligand modes for $[Pt(bpy)_2]^{2+}$ [22, 34]. However, mostly these vibrational modes in the energy range up to ≈ 600 cm^{-1} are mixed. But for higher vibrational energies, one can classify all modes (fundamentals) as internal ligand vibrations, apart from M-L progressions or combination, which are easily recognizable. Note that M-L satellites in the $\mathbf{T_1}$ spectra are much less important for Pd(2-thpy)$_2$ than for Pt(2-thpy)$_2$ (see Sect. 6 and Ref. [18]).

3.1.2.1
Vibrational Energies of the Ground State S_0

In Table 1, the energies of ground state vibrational modes, as determined from the emission spectrum (see Fig. 3), are compared to IR data (from [56]), to energies of ligand modes (from [56, 93]), and to vibrational energies of Pt(2-thpy)$_2$ (see also Sect. 4.2.4 and Ref. [59]). All these data exhibit a good correspondence which additionally confirms the assignment of the transition at 18,418 cm^{-1} as the electronic origin.

Note that the vibrational energies of M-L character of Pt(2-thpy)$_2$ deviate slightly from those of Pd(2-thpy)$_2$. The tentative correlation given in Table 1 shows that the values for Pt(2-thpy)$_2$ are shifted by several cm^{-1} to higher vibrational energies (blue shifted). This is a known effect (e.g. compare Ref. [94]), which may be explained by the larger overlap between metal and ligand orbitals in the platinum compound. With this behavior in mind and using the intensity distributions of the vibrational satellite structures of the emission spectra for the two compounds one obtains the correlations given in Table 1. (Compare Fig. 3 to Figs. 13 and 14, reproduced below.)

3.1.2.2
Vibrational Energies of the Excited State T_1

Table 1 summarizes a large number of vibrational energies of the excited state $\mathbf{T_1}$, as determined from the excitation spectrum (Fig. 4). Although, one does not

Table 1. Vibrational energies (in cm^{-1}) of $Pd(2\text{-thpy})_2$ dissolved in n-octane from emission and excitation spectra compared to IR data (vs = very strong, s = strong, m = medium, w = weak). (Compare Figs. 3, 4, and Refs. [56, 74])

Emission Vibrations of $\mathbf{S}_0$ 1.3 K	Excitation Vibrations of $\mathbf{T}_1$ 1.3 K	IR^{a} 300 K	Assignments
0–0 ($\mathbf{T}_1 \rightarrow \mathbf{S}_0$) 18,418 ± 1	0–0 ($\mathbf{S}_0 \rightarrow \mathbf{T}_1$) 18,418 ± 1		electronic origin (substates **I**, **II**, and **III**)
32 m	32 s		lattice modes^{b}
50 w	52 w		lattice modes^{b}
79 m	73 m		
111 w	107 w		
125 w			
150 m	148 m		
196 w			
211 m	208 m	215 w	
229 w		229 s	
261 w		265 s	M-L^{c} 266^{d}
284 m			
292 m	290 m		M-L 295^{d}
364 s	360 w	359 m	M-L 376^{d}
376 s	382 s		M-L 383^{d}
424 w			M-L 433^{d}
447 s	446 s		M-L 458^{d}
451 w		455 w	
528 m		528 w	531^{d}
	575 m		
	592 m		
625 s		623 w	630^{e}
643 m			
650 s	637 m		653^{d}
710 w		713 w-m	711^{e}
716 vs	695 s	720 m	718^{d}
874 w		873 w	
	930 m		
989 s		985 s	988^{e}
1021 w	1017 w	1022 w	
1025 m			
1076 w			
	1086 s		
	1118		1086 + 32
1096 w		1102 m	
1153 w	1150 w	1155 s	
1162 w			716 + 447
	1206 s		
	1237 m		
	1267 m		
1275 m	1276 m	1276 m	
1286 w			
1299 w		1296 m	1301^{e}
1366 w			716 + 650
	1387 w		2 × 695

Table 1. *(Continued)*

Emission Vibrations of $\mathbf{S}_0$ 1.3 K	Excitation Vibrations of $\mathbf{T}_1$ 1.3 K	IR[a] 300 K	Assignments
0–0 ($\mathbf{T}_1 \rightarrow \mathbf{S}_0$) 18,418 ± 1	0–0 ($\mathbf{S}_0 \rightarrow \mathbf{T}_1$) 18,418 ± 1		electronic origin (substates **I**, **II**, and **III**)
1392 m			
1398 s	1397 w	1398 m	1399[e], 1400[d]
1427 w			2 × 716
1461 w		1464 w	
1468 w			
1488 vs.	1485 s		1484[d]
	1557 s	1564 m	
	1590 m		1557 + 32
		1596 s	
1607 m			
	1664 w		1086 + 575
1704 m			716 + 990
	1775 w		1086 + 695
1850 m			1488 + 364
1865 w			1488 + 376
1936 w			1488 + 447
1991 w			716 + 1276
2113 m			716 + 1398
	2169 w		2 × 1086
2202 m			1488 + 716
2476 w			1488 + 990
	2641 w		1086 + 1557
	2857 w		2 × 1086 + 695
2881 w			1488 + 1398
2971 w			2 × 1488
	3246 w		3 × 1086
	3325 w		1086 + 1557 + 695
	3553 w		2 × 1086 + 2x695
	3948 w		3 × 1086 + 695
	4314 w		4 × 1086
	4796 w		3 × 1086 + 1557

[a] IR spectrum measured in KBr and polyethylene pellets, respectively, with a Nicolet 60SX FT-IR spectrometer (resolution 4 cm^{-1}).

[b] These modes are also found to couple to a number of vibrational satellites. Modes up to about 150 cm^{-1} can be influenced significantly by chromophore-cage interactions (see Sect. 3.1.6 and Ref. [57]).

[c] The M–L modes posses a significant metal-ligand character.

[d] Vibrational energies of $Pt(2\text{-thpy})_2$ given for comparison (see Sect. 4.2.4 and Refs. [59, 95]).

[e] Ligand vibrations, data from Ref. [93].

immediately recognize a mirror symmetry between the emission and excitation spectra, a careful inspection of the satellite energies and the intensity distributions allows us still to correlate a significant number of $\mathbf{T_1}$ modes with those of $\mathbf{S_0}$. (Compare Figs. 3a and 4a.) It is seen from this correlation (Table 1) that the low-energy modes of the matrix are nearly unshifted in energy (e.g. 32 cm^{-1} ($\mathbf{S_0}$)/32 cm^{-1} ($\mathbf{T_1}$)), while, for example, a vibration in the medium energy range, the 716 cm^{-1} fundamental of the ground state $\mathbf{S_0}$, exhibits one of the largest shifts, namely by 21 cm^{-1} to 695 cm^{-1} ($\mathbf{T_1}$). This corresponds to an energy shift of 3%. In the higher energy range, the shifts are again much smaller (e.g., 1398 cm^{-1} ($\mathbf{S_0}$)/1397 cm^{-1} ($\mathbf{T_1}$); 1488 cm^{-1} ($\mathbf{S_0}$) 1485 cm^{-1} ($\mathbf{T_1}$). In summary, it may be concluded – at least with respect to those modes being correlated in Table 1 – that the force constants of the pertinent vibrations in the electronic ground state $\mathbf{S_0}$ and in the excited triplet state $\mathbf{T_1}$ are not very different.

Not every vibrational mode of the excited $\mathbf{T_1}$ state can be assigned to a mode of the ground state $\mathbf{S_0}$. In particular, the intense 1086 cm^{-1} satellite observed in the excitation spectrum (Fig. 4a) does not have any obvious counterpart in the emission spectrum. Therefore, it might tentatively be assumed that this peak could represent a further electronic origin at 19504 cm^{-1} (18,418 cm^{-1} + 1086 cm^{-1}). In order to clarify this point, we recorded a line-narrowed excitation spectrum up to ≈ 23 300 cm^{-1}. This spectrum exhibits a rich structure up to about 4800 cm^{-1} beyond the electronic $\mathbf{S_0} \rightarrow \mathbf{T_1}$ origin at 18,418 cm^{-1} (spectrum not reproduced, but see Ref. [74]). A careful analysis of this highly resolved structure shows that practically all transitions (lines) observed have to be assigned to progressions and/or combinations of fundamentals that are known from Fig. 4a and Table 1. In particular, the occurrence of a 1086 cm^{-1} progression up to the fourth member and of several combinations with this 1086 cm^{-1} mode clearly excludes its assignment to an additional electronic origin (see Table 1). Moreover, it seems even to be possible to conclude that in the range up to ≈ 23,800 cm^{-1} a further electronic origin does not occur (compare also Sect. 3.2).

3.1.2.3
Similar Geometries of S_0 and T_1

The intensities of all individual vibrational satellites are weak compared to the intensity of the electronic origin. This is valid for the emission as well as for the excitation spectrum, shown in Figs. 3a and 4a. (Note the factors given that enhance the intensities of the satellite regions.) Already this result indicates that shifts of the nuclear equilibrium positions of the electronic states involved are relatively small. Due to the fact that several Franck-Condon progressions are clearly observed (e.g. $\mathbf{S_0}$: 716 cm^{-1}, 2 × 716 cm^{-1}; 1488 cm^{-1}, 2 × 1488 cm^{-1}; $\mathbf{T_1}$: 695 cm^{-1}; 2 × 695 cm^{-1}; 1086 cm^{-1}, 2 × 1086 cm^{-1}; 3 × 1086 cm^{-1}, 4 × 1086 cm^{-1}), one can easily determine the Huang-Rhys parameters S for these modes. The S value characterizes the respective vibrational progression. This parameter gives quantitative information about shifts of nuclear equilibrium positions along the coordinates of a totally symmetric mode that is involved.

This Huang-Rhys parameter S is related to the Franck-Condon factor for the corresponding transition. It is possible to derive a simple expression for the low-temperature limit and thus one can easily determine the values of the S parameters from the spectra. (For details see Sect. 4.2.3 and e.g. the Refs. [96–100].) One obtains

$$S = v \cdot (I_v/I_{v-1}) \qquad (1)$$

where v is the vibrational quantum number and I_v is the intensity of the respective member of the Franck-Condon progression. For Pd(2-thpy)$_2$, one finds for all progressions observed that the Huang-Rhys parameters $S \le S_{max} \approx 0.3$.

The information contained in this parameter is particularly valuable, when different compounds are compared. For example, for $[Pt(bpy)_2]^{2+}$[34] and $[Rh(bpy)_3]^{3+}$[19] the same S_{max} value has been found. For these compounds, the lowest triplets are assigned as ligand centered states of $\pi\pi^*$ character with only very small metal d-orbital admixtures. On the other hand, for Pt(2-thpy)$_2$, the largest Huang-Rhys parameter is less than 0.1. (Sects. 4.2.4 and 4.2.5). Since in Pt(2-thpy)$_2$, the MLCT contribution in the lowest triplet state is significantly larger than in the lowest triplet of Pd(2-thpy)$_2$, it is suggested that an increase of metal admixture leads to more similar nuclear equilibrium positions of the ground state $\mathbf{S_0}$ and the excited state $\mathbf{T_1}$. This is an important trend which will be further substantiated in Sect. 5. (Compare also Sect. 4.2.4 and the Refs. [18, 19, 21, 22].)

In summary, it should be kept in mind that a Huang-Rhys parameter of 0.3 must still be regarded as very small. This becomes obvious when this value is compared to the observed range of S values. These are frequently larger than one and one also finds S values greater than ten for other compounds (e.g. compare Refs. [96–101]). Therefore, the results found for Pd(2-thpy)$_2$ show that the nuclear equilibrium positions of the triplet state $\mathbf{T_1}$ and of the ground state $\mathbf{S_0}$ are rather similar.

For completeness, it is mentioned already here that besides the occurrence of Franck-Condon induced vibrational satellites one also observes Herzberg-Teller (HT) induced satellites in the emission spectrum shown in Fig. 3a. These are mainly found in the emission from the triplet substate **I**, since the transition between substate **I** and the ground state $\mathbf{0(S_0)}$ is strongly forbidden at the electronic origin. One representative HT-satellite is induced by the 528 cm^{-1} vibration. We come back to this important issue in Sects. 3.1.3 to 3.1.5. The background for this assignment becomes particularly clear from the companion studies with the platinum compound (Sects. 4.2.2 and 4.2.4).

3.1.2.4
Anharmonicity

The triplet $\mathbf{T_1}$ excitation spectrum shows a clearly resolved progression of the 1086 cm^{-1} fundamental (Table 1). However, with increasing vibrational quantum number, the energy differences between two successive members of the Franck-Condon progression decrease from 1086 cm^{-1} ($v = 0 \rightarrow v = 1$), to 1083 cm^{-1} ($1 \rightarrow 2$), to 1077 cm^{-1} ($2 \rightarrow 3$), and to 1068 cm^{-1} ($3 \rightarrow 4$) (calculated from Table 1). This behavior is ascribed to the effect of an anharmonicity of the corresponding vibrational potential of the $\mathbf{T_1}$ state. From the data given, this anharmonicity constant is easily determined and amounts to $x_e = 0.002$ (e.g. compare Ref. [102]). This value is significantly smaller than found, for example for diatomic molecules, which exhibit x_e values that are frequently one order of magnitude larger, like in HCl [94, 102].

3.1.2.5
Homogeneous Broadenings of Vibrational Satellites and Times of Intrastate Conversion

In this subsection, an interesting effect will be pointed out which has to our knowledge not been discussed previously for organometallic compounds. The excitation spectrum of Pd(2-thpy)$_2$, measured at $T = 1.3$ K, shows that the electronic origin line at 18,418 cm^{-1} has a Gaussian lineshape with a fullwidth at half maximum (fwhm) of 2.4 cm^{-1} (compare Fig. 4b and Ref. [74]). Obviously, the width of this line is determined by inhomogeneities [103,104] that result mainly from slightly different chromophore-cage interactions. On the other hand, the widths of the vibrational satellites increase distinctly with increasing energy of the vibrational fundamental. For example, one finds the following trend for the satellites [74] (fwhm $\Delta\bar{\nu}$ values are given in parentheses): 382 cm^{-1} ($\Delta\bar{\nu} = 3$ cm^{-1}); 695 cm^{-1} (5 cm^{-1}); 1086 cm^{-1} (9 cm^{-1}); 1557 cm^{-1} (8 cm^{-1}). Moreover, the spectra indicate that the lineshape functions of these satellites[1] cannot be approximated with sufficient accuracy by Gaussian profiles, while a Lorentzian lineshape function seems to fit increasingly better with growing halfwidth. This behavior can be understood on the basis of an increasing homogeneous broadening of the satellite lines (e.g. compare Ref. [103]). The homogeneous broadening effect may be related at low temperatures to the lifetime of this vibrationally excited state. Presumably, this lifetime is determined by the time required for relaxation to the zero-point vibrational level of the triplet potential. This time represents the intrastate conversion time τ_{ic}. With increasing energy of the vibrational fundamental, the homogeneous linewidth becomes broader and thus the vibrational relaxation time gets shorter.

For example, a homogeneously broadened line with a halfwidth of $\Delta\bar{\nu} = 5$ cm^{-1} (fwhm) can be related in the low temperature limit to the lifetime of the corresponding vibrational state by

$$\tau_{ic} = (2\pi c \Delta\bar{\nu})^{-1} \tag{2}$$

wherein c is the velocity of light measured in cm/s, if $\Delta\bar{\nu}$ is measured in cm^{-1} (e.g. see the Refs. [103, 104]). This expression is derived from the Heisenberg uncertainty principle according to $\Delta E \cdot \tau = h \cdot \Delta\nu \cdot \tau = h \cdot c \cdot \Delta\bar{\nu} \cdot \tau \approx \hbar$. The resulting value for the example given is $\tau_{ic} \approx 1 \times 10^{-12}$ s.

In conclusion, the experimental results indicate that the time of vibrational relaxation within a triplet substate is of the order of one picosecond. This time becomes shorter by approximately a factor of two within the series of fundamentals discussed above. Note that this time of intrastate conversion (ic) corre-

---

[1] The information is based on line-narrowed excitation spectra [74].

sponds to a relaxation *within* the potential hypersurface of one individual triplet sublevel, while the time for a crossing between different triplet sublevels is longer by orders of magnitudes. (Compare Sects. 3.1.3, 4.2.7, and 4.2.9, and Ref. [60]).

3.1.3
Triplet Populations and Decays

In the preceding sections, properties of Pd(2-thpy)$_2$ were discussed on the basis of time-integrated spectra. Due to the fact that the three triplet sublevels **I**, **II**, and **III** of $\mathbf{T}_1$ could not be resolved spectrally by the methods discussed in Sects. 3.1.1 and 3.1.2, the observed properties were ascribed to $\mathbf{T}_1$ as one state. However, it is known from other investigations of the triplet state, in particular, from investigations of organic compounds that the three substates are zero-field split on the order of 0.1 cm^{-1} and that these substates exhibit partly very different properties. (Compare, for example Refs. [105–112]). In several respects the situation is similar for organometallic compounds like Pd(2-thpy)$_2$ and related complexes. This important behavior is not well known. Therefore, it is subject of the present and the next two sections to focus on individual properties of the substates **I**, **II**, and **III** of the $\mathbf{T}_1$ state.

Figure 5 shows a simplified energy level diagram for the lower lying states of Pd(2-thpy)$_2$ including different excitation, relaxation, and emission pathways. For complexes with open-shell metal ions, one usually does not observe any fluorescence (singlet emission), because after an excitation into a higher lying singlet, the intersystem crossing (isc) is as fast as 10^{-13} to 10^{-12} s (compare [72, 75]). For Pd(2-thpy)$_2$ the intersystem crossing time is estimated in Sect. 3.2 to $\tau_{\mathrm{isc}} \approx 8 \times 10^{-13}$ s. By this process, the three triplet sublevels are populated, however, individually. This individual process of population can lead to the so-called spin polarization (see below, and e.g. Ref. [112]).

3.1.3.1
Non-Thermalized Triplet Sublevels

At low temperature, for example at $T = 1.3$ K, the times of relaxation between the triplet sublevels, the so-called *spin-lattice relaxation* (*slr*) times, are normally much longer than the emission decay times, if the energy separations between the triplet sublevels lie, for example, between 0.1 and 0.2 cm^{-1}. This property is due to the small density of vibrational states of the lattice (matrix) in this energy range and due to small interactions of the triplet substates with lattice vibrations. Thus, the excess energy of ≈ 0.1 cm^{-1} is not easily transferred to the lattice. Further, a relaxation from one triplet substate to another one requires a spin-flip, which additionally reduces the relaxation rates. An estimate, though for the different compound Pt(2-thpy)(CO)(Cl), gives a slr time of the order of one second at low temperature [24, 65]. The general importance of these processes of spin-lattice relaxation was already recognized more than six decades ago [113–115]. Since then, the field has developed significantly as is, for example, outlined in the Refs. [64, 65, 116–123]. In Sect. 4.2.6 we will discuss these pro-

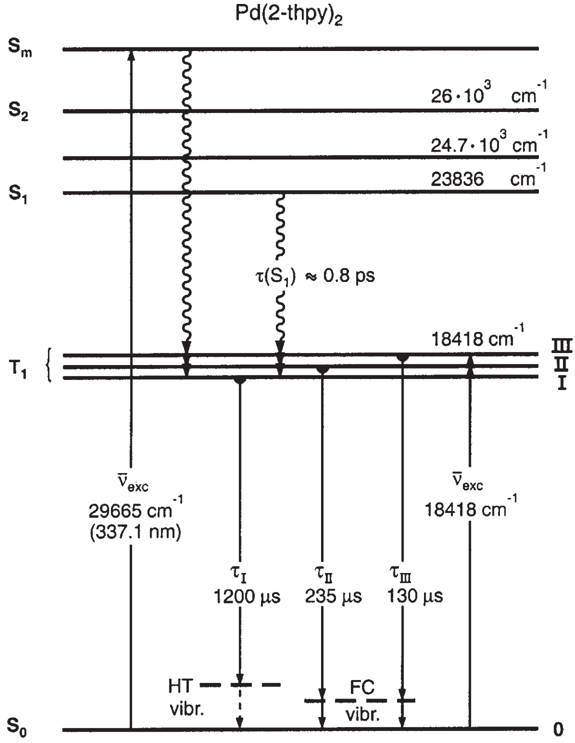

Fig. 5. Energy level diagram for Pd(2-thpy)$_2$ dissolved in n-octane. The $\mathbf{T_1}$ state at 18,418 cm^{-1} is zero-field split on the order of 0.2 cm^{-1}. The emission decay times refer to the individual triplet substates **I**, **II**, and **III**, respectively, at $T = 1.3$ K. (Compare Fig. 6.) These substates are radiatively deactivated as purely electronic transitions, as well as by Franck-Condon (FC) and Herzberg-Teller (HT) vibrational activity, respectively. This leads the different vibrational satellites. (Compare also Sects. 4.2.2 and 4.2.3.) The lifetime of the $\mathbf{S_1}$ state is determined from the homogeneous linewidth of the spectrally resolved $\mathbf{S_0} \rightarrow \mathbf{S_1}$ electronic origin. (Sect. 3.2) The electronic state at 24.7 × 10^3 cm^{-1} is not yet assigned

cesses and their significance for the population and emission decay properties of triplet substates of organometallic compounds in some detail (compare also Refs. [24, 64, 65]). In conclusion, at low temperature, the spin-lattice relaxation times are often longer than the emission decay times. Thus, a thermal equilibration of the individual substates does not take place.

3.1.3.2
Non-Resonant Excitation and Emission Detection on Selected Vibrational Satellites

After pulsed excitation into a higher lying singlet state $\mathbf{S_m}$ (e.g. at $\lambda_{exc} = 337{,}1$ nm $\triangleq$ 29,665 cm–1, pulse width 3 ns), the three triplet sublevels of Pd(2-thpy)$_2$ are populated individually and emit at low temperature, also individually. In Fig. 6, a typical emission decay curve is depicted employing a detection at the electro-

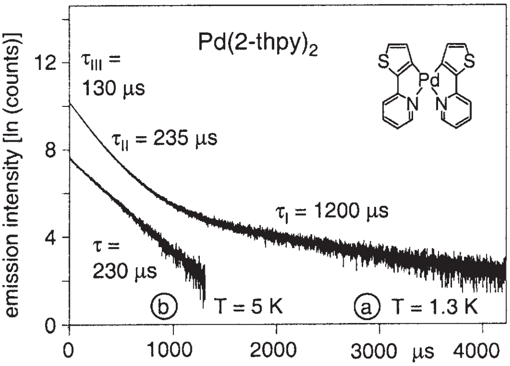

Fig. 6. Emission decay curves of $Pd(2\text{-}thpy)_2$ dissolved in an n-octane Shpol'skii matrix, (a) $T = 1.3$ K and (b) $T = 5$ K. The emission is monitored on the electronic origin of the transition $T_1 \rightarrow S_0$ at 18,418 cm^{-1}. ($\lambda_{exc} = 337{,}1$ nm $\triangleq$ 29,665 cm^{-1})(Compare Ref. [58])

nic origin at 18,418 cm^{-1} (plot (a)). As expected, the decay is best fitted by three exponentials, corresponding to the non-thermalized emissions from the three substates **I**, **II**, and **III** of the $\mathbf{T_1}$ state. The observed decay times are $\tau_I = (1200 \pm 50)$ μs, $\tau_{II} = (235 \pm 15)$ μs, and $\tau_{III} = (130 \pm 10)$ μs [56–58]. Note that this assignment does not imply an issue concerning the energy sequence of the three substates, which is not yet known.

Using the emission decay curve, it is also possible to determine the relative intensity of a specific decay component by time-integration. One obtains the result that the states **I**, **II**, and **III** contribute to the emission at the electronic origin at 18,418 cm^{-1} with 8%, 38%, and 54%, respectively. (Table 2) This intensity distribution is determined by the initial populations of the three states after an excitation into a higher lying state $\mathbf{S_m}$ and by the individual radiative decay rates of these states to the electronic ground state. Within limits of experimental error, the same initial populations are obtained, when the excitation energy is chosen to correspond to the $\mathbf{S_0} \rightarrow \mathbf{S_1}$ transition at 23,836 cm^{-1} (see also Sect. 3.2). Note that it is important for such a comparison that the *detection* energy is kept constant (see below). Therefore, for both excitation energies mentioned above, the emission was detected at the electronic origin of the $\mathbf{T_1} \rightarrow \mathbf{S_0}$ transition. (See Table 2, Fig. 6a, and Fig. 7 plot (a)).

Interestingly, the decay curve changes strongly, when only the *detection* energy is altered, but the *excitation* energy is unchanged (e.g. $\mathbf{S_0} \rightarrow \mathbf{S_1}$ excitation). For example, a detection at the 528 cm^{-1} vibrational satellite yields an emission decay curve as depicted in Fig. 7, plot (b). (Compare plot (b) with (a).) As expected, the emission detected at the vibrational 528 cm^{-1} satellite decays with the same three time constants. However, the relative intensities are strongly different. As is seen in Table 2, the emission at this satellite arises predominantly from state **I** (55%), while for a detection at the electronic origin, state **I** contributes only with 6%. This behavior is a consequence of the fact that the radiative deactivation from state **I** via the 528 cm^{-1} vibrational satellite is preferred relative to the radiative deactivation of substate **I** directly to the electronic ground state **0**.

Table 2. Emission decay times (μs) and relative intensities for different radiative decay paths of T_1 of Pd(2-thpy)$_2$ in n-octane at T = 1.2 K for selected excitation and detection energies (cm^{-1})

Emission decay time of sublevel	Relative emission intensities			
	$\bar{\nu}_{exc} = 29{,}665$[a] ($S_0 \rightarrow S_n$) $\bar{\nu}_{det} = 18{,}418$ ($T_1 \rightarrow S_0$)	$\bar{\nu}_{exc} = 23{,}836$[b] ($S_0 \rightarrow S_1$) $\bar{\nu}_{det} = 18{,}418$ ($T_1 \rightarrow S_0$)	$\bar{\nu}_{exc} = 23{,}836$[b] ($S_0 \rightarrow S_1$) $\bar{\nu}_{det} = 17{,}890$ ($T_1 \rightarrow S_0 - 528$ HT)[c]	$\bar{\nu}_{exc} = 18{,}418$[b] ($S_0 \rightarrow T_1$) $\bar{\nu}_{det} = 17{,}971$ ($T_1 \rightarrow S_0 - 447$ FC)[d]
I 1200 ± 50	8%	6%	55%	0%
II 235 ± 15	38%	34%	36%	70%
III 130 ± 10	54%	60%	9%	30%

[a] Fig. 6a and Ref. [58]

[b] Fig. 7 and Ref. [74]

[c] Fig. 7b. Detection carried out on a vibrational satellite that belongs selectively to the emission of substate **I**. This 528 cm^{-1} mode represents a Herzberg-Teller (HT) active vibration.[58] (Compare also Sect. 3.1.4.)

[d] Fig. 7c. The detection is carried out on a vibrational satellite that belongs to the emission from the triplet substates **II** and **III**. The 447 cm^{-1} mode represents a Franck-Condon (FC) active vibration.[58] (Compare Sect. 3.1.4.)

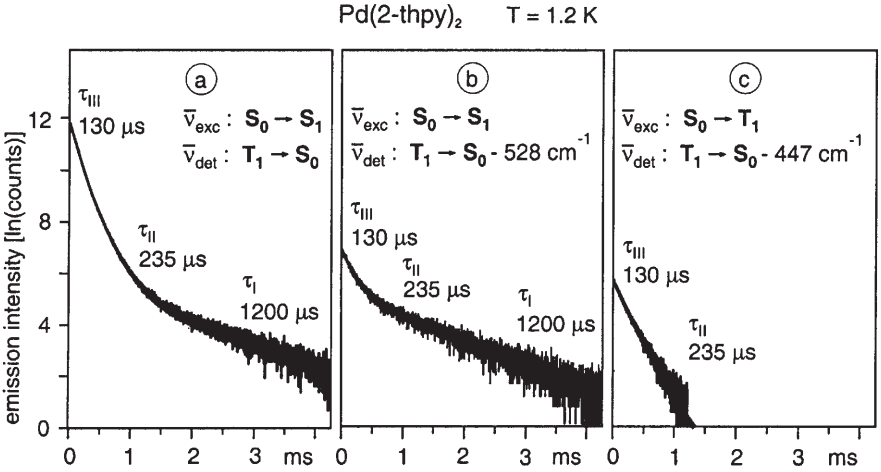

Fig. 7. Emission decay properties at T=1.2 K of Pd(2-thpy)$_2$ dissolved in an n-octane Shpol'skii matrix. The diagram demonstrates that the decay behavior depends on excitation and detection energies. (Compare also Table 2 and Ref. [74].) (**a**) Excitation at 23,836 cm^{-1} (lowest singlet); detection at 18,418 cm^{-1} (electronic origin of the $T_1 \rightarrow S_0$ transition) Within limits of experimental error, the same decay curve is obtained for an excitation energy of 29,655 cm^{-1} (Fig. 6a)). (**b**) Excitation as in (**a**); detection at 17,890 cm^{-1} (528 cm^{-1} vibrational satellite in the emission from substate **I**). (**c**) Resonant excitation at 18,418 cm^{-1}; detection at 17,971 cm^{-1} (447 cm^{-1} vibrational satellite in the emission from the substates **II** and **III** of T_1)

A similar behavior is also observed for several other vibrational satellites (e.g. 229, 261, 710 cm^{-1}).

The behavior described is a typical and important indication of a forbidden transition at the electronic origin between the states **I** and **0**. Hence one observes the long decay time and the vibronically (Herzberg-Teller) induced radiative pathway. (For background information compare, for example, the Refs. [22, 124–129] and Sects. 3.1.4, 3.1.5, and 4.2.2.) Obviously, the combination of frequency- and time-resolved measurements allows one to obtain an insight into radiative properties of individual triplet sublevels, although the optical resolution in these experiments is at least one order of magnitude lower than the splitting of $\mathbf{T_1}$ (zfs). In Sect. 3.1.4 we come back to this interesting possibility, by presenting the results of the better adapted method of time-resolved emission spectroscopy. In Sect. 3.1.5, we discuss the important complementary methods of ODMR spectroscopy (optically detected magnetic resonance) and PMDR spectroscopy (phosphorescence microwave double resonance), which provide more detailed insights into the nature of the triplet $\mathbf{T_1}$ state.

3.1.3.3
$S_0 \rightarrow T_1$ Resonant Excitation

In contrast to the situation that is usually found for organic compounds with low transition probability for the singlet-triplet transition, it is often possible to excite the triplet state of organometallic compounds resonantly and to observe the emissions from different substates. For $Pd(2\text{-thpy})_2$, such an experiment provides interesting results, because the probability for the transition from the electronic ground state $\mathbf{0(S_0)}$ to sublevel **I** of $\mathbf{T_1}$ is extremely low. This is already indicated by the long emission decay time of τ_I ($T = 1.2$ K) = 1200 µs.[2] On the other hand, the substates **II** and **III** are excitable from the ground state **0**. Thus, by using the excitation energy of 18,418 cm^{-1}, that corresponds to the $\mathbf{S_0} \rightarrow \mathbf{T_1}$ origin, only the substates **II** and **III** are excited.[3] Since furthermore, the slr rates which might thermalize the three triplet substates are negligible at $T = 1.2$ K, it is expected that the resonant $\mathbf{S_0} \rightarrow \mathbf{T_1}$ excitation will provide a distinct spin alignment. Indeed, this selective population of the two states **II** and **III** is clearly reflected in the emission decay behavior at $T = 1.2$ K, as is seen in Fig. 7, plot (c). Only the two shorter components of $\tau_{III} = 130$ µs and $\tau_{II} = 235$ µs occur, while the long decay component of $\tau_I = 1200$ µs is hardly detectable[4] (Table 2).

---

[2] Companion studies of $Pt(2\text{-thpy})_2$ show directly that the transition between the states **I** and **0** cannot be observed at the electronic origin (see Sect. 4.2.1).

[3] The zfs of the three triplet substates is of the order of 0.2 cm^{-1} and thus far below the inhomogeneous linewidth of ≈ 2 cm^{-1} at the electronic origin of the $\mathbf{S_0} \rightarrow \mathbf{T_1}$ transition.

[4] The detection of the emission decay was not carried out at the electronic origin, but on the 447 cm^{-1} vibrational satellite to prevent troubles with the exciting laser pulse.

3.1.3.4
Spin-Lattice Relaxation

It is the aim of this subsection to briefly address two interesting aspects that are connected to effects of spin-lattice relaxation. A broader treatment will be presented in Sect. 4.2.6. (Compare also Fig. 19, below.)

1. Under resonant $\mathbf{S_0} \rightarrow \mathbf{T_1}$ excitation, the long-lived emission component of 1200 μs, being characteristic of substate **I**, is almost absent, as has been described in the previous subsection. However, a careful search for the occurrence of any residual long-decaying intensity at low temperature ($T = 1.2$ K) shows that this emission is not totally absent. For this investigation, we have chosen a specific vibrational satellite that occurs selectively in the emission of substate **I,** like the 528 cm^{-1} satellite. (Compare Sects. 3.1.4, 3.1.5 and the Figs. 8 as well as 10). Indeed, this 528 cm^{-1} satellite carries some weak, long-lived emission intensity [74]. The occurrence of this residual emission from state **I** at low temperature is not attributed to a weak absorption of the transition from the ground state **0** to substate **I.** It seems to be a more appropriate explanation that during the exciting laser pulse of 12 ns (in this experiment) the chromophore is shortly heated up. During this short time, processes of spin-lattice relaxation are switched on and provide a small population of sublevel **I.** When the excitation process is finished, the chromophore cools quickly down and subsequently the three sublevels emit independently with their individual decay times.
2. When, again under resonant $\mathbf{S_0} \rightarrow \mathbf{T_1}$ excitation, the temperature is only slightly increased to $T = 2.0$ K, the decay behavior changes already distinctly. The shortest decay component becomes shorter (125 μs), while a long-lived component grows in. This behavior is ascribed to the onset of spin-lattice relaxation between the three triplet substates. Thus, in a very simplified description, the slr process from state **III**, for example, to state **I**, shortens the decay time of state **III** by populating the long-lived state **I**. It can be estimated that the slr time which is responsible for the shortening of the decay of state **III** is of the order of milliseconds.

These latter discussions in 1. and 2. show that effects of spin-lattice relaxation can in principle be studied by an investigation of the temperature dependence of decay properties, even when the spectral resolution is one order of magnitude smaller than the zero-field splitting of the triplet. (Compare also Sect. 3.1.) However, since more adequate methods, such as the techniques of microwave double resonance are available, one should use these latter methods with preference. (See the reviews [32, 90, 130]). But when the optical resolution is sufficient due to a larger zero-field splitting, as is found for $\mathrm{Pt(2\text{-}thpy)_2}$, optical investigations of effects of spin-lattice relaxation become highly successful [24, 65] and thus will represent the methods of preference as will be shown in detail in Sects. 4.2.7 to 4.2.9.

3.1.3.5
Fast Equilibration and Emission Decay for $T \geq 5$ K

With temperature increase from $T = 1.2$ K to $T \geq 5$ K, the decay behavior changes drastically. At $T = 5$ K, the decay is already monoexponential with a decay time of $\tau(5\text{ K}) = (230 \pm 10)$ μs (Plot (b) of Fig. 6). Within limits of experimental error this value is constant at least up to $T = 40$ K [57]. Obviously, temperature increase induces an efficient spin-lattice relaxation between the three triplet substates. This leads to a fast thermalization. The observed monoexponential decay demonstrates that the slr is much faster than the shortest emission decay component.

The effective processes of slr have not yet been determined for Pd(2-thpy)_2. However, the comprehensive investigations [24, 65] carried out with similar compounds, in particular with Pt(2-thpy)(CO)(Cl) also dissolved in an n-octane matrix, indicate that the slr rate $k^{slr}(T)$ is for $T < 10$ K predominantly determined by a Raman process according to a T^5 power law. Such behavior is only expected for a compound, which does not have any electronic state within a thermally accessible energy range. Apparently, this is fulfilled for Pd(2-thpy)_2 for $T \leq 40$ K ($\triangleq 28\text{ cm}^{-1}$). (In Sect. 4.2.6, we present a detailed introduction to the different processes of slr.)

Under condition of a fast thermalization between the three triplet substates, one can derive a simple expression for the resulting decay time τ_{therm} that represents an average decay time (e.g. see the Refs. [105–107]):

$$\tau_{\text{therm}} = 3 \cdot \left(\frac{1}{\tau_{\text{I}}} + \frac{1}{\tau_{\text{II}}} + \frac{1}{\tau_{\text{III}}} \right)^{-1} \tag{3}$$

where τ_{I}, τ_{II}, and τ_{III} are the individual decay components at low temperature. Using this expression and the values determined for the individual decay components (Table 1), one obtains $\tau_{\text{therm}} = (235 \pm 20)$ μs [58]. This value is essentially identical to the measured emission lifetime of $\tau\,(5\text{ K}) = (230 \pm 20)$ μs at $T = 5$ K (Fig. 6, plot (b)).

It should be mentioned additionally that the temperature behavior described represents a further support for the assignment of the three different low-temperature decay components to one single type of chromophores.

3.1.4
Time-Resolved Emission

The studies presented in the previous Sect. 3.1.3 demonstrate that the three triplet sublevels **I**, **II**, and **III** of $\mathbf{T}_1$ are zero-field split by less than 1 cm^{-1}[5] and that they are thermally not equilibrated below $T \approx 2$ K. Thus at lower temperature, the three states emit independently with significantly different decay constants of $\tau_{\text{I}} = 1200$ μs, $\tau_{\text{II}} = 235$ μs, and $\tau_{\text{III}} = 130$ μs, respectively. Moreover, the time-

---

[5] In Sect. 3.1.5 it will be shown that the zfs is on the order of 0.2 cm^{-1}.

resolved studies indicate that the emission spectra resulting from the substates should be distinctly different. However, this information is lost in time-integrated spectra. These consist of different superimposed emissions from the three spectrally unresolved substates. Even by high-resolution optical spectroscopy, as applied in our experiments, one cannot resolve the different spectra with such small energy splittings.

However, it is possible, to record emission spectra of individual substates by applying the methods of time-resolved spectroscopy. This has been shown, to our knowledge for the first time for transition metal complexes, by Yersin et al. in Ref. [58]. Having these time-resolved spectra available, it becomes possible for example, to elucidate individual vibronic radiative deactivation paths, as will be shown in this section. Interestingly, results that are deduced from a complementary method, namely from phosphorescence microwave double resonance (PMDR) studies [61], provide a nice agreement with the results deduced from time-resolved investigations. (Compare also Sect. 3.1.5.)

The emission decay curve measured at $T = 1.3$ K (Fig. 6a) shows that the decay can be grouped into two time regions. In a short-time region with no delay, the emissions from the states **III** and **II** will strongly dominate, while after a long delay time, for example of $t = 1800$ µs, these states are depopulated, and only the monoexponential decay of state **I** is observed. Thus, it is expected that by time-resolved spectroscopy the spectra resulting from both fast-decaying sublevels **III** and **II** are separable from the spectrum that stems from the long-lived substate **I**.

Indeed, Fig. 8 shows that this separation is successful. The time-resolved spectrum recorded with no delay with respect to the exciting laser pulse ($t = 0$ µs) and integrated over a time window of $\Delta t = 10$ µs (Fig. 8b) is significantly different from the one that is recorded with a delay time of $t = 1800$ µs and integrated subsequently over a time window of $\Delta t = 1800$ µs (Fig. 8c). For comparison, we reproduce also the time-integrated spectrum in Fig. 8a, which has already been discussed on the basis of Fig. 3a.

From a comparison of the fast spectrum to the delayed one it becomes obvious that a series of vibrational satellites grows in with time, such as the satellites at 229, 261, 416, 528, and 710 cm^{-1}. The corresponding vibrational modes couple *only* to the slowly decaying sublevel **I** (bold-face numbers in the first column of Table 3).

Other satellites increase in their relative intensities with time, e.g. those at 364, 625, 1286, and 1461 cm^{-1} (Fig. 8c). Therefore, these fundamentals are important for the deactivation of state **I**, but they are also present in the fast-decaying spectrum from the substates **II** and **III**. These two types of modes that exhibit increasing relative intensities with time are summarized in the first column of Table 3. Most of these modes seem to be IR-active (Table 3, third column). On the other hand, several satellites in the fast-decaying spectrum (Fig. 8b) reduce their relative intensities with time, e.g. those at 211, 376, 716, and 1488 cm^{-1}. These modes are important for the deactivation of the two fast-decaying sublevels **II** and **III**. They are summarized in the second column of Table 3.

Figure 8 shows further that the time-integrated spectrum is mainly determined by the fast-decaying triplet sublevels (compare Fig. 8a to 8b), while the information about the slowly decaying sublevel **I** is very poor in the time-inte-

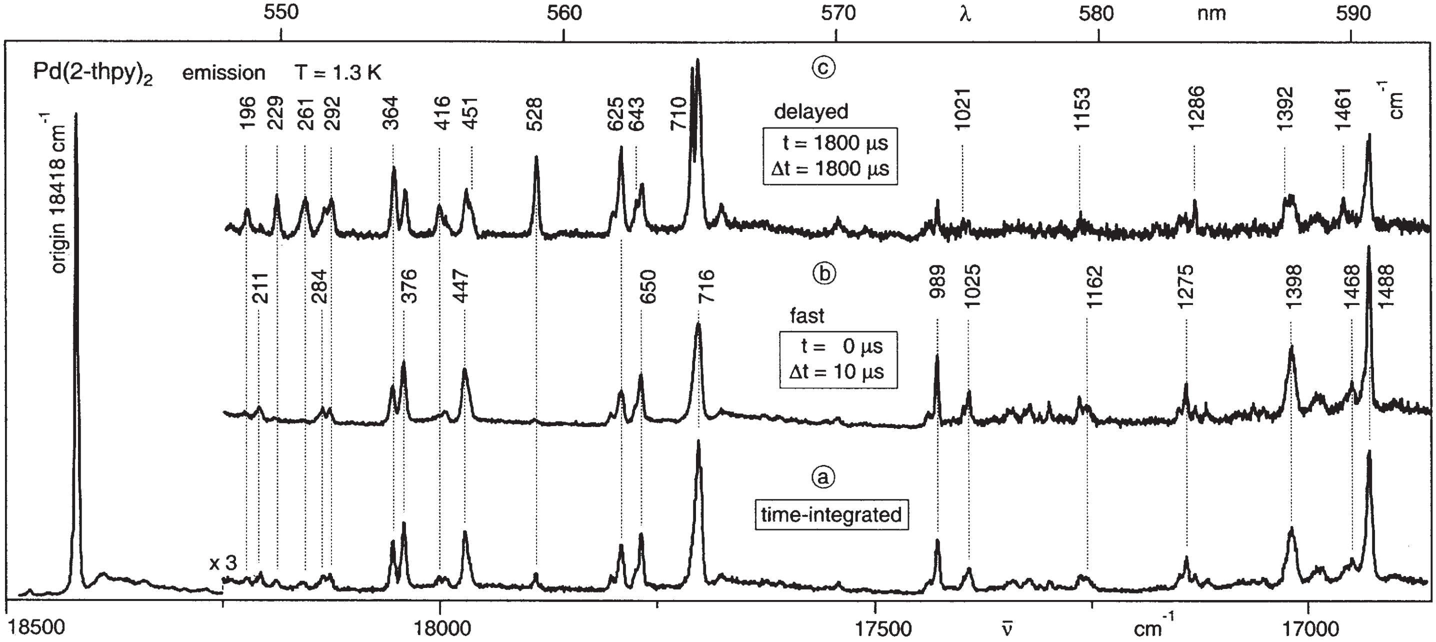

Fig. 8. Time-resolved and time-integrated emission spectra at T=1.3 K of Pd(2-thpy)$_2$ dissolved in an n-octane Shpol'skii matrix. Concentration ≈ 10^{-5} mol/l; λ_{exc} = 337.1 nm (pulse width 3 ns). (*a*) Time integrated emission; (*b*) Time-resolved emission, delay time t = 0 µs, time window (integration time) Δt = 10 µs; (*c*) Time-resolved emission, delay time t = 1800 µs, time window Δt = 1800 µs. The energies of the vibrational satellites are specified relative to the electronic origin at 18,418 cm^{-1}. (Compare Refs. [56, 58])

Table 3. Vibrational satellites of the electronic origin at 18,418 cm^{-1} of Pd(2-thpy)$_2$ dissolved in n-octane from time-resolved emission spectra (Fig. 8) compared to IR data [58]

Emission (1.3 K)		IR (300 K)[c]
Relative intensity		
increase with time[a,b]	decrease with time[a,b]	–
196 m		191 w
	211 m	215 w
229 m[d]		229 s
261 m		265 s
	284 m	
292 m		
364 s		359 m
	376 s	
416 m		413 s
	424 w	422 w
	447 s	445 w
451 w		455 w
528 s		528 w
625 **s**		623 w
643 w		642 s
	650 s	
710 s		713 w-m
	716 vs[e]	720 m
	989 s	985 s
1021 w		1022 w
	1025 m	
1153 w		1155 s
	1162 w	
	1275 m	1276 m
1286 m		
1392 m		
	1398 s	1398 m
1461 m		1464 w
	1468 w	
1481 w		1481 vs
	1488 vs[e]	

[a] vs = very strong; s = strong; m = medium; w = weak.

[b] Relative intensity is defined as the ratio of the intensity of a specific vibrational satellite to the corresponding time-resolved total vibrational emission intensity.

[c] Compare the IR data given in Table 1.

[d] Modes specified in bold-faced type exhibit a selective coupling to triplet substate **I.**

[e] Weak progression forming mode (Compare Fig. 3a and Ref. [56]).

grated spectrum (e.g. see the 229, 416, and 528 cm^{-1} satellites). Thus, it can be concluded that the fast-decaying sublevels carry most of the total emission intensity. This result is also clearly reflected in Table 2 and in the PMDR spectra shown in Fig. 10 (see below).

The most intense satellites in the fast decaying spectrum (Fig. 8b) are induced by the 716 and 1488 cm^{-1} fundamentals. These satellites represent the first members of two weak Franck-Condon progressions with small Huang-Rhys factors (see also Sect. 3.1.2 and Table 1). The occurrence of such progressions of fundamentals together with an electronic origin allows one to conclude that the corresponding vibrational modes are totally symmetric. These are Franck-Condon active and the satellites obtain their intensities from the intense electronic transitions between the sublevels **II** and **III** and the ground state **0**. The relatively high allowedness of the purely electronic transitions (0–0 transitions) can only be explained by a significant singlet admixture by first order spin-orbit coupling to these states **II** and **III**. (Compare Sect. 4.2.3 and e.g. Refs. [96–100, 124–127].)

The change of the intensity distribution of the vibrational satellites with time (compare the Figs. 8b and 8c) indicates that for these satellites different radiative deactivation mechanisms are effective. This change is particularly well reflected in the 528 cm^{-1} satellite, which is by a factor of 40 to 50 more important in the slowly decaying spectrum than in the fast-decaying one, when normalized to the 716 cm^{-1} Franck-Condon satellite. This behavior – the long decay time of 1200 µs and the change of the vibrational satellite structure – suggests that the radiative decay of sublevel **I** is controlled by vibronic perturbation mechanisms (Herzberg-Teller coupling) and that direct spin-orbit coupling is much less important. (See the background presented in Sect. 4.2.2 and Refs. [22, 124–129].) A similar behavior, and even more distinct, is also found for the radiative deactivation of the lowest sublevel **I** of $\mathrm{Pt(2\text{-}thpy)_2}$ (Ref. [59] and Sect. 4.2.4) as well as for the lowest triplet sublevel of $[\mathrm{Os(bpy)_3}]^{2+}$ [22, 129]. In particular, the modes that couple selectively to sublevel **I** of $\mathrm{Pd(2\text{-}thpy)_2}$ (229, 261, 416, 528, 710 cm^{-1}) represent very interesting candidates for investigations of the dynamics of spin-lattice relaxation processes by use of time-resolved emission spectroscopy. (Compare also Sect. 3.1.3.)

The vibrational satellite structures of the two fast decaying substates **II** and **III** could not be separated from each other by the applied method of time-resolved emission spectroscopy, because the decay times are too similar (130 µs, 235 µs). Further, both transitions between the substates **II** and **III**, respectively, and the ground state **0** are very likely connected with the same Franck-Condon active vibrations. This can directly be shown for $\mathrm{Pt(2\text{-}thpy)_2}$, for which the corresponding two emissions are spectrally well resolvable. (Sect. 4.2.4 and Refs. [59, 60].) In this situation, one would not observe any obvious difference between the spectra stemming from the two substates **II** and **III** of $\mathrm{Pd(2\text{-}thpy)_2}$.

The results discussed above have shown that time-resolved emission spectroscopy can provide detailed insight into vibronic deactivation paths of triplet substates, even when the zero-field splitting is one order of magnitude smaller than the obtainable spectral resolution ($\approx 2\ \mathrm{cm}^{-1}$). This is possible at low temperature (1.3 K), because the triplet sublevels emit independently. They are not in a thermal equilibrium due to the very small rates of spin-lattice relaxation between these substates. In the next section, we return to this interesting property by applying the complementary methods of ODMR and PMDR spectroscopy to the same set of triplet substates.

3.1.5
ODMR, PMDR, and Microwave Recovery Studies

For most organic molecules and quite a number of transition metal complexes the zero-field splitting of the lowest triplets is only of the order of 0.1 cm^{-1} (3 GHz), which is not easily resolvable by applying conventional optical techniques. In this situation, luminescence spectroscopy with additional microwave irradiation allows one in favorable cases to enhance the spectral resolution by orders of magnitude into the megahertz range (30 MHz $\triangleq$ 0.001 cm^{-1}). The importance of these methods is well established for studies of triplets of organic molecules (e.g. see Refs. [106, 107, 110, 130–133]) and more recently also of transition metal complexes (e.g. see Refs. [29–32, 61, 75, 90, 111, 134–140]). For example, information concerning the radiative character, population and decay properties, vibronic coupling routes, the fine structure parameters D and E (giving the zero-field splittings), etc. can be obtained for the individual triplet substates.

In this section, results of three different experimental methods that have been applied to Pd(2-thpy)$_2$ are reported. Information from optically detected magnetic resonance (ODMR spectroscopy), microwave-recovery measurements, and phosphorescence microwave double resonance (PMDR spectroscopy) is presented. These methods complement each other to a large extent. The discussion presented here can be limited to the basic implications of the methods, since a comprehensive review by Max Glasbeek concerning these aspects is found in Volume 213 of this series [90] and a detailed report by Glasbeek, Yersin et al. [61] concerning Pd(2-thpy)$_2$ has only recently been published.

3.1.5.1
ODMR Studies

Pd(2-thpy)$_2$ is dissolved in an n-octane matrix and is excited at low temperature ($T < 2$ K) by a c.w. source (non-pulsed, e.g. at $\lambda = 330$ nm [61]). Additionally, microwave irradiation is applied and scanned in frequency. The microwave radiation can cause transitions between the triplet sublevels in the case of resonance, and thus, the previously different and non-thermalized steady state populations of the substates are usually altered. Under suitable conditions (see below) a change of the phosphorescence intensity will result due to microwave perturbation. Usually, this effect is very weak. Therefore, microwave pulse trains are applied, for example, with a repetition rate of 150 Hz. Thus, one can monitor the microwave-induced intensity changes by a phase-sensitive lock-in technique [90].

Figure 9a (inset) shows the zero-field ODMR spectrum for Pd(2-thpy)$_2$ detected at the electronic origin of the emission spectrum at 18,418 cm^{-1}. Due to the frequency scan of the microwave radiation, one observes a signal at 2886 MHz (0.0962 cm^{-1}) with a line width (fwhm) of 20 MHz. No other zero-field ODMR signal could be observed in the frequency range from 300 MHz up to 8000 MHz. However, for a system of three triplet substates, one would expect to

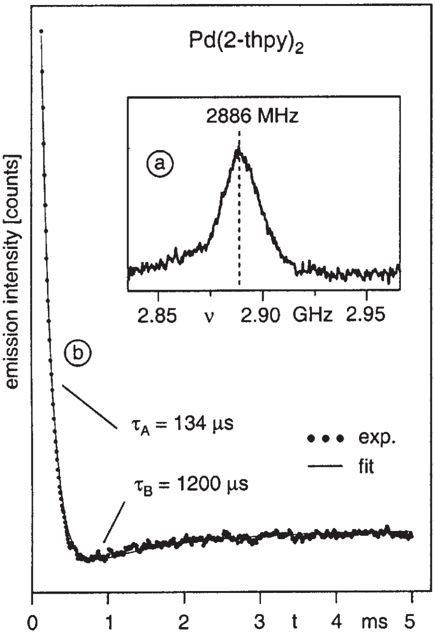

Fig. 9. ODMR investigations at T = 1.4 K of Pd(2-thpy)$_2$ dissolved in an n-octane Shpol'skii matrix. Concentration ≈ 10^{-5} mol/l; cw excitation λ_{exc} = 330 nm (30.3×10^3 cm^{-1}). Detection of the emission at 18418 cm^{-1} ($T_1 \rightarrow S_0$ transition). (**a**) Zero-field ODMR (optically detected magnetic resonance) spectrum; (**b**) Zero-field microwave recovery ODMR signal after pulsed microwave excitation with a microwave frequency of 2886 MHz. The best fit of the recovery signal is obtained with Eq. (4). (Compare Ref. [61])

observe three different transitions. If these are not found, this may be due to different reasons:

1. The resonance frequencies of the other transitions between the three substates are outside the experimentally accessible microwave range.
2. The radiative decay rates of the triplet substates that are in microwave resonance are too similar.
3. The population *differences* among the triplet substates are too small and thus microwave application will not induce sufficient change of the phosphorescence intensity.

The complementary studies of decay properties of the triplet substates at T = 1.2 K (Sect. 3.1.3, Table 2) show that the disparities between the triplet substates **I** and **II** as well as between **I** and **III** are significant, while the states **II** and **III** might exhibit too little disparities with respect to 2. and 3. Thus, one would expect to detect at least two ODMR transitions, but only one is observed. On the other hand, the relatively large transition probability of the transition $\mathbf{S_0} \rightarrow \mathbf{T_1}$ (excitation spectra can be recorded, emission decay times are relatively short, see Sects. 3.1.1 and 3.1.3) show that spin-orbit coupling is not unimportant.

(Compare also Sects. 5 to 7 and Refs. [18, 22, 24].) Therefore, it is expected that the total zfs is larger than in organic compounds and that the missing ODMR transition is well outside the microwave frequency range applied. A similar conclusion is also presented in Ref. [61], where it is further substantiated. In particular, it was derived in Ref. [61] that the observed ODMR signal at 2886 MHz corresponds to the 2 E transition. This is the energy separation between the two more closely lying triplet sublevels.[6] It is concluded that the two other transitions (D-E and D+E transitions) are outside the frequency range applied.[7] The studies presented in the next subsection will provide the information that the 2 E splitting represents the zfs between the triplet substates **I** and **III**.

3.1.5.2
Microwave-Recovery Studies

The technique of microwave-recovery provides crucial information about the substates involved in the ODMR transitions. For this experiment, Pd(2-thpy)$_2$ is optically excited by a c. w. source. This leads to specific populations of the three triplet substates. At low temperature, they are thermally decoupled and thus emit according to their specific populations and their individual decay constants (e. g. see Sect. 3.1.3 and Table 2). In the microwave recovery experiment, the steady state conditions are perturbed by a microwave pulse being in resonance with the zero-field transition at 2886 MHz. Due to the microwave pulse, the populations of the two states involved are changed. Subsequently, one monitors the recovery of the emission intensity in time until the steady state situation is reached again. The microwave pulses have, for example, a duration of 20 μs and are applied repeatedly to enable a detection with signal averaging [61].

Application of the microwave pulse with a frequency of 2886 MHz to Pd(2-thpy)$_2$ leads to a strong increase of the phosphorescence intensity, when monitored at the electronic origin at 18,418 cm^{-1}. The recovery signal (after the pulse) is depicted in Fig. 9b. Its time dependence is best fit by a biexponential function

$$f(t) = A \cdot e^{-t/\tau_A} + B \cdot e^{-t/\tau_B} \tag{4}$$

with $\tau_A = (134 \pm 6)$ μs, $\tau_B = (1200 \pm 50)$ μs, A = 0.05, and B = 0.02.

The time constants τ_A and τ_B are in excellent agreement with the decay times of $\tau_{III} = 130$ μs and of $\tau_I = 1200$ μs, respectively. (See Sect. 3.1.3, Fig. 6a, and Table 2). The third component of $\tau_{II} = 235$ μs does not appear in the microwave recovery signal. This tells us that the 2 E = 2886 MHz microwave transition occurs between the long-lived triplet sublevel **I** and the short-lived substate **III**, while sublevel **II** is not involved.

---

[6] The so-called fine structure parameters D and E were introduced to describe the zero-field splittings due to spin-spin interactions in organic molecules (e. g. see [32, 90, 130]). For transition metal compounds and in the context of this review, these parameters simply give the energy separations (zfs) between the three triplet substates.

[7] For a different situation compare, for example, the ODMR investigations on Pd(qol)$_2$ [75, 90] or [Rh(bpy)$_3$]$^{3+}$[30–32, 90].

3.1.5.3
PMDR Studies

Time-resolved emission spectra (Sect. 3.1.4, Fig. 8) show that the triplet sublevels **I** and **III** exhibit very different emission spectra with respect to their vibrational satellite structures. The long-lived state **I** is mainly vibronically (Herzberg-Teller, HT) deactivated, while the emission from state **III** is dominated by vibrational satellites due to Franck-Condon (FC) activities, whereby both types of vibrational modes exhibit different frequencies. This behavior makes it attractive to measure a PMDR spectrum.

The method of phosphorescence microwave double resonance (PMDR) spectroscopy is based, like the two other methods discussed above, on c.w. excitation of the $Pd(2\text{-thpy})_2$ compound at low temperature. Additionally, microwave irradiation is applied, whereby the frequency is chosen to be in resonance with the energy separation between the two substates **I** and **III** of 2886 MHz. With this set-up, one monitors the phosphorescence intensity changes in the course of scanning the emission spectrum. Technically, the phosphorescence spectrum is recorded by keeping the amplitude-modulated microwave frequency at the constant value of 2886 MHz and by detecting the emission spectrum by use of a phase-sensitive lock-in and signal averaging procedure (e.g. see [61, 75, 90]).

In Fig. 10b, such a PMDR spectrum is compared to a time-integrated emission spectrum (Fig. 10a). The latter is similar to the one presented in Fig. 3a. The PMDR spectrum reveals interesting intensity changes. For example, the negative signs of the 229, 261, 528 and 710 cm^{-1} vibrational satellites correspond to an emission intensity decrease upon inducing the microwave transition, while the electronic origin and the 211, 376, 447, 650 and 716 cm^{-1} satellites are connected with intensity increases. The time-resolved emission spectrum of $Pd(2\text{-thpy})_2$ has shown that in particular, the 528 cm^{-1} satellite (which results from HT activity) originates *only* from the long-lived triplet sublevel **I** with the lifetime of τ_I = 1200 µs. From the observation of the microwave-induced intensity decrease of the 528 cm^{-1} satellite in the PMDR spectrum it follows that, under c.w. optical excitation at 330 nm, the steady-state population of the triplet substate **I** with the lifetime of 1200 µs is larger than for the substate **III** with a lifetime of τ_{III} = 130 µs. Since the population of sublevel **III** is enhanced in the microwave recovery experiment (Fig. 9b), it can be concluded that the modes at 375, 447, 650 and 716 cm^{-1} that show a positive sign are mainly coupled to the triplet sublevel **III**.

The information obtained from the phosphorescence microwave double resonance (PMDR) spectroscopy nicely complements the results deduced from time-resolved emission spectroscopy. (See Sect. 3.1.4 and compare Ref. [58] to [61].) Both methods reveal a triplet substate selectivity with respect to the vibrational satellites observed in the emission spectrum. Interestingly, this property of an individual vibronic coupling behavior of the different triplet substates survives, even when the zero-field splitting increases due to a greater spin-orbit coupling by more than a factor of fifty, as found for $Pt(2\text{-thpy})_2$.

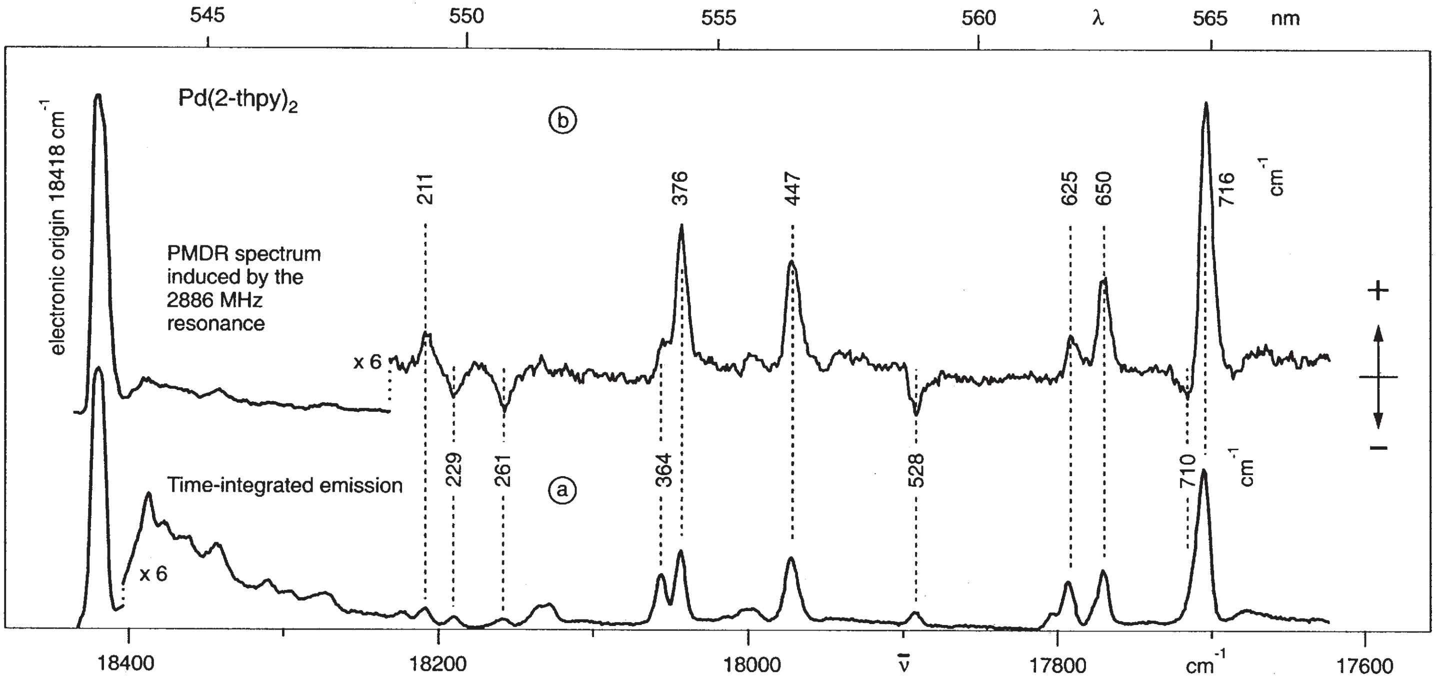

Fig. 10. (*a*) Time-integrated emission spectrum and (*b*) PMDR (phosphorescence microwave double resonance) spectrum of Pd(2-thpy)$_2$ at $T = 1.4$ K dissolved in an n-octane Shpol'skii matrix. Concentration ≈ 10^{-5} mol/l. $\lambda_{\mathrm{exc}} = 330$ nm. The PMDR spectrum is induced by a microwave irradiation with a frequency of 2886 MHz, which is in resonance with the energy difference between the triplet substates **I** and **III**. An intensity increase (+) signifies vibrational satellites that belong to an emission from the short-lived substate **III**, while a decrease (–) characterizes satellites of the emission spectrum from the long-lived substate **I** (Compare Ref. [61])

3.1.6
Emission in a Deuterated Matrix

It is known that the matrix material and thus the individual cage structure surrounding the chromophore can have an influence on the chromophore's emission properties, such as transition energies, zfs, slr rates, etc. Therefore, it is instructive to slightly alter the matrix and to investigate the resulting changes of emission properties of Pd(2-thpy)$_2$.

In this section, per-deuterated n-octane (n-octane-d$_{18}$) is used as the matrix material, and the emission properties of Pd(2-thpy)$_2$ are compared with those obtained with a per-protonated n-octane matrix (n-octane-h$_{18}$). This latter matrix was used for the investigations discussed in the preceding sections. Three different issues are addressed, namely the occurrence of different sites for Pd(2-thpy)$_2$, changes of low-energy vibrational/phonon structures, and changes of the emission decay behavior.

3.1.6.1
Different Sites

Usually a deuterated and a protonated matrix, respectively, will not provide the same cage structures for a chromophore, since the C-D binding distances of the matrix material are slightly smaller than the C-H distances [141, 142]. Indeed, in n-octane-h$_{18}$ one finds only one dominating site (site A) for Pd(2-thpy)$_2$, which is characterized by the position of the electronic origin at 18,418 cm^{-1} (Table 4). Other sites (B to D) are of minor importance for the total emission intensity. On the other hand, the n-octane-d$_{18}$ matrix provides two main sites A and B for

Table 4. Emitting sites of Pd(2-thpy)$_2$ in per-protonated and per-deuterated n-octane Shpol'skii matrices at $T = 1.3$ K. $c_{complex} = 10^{-5}$ mol l^{-1}. Cooling rate ≈ 100 K/min [57]

	Electronic origin (cm^{-1})	Relative Intensity[a]
n-octane-h$_{18}$ matrix		
site A	18,418	100
site B	18,452	0.3
site C	18,472	1.1
site D	18,578	0.5
n-octane-d$_{18}$ matrix		
site A	18,429	90
site B	18,434	100
site C	18,454	0.1
site D	18,475	0.1
site E	18,485	0.8
site F	18,590	0.4

[a] Most intense peak normalized to 100.

Pd(2-thpy)$_2$ with nearly equal emission intensities of the $\mathbf{T_1} \rightarrow \mathbf{S_0}$ electronic origin. (Table 4) Again, a number of other sites can be detected which, however, are of minor importance.

Moreover, the individual matrix-cage structure has an observable effect on the $\mathbf{T_1} \leftrightarrow \mathbf{S_0}$ transition energy. The electronic origins of the two sites A and B in n-octane-d$_{18}$ are found at higher energy of 11 and 16 cm^{-1}, respectively, when compared to origin of site A in n-octane-h$_{18}$. Although a small part of this blue shift might be ascribable to an intrinsic deuteration-induced effect on the electronic origins (compare also Sect. 4.2.10 and e.g. the Refs. [19, 22, 25, 33, 47]), the main contribution seems to be related to different cage structures. Obviously for Pd(2-thpy)$_2$, two nearly equally probable cages are provided by the per-deuterated matrix. From simple size considerations, it appears that the most likely cage structures result from a replacement of two or three n-octane molecules which are neighbors along the crystallographic *a* or *b* axis, respectively. (Compare Refs. [85a, 152].) However, the realizability of both substitutions by Pd(2-thpy)$_2$ is clearly different in the two matrices. Probably, this is due to small packing differences in n-octane-d$_{18}$ as compared to n-octane-h$_{18}$.

In an independent investigation [63], it has been shown that the lowest electronic origin of Pt(2-thpy)$_2$ in a Shpol'skii matrix is *red shifted* by high pressure application. This effect is mainly ascribed to an increase of the chromophore-cage interaction and thus to a reduction of free space. Therefore, it might conversely be assumed that a slightly larger free space for Pd(2-thpy)$_2$ (smaller chromophore-cage interaction) is the main source of the observed blue shifts of the electronic origins of Pd(2-thpy)$_2$ in both resulting cages of the n-octane-d$_{18}$ matrix as compared to the cage in the n-octane-h$_{18}$ matrix.

3.1.6.2
Low-Energy Vibrations/Lattice Modes

It is expected that deuteration of matrix molecules leads to a low-energy shift (red shift) of lattice vibrations or local phonon modes (cage modes) as compared to those of the protonated material, because the vibrating masses become larger, while the force constants are almost unchanged. Indeed, this behavior is observed in the emission spectra, when the low-energy satellites relative to the electronic origins are compared (Table 5).

The largest matrix effect is found for the 32 cm^{-1} satellite which is red shifted by 10 cm^{-1} to 22 cm^{-1}. Obviously, the matrix character of these modes is very pronounced. With increasing energy of the modes, the deuteration-induced red shift becomes clearly smaller. This behavior is ascribed to the fact that lattice/cage modes couple with low-energy vibrations of the chromophore, if symmetry restrictions do not exist. With growing vibrational energy of the chromophore, the perturbation of this mode by the low-energy lattice/cage modes becomes increasingly smaller according to first-order perturbation effects. According to Table 5, this type of mixing between complex vibrations and lattice/cage modes becomes insignificant above ≈ 150 cm^{-1}.

Table 5. Low-energy vibrational satellites (cm^{-1}) of $Pd(2\text{-thpy})_2$ in per-protonated and perdeuterated n-octane Shpol'skii matrices from emission spectra [57]. T = 1.3 K. $c_{complex} = 10^{-5}$ mol l^{-1}

n-octane-h_{18} matrix[a]	n-octane-d_{18} matrix	Assignment
18,418 cm^{-1} (site A)	18,434 cm^{-1} (site B)	electronic origin
32	22	lattice mode[b]
50		complex vibrations/lattice mode
79	75	complex vibrations/lattice mode
111		complex vibrations/lattice mode
125	122	complex vibrations/lattice mode
150	146	complex vibrations/lattice mode
–	170	
196	196	
211	211	M-L[c]
229	229	M-L[c]

[a] Compare Table 1.
[b] Mode with significant matrix character.
[c] Modes with metal-ligand (M-L) character.

3.1.6.3
Emission Decay and Matrix Effects

Figure 11 shows that deuteration of the matrix material has an interesting and not anticipated effect on the temperature dependence of the emission decay of $Pd(2\text{-thpy})_2$. At T = 1.3 K, one observes the three individual decay components of the three triplet substates **I**, **II**, and **III**, as discussed in Sect. 3.1.3. Within limits of experimental error, deuteration of the n-octane matrix does not alter this decay behavior. (Compare Fig. 11a to Fig. 6a.) With temperature increase, the emission decay times are reduced in both matrices due to effects of thermalization between the three triplet sublevels, i.e. due to the growing in of spin-lattice relaxation (e.g. see Sects. 3.1.3 and 4.2.6). These processes are particularly important for the long-lived components. For example, already at T = 2.0 K this component is reduced to 950 μs and 840 μs for the deuterated and the protonated matrix, respectively (decay curves not reproduced). This trend continues, as is shown in Fig. 11b. At T = 3.0 K, the long-decaying components are determined to 460 μs and 320 μs, respectively. Finally, near T=5 K, thermal equilibration between the three substates is reached for both matrices, and the decays become monoexponential. (Fig. 11c, compare also Sect. 3.1.3.) At this temperature, the emission decay of $Pd(2\text{-thpy})_2$ is again almost equal in n-octane-h_{18} and n-octane-d_{18}.

The results discussed show that the effect of matrix deuteration on the emission decay is only obvious in the temperature range from slightly below T = 2.0 K to slightly below T = 5.0 K, i.e. from the onset of slr up to fast thermalization. In this range, the temperature dependence of spin-lattice relaxation (slr) is different for the two matrices. In the low-temperature range, the increase of slr rate seems to be less pronounced for the deuterated matrix as compared to the protonated one. Presumably, this behavior is connected with the specific struc-

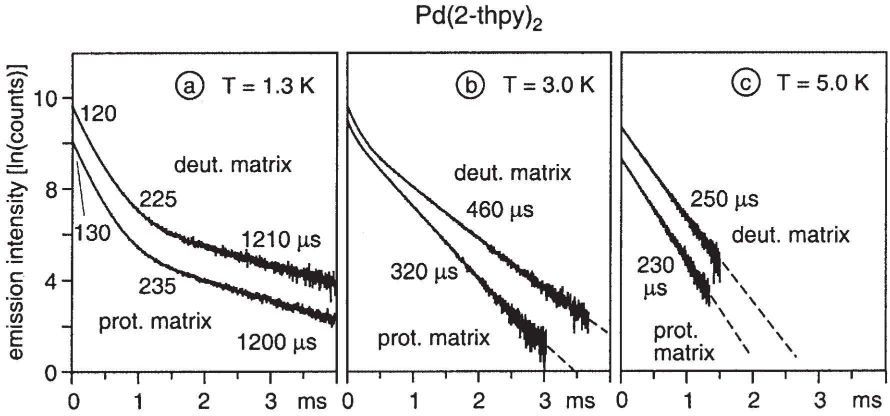

Fig. 11. Emission decay curves at different temperatures of Pd(2-thpy)$_2$ dissolved in a per-protonated and a per-deuterated n-octane Shpol'skii matrix, respectively. Concentration $\approx 10^{-5}$ mol/l; λ_{exc}=337.1 nm (29,665 cm^{-1}); cooling rate ≈100 K/min; $\bar{\nu}_{det}$ (protonated matrix) = 18,418 cm^{-1}(electronic origin of site A); $\bar{\nu}_{det}$ (deuterated matrix) = 18,434 cm^{-1} (electronic origin of site B, compare Table 4). The decay times given result from least-square fits. (Compare Ref. [57])

tures of the matrix cages. The importance of the individual cage structures is indicated by companion studies with Pt(2-thpy)$_2$ in n-octane-d$_{18}$ [143] and by studies with Pt(phpy)$_2$. For this latter compound, the significance of the individual site or the cage structure on the slr rates has recently been demonstrated [65].

Certainly, a deeper understanding of these temperature and matrix dependent processes of slr in the lowest triplet state of Pd(2-thpy)$_2$ requires further investigations. On the other hand, a detailed study of the processes of spin-lattice relaxation that govern the decay behavior of Pt(2-thpy)$_2$ has recently been carried out. In this compound, the three triplet sublevels are spectrally well resolvable due to the larger zero-field splittings and thus the corresponding decay processes are more easily accessible than in Pd(2-thpy)$_2$. (See Sects. 4.2.6 to 4.2.9 and the Refs. [24, 60, 62, 64, 65].)

3.2
Higher Lying States of Pd(2-thpy)$_2$

Little information is available in the literature on higher lying excited states of Pd(2-thpy)$_2$. Therefore, it is highly attractive to have a better resolved spectrum than the one shown in Fig. 2. This is of particular interest, since presently more detailed theoretical studies of organometallic Pd and Pt compounds become possible (compare Ref. [66]). The calculated results should be tested on a sufficiently accurate experimental basis. However, due to several reasons it is often very difficult to obtain well-resolved spectra of higher lying states. For example, homogeneous linewidths become broader due to short lifetimes of the states (see also below) and absorptions of different states and additionally of different sites overlap. Moreover, even when, for example, site selective excitation measurements are successful, well defined and well-resolved spectra are usually only obtainable for restricted spectral ranges.

For Pd(2-thpy)$_2$ some information has been reported in Ref. [74] and will be summarized subsequently. (Compare also Fig. 5):

$S_0 \rightarrow T_1$

The lowest triplet $\mathbf{T_1}$ of Pd(2-thpy)$_2$ in n-octane lies at 18,418 cm^{-1}, and the structure that is observed up to 23 214 cm^{-1} (Fig. 4 and Table 1) is assigned to vibrational satellites of fundamentals, combinations, and progressions, respectively. No other electronic transition can be detected between $\mathbf{T_1}$ and $\mathbf{S_1}$.

$S_0 \rightarrow S_1$

The next higher lying peak above the $\mathbf{S_0} \rightarrow \mathbf{T_1}$ transition is observed at 23,836 cm^{-1} in an excitation spectrum (detected at 18,418 cm^{-1}). The peak is classified as electronic origin due to the good-fit of several phonon satellites that are also observed and that are known for the n-octane matrix (e.g. 16, 32, 81, 109, and 146 cm^{-1}, see the Tables 1 and 7). The absorption coefficient is estimated to be of the order 3×10^3 l/mol cm [74], which strongly indicates the singlet character of the corresponding state. This assignment is confirmed by the observation that this electronic origin is not influenced by application of a magnetic field up to B = 12 T. For a triplet transition, on the other hand, one would expect to see Zeeman shifts and/or splittings.[8] The singlet $\mathbf{S_1}$ to triplet $\mathbf{T_1}$ separation amounts to $\Delta E(S_1 - T_1) \approx 5420$ cm^{-1}.

The width (fwhm) of the electronic origin peak at 23,836 cm^{-1} is 6.5 cm^{-1} at $T = 1.2$ K. Its lineshape can be well approximated by a Lorentzian lineshape function, while a fit to a Gaussian lineshape is unsuccessful [74]. This indicates that the peak is homogeneously broadened [103, 104]. Thus, the width of 6.5 cm^{-1} can be related to the lifetime of this $\mathbf{S_1}$ state to $\tau(S_1) \approx 8 \times 10^{-13}$ s. (Compare Eq. (2).) Further, the high phosphorescence intensity that is observed from the $\mathbf{T_1}$ state when the $\mathbf{S_1}$ state is excited, indicates that the lifetime of this $\mathbf{S_1}$ state is largely determined by the intersystem crossing process from $\mathbf{S_1}$ to $\mathbf{T_1}$. This would correspond to the rate of $k_{isc} \approx 1/\tau(S_1) \approx 10^{12}$ s^{-1}. A value of the same order of magnitude has also been determined for Pd-phthalocyanine [144].

Transition at ≈ 24,700 cm^{-1}

In the energy range between about 24,600 cm^{-1} and 25,600 cm^{-1} one observes a broad excitation band with some resolved satellite structure at $T = 1.2$ K. If the electronic origin is assumed to be at 24,666 cm^{-1}, a number of satellites can be assigned to vibrations that have already been determined for the $\mathbf{T_1}$ state, such

---

[8] Equivalent investigations concerning the singlet character of higher lying states have also been carried out for Pt(2-thpy)$_2$ (Sect. 4.3) and Pt(qol)$_2$ [72].

as vibrations at 290, 385, 446, and 695 cm^{-1} as well as the (290 ± 446) cm^{-1} combination at 736 cm^{-1}. [74] (Compare Fig. 4a and Table 1.) Apart from the 695 cm^{-1} fundamental, these modes have been classified as metal-ligand vibrations. This behavior would indicate an assignment to a state with significant MLCT character [18, 21, 22, 59]. Under application of magnetic fields up to B=12 T one observes some changes of the intensity distribution of the satellites. Such a behavior is not expected to occur for a singlet. Thus, it is indicated that this structure may be traced back to a second triplet state. However, a clear classification is not yet possible on the basis of the information available.

In conclusion, it is expected that the transitions addressed in this section and summarized in Fig. 5 are part of, or are hidden under the absorption feature between ≈ 24,000 and ≈ 30,000 cm^{-1} of Pd(2-thpy)$_2$ dissolved in CH_2Cl_2 (Fig. 2). However, the transition energy of this broad band with its shoulder should not be compared too rigorously with the energies of the resolved structures, because solvent shifts can easily exceed values of 10^3 cm^{-1}.

Further, a detailed comparison with the theoretical study of Ref. [66] is not really possible due to the non-inclusion of spin-orbit coupling. Nevertheless, it may be pointed to the similar values that are found for the singlet $\mathbf{S}_1$ to triplet $\mathbf{T}_1$ separation. From the experiment one obtains a value of ≈ 5420 cm^{-1} as compared to the calculated value of ≈ 4750 cm^{-1}. The energy position of the second excited singlet $\mathbf{S}_2$ has not yet been determined by highly resolved excitation spectra. Very probably, this $\mathbf{S}_2$ state is connected with the peak that occurs near 26,000 cm^{-1} in the absorption spectrum shown in Fig. 2. Interestingly, this energy is also predicted by the calculations of Ref. [66] for the position of $\mathbf{S}_2$. For completeness, it is mentioned that according to Ref. [66] the lowest MC-dd* states are expected to occur above 27,000 cm^{-1}.

4

Pt(2-thpy)$_2$

An introduction to optical properties of Pt(2-thpy)$_2$ is given by presenting the room temperature absorption and the 80 K emission spectra of the dissolved complex (Fig. 12). The spectra are reproduced from the Refs. [53, 145]. The most intense absorption band near 32,800 cm^{-1} (Fig. 12a) is assigned to a transition from the singlet ground state $\mathbf{S}_0$ to a singlet dominantly of LC-$\pi\pi^*$ character or within the approximation of a C_{2v} point group symmetry to a $^1\mathbf{A}_1 \rightarrow {}^1\mathbf{A}_1$ transition [66]. (Compare also [53].) The correspondence of the low-energy shoulders on this dominant absorption band to the states calculated in Ref. [66] is not clear, they may correspond to ^{1}LC and to higher lying ^{1}MLCT states, respectively. The lower lying peak near 23,800 cm^{-1} (≈ 420 nm) and the shoulder near 21,700 cm^{-1} (≈ 460 nm) are both assigned in Ref. [53] to ^{1}MLCT states. Within the CASPT2 ab initio study [66], these states are also ascribed to exhibit dominant MLCT character. (For more details see Sect. 4.3.)

A weak absorption peak with a molar extinction coefficient of ≈ 90 l/mol cm [145] occurs near 17,500 cm^{-1} for Pt(2-thpy)$_2$ dissolved in CH_2Cl_2. This peak corresponds to the lowest triplet state $\mathbf{T}_1$ which will be discussed in great detail in the next sections. It will be shown that this state is classified as being mainly

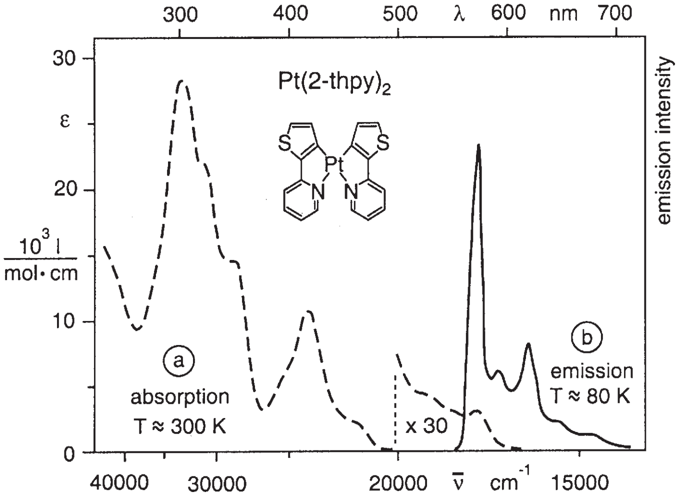

Fig. 12. (*a*) Absorption spectrum of Pt(2-thpy)$_2$ dissolved in CH$_2$Cl$_2$, from Ref. [145]. (*b*) Emission spectrum of Pt(2-thpy)$_2$ dissolved in butyronitrile, from Ref. [53]

of ^{3}LC-$\pi\pi^*$ character with significant MLCT admixtures (compare also [18, 59]). Interestingly, the theoretical studies of Ref.[66] come to the same interpretation.

For completeness it is mentioned that MC-dd* states are expected to occur above ≈ 32,000 cm^{-1} [66].

The emission displayed in Fig. 12b has been assigned as a phosphorescence (triplet → singlet emission) due to the relatively long decay time of 12 µs at 80 K in butyronitrile and of ≈ 5 µs at 293 K in acetonitrile. The quantum yield is reported to be as high as 30% at room temperature [53]. The structure in the emission spectrum is assigned to vibrational satellites as will be shown below (Sect. 4.2.4).

4.1
Different Shpol'skii Matrices

Pt(2-thpy)$_2$ was investigated in different n-alkane Shpol'skii matrices (n-hexane, n-heptane, n-octane, n-nonane, and n-decane), using 1,4-dioxane as an intermediate solvent. All these matrices led to highly resolved spectra showing electronic origins (Sect. 4.2.1) and rich vibrational and phonon satellite structures (Sect. 4.2.4). The smallest halfwidth obtained is 2 cm^{-1} (fwhm, $T = 1.3$ K), which is more than a hundred times smaller than found in a glass forming matrix like butyronitrile (see Fig. 12b). In every matrix several Pt(2-thpy)$_2$ sites are found, although for n-octane and n-decane one site dominates strongly. Taking the different matrices mentioned above, one finds that the different sites of Pt(2-thpy)$_2$ are distributed over an energy range of about 400 cm^{-1}. Table 6 gives the spectral positions of the electronic origins of those sites, which contribute by more than 5% to the emission intensity.

Table 6. Electronic origins of different sites of Pt(2-thpy)$_2$ in several Shpol'skii matrices (T = 4.2 K) (from Ref. [59])

n-Alkane[a]	Number of intense sites[b]	Electronic origins [cm^{-1}]			Origin halfwidths [cm^{-1}]	Intensities of different sites[c] [%]
		I	II	III		
hexane	4	–[d]	17176	–[d]	9	10[e]
		17132	17139	17147	5	41[e]
		17126	17133	–[d]	4	14[e]
		17100	17107	17115	3	22[e]
heptane	2	17175	17182	17191	3	51
		17076	17084	17092	4	31
octane	1	17156	17163	17172	2–3	98
nonane	4	–[d]	17286	–[d]	16	25
		–[d]	17222	–[d]	10	7
		17186	17192	–[d]	4	17
		17171	17177	17187	3	38
decane	1	17159	17166	17177	5	92

[a] As intermediate solvent 1,4-dioxane was used. Concentration of Pt(2-thpy)$_2$ $\approx 10^{-5}$ mol/l.

[b] Only sites are considered which contribute with more than 5% to the emission intensity.

[c] The intensity found in all sites is normalized to 100%. The intensities of the specific sites are estimated by comparing the intensities of the electronic origins at T = 4.2 K.

[d] Triplet component not resolved due to a large halfwidth.

[e] Mostly, a broad background emission with a halfwidth of about 350 cm^{-1} is also detectable, however, with a cooling rate of about 20 K/s this background does not occur.

Distinct differences for the various matrices are observed with regard to the coupling of Pt(2-thpy)$_2$ to lattice modes (phonons). These occur in the spectra as resolved phonon satellites and/or as unresolved phonon wings. Such satellites accompany all electronic transitions and also satellites of vibrational fundamentals. For example, in Tables 1, 5, and 7 (shown later) energies of lattice mode satellites are given for n-octane.

An inspection of Table 6 shows that n-octane represents a well suited matrix for spectroscopic investigations since one finds only one strongly dominating site with a small halfwidth of the electronic origin of about 2 cm^{-1} (fwhm). Therefore, the following investigations were carried out with n-octane. The use of different intermediate solvents (1,4-dioxane or tetrahydrofuran) did not result in any observable change of the spectra, at least for the concentrations chosen. Thus, it is concluded that the molecules of the intermediate solvent are not near neighbors of the chromophore sites investigated.

4.2

The Lowest Triplet State of Pt(2-thpy)$_2$

Chemical substitution of the central metal ion from Pd(II) to Pt(II) has very interesting consequences on photophysical properties of the lowest triplet state

$\mathbf{T_1}$. Due to the larger metal/MLCT admixture to this triplet and the greater spin-orbit coupling constant[9] of Pt(II) compared to Pd(II), one obtains an increase of the zero-field splitting of $\mathbf{T_1}$ by a factor of the order of 10^2 (Fig. 1). One finds a splitting of the sublevels by 7 cm^{-1} and 9 cm^{-1}, respectively, resulting in a total zfs of 16 cm^{-1}, as will be specified below. These values are large enough to allow us to resolve the three different triplet substates spectrally, and thus to investigate the substates individually. Hence, several interesting and previously unknown photophysical properties that are connected with triplet substates can be elucidated.

The Figs. 13 to 16 show time-integrated emission and excitation spectra of $Pt(2\text{-}thpy)_2$ dissolved in n-octane. These spectra correspond to the dominant site of $Pt(2\text{-}thpy)_2$.

4.2.1
Electronic Origins (0–0 Transitions) and T_1 Substates

The spectral features of highest energy in emission (Figs. 13, 14) and of lowest energy in excitation (Fig. 15) are assigned to electronic origins (0 – 0 transition). Figure 16 depicts the region of the electronic origins on a spectrally expanded scale. Three origins are identified. They are denoted as origins I, II, and III in order of increasing energy and are situated at 17,156 cm^{-1}, 17,163 cm^{-1}, and 17,172 cm^{-1}, respectively. These origins correspond to the transitions between the singlet ground state **0** ($\mathbf{S_0}$) and the three triplet $\mathbf{T_1}$ substates **I**, **II**, and **III**. The lines II and III are found at the same energies in emission and in excitation, while line I is not observed at zero magnetic field (Fig. 16 a).[10] All three origins are accompanied by rich vibrational satellite structures (Figs. 13 to 15). In particular, the vibrational energies determined from the $T = 1.3$ K emission spectrum (Fig. 13) fit well to vibrational energies observed in an IR spectrum (Sect. 4.2.4, Table 7), when the position of the electronic origin I is set to 17,156 cm^{-1}.

An independent confirmation for the position of this origin I is obtained, when a magnetic field is applied. With increasing field strength, the electronic origin line (line I_B)[11] grows in due to a B-field-induced interaction of substate **I** with higher lying triplet sublevel(s). (Fig. 16 d to f) A similar behavior has been observed for $[Os(bpy)_3]^{2+}$and has been thoroughly discussed in Refs. [22, p. 223] and [129]. Figures 16 d) to f) show also distinct Zeeman shifts for the lines I_B and

---

[9] Approximate values of the spin-orbit coupling parameter ξ_{nd} can be deduced from plots given in Ref. [146] for Pd^{2+} to $\approx 1.3 \times 10^3$ cm^{-1} and for Pt^{2+} to $\approx 4.8 \times 10^3$ cm^{-1}. These values correspond approximately to those given in Ref. [147].

[10] In a previous report of our group [59] the occurrence of an extremely weak line I in emission was reported. This result is not reproduced by the spectrum shown in Fig. 16 a. Presumably, under certain conditions, such as specific cooling rates, the chromophore's environment (matrix cage) can become slightly different. For example, it may be less symmetric. Such a behavior would explain the occurrence of an extremely weak line I under specific conditions.

[11] The index B characterizes the situation under application of a magnetic field B.

III_B of $Pt(2\text{-thpy})_2$ and thus manifest additionally the triplet nature of this set of sublevels.[12]

For completeness, it is already mentioned here that the relatively high intensity of the origin line II at $T = 1.3$ K (Figs. 13 and 16a) is not in accordance with a Boltzmann distribution for two states which are separated by 7 cm^{-1}. It will be pointed out in Sects. 4.2.7 and 4.2.8 that the emission from state **II** cannot be frozen out. This is a consequence of the relatively slow spin-lattice relaxation from state **II** to state **I** (compare also the Refs. [24, 62, 64, 65]).

Here it is pertinent to refer briefly to an investigation of the pressure-induced shift of the electronic origin II of $Pt(2\text{-thpy})_2$ in n-decane at $T \approx 5$ K. This electronic transition is red shifted linearly by $\Delta\bar{\nu}/\Delta p = -(3 \pm 1)$ cm^{-1}/kbar in the investigated pressure range up to p = 14 kbar [63]. The pressure-induced shift is relatively small as compared to values found for other compounds (see Table 1 of Ref. [63]). It is suggested in Ref. [63] that pressure-induced shifts of electronic transitions usually contain significant contributions from changes of chromophore-matrix interactions and that these contributions are particularly small for compounds dissolved in n-alkane Shpol'skii matrices. (For a recent review concerning high-pressure investigations of other compounds, see Ref. [150].)

4.2.1.1
Symmetry and Grouptheoretical Assignments

A clear grouptheoretical assignment of the three triplet substates is not yet possible, but it is appropriate to describe the current state of understanding in this respect.

The crystal structure determination has shown that the point group symmetry of $Pt(2\text{-thpy})_2$ strongly deviates from a C_{2v} symmetry and thus is as low as C_1 [151]. Thus, a grouptheoretical assignment would not make sense. On the other hand, spectroscopic investigations indicate that $Pt(2\text{-thpy})_2$ in n-octane exhibits a higher symmetry, as is indicated by three different features: 1. The transition from the lowest triplet sublevel **I** to the ground state **0** is strongly forbidden. (Fig. 16a) This behavior indicates that a selection rule still applies. 2. Substate **I** strongly reacts to symmetry breaking processes, such as perturbations due to low-symmetric vibrations. These induce significant radiative allowedness and give rise to the occurrence of vibrational satellites as reflected by the emission spectrum shown in Fig. 13. (Details concerning these so-called Herzberg-Teller

---

[12] Interestingly, the spectra depicted in Figs. 16 d) to f) seem to reflect a situation of oriented chromophores or of a high-field limit. (Compare the results found for $Pd(2\text{-thpy})_2$ discussed in Sect. 3.1.1 and see the Refs. [81, 91]). However, even the magnetic field strength of B = 12 T is far too small to reach the high-field limit for a compound with a zfs of 16 cm^{-1}. Moreover, the microcrystals of the n-octane matrix are expected to be statistically distributed. This should lead to a less resolved and less distinct Zeeman pattern than is seen in Fig. 16. A conclusive explanation for this behavior has not yet been developed. Presumably, the assumption of a statistical distribution has to be modified [148]. The quartz glass cell might lead to a preorientation of the microcrystals at the glass surface in the course of the cooling procedure (compare also [149]). Obviously, these effects require further investigations.

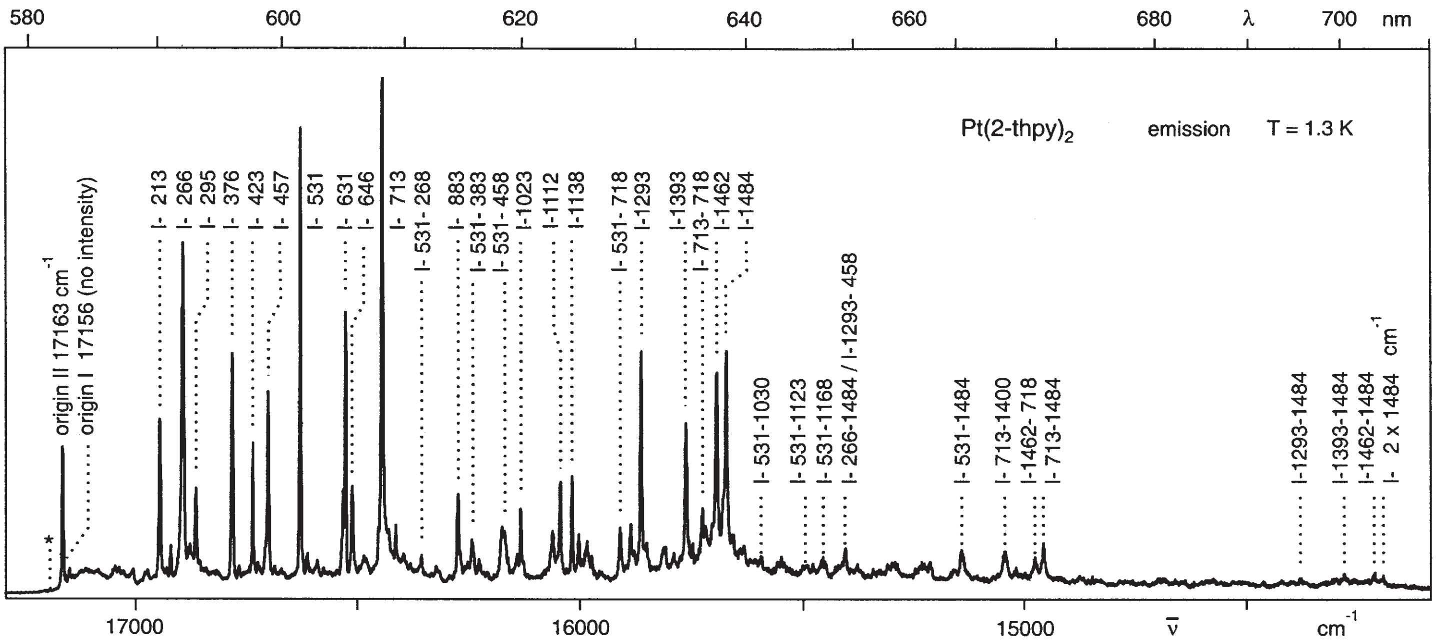

Fig. 13. Emission spectrum of Pt(2-thpy)$_2$ dissolved in n-octane (Shpol'skii matrix) and monitored at $T = 1.3$ K. Concentration $\approx 10^{-5}$ mol/l. $\lambda_{exc} =$ 457.9 nm. The vibrational satellites are characterized by their energy separations from the electronic origin I at 17,156 cm^{-1}. The *asterisk* denotes an electronic origin of a site of minor importance. An extension of the region of the electronic origins is shown in Fig. 16. (Compare Ref. [59])

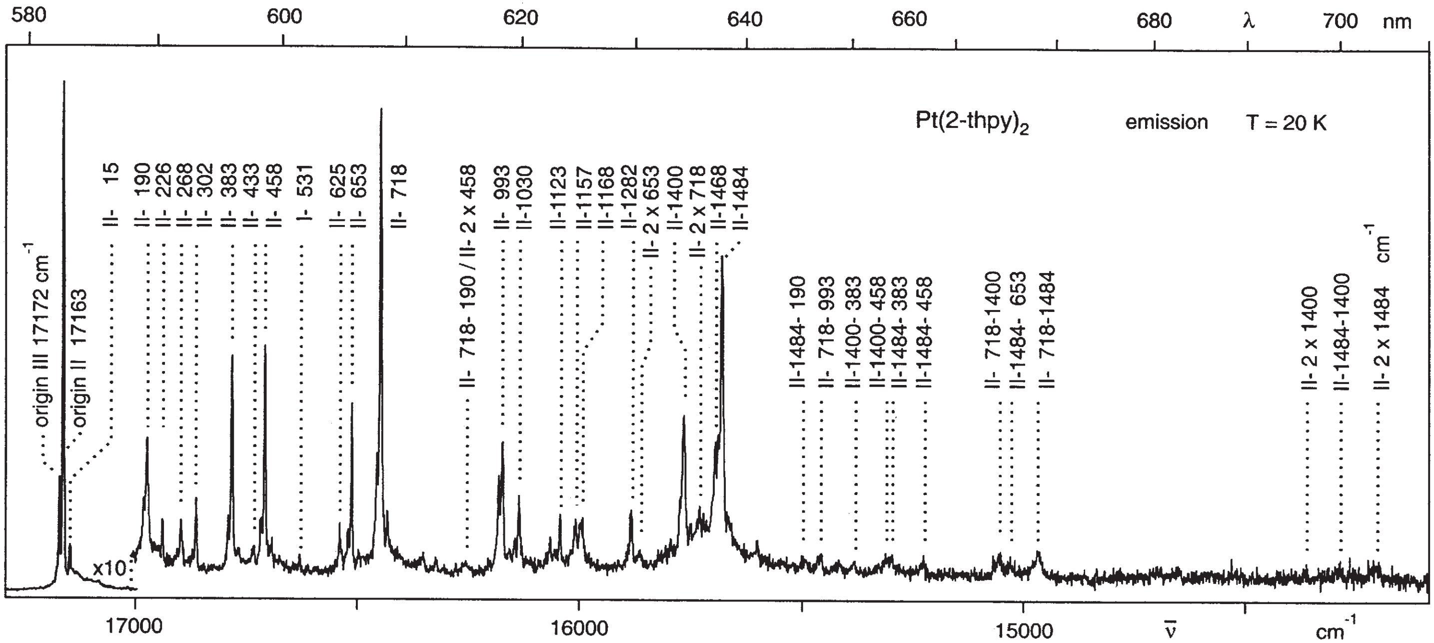

Fig. 14. Emission spectrum of Pt(2-thpy)$_2$ dissolved in n-octane and recorded at $T = 20$ K. Concentration $\approx 10^{-5}$ mol/l. $\lambda_{\text{exc}} = 457.9$ nm. The vibrational satellites are characterized by their energy separations from the electronic origin II at 17,163 cm^{-1}, apart from the weak 531 cm^{-1} satellite which belongs to the emission of state **I**. The region of the electronic origins is reproduced in Fig. 16 on an enlarged scale. (Compare Ref. [59])

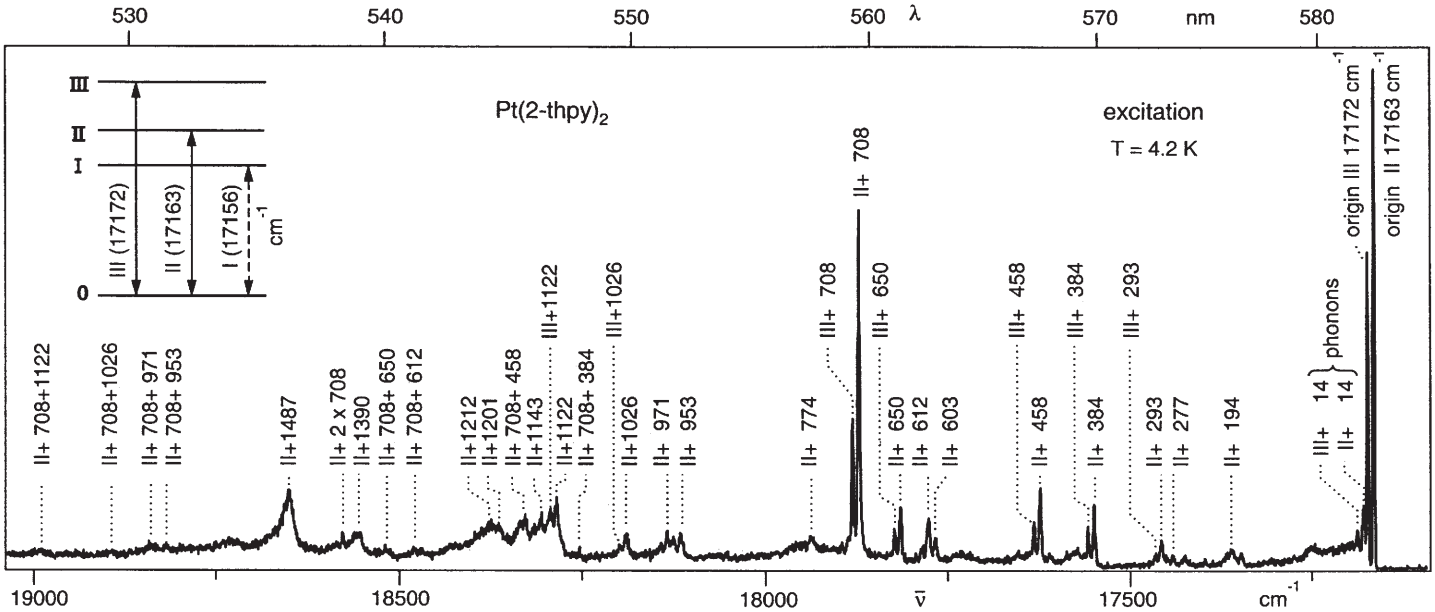

Fig. 15. Excitation spectrum of Pt(2-thpy)$_2$ dissolved in n-octane and recorded at $T = 4.2$ K. Concentration $\approx 10^{-5}$ mol/l. $\bar{\nu}_{\mathrm{det}}$ 16,445 cm^{-1} (≙ 17,163^{-1} (origin II) – 718 cm^{-1} (vibration)). The vibrational satellites are characterized by their energy separations from the electronic origin II at 17,163 cm^{-1} and origin **III** at 17,172 cm^{-1}, respectively. The region of the electronic origins is reproduced on an enlarged scale in Fig. 16. The *inset* depicts an energy level diagram for the three triplet substates. The transition **0** ↔ **I** is strongly forbidden. A more complete energy level diagram is shown in Fig. 29. (Compare also Ref. [59])

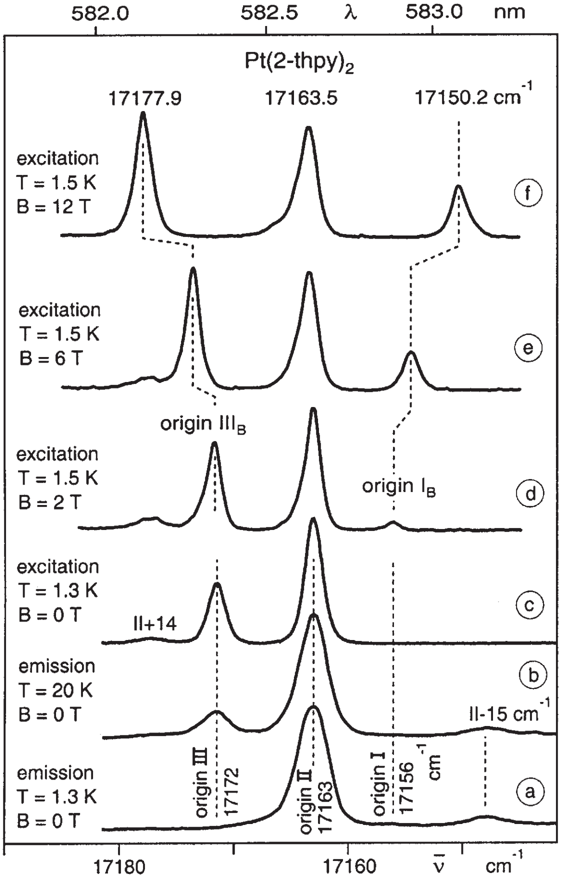

Fig. 16. Region of the electronic origins I, II, and III corresponding to the $\mathbf{T}_1 \leftrightarrow \mathbf{S}_0$ transition of Pt(2-thpy)$_2$ dissolved in n-octane. (*a*) Emission spectrum measured at $T = 1.3$ K and zero magnetic field, $\lambda_{\text{exc}} = 457.9$ nm. (Compare Fig. 13.) (*b*) 20 K emission at B = 0 T. (Compare Fig. 14.) (*c*) Excitation spectrum measured at $T = 1.3$ K, B = 0 T, $\bar{\nu}_{\text{det}} = 16{,}445$ cm^{-1} (≙ 17,163 cm^{-1} (origin II) – 718 cm^{-1} (vibration)), (*d*), (*e*), (*f*) Excitation spectra measured at $T = 1.5$ K for different magnetic field strengths. $\bar{\nu}_{\text{det}}$: 718 cm^{-1} vibrational satellite in the emission of the magnetic-field perturbed lowest triplet substate $\mathbf{I}_\mathbf{B}$. (Compare also Refs. [59,74])

couplings are discussed in Section 4.2.2.) 3. Both ligands of Pt(2-thpy)$_2$ are electronically largely equivalent, since the wavefunctions of the three triplet sublevels are delocalized over the two ligands (and the metal), as is demonstrated in Ref. [23] and in Sect. 4.2.11. In conclusion, these properties justify discussion of the Pt(2-thpy)$_2$ chromophore dissolved in the n-octane matrix in a higher point group, namely in C_{2v} corresponding to a planar arrangement of the ligands.

With respect to the question of symmetry of Pt(2-thpy)$_2$, it is also of interest to compare the energy difference for different geometries of Pt(2-thpy)$_2$. For example, a geometry optimization based on a DFT (density functional theory) method resulted in a distorted ground state structure, in which the ligands are rotated by ≈ 17° with respect to each other [66]. The energy difference of this optimized structure with respect to the flattened C_{2v} structure is only as small as 1.7 kcal/mol [66] (≈ 600 cm^{-1} for one molecule). Obviously, the corresponding *intra*-molecular potential hypersurface is rather shallow. Therefore, *inter*-molecular forces induced by the matrix cage can easily influence the geometry of the doped molecule. This might also happen for Pt(2-thpy)$_2$, since the n-alkane matrices host preferably planar molecules[80–86, 152]. Thus, the energy required for flattening Pt(2-thpy)$_2$ might well be available in the course of the crystallizing process.

Under the assumption of a C_{2v} parent group for Pt(2-thpy)$_2$, it seems to be reasonable to assign substate **I** to the $\mathbf{A_2}$ and the ground state to the $\mathbf{A_1}$ representation in the C_{2v} double group which includes orbital and spin symmetries. The $\mathbf{A_2}$ assignment is given, because this is the only representation for which a transition to the electronic ground state is electric dipole-forbidden and hence strongly sensitive to symmetry breaking processes. With the additional spin-forbiddenness for the triplet-singlet transition, one can understand, why the transition probability of the **I** ↔ **0** transition is so small.

The ab initio calculations of Ref. [66] lead to an assignment of the lowest triplet (with a calculated transition energy of ≈ 18 200 cm^{-1}) to $^3\mathbf{A_1}$ (in C_{2v}). From this representation it follows under spin-orbit coupling (not included in Ref. [66]) that the triplet splits into the three substates $\mathbf{A_2}$, $\mathbf{B_1}$ and $\mathbf{B_2}$ (e.g. compare Ref. [153]). Thus, if the assignment of Ref. [66] holds, one obtains a sublevel with the symmetry $\mathbf{A_2}$ for state **I**, while the two other triplet substates **II** and **III** have $\mathbf{B_1}$ and $\mathbf{B_2}$ representations, respectively. However, an individual assignment of these two other states is not yet possible. Both transitions between the ground state $\mathbf{A_1}$ and these triplet substates $\mathbf{B_1}$ and $\mathbf{B_2}$ are formally dipole allowed [153].[13] Indeed, the experiment shows that both substates **II** and **III** can directly be excited from the ground state (Figs. 15 and 16c). Moreover, the room temperature absorption spectrum (Fig. 12) indicates that the corresponding origins together exhibit an absorption coefficient of ≈ 90 l/mol cm. Thus, the transitions to the two triplet substates **II** and **III** are considerably more allowed than in organic compounds. Obviously, the triplet sublevels **II** and **III** of Pt(2-thpy)$_2$ are first-order spin-orbit coupled to higher lying singlets with the same symmetries of $\mathbf{B_1}(^1\mathbf{B_1})$ and $\mathbf{B_2}(^1\mathbf{B_2})$ representations, respectively.[14] This mixing weakens the spin-selection rules.

It is expected that the considerations discussed in relation to a planar C_{2v} symmetry remain at least approximately valid for a slightly distorted geometry.

---

[13] According to the restricted accuracy of the CASPT2 calculations [66], it is not excluded that the substates of a different triplet term, namely of $^3\mathbf{B_2}$, can become the lowest ones under inclusion of spin-orbit coupling. $^3\mathbf{B_2}$ would lead to $\mathbf{A_1}$, $\mathbf{A_2}$, and $\mathbf{B_1}$ substate symmetries in C_{2v}. In this case, transitions between the ground state $\mathbf{A_1}$ and the sublevels of symmetries $\mathbf{A_1}$ and $\mathbf{B_1}$ are formally dipole allowed. With this alternative assignment one would also expect to have two allowed transitions and one forbidden transition.

[14] The spin-orbit coupling operator is totally symmetric.

4.2.2
Vibronic Coupling and False Origins – Background

The vibrational satellite structures that occur in the emission and excitation spectra (e.g. see Figs. 13 to 15) result from different vibrational activities, namely from vibronic or Herzberg-Teller activity, as introduced in this section, and from Franck-Condon activity, as discussed in the next section.

Vibronic coupling provides very important radiative deactivation paths, when the purely electronic transition between an excited state and the ground state is strongly forbidden. This is the case, for example, for the transition between the lowest triplet sublevel **I** of Pt(2-thpy)$_2$ and the ground state **0**. Still, one observes an intense emission which, however, is only found in the vibrational satellites.

Since it is indicated that the transition at the electronic origin is spin *and* symmetry forbidden (Sect. 4.2.1.1), one has to consider mechanisms that provide singlet character with the adequate symmetry to state **I**.[15] Such mechanisms which induce intensities to the vibrational satellites but not to the electronic origin are well known as vibronic or Herzberg-Teller coupling mechanisms. The theoretical background is comprehensively discussed in the literature [124–129]. Here, only a short discussion of mechanisms that can provide the required coupling routes is given. These routes are schematically illustrated in Fig. 17.

a) *Spin-vibronic coupling* yields a mixing of wavefunctions of two electronic states by a vibration-induced change of spin-orbit coupling (soc). For organic compounds this mechanism is often neglected due to the small value of the soc constant. In contrast, for compounds of the platinum metal group, this mechanism can be very important. Specifically, vibrations of the central metal ion – that are connected with variations of electron density of nd-character in the spatial region of the organic ligands – can induce significant changes in the effective soc, in particular for ^{3}LC-$^3\pi\pi^*$ states. Good candidates for such vibrations are metal-ligand vibrations. Such a coupling route is schematically sketched in Fig. 17a. $\hat{H}_{so}$ is the soc Hamiltonian, **I** represents the unperturbed lowest triplet sublevel, $\mathbf{S_m}$ is a higher lying (unperturbed) singlet. The matrix element given in Fig. 17a signifies that the vibration with the normal coordinate Q modulates the spin-orbit coupling operator. This mechanism induces intensity to the specific vibrational satellite with the energy $\bar{\nu}_Q$. Obviously, this vibronic mechanism can be effective for a large number of different vibrational modes Q and thus usually involves different intensity-providing higher lying singlets.

b) *Vibronic coupling and spin-orbit coupling* as a two-step mechanism can also be responsible for the occurrence of vibrational satellites. This specific, combined mechanism is proposed, since it is not expected that internal ligand vibrations, such as high-energy fundamentals in the energy range of the

---

[15] The model discussed here is not only valid for Pt(2-thpy)$_2$. However, we apply in this more general section a nomenclature which refers to the triplet sublevels of Pt(2-thpy)$_2$ to allow a more easy reading. The direct application to Pt(2-thpy)$_2$ is presented in Sect. 4.2.4.

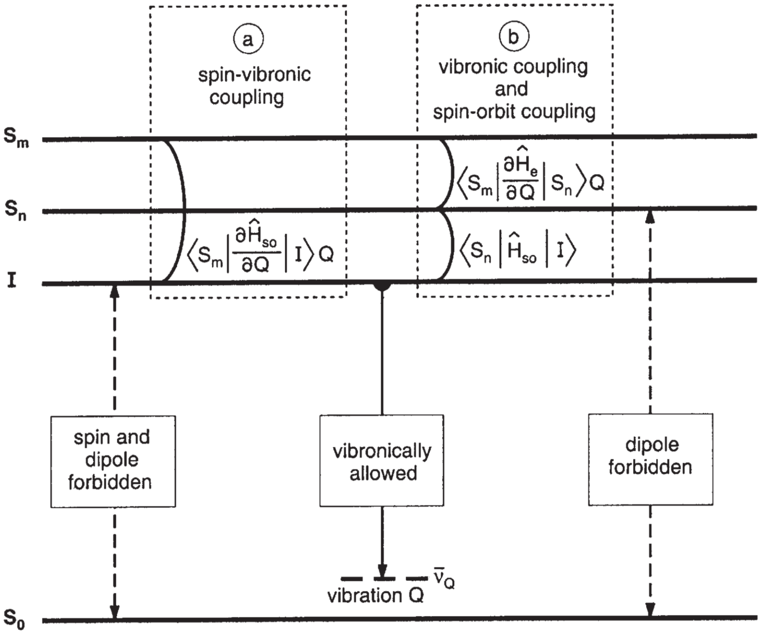

Fig. 17. Vibronic coupling mechanisms (Herzberg-Teller couplings). The purely electronic transition between the excited state **I** (triplet substate) and the ground state **0** (S_0) is spin and symmetry forbidden, i.e. no intensity is found at the electronic origin I. Two mechanism are proposed. Coupling route (*a*) is probably more important for vibrations of metal-ligand character, while mechanism (*b*) preferentially induces satellite intensities by internal ligand vibrations. The electronic state $\mathbf{S_n}$ is a singlet, for which an electronic transition is dipole forbidden to the electronic ground state $\mathbf{S_0}$. On the other hand, the state $\mathbf{S_m}$ represents a singlet that carries sufficient transition probability. For detailed explanations see the text

order of 10^3 cm^{-1} will induce an efficient variation of spin-orbit coupling, since the metal is almost not involved in these vibrations due to its large mass. Therefore, mechanism (a) would not explain the occurrence of the high energy satellites. However, the two-step mechanism (b) according to Fig. 17b can give an explanation. In a first step, direct spin-orbit coupling provides singlet character from state $\mathbf{S_n}$ to the lowest triplet substate **I**. Since the spin-orbit coupling Hamiltonian $\hat{H}_{so}$ is totally symmetric, the admixed wavefunction of state $\mathbf{S_n}$ has the same symmetry as state **I**. Therefore, this mixing route lifts only the spin forbiddenness of the transition from state **I** to the ground state **0** but not the symmetry restriction. Consequently, a radiative deactivation of state **I** is still dipole forbidden in this approximation. However, if in a second step it is taken into account that the state $\mathbf{S_n}$ is also vibronically perturbed according to usual vibronic coupling, the required symmetry character can be obtained. (Fig. 17b) In this mechanism a vibration-induced variation of the electronic Hamiltonian $\hat{H}_e$ provides a mixing with a further state $\mathbf{S_m}$, for which the electronic transition is sufficiently dipole allowed. In conclusion, the combination of both steps of the mixing route sketched in Fig. 17b is required to provide intensity to the vibrational satellites. Also these mechanisms can be induced by a number of different vibrations Q and different admixing singlet states of the type $\mathbf{S_m}$.

The coupling routes (a) and (b) discussed above are illustrated in Sect. 4.2.4.2 also on the basis of grouptheoretical selection rules in the scope of the C_{2v} point group symmetry.

4.2.3
Franck-Condon Activity – Background

In a situation, when the purely electronic transition between an excited state and the ground state is allowed or not totally forbidden, a different vibrational activity, the Franck-Condon activity, can become dominant. This can lead, for example, to the occurrence of progressions. Although, the Franck-Condon effect is well known, it is appropriate to summarize briefly the background and to introduce the useful Huang-Rhys parameter. This summary is largely based on the descriptions found in the Refs. [96–100, 154], in particular it is referred to Ref. [99, p. 200].

Figure 18a depicts the harmonic potentials for a model system with one normal coordinate Q (vibrational coordinate) in the electronic ground state **0** and the excited state **II.**[16] It is assumed that the potentials are (nearly) equal, but are shifted by ΔQ with respect to each other, i.e. the vibrational frequencies of both states are also (nearly) equal. Generally, the wavefunctions of electronic-vibrational states depend on both, the coordinates of the electrons and nuclei, and thus the wavefunctions are very difficult to handle. However, when it is taken into account that the electronic motion is much faster than the vibrational motion, one can factorize the vibrational and the electronic part of the wavefunction. This leads to the Born-Oppenheimer approximation with the

$$\begin{aligned}&\text{ground state: } \psi_0(\mathrm{v}) = \phi_0 \cdot \chi_0(\mathrm{v})\\&\text{and the excited state } \psi_{\mathrm{II}}(\mathrm{v}') = \phi_{\mathrm{II}} \cdot \chi_{\mathrm{II}} \cdot (\mathrm{v}')\end{aligned} \tag{5}$$

wherein ϕ_0 and ϕ_{II} are the electronic wavefunctions and $\chi_0(\mathrm{v})$ and $\chi_{\mathrm{II}}(\mathrm{v}')$ are harmonic oscillator functions with vibrational quantum numbers v and v′ for the electronic ground state **0** and the excited state **II**, respectively. The harmonic oscillator functions are similar sets of wavefunctions, and they are defined with respect to different zero-positions of the variable Q.

The intensity of a transition between the excited electronic state **II** and the ground state **0** is essentially given by

$$\mathrm{I}_{\mathrm{II},0}(\mathrm{v}',\mathrm{v}) \sim |\langle\psi_{\mathrm{II}}(\mathrm{v}')|\hat{\mu}|\psi_0(\mathrm{v})\rangle|^2 \tag{6}$$

where $\hat{\mu}$ is the usual electronic dipole operator. By inserting the Born-Oppenheimer wavefunction (Eq. (5)), one obtains for the low-temperature emission

---

[16] In Sect. 4.2.4, it will be shown that this state may be identified with the triplet substates **II** and **III**, respectively, of Pt(2-thpy)$_2$.

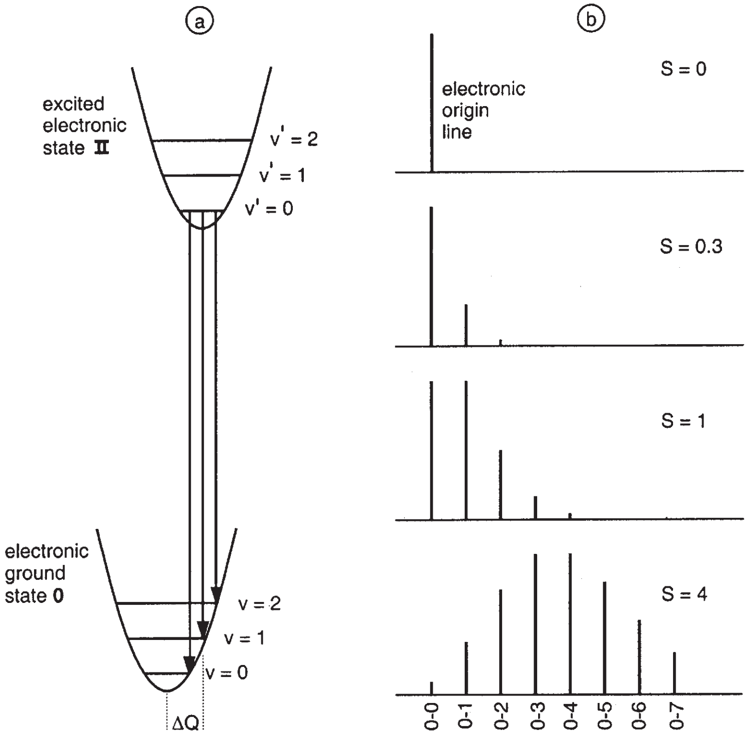

Fig. 18. Franck-Condon progressions. (**a**) The equilibrium positions of the potential surfaces of the excited state **II** and the ground state **0** are shifted by ΔQ. This leads to a progression, if the dipole moment of the transition between the states **II** and **0** is non-zero. The progression is characterized by vertical transitions that are depicted for a low-temperature emission. (**b**) The intensity distribution of a progression of vibrational satellites depends on the Huang-Rhys parameter S which is proportional to $(\Delta Q)^2$ (see Eq. (12)). The examples given in (b) are calculated according to Eq. (13). The peaks of highest intensity are normalized for the different diagrams. It is marked that the maximum Huang-Rhys parameter for $Pd(2\text{-thpy})_2$ and $Pt(2\text{-thpy})_2$ have been determined to ≈ 0.3 and ≈ 0.08, respectively. (Compare also Sect. 4.2.4)

intensity of a transition from the zero-point vibrational level (v′ = 0) to a level v of the electronic ground state (Fig. 18a)

$$I_{II,0}(v' = 0, v) \sim |\langle \phi_{II} | \hat{\mu} | \phi_0 \rangle|^2 \cdot |\langle \chi_{II}(v' = 0) | \chi_0(v) \rangle|^2 \tag{7}$$

The first term of the right hand side of Eq. (7) represents the squared electronic dipole matrix element and specifies the intensity of the purely electronic transition. The second term is the Franck-Condon factor, that is discussed below in more detail. It leads to the well-known Franck-Condon progression of vibrational satellites that progress in the spectrum by the energy $\bar{\nu}_Q$ of the normal mode under consideration.

The total emission intensity I_{tot} is obtained by summing up all possible transitions from the v′ = 0 level to the different vibrational states v

$$\mathrm{I_{tot}} = \sum_{\mathrm{v}} \mathrm{I_{II,0}}\,(\mathrm{v}' = 0, \mathrm{v}) \sim |\langle \phi_{\mathrm{II}} | \hat{\mu} | \phi_0 \rangle|^2 \cdot \sum_{\mathrm{v}} |\langle \chi_{\mathrm{II}}(\mathrm{v}' = 0) | \chi_0(\mathrm{v}) \rangle|^2 \tag{8}$$

Since the vibrational state $\chi_{\mathrm{II}}(\mathrm{v}' = 0)$ is normalized, it applies [99]

$$\sum_{\mathrm{v}} |\langle \chi_{\mathrm{II}}(\mathrm{v}' = 0) | \chi_0(\mathrm{v}) \rangle|^2 = 1 \tag{9}$$

and one obtains for the total radiative intensity for the transition between the states **0** and **II**.

$$\mathrm{I_{tot}} \sim |\langle \phi_{\mathrm{II}} | \hat{\mu} | \phi_0 \rangle|^2 \tag{10}$$

This means that the total emission intensity $\mathrm{I_{tot}}$ depends only on the purely electronic transition dipole moment. Thus, the electronic allowedness represents the source of intensity which is distributed according to the Franck-Condon factor to the different vibrational satellites. With respect to the symmetry of the Franck-Condon active vibrations, it is remarked that this factor can only be nonzero for totally symmetric modes (if it is referred to fundamentals), since the vibrational ground state $\chi_{\mathrm{II}}(\mathrm{v}' = 0)$ is totally symmetric (e.g. see [154, p. 113]).

The Franck-Condon factor is given by the squared overlap integral of displaced harmonic oscillator functions (Hermite functions). It can be related [154, p. 113] to the so-called Huang-Rhys parameter (or factor) S according to

$$|\langle \chi_{\mathrm{II}}(\mathrm{v}' = 0) | \chi_0(\mathrm{v}) \rangle|^2 = \frac{e^{-S} S^{\mathrm{v}}}{\mathrm{v}!} \tag{11}$$

This Huang-Rhys parameter is directly connected with the shift ΔQ of the equilibrium positions of the involved electronic states. (Fig. 18a) According to the Refs. [96] and [154, p. 112], for example, one obtains

$$S = \frac{\pi c M \bar{\nu}_Q}{\hbar} (\Delta Q)^2 \tag{12}$$

wherein c is the velocity of light and M is the effective mass (= reduced mass) of the vibration Q. The value of M is usually not known, unless a normal coordinate analysis is available.

From relation (11) and by use of Eqs. (7) and (10), one can derive interesting and easily applicable expressions, which are very useful for characterizations of properties of an excited state as compared to the ground state. For the intensity ratio of successive vibrational satellites of a Franck-Condon progression one finds from Eq. (11), using the abbreviation $\mathrm{I_v} = \mathrm{I_{II,0}}\,(\mathrm{v}' = 0, \mathrm{v})$ for $\mathrm{v} \neq 0$:

$$\frac{\mathrm{I_v}}{\mathrm{I_{v-1}}} = \frac{S}{\mathrm{v}} \tag{13}$$

This relation has already been applied to determine the maximum Huang-Rhys parameter for the $\mathbf{T_1} \rightarrow \mathbf{S_0}$ transition of $\mathrm{Pd(2\text{-}thpy)_2}$ (see Eq. (1)).

Further, one obtains the result that the intensity at the electronic origin (0–0 transition) I_0 is given by

$$I_0 = I_{tot} \cdot e^{-S} \tag{14}$$

As a consequence of the above equations it is seen that for $S = 0$, the total intensity I_{tot} is contained in the electronic origin line (Eq. (14)) and the displacement ΔQ between the two electronic states is zero (Eq. (12)). With increase of ΔQ and thus also of S, the intensity of the electronic origin line decreases and the vibrational satellites of the Franck-Condon progression grow in (Eq. (13)). The behavior is illustrated in Fig. 18b for several different values of the Huang-Rhys parameter S. Thus the satellites gain intensity only by borrowing it from the electronic origin line. If the electronic transition is forbidden, Franck-Condon satellites also do not occur. This situation is found, for example, for the **0** ↔ **I** transition of $Pt(2\text{-thpy})_2$ (see Sects. 4.2.1 and 4.2.4.).

The S value represents a characteristic parameter, in particular, when different compounds are compared. Thus, it is possible to characterize changes of the binding situation that occur between excited electronic states and ground states for different types of electronic transitions. For example, for the $\mathbf{T_1} \rightarrow \mathbf{S_0}$ transitions of $Pd(2\text{-thpy})_2$ and of $Pt(2\text{-thpy})_2$ one finds maximal Huang-Rhys parameters of ≈ 0.3 and ≈ 0.08, respectively (see Sects. 3.1.2.3, 4.2.4.3, and 4.2.5). From this result it follows that the geometry changes between ground and excited states are significantly smaller in $Pt(2\text{-thpy})_2$ than in $Pd(2\text{-thpy})_2$. This difference is ascribed to the larger MLCT admixtures in $Pt(2\text{-thpy})_2$ by which the spatial extensions of the electronic wavefunctions are enlarged. Due to this effect, the excitation leads to a smaller charge density change per ligand and thus has less influence on the specific binding properties in $Pt(2\text{-thpy})_2$ than in $Pd(2\text{-thpy})_2$ [18].

A similar trend of decreasing changes of equilibrium positions due to an excitation is also found for the lowest singlet-triplet transitions in the series of $[Rh(bpy)_3]^{3+}$, $[Pt(bpy)_2]^{2+}$, $[Ru(bpy)_3]^{2+}$, and $[Os(bpy)_3]^{2+}$complexes. In this series, the metal/MLCT character of the lowest triplet state increases (compare Fig. 1) and one finds maximal Huang-Rhys parameters of ≈ 0.3, ≈ 0.3, ≈ 0.1, and ≈ 0.08, respectively [18, 19, 21, 22]. Further, the decrease of this parameter by a factor of three to four in this series probably also reflects the transition from a localized to a delocalized situation. Specifically, the excited states of compounds with larger S parameters are localized onto one ligand, while the states of those compounds with smaller S parameters are delocalized over two (or three) ligands and the metal. We come back to this interesting problem in Sects. 4.2.10, 4.2.11, and 5 (See also Tables 9 and 10).

4.2.4
Vibrational Satellites and Radiative Deactivation Routes in $Pt(2\text{-thpy})_2$

4.2.4.1
Satellite Structures of the 1.3 K Emission

The emission spectrum of $Pt(2\text{-thpy})_2$ recorded at $T = 1.3$ K exhibits a rich and highly informative vibrational satellite structure (Fig. 13). This structure seems to belong to the electronic origin II at 17,163 cm^{-1}. But the vibrational energies as determined relative to this 0–0 transition do *not* fit to vibrational energies available from IR measurements (Table 7) and they cannot be related to vibrational energies found for Pd(2-thpy)$_2$ (Table 1). On the other hand, setting the origin for these satellites to the position of electronic origin I at 17,156 cm^{-1} which, however, does not carry any intensity, one obtains an excellent correspondence of the satellite energies to those of known vibrational modes (Table 7). This procedure allows us to determine the position of a missing electronic origin line. As discussed in Sect. 4.2.1, the position of this origin I can also be observed directly under application of a magnetic field of $B \geq$ T. (Fig. 16d and Ref. [74]) Interestingly, none of the satellites that are clearly identified in the 1.3 K time-integrated emission spectrum belongs to the electronic origin II at 17,163 cm^{-1}, apart from a 15 cm^{-1} phonon satellite (Fig. 16a) and some spectral background.[17]

Similarly, as has been discussed for Pd(2-thpy)$_2$, the vibrational satellites that correspond to fundamentals can be ascribed to three different groups. Modes which occur up to ≈ 100 cm^{-1} relative to an electronic origin have significant lattice or chromophore-cage mode character. It should even be taken into account that a mixing of chromophore vibrations with cage modes is still obvious up to ≈ 150 cm^{-1} (compare Sect. 3.1.6 and Ref. [57]). Overlapping with this energy range and up to 500/600 cm^{-1}, one finds metal-ligand (M-L) vibrations, which can, for example, be identified by a comparison of vibrational energies of Pd(2-thpy)$_2$ to those of Pt(2-thpy)$_2$.(Table 1) Fundamentals with vibrational energies higher than ≈ 600 cm^{-1} represent internal ligand modes.

The structure of the 1.3 K emission of Pt(2-thpy)$_2$ (Fig. 13) is characterized by the absence of an electronic origin I, but by an occurrence of intense vibrational satellites. Since (1) the satellites do not show any pronounced progression and since (2) the electronic origin does not carry any intensity, it can be concluded that the satellites do not result from Franck-Condon activity. (Compare Sect. 4.2.3.) All satellites that correspond to fundamentals are vibronically (Herzberg-Teller) induced. They all represent false origins. According to Sect. 4.2.2, at least two different mechanisms should be considered that can provide intensity to vibrational satellites, which occur when the purely electronic transition is spin- and symmetry-forbidden. For the low-energy vibrations below ≈ 500 cm^{-1}, which exhibit pronounced metal-ligand character (e.g. the 266, 295, 376 cm^{-1} modes, Tables 1 and 7), it is very probable that the vibrating platinum ion can induce a spin-vibronic coupling (Fig. 17a). This process, however, does not seem to be of importance for high-energy fundamentals such as the 1023, 1138, 1293, 1393, 1462 cm^{-1} modes (Fig. 13 and Table 7). The effective intensity mechanism for these satellites is rationalized by a two-step coupling scheme that involves the usual vibronic coupling combined with first order spin-orbit coupling (Fig. 17b).

---

[17] In Sect. 4.2.7 it will be shown that the emission of the background decays also at $T = 1.3$ K biexponentially with time constants of 600 ns and 110 μs. This is due to the fact that both states **I** and **II** are not in a fast thermal equilibrium. By time-resolved emission spectroscopy one can separate the super-imposed emissions of the two states. Details are discussed in Sect. 4.2.8.

Table 7. Electronic origins and vibrational satellites[a,b] [cm^{-1}] in emission and excitation of Pt(2-thpy)_2 in n-octane compared to vibrational energies of Pd(2-thpy)_2 in n-octane[c] (accuracy: ± 1.5 cm^{-1}). For Pt(2-thpy)_2 also IR data[d)] are given. (Compare Ref. [59])

Pt(2-thpy)_2				Pd(2-thpy)_2		Pt(2-thpy)_2
1 Emission	2 Emission	3 Excitation	4 IR	5 Emission	6 Excitation	7 Assignments
electronic origin I: 17156 cm^{-1}	electronic origins II: 17163 cm^{-1} III: 17172 cm^{-1}			electronic origins I, II, III: 18418 cm^{-1}		
$T = 1.3$ K	$T = 20$ K		$T = 4.2$ K	$T = 298$ K		$T = 1.3$ K
15 w	15 m	14 m				lattice mode[e]
	62 w	59 w				lattice mode[e]
	81 w	≈ 82 w				
112 w						
				111 w	107 w	
120 w						
				124 w		
131 w						
	147 w			150 m	148 m	
152 w						M-L[f], HT[g]
				167 w		
179 w						HT
184 w				178 w		HT
	190 m	194 m	192 m			
				196 w		
				211 m	208 m	
213 s			212 w			HT
	226 w					
		234 w				
				229 w		HT
237 m			235 m			HT
266 vs			271 m	261 w		M-L, HT
	268 w					
		277 w				
				284 m		
295 m			290 m	292 m	290 m	M-L, HT
	302 w	293 w				
376 s				364 s		M-L, HT
	383 m	384 s		376 s	382 s	M-L, FC[g,h]
		409 w			405 m	
423 s			418 s	416 w	415 m	HT
	433 w		431 w	424 w	427 w	M-L
457 s				451 w		HT
	458 m	458 s	459 m	447 s	446 s	M-L, FC[h]
531 vs			528 m	528 m		L[i], HT
		603 m				
626 m	625 w	612 m	625 s	616 w	616 w	
631 s			630 s	625 s		HT
646 m			644 w	643 m		HT

Table 7. *(Continued)*

Pt(2-thpy)$_2$				Pd(2-thpy)$_2$		Pt(2-thpy)$_2$
1 Emission	2 Emission	3 Excitation	4 IR	5 Emission	6 Excitation	7 Assignments
electronic origin I: 17156 cm^{-1}	electronic origins II: 17163 cm^{-1} III: 17172 cm^{-1}			electronic origins I, II, III: 18418 cm^{-1}		
$T = 1.3$ K	$T = 20$ K		$T = 4.2$ K	$T = 298$ K		$T = 1.3$ K
	653 m	650 s		650 s		FC^h
713 vs			711 w	710 s		HT
	718 s	708 vs	718 vs	716 vs	695 s	FC^h
		774 w				
883 m			879 w	874 w		HT
		953 w				
	985 w	971 w	988 s			
	993 m			989 s		
1023 m			1020 w	1021 w		HT
	1030 w	1026 m	1026 w	1025 m	1017 w	
1112 m			1117 w			HT
	1123 w	1122 s				
1138 m			1133 w			HT
1155 w			1155 s	1153 w		HT
	1157 w	1143 w			1150 w	
	1168 w					
		1201 w				
		1212 m			1206 s	
1270 m						HT
	1282 w		1282 m	1275 m	1276 m	
1293 s			1289 w	1286 w		HT
1393 s				1392 m		HT
	1400 m	1390 m	1398 m	1398 s	1397 w	FC
1462 s			1459 m	1461 w		HT
	1468 w			1468 w		
1484 s	1484 s	1487 s	1481 vs	1488 vs	1485 s	FC^h + HT

[a] vs: very strong, s: strong, m: medium, w: weak.

[b] Combinations (e.g. (718 + 1484) cm^{-1}) and overtones (e.g. 2 × 718 cm^{-1}) are not given here, but see Figs. 13 and 14.

[c] See Ref. [56] and Table 1.

[d] Accuracy: ± 4 cm^{-1}.

[e] Only the phonon satellites of the origins are given. Presumably, the intensity of the 15 cm^{-1} phonon satellite of the origin I is HT induced. The spectrum reproduced in Figure 13 shows that many vibrational satellites are also accompanied of phonon satellites.

[f] The vibrational modes between ≈ 150 cm^{-1} and ≈ 500 cm^{-1} can exhibit a significant metal-ligand (M-L) character.

[g] Characterization of the radiative deactivation processes. HT: Herzberg-Teller active vibrational mode; FC: Franck-Condon active mode.

[h] Second member of a progression is observed.

[i] Vibrational satellites above ≈ 500 cm^{-1} are assigned to ligand (L) modes.

4.2.4.2
Grouptheoretical Coupling Routes

It is useful to illustrate the discussed mechanisms also on the basis of grouptheoretical examples. According to the discussion in Sect. 4.2.1.1, it is indicated that state **I** can be assigned to an $\mathbf{A_2}$ representation in the C_{2v} (parent) point group (double group). Vibronic intensity due to spin-vibronic coupling is only possible, if the matrix element in Fig. 17a does not vanish. This is only fulfilled, if the corresponding grouptheoretical product contains the totally symmetric representation A_1. Due to the fact that the symmetry of $\partial\hat{H}_{SO}/\partial E$ is the same as that of the vibrational mode with the normal coordinate Q, one finds by use of grouptheory [153] that vibrational modes of a_2, b_1, and b_2 symmetry can induce a spin-vibronic coupling to $\mathbf{A_1}$, $\mathbf{B_2}$, and $\mathbf{B_1}$ singlet states, respectively. These processes can provide intensity to the corresponding vibrational satellites. Since a normal coordinate analysis is not yet available for Pt(2-thpy)$_2$, the satellites that are found in the 1.3 K emission spectrum have not yet been assigned grouptheoretically.

The two-step mechanism shown in Fig. 17b gives the same grouptheoretical coupling routes as mechanism (a). This is interpreted as follows. Direct spin-orbit coupling of a triplet sublevel of A_2 symmetry with a singlet is only possible, if this singlet has the same representation. But this coupling will not provide any intensity to the triplet sublevel, since the $\mathbf{A_2} \leftrightarrow \mathbf{A_1}$ transition is dipole forbidden in the C_{2v} point group. However, when it is taken into account that this singlet $\mathbf{A_2}$ state is vibronically coupled to other $\mathbf{A_1}$, $\mathbf{B_1}$, and $\mathbf{B_2}$ singlet states by vibrational modes of a_2, b_2 and b_1 character, respectively, one obtains mechanisms that can provide intensity to the vibrational satellites. Again, the intensities of the false origins are borrowed from these singlet states of A_1, B_1, and B_2 symmetries.

In summary, all fundamentals that are observed as satellites in the 1.3 K emission spectrum of Pt(2-thpy)$_2$ (Fig. 13, Table 7) represent false origins, i.e. they are vibronically induced (Herzberg-Teller, HT induced). Two mechanisms are proposed, which both lead to the same grouptheoretical results for the symmetries of the Herzberg-Teller active modes. However, the coupling routes are different. The spin-vibronic coupling (mechanism (a) in Fig. 17a) seems to be important for low-energy metal-ligand vibrations, while the Herzberg-Teller activity of the high-energy internal ligand modes requires combined coupling mechanisms as sketched in Fig. 17b. Those modes that are identified as false origins are characterized by HT in Table 7.

The low-temperature emission spectrum (Fig. 13) shows besides the false origins (e.g. fundamentals of 213, 266, 376, 531, 713, 1293, 1462 cm^{-1}, etc., compare Table 7) also combinations, i.e. other fundamentals are built upon these false origins (e.g. (531 + 383), (531 + 718), (531 + 1168), (713 + 718), (713 + 1400) cm^{-1}, etc.). These other vibrational modes are assigned below to totally symmetric Franck-Condon (FC) modes.

4.2.4.3
Satellite Structure of the 20 K Emission

With temperature increase, for example to $T = 20$ K, the electronic origins II and III at 17,163 $\mathrm{cm^{-1}}$ and 17,172 $\mathrm{cm^{-1}}$ grow strongly in. This is attributed to the thermal population of these two higher lying states. Also, the vibrational satellite structure changes. Vibrational satellites that correspond to fundamentals different from those found in the 1.3 K emission spectrum, grow in. Thus, the spectrum changes drastically (Compare Fig. 14 to Fig. 13). Moreover, satellites that dominate at $T = 1.3$ K , such as the 531 $\mathrm{cm^{-1}}$ satellite, become relatively weak at higher temperature. Further, in the 20 K emission spectrum, the electronic origin lines II and III are the dominant peaks. This is due to the fact that, in contrast to the situation of origin I, they carry significant allowedness. This is evidenced, for example, by the possibility to excite these states directly (Figs. 15 and 16, compare also Sect. 4.2.1.).

The vibrational satellites in the 20 K emission spectrum are observed as vibrational doublets, which exhibit the same energy separation of 9 $\mathrm{cm^{-1}}$ as the two electronic origins II and III. Thus, the same vibrational mode is active in the radiative process of both electronic states **II** and **III**. In Fig. 14, only satellites of origin II (at 17,163 $\mathrm{cm^{-1}}$) are specified.

The 20 K emission spectrum shown in Fig. 14 exhibits vibrational satellites due to activity of fundamentals (e.g. 190, 383, 458, 718, 1400, 1484 $\mathrm{cm^{-1}}$, etc.), of combinations of these fundamentals (e.g. (190 + 1484), (383 + 1400), (458 + 1484), (718 + 1400), (718 + 1484) $\mathrm{cm^{-1}}$, etc.), and for the most intense satellites, one observes also the second members of progressions (e.g. 1×718 $\mathrm{cm^{-1}}$, 2×718 $\mathrm{cm^{-1}}$; 1×1484 $\mathrm{cm^{-1}}$, 2×1484 $\mathrm{cm^{-1}}$). These results can be rationalized well, when all vibrational satellites with significant intensity are assigned to correspond to totally symmetric fundamentals. This assignment is also in accordance with the observation that the same fundamentals are built upon the false origins occurring in the 1.3 K emission spectrum. (Fig. 13) An assignment to an alternative symmetry would not allow us to explain the very distinct differences of vibrational activities found in the emission of the states **I** and **II**, respectively.

Moreover, these totally symmetric fundamentals are assigned to be Franck-Condon active (compare Sect. 4.2.3.) and indeed, for the most intense satellites one finds also weak overtone satellites. By use of Eq. (13) and of the satellite intensities as determined from the emission spectrum of Fig. 14, one can calculate the corresponding Huang-Rhys parameters S. For the most "distinct" progressions of the 718 and the 1484 $\mathrm{cm^{-1}}$ modes one obtains the same very small value of $S \approx 0.08$. The occurrence of other progressions, namely of the fundamentals of 383, 458, and 653 $\mathrm{cm^{-1}}$ is also indicated. (Fig. 14 and Table 7) However, one does not observe progressions for every totally symmetric fundamental. These might exhibit still smaller S parameters, but even for a similar Huang-Rhys parameter of $S \approx 0.08$ most of the corresponding overtone satellites would be hidden in the noise of the spectrum.

4.2.4.4
Vibrational Ligand-Ligand Coupling

One of the fundamentals, the 1484 cm^{-1} mode, exhibits a specific behavior, since it seems to be Herzberg-Teller as well as Franck-Condon active. The corresponding satellite occurs as false origin in the emission of state **I** (Fig. 13) and as a progression forming mode in the spectrum of state **II** (and **III**).(Fig. 14) A totally symmetric mode can lead to a progression, but would not provide any vibronic allowedness to an $\mathbf{A}_2$ state in C_{2v} symmetry. In Ref. [59], it was proposed that this behavior might be taken as an indication of a symmetry deviation from C_{2v}. However, such a deviation should also provide some intensity to the origin line I which, however, is absent.(Fig. 16a) An alternative explanation might be that two different vibrations, a totally symmetric one and a non-totally symmetric one, are – within a spectral resolution of 1 to 2 cm^{-1} – not distinguishable. These two modes could be interpreted as symmetric and antisymmetric combinations (plus and minus combinations) of vibrations of the two ligands of Pt(2-thpy)$_2$. Possibly, a similar interpretation holds also for other fundamentals. One further example might be given by the totally symmetric 718 cm^{-1} and the non-totally symmetric 713 cm^{-1} mode. In this latter situation, the vibrational coupling between the two ligands would be distinctly larger than for the 1484 cm^{-1} ligand vibrations.

In conclusion, the occurrence of the relatively strong electronic origins II and III combined with Franck-Condon progressions indicates that direct first-order spin-orbit coupling is effective by admixing singlet character to the states **II** and **III**. Further, due to the facts that the progressions built upon the false origins that are found in the emission of state **I** as well as on the origins II and III are extremely weak in all cases (Huang-Rhys factors of ≈ 0.08), it is concluded that the three electronic states **I**, **II**, and **III** exhibit only very small shifts of the equilibrium positions of the potential hypersurfaces relative to the ones of the electronic ground state **0**. (See Eq. (12).) Those fundamentals, which are identified as members of Franck-Condon progressions (detection of overtones) are characterized by FC in Table 7 (column 7).

For completeness, it is also mentioned that pressure-induced shifts of several vibrational satellites have been determined. These measurements were carried out at $T \approx 5$ K and one could monitor the more intense vibrational satellites that correspond to Franck-Condon active modes up to $p \approx 14$ kbar for Pt(2-thpy)$_2$ dissolved in n-decane. In this matrix, some of the vibrational modes are found at slightly different energies. Here, we only want to give the values of pressure-induced shifts (blue shifts) that have been observed (error: $\pm$ 0.1 cm^{-1}/kbar): 383 cm^{-1} (shift: $\Delta\bar{\nu}/\Delta p = +\ 0.85$ cm^{-1}/kbar), 457 cm^{-1} ($\pm$ 0.0), 718 cm^{-1} (+ 0.25), 1400 cm^{-1} (+ 0.6), and 1489 cm^{-1} (+ 0.75) [63]. (With respect to further investigations under high pressure application compare the recent review by K. Bray [150].)

4.2.5
Vibrational Energies of the Excited T_1 State

Figure 15 shows the excitation spectrum in the region of the lowest triplet of $Pt(2\text{-thpy})_2$ in n-octane at $T = 4.2$ K. The spectrum is monitored on a vibrational satellite (718 cm^{-1}) of origin II ($\bar{\nu}_{det} = 16{,}445$ cm^{-1}). The energy range of the electronic origins is also reproduced in Fig. 16c in an enlarged scale. The transitions **0** → **II, III** are clearly detectable, while the **0** → **I** transition is not observable in the excitation spectrum. This is a consequence of the extremely low probability of this transition. The spectrum is dominated by the origins II and III and a large number of associated vibrational satellites. Since one observes a "doublet" structure for nearly every satellite (Fig. 15), it is concluded that almost the same vibrational modes are active in both electronic transition. Thus, one can restrict the discussion to the vibrational energies of just one of the substates, for example, to substate **II**.

It is of interest to correlate the vibrational energies of these electronically excited states to the vibrational energies of the ground state **0**. This correlation will mainly be based on a comparison of the intensity distribution in the emission spectrum (Fig. 13) to the one in the excitation spectrum (Fig. 15). Although, this does not always provide an unequivocal assignment, several correlations are still possible. For example, the dominating ground state mode observed in emission at 718 cm^{-1} corresponds to the dominating 708 cm^{-1} mode of the excited state **II** (and **III**). A series of further correlations is summarized in Table 7 (compare columns 2 and 3). These correlated modes exhibit relatively similar vibrational energies. This points to relatively similar binding properties in the electronic ground state and in substate **II** as well as in substate **III**.

The excitation spectrum does not show any vibrational satellite that is assignable to substate **I**. In particular, an excitation satellite that might correspond to one of the most intense HT active satellites, the 531 cm^{-1} peak, is completely absent.

Similarly, as outlined in Sect. 4.2.4.3, all more intense vibrational satellites that occur in the excitation spectrum (Fig. 15) are assigned to totally symmetric Franck-Condon active fundamentals. (Compare also Sect. 4.2.3.) For the most intense satellite, corresponding to the 708 cm^{-1} mode, one observes also the second progression member (2×708 cm^{-1}). The same Huang-Rhys parameter of $S \approx 0.08$ is obtained for this progression as is found for the 718 cm^{-1} progression of the ground state mode. S is determined by use of Eq. (13). Again, this result allows us to conclude that the equilibrium positions of the potential hypersurfaces of the states **II** and **III** are very similar to those of the ground state. The same conclusion has already been drawn from the vibrational satellite structure of the emission spectrum (Sect. 4.2.4.3).

For completeness, it should be added that excitation spectra have been recorded up to the energies where the low-lying singlets occur. Namely, the lowest singlet $\mathbf{S}_1$ is found at 20,450 cm^{-1} [74, 95]. In the energy range between the electronic origins of $\mathbf{T}_1$ and of $\mathbf{S}_1$, one observes only vibrational satellites, which belong to the substates of $\mathbf{T}_1$ electronic origin(s). No other purely electronic transitions could be identified in this energy range [74]. In this respect, the experimental results do not correlate to the ab initio calculation of Ref. [66].

4.2.6
Spin Lattice Relaxation – Background

The emission decay properties and the population dynamics of the different triplet sublevels are, at low temperature, very often essentially determined by the times of relaxation between these substates. The relaxation times can be very long, when the energy separations between the substates are of the order of several wavenumbers or less. This behavior is related to the property that the excess energy of a higher triplet sublevel is not easily transferred to the lattice due to the small density of states of lattice vibrations (phonons) in this energy range and due to the requirement of spin-flips for transitions between these substates. As already mentioned in Sect. 3.1.3, this type of relaxation is called *spin-lattice relaxation* (*slr*). Although, it has been known for decades that such slow processes are significant (e.g. see the Refs. [99, 113–121], the almost general importance of these effects also for organometallic compounds has not yet been fully recognized. Three processes are important and govern the relaxation properties between closely lying electronic states, namely the *direct*, the *Orbach*, and the *Raman process* (see Refs. [99, 116–121] and Fig. 19). In the literature, different mechanisms have been discussed which may induce a spin-flip due to an interaction of phonons with the triplet sublevels of the molecule (e.g. see [99, 113–123]). It is important that phonon modes can cause fluctuations of molecular properties, such as intramolecular distances, and thus can modulate electronic charge distributions, spin-orbit coupling, mixing coefficients between different states, etc. However, it is not in the scope of the present investigation to discuss these mechanisms.

The temperature dependence of the rates of spin-lattice relaxation is usually described by considering the three different processes mentioned. They are schematically sketched in Fig. 19. (Compare also Refs. [22, 24, 60, 62, 64, 65].) **I**, **II**, and **III** represent, for example, the three triplet sublevels which are split by several cm^{-1}. It is assumed that one of the higher lying states, for example state **II**, is populated by a relaxation from a still higher lying state or by a resonant excitation of just this electronic state.

In the subsequent sections, these three slr processes are briefly explained.

4.2.6.1
The Direct Process

A relaxation from state **II** to state **I** may occur by an emission of one phonon with the energy $\Delta E_{II,I}$, which is transmitted to the lattice (Fig. 19a).[18] This process is called *the direct process* of spin-lattice relaxation. The corresponding rate $k_{II,I}^{slr}$

---

[18] For higher temperatures, also an absorption of a phonon is important that triggers a back process from state **I** to state **II**. Both up and down processes give rise to the direct process.

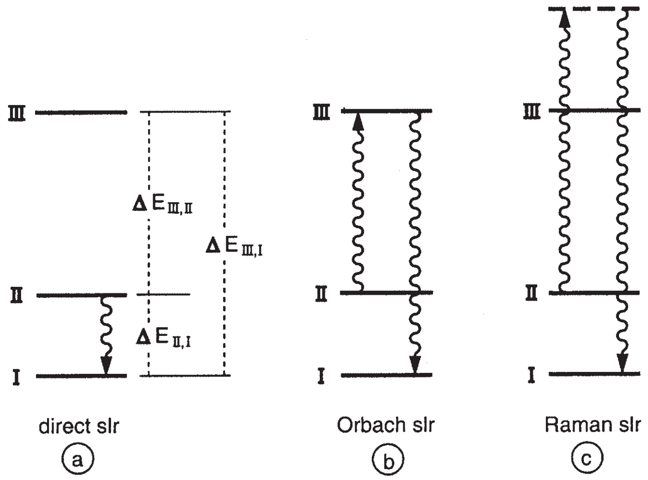

Fig. 19. Schematic diagram to illustrate the different processes of spin-lattice relaxation (slr). The states **I, II,** and **III** represent, for example, triplet substates of organometallic or related compounds. The corresponding zero-field splittings (zfs) lie in the energy range of ≈ 0.1 to about 10^2 cm^{-1}. (Compare also Fig. 1)

(*direct*) dominates rates of other processes of slr at low temperature T and exhibits only a weak temperature dependence. For this rate one obtains (e.g. see the Refs. [99, 116, 118, 24, 64, 65]):

$$k^{slr}_{II,I}\,(direct) = \frac{3}{2\pi\hbar^4\rho \mathrm{v}^5}\cdot|\langle II|V|I\rangle|^2\cdot(\Delta E_{II,I})^3\cdot\coth(\Delta E_{II,I}/2k_BT) \qquad (15)$$

ρ is the mass density of the matrix material, v the (average) velocity of sound of the matrix, and k_B the Boltzmann constant. Thus, the rate is proportional to the square of the matrix element and to the third power of the energy difference $\Delta E_{II,I}$. It is remarked that for T → 0, coth $(\Delta E_{II,I}/2k_BT)$ approaches one.

4.2.6.2
The Orbach Process

At higher temperature, the relaxation may also proceed indirectly by the two-phonon *Orbach process.* (Fig. 19b) Schematically, in this process, one phonon of the energy $\Delta E_{III,II}$ is absorbed, while a second phonon of the energy $\Delta E_{III,I}$ is emitted. (The inverse process has also to be taken into account.) The rate of the *Orbach* process has been determined only recently also for a general pattern of zero-field split states, as one finds often for the compounds of interest here. The corresponding low-temperature approximation, representing an *extended Orbach* approximation, was derived in Refs. [64, 65]. A slightly approximated expression is given by the following equation [24, 65]

$$k_{II,I}^{slr}\,(Orbach) = \frac{C_{III,\,II}C_{III,\,I}\,(e^{\Delta E_{III,\,II}/k_BT} + e^{\Delta E_{III,\,I}/k_BT})}{C_{III,\,I}e^{\Delta E_{III,\,I}/k_BT}\,(e^{\Delta E_{III,\,II}/k_BT} - 1) + C_{III,\,II}e^{\Delta E_{III,\,II}/k_BT}\,(e^{\Delta E_{III,\,I}/k_BT} - 1)} \qquad (16)$$

with the abbreviations

$$C_{III,\,I} = \frac{3}{2\pi\hbar^4\rho\mathrm{v}^5}\cdot|\langle III|V|I\rangle|^2\cdot(\Delta E_{III,\,I})^3$$

$$C_{III,\,II} = \frac{3}{2\pi\hbar^4\rho\mathrm{v}^5}\cdot|\langle III|V|II\rangle|^2\cdot(\Delta E_{III,\,II})^3 \qquad (17)$$

$$C_{II,\,I} = \frac{3}{2\pi\hbar^4\rho\mathrm{v}^5}\cdot|\langle II|V|I\rangle|^2\cdot(\Delta E_{II,\,I})^3$$

The parameters and matrix elements used are defined above or correspond directly to the definitions given. The energy separations are specified in Fig. 19.

From the more general equation (16) one can obtain the original *Orbach expression*, which was derived under the assumption of specific energy differences, namely of $\Delta E_{III,\,I} \approx \Delta E_{III,\,II} = \Delta E$ (compare the Refs. [99, 116, 117, 118, 121]:

$$k_{II,\,I}^{slr}\,(Orbach) \approx \frac{2C_{III,\,II}C_{III,\,I}}{(C_{III,\,I} + C_{III,\,II})}\cdot\frac{1}{e^{\Delta E/k_BT} - 1} \qquad (18)$$

This expression can further be simplified for $exp(\Delta E/k_BT) \gg 1$ or $\Delta E \gg k_BT$. Thus, one obtains

$$k_{II,\,I}^{slr}\,(Orbach) \approx const\cdot(\Delta E)^3\cdot e^{-\Delta E/k_BT} \qquad (19)$$

This simple approximation has – together with the consideration of the *direct process* according to Eq. (15) – successfully been used to fit the temperature dependence of the spin-lattice relaxation rate of $[\mathrm{Ru(bpy)_3}]^{2+}$doped into $[\mathrm{Zn(bpy)_3}](\mathrm{ClO_4})_2$ up to $T \approx 10$ K [22]. However, application of the approximations given in Eqs. (18) and (19) does not lead to a successful fit of the experimental data obtained for $\mathrm{Pt(2\text{-}thpy)_2}$, since the conditions given above concerning the energy differences for these approximations do not hold.

For completeness it is mentioned that the rate according to the *Orbach process* vanishes for $T \rightarrow 0$ K and also for $\Delta E \rightarrow 0$ cm^{-1}.

4.2.6.3
The Raman Process

In addition to the processes given in Fig. 19a and b, a two-phonon *Raman scattering process* can also lead to a relaxation from state **II** to state **I** according to Fig. 19c. The temperature dependence of the corresponding rate is usually approximated by [116, 118, 119, 120]:

$$k_{II,\,I}^{slr}\,(Raman) = R\cdot T^n \qquad (20)$$

with a constant R and $n = 5$ or $n = 7$ for non-Kramers ions [119]. For the compounds studied here, the T^5 dependence fits the experimental observations much better than the T^7 dependence observed for other systems (e.g. see Refs. [109, 116]).

4.2.7

Emission Decay and Rise Dynamics

In section 4.2.1 it has been shown that the $\mathbf{T}_1$ state of Pt(2-thpy)$_2$ splits into three substates separated by 7 cm^{-1} and 9 cm^{-1} with a total zfs of 16 cm^{-1} (Fig. 20). The size of this splitting and the zfs pattern lead to interesting emission decay and rise properties. These reflect an almost general, but not well known dynamical behavior which occurs in many triplet sublevel systems of organometallic or related compounds, though quite differently (e.g. see [19–24, 57, 58, 60–65, 72–75, 155]). Interestingly, the situation found for Pt(2-thpy)$_2$ is more favorable for optical investigations than the one of Pd(2-thpy)$_2$ (see Sects. 3.1.1, 3.1.3, and 3.1.5), because the zfs of Pt(2-thpy)$_2$ is large enough to be well resolved by high-resolution spectroscopy. Combined with time resolution, one can elucidate details of dynamical processes within the triplet sublevel system, in particular, by investigating the individual triplet substates.

4.2.7.1

Emission Decay and Rise Properties for Different Excitation and Detection Energies

Figure 20 shows that the emission decay and rise behavior depends on the excitation and detection energies at low temperature (T = 1.3 K). Such behavior seems to be rather general for compounds with similar zero-field splittings [22, 24, 60, 62, 65] The dynamical properties of Pt(2-thpy)$_2$ are discussed by use of four different examples:

(a) A resonant excitation with a short laser pulse of substate **III** at 17,172 cm^{-1} is followed by relatively fast slr to the two low lying substates **I** and **II**. An emission of state **III** is not observed, but one finds an emission rise of the order of 30 ns when the emission of state **I** is detected selectively, for example at the energy of the 531 cm^{-1} vibrational satellite (compare Fig. 13). The result is shown in inset (a) of Fig. 20. (Compare Refs. [60, 62].) The specific slr rate for the process from substate **III** to state **I** has been determined in Ref. [65] as $k^{slr}_{III,I}$ (T = 1.3 K) ≈ 2×10^7 s^{-1}. After the rise of ≈ 30 ns one observes the usual emission decay of sublevel **I** with τ_{I} = (110 ± 3) µs. According to Sect. 4.2.6, *Orbach* and *Raman processes* are usually unimportant at T = 1.3 K. Thus, the fast slr processes are ascribed to *direct processes*.

(b) Of particular interest is the emission decay of substate **II**. After a pulsed and resonant excitation of the $\mathbf{0} \rightarrow \mathbf{II}$ transition at 17,163 cm^{-1}, one observes a strictly monoexponential decay for more than five lifetimes with a decay constant of (600 ± 10) ns, if the emission is detected selectively, on a vibrational satellite that corresponds to the state **II** emission, for example on the

653 cm^{-1} satellite (see Fig. 14). The corresponding decay rate is $k_{exp} = 1/600$ ns $= 1.67 \times 10^6$ s^{-1}. This decay is mainly determined by the *direct process* of slr from state **II** to state **I** (for a slight correction see the next subsection), since at $T = 1.3$ K, the other two slr processes are again inefficient (Sect. 4.2.6). Later in section 4.2.7.2, we will discuss the rate of slr between these two substates **II** and **I** in detail. (Compare Fig. 20b and Refs. [24, 60, 62, 64, 65])

(c) If the interpretation of a relaxation from sublevel **II** to sublevel **I**, as discussed above, is valid, it should be possible to observe the corresponding rise of the emission of state **I**. This behavior is indeed found as seen in Fig. 20c. For this experiment, the excitation is kept as before (see b)), but the emission is monitored on a vibrational satellite that belongs selectively to the state **I** emission (e.g. the 531 cm^{-1} satellite, see Fig. 13). After the emission rise, sta-

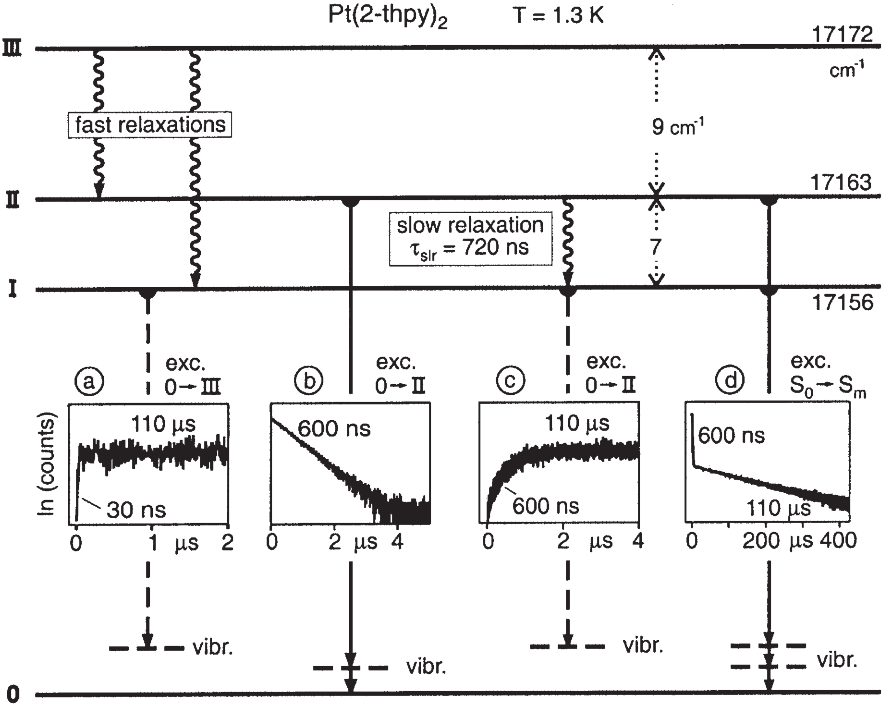

Fig. 20. Triplet substates of Pt(2-thpy)$_2$ and dynamical processes of spin-lattice relaxation at $T = 1.3$ K. Pt(2-thpy)$_2$ is dissolved in n-octane with a concentration of $\approx 10^{-5}$ mol/l. (*a*) Resonant excitation at origin III (17,172 cm^{-1}), detection of the emission from state **I** on the 531 cm^{-1} vibrational satellite at 16 625 cm^{-1}. (*b*) Resonant excitation at the origin II (17,163 cm^{-1}), detection of the emission of state **II** at the 653 cm^{-1} vibrational satellite at 16,510 cm^{-1}. (*c*) Same excitation as in (*b*), but detection of the emission of state **I** at the 531 cm^{-1} satellite at 16,625 cm^{-1}, see (*a*). (*d*) Excitation into a higher lying singlet (e.g. $\lambda_{exc} = 337.1$ nm), detection at 16,444 cm^{-1} with bandwidth of ≈ 5 cm^{-1}. Thus, one monitors the emissions from state **I** on the 713 cm^{-1} vibrational satellite and the emission from state **II** on the 718 cm^{-1} satellite. (Compare the Refs. [60, 62, 65])

te **I** decays with the usual emission decay time of sublevel **I** of τ_I = 110 µs. (Compare Refs. [24, 60, 62].)

(d) Finally, when Pt(2-thpy)$_2$ is excited non-selectively, for example into an excited singlet – which corresponds to the usual experimental situation – one finds the two decay components of 600 ns and 110 µs, since by the relaxation both substates **I** and **II** are populated and both states exhibit their individual emissions. (Compare Fig. 20d and Ref. [65].)

4.2.7.2
Spin-Lattice Relaxation at T = 1.3 K

The experimentally determined emission decay rate k_{exp} of the higher lying triplet sublevel **II** is not only determined by the slr rate k^{slr} but also by the usual radiative and non-radiative decay rates of state **II** to the electronic ground state **0** with $k_{\text{II},0} = 1/\tau_{\text{II}}$. Thus, the slr rate is obtained by [24, 60, 65]

$$k^{\text{slr}} = k_{\text{exp}} - k_{\text{II},0} \tag{21}$$

The emission decay time τ_{II} of state **II** (or the decay rate k_{II}) is not directly measurable, but it can be determined from the temperature dependence of the decay rate of the emission to the ground state after the thermal equilibrium between the triplet sublevels is attained (e.g. after several µs). The corresponding procedure is well known (e.g. compare Refs. [105, 156, 157]) and has also been applied to Pt(2-thpy)$_2$ [65]. From this investigation one obtains a decay rate of $k_{II,\,0}$ = (2.78 ± 0.2) × 10^5 s^{-1} (τ_{II} = 3.6 µs) for substate **II**. With this value and with k_{exp}= 1.67 × 10^6 s^{-1} (see example (b) in Section 4.2.7.1) and by use of Eq. (21) one can determine the slr rate to k^{slr} (T = 1.3 K) = 1.39 × 10^6 s^{-1}. This rate corresponds to a slr time of τ_{slr} = 720 ns. (Compare Fig. 20.)

At T = 1.3 K, the slr rate is exclusively determined by the *direct process*, as will be shown explicitly below. By use of Eq. (15) and with the values of k^{slr} (1.3 K) = 1.39 × 10^6 s^{-1} and $\Delta E_{\text{II,I}}$ = 7 cm^{-1} and under assumption of reasonable values for the mass density ($\varrho \approx$ 0.9 g/cm^3, as determined from the crystal structure of n-octane [85]) and the velocity of sound (v ≈ 1.3 km/s for a similar compound [109,158]) one can estimate the size of the matrix element $|\langle \text{II}|\text{V}|\text{I}\rangle|$ to 1.1 cm^{-1} [65]. This interaction energy expresses the size of coupling of the triplet substates **II** and **I** induced by the phonon perturbation. Interestingly, application of a magnetic field of B = 10 T reduces this matrix element to about 0.7 cm^{-1}. In Ref. [24], it has been proposed that this reduction could be related to a field-induced reorientation of the spin system from the molecular frame towards the external magnetic field axis.

4.2.7.3
Temperature Dependence of Spin-Lattice Relaxation

The temperature dependence of the slr rate may be used to determine the importance of the different slr processes. Figure 21 shows that the rate of spin-lattice relaxation from state **II** increases strongly with temperature. The data

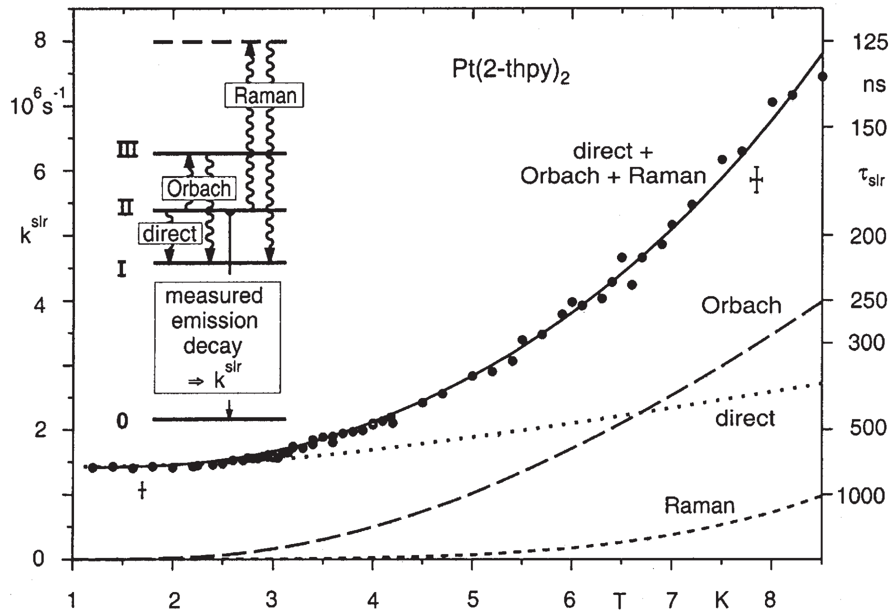

Fig. 21. Temperature dependence of the rate k^{slr} and time τ_{slr} of spin-lattice relaxation of state **II** of Pt(2-thpy)$_2$ dissolved in n-octane. The experimental data (*points*) result from the emission decay times of state **II**, but they are corrected according to Eq. (21). The *solid line* represents a fit according to Eq. (22), while the *broken* and *dotted lines* give the contributions of the respective processes. The *inset* shows the triplet sublevels and depicts schematically the three different processes of spin-lattice relaxation. (Compare Ref. [24])

points are determined from the decay time of the emission of state **II** after correcting the corresponding rates according to Eq. (21). The experimental data can be well fitted, when all three processes of slr, sketched in Fig. 19, are taken into account. In particular, for this specific situation of nearly equally zero-field split triplet sublevels, one has to apply an *extended Orbach expression* according to Eq. (16).[19] Thus, application of the results of Sect. 4.2.6, in particular of the Eqs. (15), (16), and (20) leads to Eq. (22).

$$k^{slr}(T) = k^{slr}(direct) + k^{slr}(Orbach) + k^{slr}(Raman) \tag{22}$$

This expression describes the temperature dependence of the slr from state **II** to state **I** of Pt(2-thpy)$_2$ and is used for the fitting procedure.(Compare Refs. [24, 64, 65].) Eq. (22) contains six parameters after insertion of Eqs. (15), (16), and (20). However, these are reduced to only two free fit parameters, since all energy sepa-

---

[19] In a first report [60], we used the simplified *original Orbach expression* (Eq. (19)), but the fitting procedure led only to an approximate description of the experimental data. In particular, this difficulty triggered our studies [64, 65] to develop the *extended Orbach description*.

rations are known from highly resolved spectra (Fig. 20), the ratio $C_{III,I}/C_{III,II}$ is determined as ≈ 1.2 [65, 148] from time-resolved excitation spectra, as presented in Sect. 4.2.9, $C_{II,I}$ is equal to the low-temperature limit of the spin-lattice relaxation rate k^{slr} (*direct*, $T = 1.3$ K) $= 1/\tau_{slr} = 1.39 \times 10^6\ s^{-1}$ (see above), and the exponent of Eq. (20) can be set to $n = 5$ (see below). Thus the fitting procedure leads to the two unknown parameters and gives the solid line in Fig. 21. (For further details see Ref. [65].)

The results obtained are also used to demonstrate graphically the relative magnitudes of the three different processes that give the total rate of spin-lattice relaxation k^{slr} (T). For the temperature range between $1.3\ K \leq T \leq 3$ K, the total rate k^{slr} is nearly exclusively determined by the *direct process*. Above $T \approx 3$ K and above ≈ 6 K, the *Orbach* and the T^5 *Raman process*, respectively, become important. Although, the *Raman process* is less significant than the two other processes, its inclusion with $R = (10 \pm 3)\ K^{-5}\ s^{-1}$ improves the fit. (R results from the fitting procedures, see Eq. (20).) However, a fit of the data points with a T^7 power law for the *Raman process* is also possible with slightly different values for the two free fit parameters. But this uncertainty is not unexpected, when one takes into account the contribution of k^{slr} (Raman) with respect to the experimental error. (Fig. 21) On the other hand, it has been shown for Pt(2-thpy)(CO)(Cl) that a T^5 dependence is required [24, 65] Therefore, it seems to be reasonable to adopt this power law also for Pt(2-thpy)$_2$, since both compounds were investigated in the same matrix material (n-octane).

In conclusion, the times of relaxation between different triplet substates can be relatively long, such as 720 ns for Pt(2-thpy)$_2$ at $T = 1.3$ K. As a consequence, the emission of higher lying states cannot be frozen out. Therefore, the usually monitored time-integrated emission spectra mostly represent super-imposed spectra that stem from different excited states. Moreover, in this situation, the emission decay behavior depends on the excitation and the detection energy. At low temperature, usually the *direct process* of slr dominates for compounds with zero-field splittings of the triplet by several cm^{-1}, while with temperature increase the slr becomes distinctly faster due to growing in of the *Orbach* and/or the *Raman process*. The specific temperature dependence of the slr rate and the importance of an individual process is essentially determined by the size and pattern of zero-field splitting of the lowest triplet. In particular, when a real electronic state, like state **III**, is present (see Fig. 19b and the inset of Fig. 21), the *Orbach process* will dominate the *Raman process*. On the other hand, the latter process will govern the temperature dependence of slr, if this third state is absent [24, 65]. Since the pattern and size of zfs is chemically tunable, as is schematically depicted in Fig. 1, the effective slr can also be varied chemically. This aspect has recently been studied in the Refs. [24, 65] for a series of compounds. Important differences in the relaxation behavior become also obvious, when the properties of spin-lattice relaxation found for Pt(2-thpy)$_2$ (this section) are compared to those observed for Pd(2-thpy)$_2$ (Sects. 3.1.3 and 3.1.5).

4.2.8
Time-Resolved Emission

In the previous section, it was shown that emission of $Pt(2\text{-thpy})_2$ decays at $T = 1.3$ K biexponentially with time constants of (600 ± 10) ns and (110 ± 3) μs, when the compound is excited non-selectively, for example in the uv. This behavior is a consequence of a population of state **II** by the intersystem crossing processes and of the relatively slow depletion of this state **II** with a time constant of 600 ns. This decay is mainly determined by the spin-lattice relaxation from state **II** to state **I**. State **I** is also populated directly by the fast intersystem crossing route and emits with its intrinsic decay time of 110 μs. Thus, during the first micro-seconds after the laser pulse, state **II** is still populated and one obtains super-imposed emissions stemming from two states with strongly different decay times. According to the large difference of these time constants discrimination of the two emission spectra will be possible by applying time-resolved spectroscopy.

Indeed, this is successful as has been demonstrated in Ref. [60] and as shown in Fig. 22. Figure 22a reproduces the emission spectrum detected immediately after the exciting laser pulse ($\lambda_{\mathrm{exc}} = 337.1$ nm, pulse widths 0.5 ns) with no time delay ($t = 0$ ns) and integrated during a time window of $\Delta t = 500$ ns. Thus, one obtains the *fast* and non-delayed emission spectrum which predominantly results from state **II**. A totally different spectrum is recorded, when the emission is monitored after a time being long compared to the slr time of 720 ns. For example, with a delay of $t = 10$ μs after the laser pulse and using an integration time of $\Delta t = 60$ μs (time window), one obtains the emission spectrum as reproduced in Fig. 22b. It represents the emission of state **I**.

The delayed emission spectrum is very similar to the time-integrated emission spectrum measured at $T = 1.3$ K. (Compare the Figs. 22b to 13.) Therefore, this delayed spectrum is similarly assignable as described in Sects. 4.2.1 and 4.2.4. In particular, all vibrational satellites that are marked in Fig. 22b represent false origins. Their intensities are vibronically (Herzberg-Teller) induced. Also this delayed emission spectrum does not reveal any intensity at the position of the electronic origin I.[20]

The fast and non-delayed emission spectrum (Fig. 22a) shows nearly the same structure as the time-integrated spectrum measured at $T = 20$ K. (Fig. 14) However, the satellites that result from state **III** (9 cm^{-1} higher lying peaks of the "doublet" structure in the 20 K emission spectrum) do not occur in the fast spectrum. Obviously, at $T = 1.3$ K, an emission of state **III** is not observed. This is due to the very fast slr processes to the lower lying triplet substates **II** and **I**. (Compare also Sect. 4.2.9.) Thus, the fast spectrum represents the non-thermalized emission spectrum of state **II**. The Boltzmann distribution does not apply immediately after the excitation pulse, since the thermal equilibration is relatively slow. (For details see Refs. [22, 24].) This state **II** emission spectrum is assigned

---

[20] The occurrence of the electronic origin II in the time-delayed spectrum is not expected on first sight. However, its appearance is a consequence of a thermal repopulation of state **II** – according to a Boltzmann distribution which applies after a sufficiently long delay time (see Refs. [22,24]) – and of the relatively large transition probability of the **II** → **0** transition.

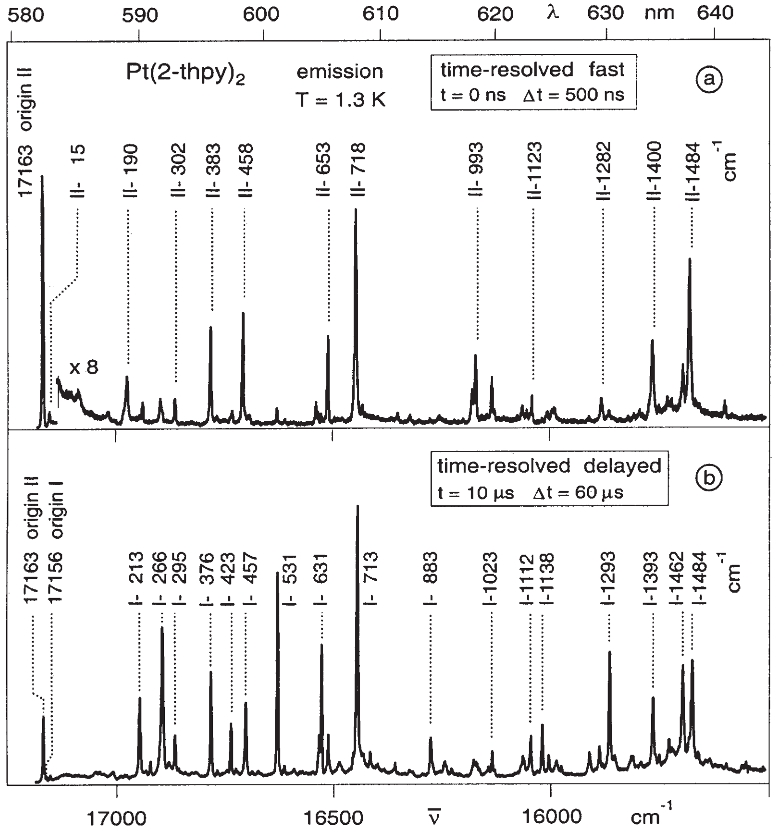

Fig. 22. Time-resolved emission of Pt(2-thpy)$_2$ dissolved in n-octane (c ≈ 10^{-5} mol/l) and monitored at T = 1.3 K. Excitation: λ_{exc} = 337.1 nm, pulse width ≈ 0.5 ns, repetition rate: 100 Hz. (a) The emission is detected without any delay and integrated over Δt = 500 ns. (b) Detection of the emission after a delay of t = 10 μs and integrated over Δt = 60 μs. The energies of the vibrational satellites are given in cm^{-1} relative to the electronic origin II (a) and origin I (b), respectively. (Compare Ref. [60])

similarly as is discussed in Sects. 4.2.1 and 4.2.4. In particular, the electronic origin II strongly dominates the spectrum and most of the vibrational satellites are induced by Franck-Condon active vibrations.

In conclusion, it is possible for Pt(2-thpy)$_2$, to separate the emission spectra that are super-imposed in time-integrated spectra by time-resolved emission spectroscopy. It is important that one also obtains a low-temperature (1.3 K) emission spectrum from a higher lying state with the corresponding high spectral resolution. This possibility is a consequence of the relatively slow spin-lattice relaxation. Or vice versa, since the monitored time-resolved emission spectra are clearly assignable to different triplet substates, these results nicely support the concept of a slow spin-lattice relaxation as developed above. Moreover, the results presented reveal even more distinctly a triplet substate selectivity with respect to the vibrational satellites than found for Pd(2-thpy)$_2$ (see Sects. 3.1.4 and 3.1.5).

4.2.9
Determination of Relaxation Paths by Time-Resolved Excitation Spectroscopy

The subject of this section is to introduce an interesting new method which allows us to determine very fast relaxation paths (order of one ps) by time-resolved measurements with a time-resolution of the order of microseconds only. This method is based on specific relaxation properties which occur within the system of the three triplet substates. For the subsequent discussion, it is of special importance that after a pulsed excitation at the electronic origin III and origin II, respectively, state **I** (with the long-lived emission) is populated with different rates. Thus, with a *delayed* detection of the emission, the excitation intensity ratio I_{III}/I_{II} at the electronic origins III and II is larger than with a *fast* detection.[21] The reason is that the fast measurement yields the direct response of the short-lived state **II**, while the delayed one displays the response of the long-lived state **I**. Since after excitation of state **III**, state **I** is populated more efficiently than state **II** by about 20% [65], the larger excitation intensity ratio I_{III}/I_{II} in the delayed measurement relative to the fast one is qualitatively explained.

4.2.9.1
Time-Resolved Excitation Spectra

According to the above discussions, the occurrence of differently efficient relaxation paths within the triplet system implies that the intensities of the excitation peaks of the two electronic origin lines III and II will depend on the delay time of detection. We will call such excitation spectra, for which the emission is detected with different delay times, *time-resolved excitation spectra.*

In Fig. 23, low-temperature (T = 1.3 K) time-resolved excitation spectra are shown [60]. The structures represent the origins corresponding to the triplet sublevels **II** (at 17,163 cm^{-1}) and **III** (at 17,172 cm^{-1}) and a number of vibrational satellites. An assignment of these is presented in Sect. 4.2.5 by use of time-integrated excitation spectra (Fig. 15). The electronic origin I is not observed, since this transition is strongly forbidden. (Sect. 4.2.1) Both time-resolved excitation spectra are detected at an emission energy centered at 16,444 cm^{-1} with a bandwidth of 3 to 4 cm^{-1}. By use of this detection energy the emissions of state **I** and of state **II** can be monitored simultaneously.[22] The *fast, non-delayed* excitation spectrum (Fig. 23a) is detected with no delay after the laser pulse (t = 0 ns) and with a time window of Δt = 2 µs, while the *delayed* excitation spectrum

---

[21] The detection should be carried out by comprising vibrational satellites of the emission of both states **I** and **II**. For details see next subsection.

[22] This detection energy is chosen, since the 713 cm^{-1} vibrational satellite of the state **I** emission lies at 16,443 cm^{-1} ((17,156 – 713) cm^{-1} = 16,443 cm^{-1}, Fig. 13), and the 718 cm^{-1} satellite of the state **II** emission is found at 16,445 cm^{-1} ((17,163–718) cm^{-1} = 16,445 cm^{-1}, Fig. 14).

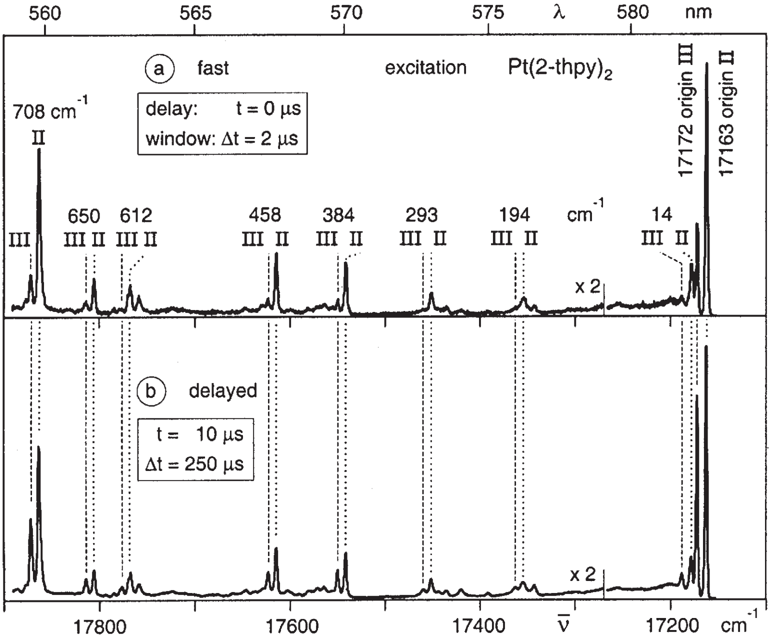

Fig. 23. Time-resolved excitation spectra of Pt(2-thpy)$_2$ in an n-octane matrix at T=1.3 K. (a) Time-resolved detection of the emission with no delay time and with an integration time (time window) of Δt = 2 μs. (b) Time-resolved detection of the emission with a delay time of t = 10 μs and a time window of Δt = 250 μs. The emission is detected at 16,444 cm^{-1} with a spectral bandwidth of ≈ 3 cm^{-1}. This allows us to monitor the vibrational satellites at origin I – 713 cm^{-1} ($\triangleq$ 16,443 cm^{-1}) and at origin II – 718 cm^{-1} ($\triangleq$ 16,445 cm^{-1}) simultaneously. The spectra are normalized with respect to the intensity of origin II. The spectra are only reproduced up to ≈ 720 cm^{-1} from the electronic origins, but the same intensity ratio for the vibrational satellites of 2.2 ± 0.2 (see text) is found for the whole range of our measurements up to ≈ 1500 cm^{-1}. (Compare also the time-integrated excitation spectrum shown in Fig. 15 and Ref. [60])

(Fig. 23b) is measured after a delay time of t = 10 μs and monitored with an integration time of Δt = 250 μs (time-window). After this long delay time the short-lived emission has totally decayed, i.e. the initial population of state **II** is depleted.

Interestingly, the predicted behavior with regard to the intensity ratios of the electronic origins is clearly observed in Fig. 23. The origin line III of the *fast* excitation spectrum (Fig. 23a) is significantly less intense than the same origin line III in the *delayed* spectrum (Fig. 23b). Both spectra are normalized with respect to the intensity of origin II. From the spectra, one determines an intensity ratio of 2.2 ± 0.2 for the origin lines III (ratio: delayed/fast). An estimate of this ratio considering the processes that determine the population dynamics of the three substates yields approximately the same value.

4.2.9.2
Determination of Relaxation Paths

The method and the results discussed in the preceding section can be utilized to investigate an interesting question: Consider an excitation of a vibrationally excited state of a specific triplet substate, for example, of substate **III**. Does the relaxation path proceed downwards to the zero-point vibrational level of just this triplet substate? Or, alternatively, does the relaxation path cross via a higher lying vibrational-phonon state to a different substate? This question refers to relaxation processes that occur on a picosecond time scale. However, here, the answer can be given by use of time-resolved excitation spectra with a microsecond time resolution on the basis of a comparison of intensities of spectrally resolved transitions. (Compare Fig. 24.)

The time-resolved excitation spectra (Fig. 23) show that *all vibrational satellites*, including phonons, progressions, and combinations [148], corresponding to origin III, exhibit an intensity ratio of 2.2 ± 0.2, when the intensity of a *delayed* excitation satellite is compared to the intensity of a *fast* satellite.[23] This is valid at least up to satellites of ≈ 1500 cm^{-1} above the electronic origin. (Range of our measurements, Fig. 23 reproduces only the range up to 720 cm^{-1}, but see Ref. [148]). The same intensity ratio of 2.2 ± 0.2 has also been determined for the electronic origins.

If it is assumed that the crossing between the different substate systems proceeds via an excited vibrational/phonon state, the intensity ratio of the *delayed* excitation peak relative to the *fast* one would for that specific vibrational satellite (and presumably all higher lying ones) differ distinctly from the ratio found for the electronic origins. However, such behavior is *not* observed, at least for vibrational states up to ≈ 1500 cm^{-1} above the zero-point vibrational levels of the triplet substates. Thus, it can be concluded that *the relaxation from an excited vibrational state takes place by a fast process within the individual potential hypersurface of each triplet sublevel to its zero-point vibrational level* (intrasubstate relaxation). Subsequently, a comparatively slow slr and/or emission occurs from that electronic state. This result is schematically depicted in Fig. 24.

For completeness, it should be mentioned that this method of time-resolved excitation spectroscopy can also be utilized successfully to correlate excited state vibrational satellites to their electronic substates by their specific time dependences. This is helpful, for example, when the satellites are superimposed in time-integrated excitation spectra [60, 148].

Time-resolved excitation spectra were also monitored for the energy range of about 20,000 to 22,000 cm^{-1}, where one observes the next higher lying singlet-singlet transition which also exhibits a resolved vibrational structure. (Compare also Sect. 4.3.) For this situation, we would not expect to observe any specific time dependence of the vibrational satellite structures in time-resolved excitation spectra, since these singlet state vibrations would certainly not interact selectively with a specific potential hypersurface of a lower lying triplet sublevel.

---

[23] Satellite peaks corresponding to origin II are used for normalization.

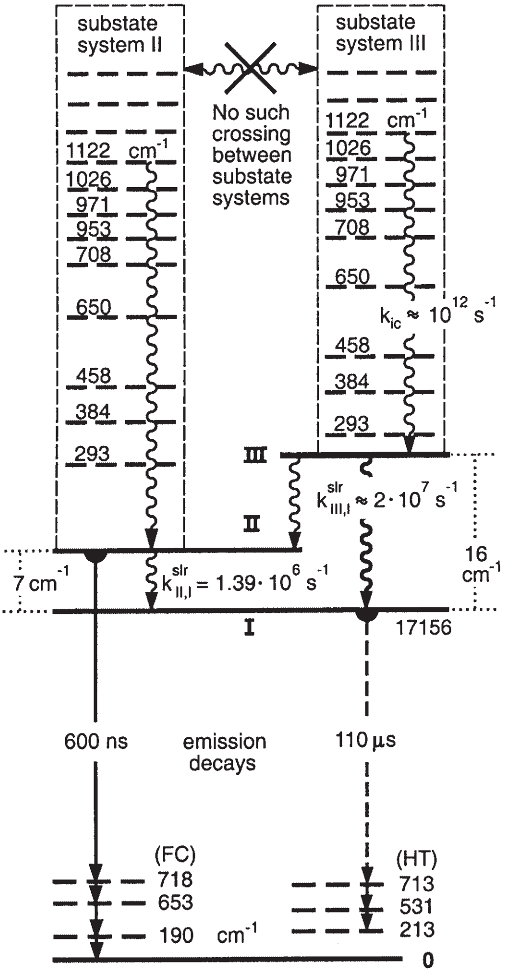

Fig. 24. Triplet substates **I**, **II**, and **III** of Pt(2-thpy)$_2$ dissolved in an n-octane matrix, T=1.3 K. The vibrational levels of the excited states are given as examples. They refer to the substates **II** and **III**, respectively. By use of the new method of time-resolved excitation spectroscopy (Sect. 4.2.9), it is demonstrated that an inter-substate crossing does not occur via excited vibrational states, but it takes place after a fast relaxation to the zero-point vibrational level of the respective triplet substate by relatively slow processes of spin-lattice relaxation [60]. The rates $k^{slr}_{II,I}$ [24, 60, 62, 64, 65] and $k^{slr}_{III,I}$ [65] are determined in the references given (see also text). The intra-state relaxation rate of $k_{ic} \approx 10^{12}$ s^{-1} has been estimated for Pd(2-thpy)$_2$ (Sect. 3.1.2.5). Several vibrational levels of the ground state are also given. FC and HT, respectively, refer to Franck-Condon and Herzberg-Teller activity in the respective radiative deactivations. (Compare Sect. 4.2.4)

Indeed, the time-resolved singlet excitation spectra do not show any time effect, as is demonstrated in Ref. [60].

In conclusion, time-resolved excitation spectroscopy or, more correctly, excitation spectroscopy with time-resolved detection of emission, opens access to studies of intra- and inter-system crossing paths, i.e. of relaxation paths within or between hypersurfaces of different triplet substate systems. This method – applied for the first time in our investigation [60] for transition metal complexes – complements other measurements of pico-/subpico-second time resolution. In particular, it is shown that after an excitation of a vibrational state of an excited electronic triplet substate, the relaxation proceeds *within* the same triplet substate system downwards to the zero-point vibrational level. Subsequently, an inter-system crossing to a different sublevel system occurs in a relatively slow process by spin-lattice relaxation. This result fits well to the concept that a spin-flip is usually slower than the process of intra-state relaxation.

Interestingly, this new method of time-resolved excitation spectroscopy seems to be of rather general applicability. For example, similar results have already been obtained for $[Ru(bpy)_3]^{2+}$[60], Pt(2-thpy)(CO)(Cl) [148], and $Pt(phpy)_2$ [148].

4.2.10
Localization/Delocalization – Background and Fingerprints

The question of whether an excited state of a metal complex is spatially localized or delocalized over different ligands and the metal has been addressed to several compounds. In most cases, a clear answer is not possible, whenever the spectral information is hidden below broad and unresolved bands. This situation is usually met when solutions or frozen solutions are investigated at room temperature or at 80 K. Therefore, it is required to measure well-resolved spectra to reach conclusive answers. From a series of investigations carried out recently [21–23], it was deduced that the spatial extension of an excited state of complexes, such as those discussed here[24], is controlled by the amount of metal or MLCT character in these states. This property crucially determines the metal-mediated electronic ligand-ligand coupling. It is important that the resulting coupling energy exceeds any distortion energy induced, for example, by unsymmetric environments. Corresponding concepts have already been developed in solid state physics for localization mechanisms of excitons (selftrapped excitons) or electrons (localized polarons) [159–165]. The basic message is that the localization occurs if the distortion energy gained by the localization is larger than the coupling energy that leads to the electronic delocalization. In principle, these concepts are transferable to the compounds being of interest in the present investigation.[155] However, the corresponding coupling and distortion energies are not known explicitly for any of these complexes. Thus, the balance mentioned cannot be made directly. Nevertheless, an experimental access to this question of localization or delocalization is possible by isotopic labeling of the

---

[24] Here, complexes for which in the electronic ground state the ligands are related by symmetry operations are referred to.

different ligands, i.e. by partial deuteration. In this situation, highly resolved emission spectra clearly reflect fingerprints that carry the required information (see below and the Refs. [18, 19, 21–23, 33, 47, 48]). From such investigations, it has been deduced that in complexes with small metal character in the lowest excited triplet states, such as $[Rh(bpy)_3]^{3+}$[19–22, 33] and $[Pt(bpy)_2]^{2+}$ [21, 22, 34] with zero-field splittings of the order of 0.1 cm^{-1}, these states are ligand centered (LC) and localized on one ligand. These compounds are found on the left hand side of Fig. 1. On the other hand, compounds, which exhibit distinct MLCT character in the lowest triplets, experience a significant metal-induced ligand-ligand coupling. This leads to excited states that are delocalized over the metal and the different ligands, as in $[Ru(bpy)_3]^{2+}$and $[Os(bpy)_3]^{2+}$ [21, 22, 33, 47, 48]. The lowest triplets of these latter compounds are characterized by relatively large zfs of 61 cm^{-1} and 211 cm^{-1}, respectively [22] (see Fig. 1, right hand side).

The bpy-metal complexes shown in Fig. 1 seem to reflect two extreme situations. Consequently, it is of interest to investigate a compound, which lies between these positions with regard to the metal character. Fortunately, orthometalated Pt(II)-compounds, and in particular $Pt(2\text{-}thpy)_2$, fit well into the series discussed. The triplet state of $Pt(2\text{-}thpy)_2$ is assigned to be mainly of LC character, but an MLCT admixture leads to a total zfs of 16 cm^{-1}. For this situation of a distinctly smaller MLCT character and consequently a smaller metal-induced electronic ligand-ligand coupling as compared to $[Ru(bpy)_3]^{2+}$ and $[Os(bpy)_3]^{2+}$, it is not clear to which of the two situations $Pt(2\text{-}thpy)_2$ belongs. Thus, it is of interest to discuss, whether for this "intermediate" compound the metal-induced electronic ligand-ligand coupling is sufficiently large to delocalize the lowest excited triplet, or whether the coupling is still so small that already weak distortions, such as those induced, for example, by the environment, are sufficient to localize the excitation on one ligand.

It will be shown that the question of whether a localized or a delocalized excited state occurs can be answered also for $Pt(2\text{-}thpy)_2$ by using the technique of isotope labeling combined with high-resolution spectroscopic methods and emission decay measurements. For this study, one compares suitable photophysical properties of perprotonated and perdeuterated compounds to those of partially deuterated ones. This procedure provides reliable fingerprints concerning the localization/delocalization behavior [18, 21–23, 33, 47, 48].

4.2.10.1
Perprotonation/Perdeuteration

Perdeuteration of transition metal complexes, such as $[Rh(bpy)_3]^{3+}$, $[Ru(bpy)_3]^{2+}$, $[Os(bpy)_3]^{2+}$, $Pt(2\text{-}thpy)_2$, etc. leaves the complex symmetry usually unchanged. Nevertheless, a number of characteristic effects can be observed:

Vibrational frequencies

Commonly, all vibrational frequencies of a perdeuterated complex are found to be shifted to lower energies (red shifts), if compared with those of the perprotonated compound. The amount of red shift is connected to the contribution of C-H/C-D vibrational component of the corresponding vibrational mode. Red shifts of more than 50 cm^{-1} for ligand vibrations in the 1000 to 1500 cm^{-1} range are not unusual. (For example, see Refs. [18, 19, 21–23, 33, 34, 47, 48, 166–172] and compare the results found for $Pt(2\text{-thpy})_2$ that are shown in Fig. 25, see below.)

Emission intensity and decay time

Usually, the emission intensity and decay time increase upon deuteration of a molecule due to decreasing non-radiative deactivation. This is a consequence of the higher number of vibrational quanta, which are necessary to fit the energy difference between the electronic ground state and the excited state in the deuterated case. Thus, the Franck-Condon factors between the lowest vibrational level of the excited electronic state and the isoenergetic, highly vibrationally excited levels of the electronic ground state become smaller (e.g. see Refs. [98, 173]). The consequence is a reduction of the non-radiative deactivation. For example, factors of emission intensity increase of three (e.g. see Refs. [25, 169]) and even a hundred [174] have been observed. (Compare also the decay times given for $Pt(2\text{-thpy})_2$ in Fig. 26, see below.)

Vibrational satellite structure

The vibrational satellite structure, for example of the emission spectrum, is altered due to two different effects. First, because of the red shift of the vibrational modes, as mentioned above, one observes the satellites at lower energies relative to the electronic origin. Secondly, the vibronic coupling property of a vibrational mode depends on the specific normal coordinate of that individual mode. Since the coordinates partly change with deuteration, the intensity of the corresponding vibronic satellite may be modified distinctly. (Compare the Refs. [168, 169, 173, 175].) This effect is also observed, when the vibronic intensities found for $Pt(2\text{-thpy-}h_6)_2$ are compared to those of $Pt(2\text{-thpy-}d_6)_2$, as is shown below in Fig. 25 and in Ref. [23].

Shifts of electronic origins (0–0 transitions)

An important isotope effect seems to be less well known, although it has already been well studied for organic molecules (e.g. see Refs. [170–173, 175–178, 25]) and metal complexes (e.g. see Refs. [18, 19, 21–23, 25, 33, 34, 47, 48, 169]). Due to this effect, the electronic origins are mostly shifted to higher energies upon deuteration. (See also Table 10, below.) This behavior results from the physical principle according to which a purely electronic transition between two electronic states occurs always between the zero-point vibrational energies of these states. A reduction of vibrational energies, being always connected with a deuteration, leads to a decrease of the zero-point vibrational energies in the ground state and the excited state. Due to different force constants in these states the reductions are different. Consequently, a shift to higher energy (blue shift) of the electronic origin line results upon deuteration, if the vibrational force constants of the electronic ground state are (on the average) larger than those of the excited state (e.g. see Ref. [25]). Often, the amount of blue shift is largely independent of the matrix material (see below and Ref. [171]). In this situation, the value of blue shift may be used to characterize changes of force constants according to the excitation process [25, 178].

4.2.10.2
Deuteration of One Ligand

The question of whether different ligands of a homoleptic complex are electronically involved in the low-lying excited states can be answered by investigating spectral changes, which result from a partial deuteration, for example, of one ligand. Interestingly, one observes clearly different spectroscopic features, if the localized situation is compared to the delocalized one. This method has been thoroughly tested for several compounds [19, 21–23, 25, 33, 34, 47, 48]. Nevertheless, it is useful to summarize the crucial points.

Fingerprints of a Localized Situation

In homoleptic complexes with weak electronic coupling between symmetry-related ligands, a small energy gain induced by a weak distortion may already exceed the coupling energy. For example, deuteration of one ligand can represent such a distortion. Consequently, the ligands can in many respects be regarded separately. In this situation, the electronic origin of the deuterated ligand will be blue shifted and thus will be separated from the origin(s) of the other ligand(s). This blue shift will approximately correspond to the amount that would be observed, if the complex had only one single ligand. The value may be as large as 60 cm^{-1}, as has been found for $[Rh(bpy)_3]^{3+}$ [19].

Interestingly, absorption and excitation spectra react differently to partial deuteration than emission spectra. One observes superimposed *absorption* or *excitation* spectra, which correspond to the protonated *and* the deuterated ligand, respectively, both reflecting their individual electronic origins and vibrational satellite structures. On the other hand, the *emission* spectra will show different features, due to a fast intramolecular energy transfer from the deuterated ligand to the protonated one. The deuterated ligand with its higher transition energy can act as donor, and the protonated ligand with the lower transition energy can be the acceptor. The resonance condition for an energy transfer is fulfilled if the spectral overlap integral is non-zero. This is usually the case. Since donor and acceptor belong to the same molecule it can be easily visualized that even a weak electronic coupling can still induce an efficient intra-molecular radiationless energy transfer. (Compare Ref. [22], p. 170.) Thus, even if the energetically higher lying electronic origin of the deuterated ligand is excited selectively, the emission will occur only from the energetically lower lying protonated ligand(s) due to the fast excitation energy transfer. Consequently, the vibrational satellite structure of the emission spectrum will exhibit the characteristic vibrational frequencies of the *protonated* ligand(s) in this localized situation [19, 21, 22, 33, 34].

For completeness it should be mentioned that the behavior described above implies that the vibrational coupling between different vibrations through space or induced by the heavy metal ion is weak. This is at least valid for the high frequency internal ligand modes, as shown in Refs. [19, 21–23, 33, 34] for the types of compounds that are of interest here. The weakness of the vibrational coupling of high frequency modes is also addressed in the Refs. [179–183], though for other compounds.

In conclusion, the most important criterion for the assignment of a ligand localized situation is reflected in the vibrational satellite structure of the emission spectrum of the partially deuterated compound. If this structure is determined by high-energy vibrational satellites of the protonated ligand, which is the most probable case for a weakly coupled situation, the involved states will be localized on the protonated ligand(s). This is a special case of a more general rule, saying that the vibrational satellite structure (corresponding to a specific electronic origin) reflects that spatial region of a molecule in which electronic charge is redistributed during an electronic transition. (Compare also Ref. [183].)

Fingerprints of a Delocalized Situation

In a situation of electronically delocalized excited states with a necessarily significant electronic ligand-ligand coupling, the resulting states are characterized by properties of the whole molecule. Consequently, a deuteration of one ligand will affect the whole molecule. Therefore, one expects to observe three characteristic features for the delocalized situation.

1. Partial deuteration should not lead to additional electronic origins (0–0 transitions). In particular, an equal set of three triplet sublevels should occur. Just this behavior is found for delocalized states of organic molecules [171, 172, 176–178].
2. The lowest electronic transition(s) will usually be shifted to higher energy. However, since only part of the molecule is deuterated, the amount of blue shift will only be part of that of the perdeuterated compound, provided that matrix-induced site effects are small.
3. The most characteristic feature, however, will be observed in the structure of the vibrational satellites. The change of the electronic charge distribution due to an electronic transition is experienced by the whole molecule, in particular of both the deuterated and the protonated ligands. Thus, the emission spectrum will exhibit ligand satellites of both *protonated and deuterated* ligands. It is very important that these satellites belong to the *same electronic 0–0 transition.*

Recall that in this situation the purely vibrational coupling of internal high-frequency ligand vibrations of different ligands is also small due to the large mass of the metal [19, 21–23, 33, 34, 179–182].

Indeed it has been shown that the three criteria are valid for partially deuterated $[Ru(bpy)_3]^{2+}$ [21, 22, 33, 48] and $[Os(bpy)_3]^{2+}$ [22, 47]. It will be shown in Sect. 4.2.11 that these criteria are also fulfilled for partially deuterated $Pt(2\text{-}thpy)_2$. But these criteria are not satisfied for partially deuterated $[Rh(bpy)_3]^{3+}$ [19, 21, 22, 33] and $[Pt(bpy)_2]^{2+}$ [22, 34], in which the excited states are ligand centered localized.

4.2.11
Spatially Delocalized States in $Pt(2\text{-}thpy)_2$

The information with respect to the spatial extension of the lowest excited triplet state of $Pt(2\text{-}thpy)_2$ can be obtained by use of the criteria developed in the preceding section. For their application it is required to investigate first, how the electronic and vibrational structure of the perprotonated compound, Pt(2-thpy-h_6)$_2$, is altered due to a perdeuteration to Pt(2-thpy-d_6)$_2$. Having this information available, one can study Pt(2-thpy-h_6)(2-thpy-d_6) and thus one can come to a judgement with regard to the involvement of both ligands in the respective electronic transition.

4.2.11.1

Pt(2-thpy-d_6)$_2$ Compared to Pt(2-thpy-h_6)$_2$

Electronic origins and vibrational satellites

Figure 25 compares the 1.3 K emission spectrum of perprotonated Pt(2-thpy)$_2$ to that of the perdeuterated compound. The assignment of the spectrum of Pt(2-thpy-d_6) follows that presented for Pt(2-thpy-h_8)$_2$. (See Sects. 4.2.1 and 4.2.4.) Both electronic origins I and II of Pt(2-thpy-d_6)$_2$ are blue shifted by (36 ± 1) cm^{-1} (see also Fig. 26). The same value is also found for origin III [23], showing that the relative splittings, i.e. the zero-field splittings, are maintained. Interestingly,

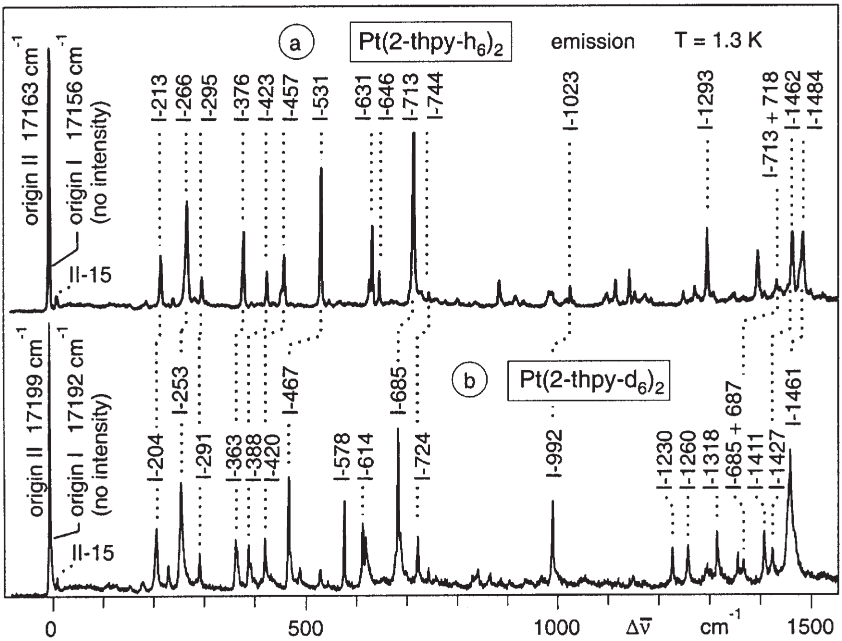

Fig. 25. Emission spectra (time-integrated) of (*a*) Pt(2-thpy-h_6)$_2$ and (*b*) Pt(2-thpy-d_6)$_2$ dissolved in n-octane (Shpol'skii matrix) at a concentration of 10^{-5} mol/l. λ_{exc} = 457.9 nm. The wavenumber scale gives the separation from the respective electronic origin I (set to zero). For both compounds, origin I does not carry any emission intensity. All vibrational satellites that correspond to fundamentals are false origins, i.e. they are vibronically (Herzberg-Teller) induced. Several vibrational modes of the perprotonated compound are correlated to those of the perdeuterated one, they are connected by *dotted lines*. The spectrum (*a*) corresponds to the one reproduced in Fig. 13. (Compare Ref. [23])

the same blue shifts of 36 cm^{-1} with maximum deviations of ± 2 cm^{-1} were found in seven different n-alkane matrices for 30 different sites [143]. Thus, it can be concluded that the influence of the matrix or the individual site is of little importance for the amount of blue shift. This indicates that the blue shift represents mainly a molecular property. The occurrence of this shift is a consequence of a reduction (on average) of the vibrational force constants of the triplet substates relative to the force constants of the electronic ground state. However, it can be concluded that the force constants do not strongly differ (on average), since the amount of blue shift is relatively small. (Compare Ref. [25] and Sect. 5.) A similar conclusion has already been drawn from a comparison of the excited state vibrational frequencies of $\mathbf{T}_1$ to those of the ground state $\mathbf{S}_0$. (Sect. 4.2.5)

Similarly as found for the perprotonated compound (Sect. 4.2.1), the electronic origin I of Pt(2-thpy-d_6)$_2$ does not carry any intensity, while the purely electronic transition between the ground state **0** and substate **II** is significantly allowed.

The mechanisms that induce the intensities of the vibrational satellites in the 1.3 K emission of state **I** are assigned to be the same as discussed in Sect. 4.2.4.1 for the perprotonated compound, i.e. all vibrational satellites that correspond to fundamentals represent false origins, they are Herzberg-Teller induced. (Compare Sect. 4.2.2.)

The vibrational satellite structure corresponding to the emission of the electronic state **I** is distinctly altered due to the perdeuteration. As expected (Sect. 4.2.10.1), all vibrational frequencies are red shifted, apart from the phonon satellite of 15 cm^{-1}. However, by using the intensity distributions of the vibrational satellites, it is possible to correlate many of the vibrational modes of the perprotonated to those of the perdeuterated compound, as is carried out in Fig. 25.

It is important that, according to Fig. 25, the information concerning the correspondence of high frequency vibrations of the deuterated ligand relative to those of the protonated ligand is available. A similar correlation has also been carried out for those vibrational modes that are Franck-Condon active with respect to the emission from state **II**, for details see Ref. [23].

Emission decay and spin-lattice relaxation times

As expected, perdeuteration leads to an increase of the emission decay time. In particular, it is found that the decay time at $T = 1.3$ K of the lowest triplet sublevel **I** increases from τ_I([Pt(2-thpy-h_6)$_2$]) = 110 μs to τ_I ([Pt(2-thpy-d_6)$_2$]) = 140 μs (Fig. 26).

Interestingly, the spin-lattice relaxation time according to the *direct process* involving the triplet substates **II** and **I** remains unchanged within limits of experimental error. For Pt(2-thpy-h_6)$_2$ and for Pt(2-thpy-d_6)$_2$ the slr times at $T = 1.3$ K are τ_{slr} (720 ± 10) ns and (710 ± 10) ns, respectively (see Sect. 4.2.7.2 and Ref. [23]). Obviously, perdeuteration of the chromophore does not strongly influence the slr at low temperatures. Moreover, it is indicated that the matrix cages of the two compounds in n-octane are similar. Otherwise one would expect to observe distinctly different slr times as has been shown for Pt(phpy)$_2$ (compare Fig. 1) in n-octane [64].

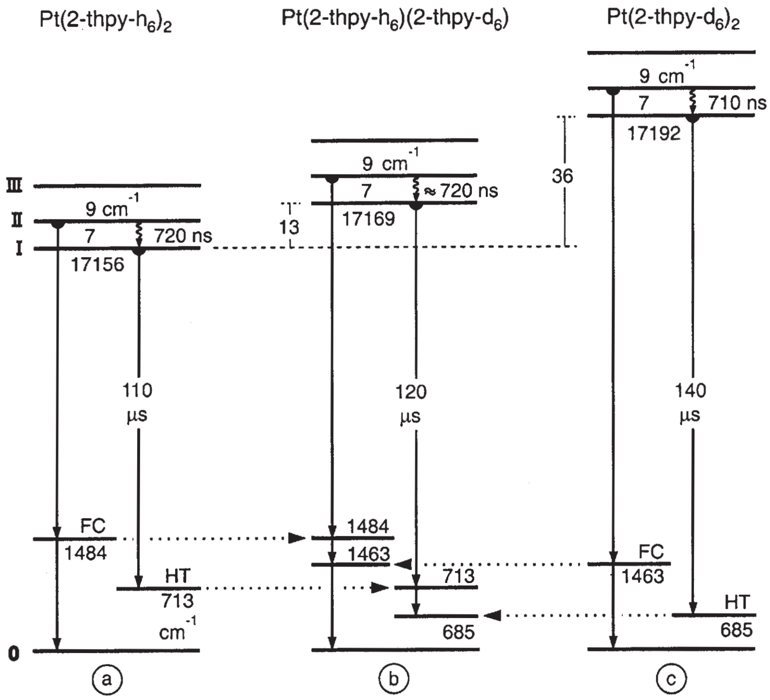

Fig. 26. Energy level diagram for the triplet sublevels of (*a*) perprotonated, (*b*) partially deuterated, and (c) perdeuterated Pt(2-thpy)$_2$ dissolved in an n-octane matrix (Shpol'skii matrix). Emission decay times and spin-lattice relaxation times are given for $T = 1.3$ K. Several vibrational satellites are specified, HT = Herzberg-Teller active vibration, FC = Franck-Condon active vibration. The emission spectrum of the partially deuterated compound (*b*) exhibits vibrational satellites of the two different ligands. (Compare Fig. 27b.) The data given for Pt(2-thpy-h$_6$)(2-thpy-d$_6$) (*b*) refer to the lower lying site A. (Compare Ref. [23])

4.2.11.2
Pt(2-thpy-h$_6$)(2-thpy-d$_6$)

Partial deuteration of Pt(2-thpy)$_2$ leads to very characteristic isotope effects, which will be addressed in this section. An evaluation with respect to the spatial extension in the excited state(s) requires detailed knowledge about the electronic origins and the structure of the vibrational satellites observed in the emission spectra, as was illustrated in Sect. 4.2.10.2.

Two sites in n-octane
Pt(2-thpy-h$_6$)(2-thpy-d$_6$) can also be doped into an n-octane matrix as the two percompounds, and one also obtains highly resolved spectra. However, due to slightly different chromophore-matrix interactions, the partially deuterated dopant is built in on two different chromophore sites A and B, which give rise to nearly equally intense emissions. The lowest electronic origin I of site A lies at 17,169 cm^{-1}, while the corresponding 0–0 transition of site B is found at 8 cm^{-1}

higher energy. Similarly, as for the two percompounds, the purely electronic transitions between the states **I** and **0** are strongly forbidden for both sites. Again, the second electronic origins II(A) at 17,176 cm^{-1} and II(B) at 17,184 cm^{-1}, respectively, carry significant allowedness and can therefore directly and selectively be excited. Thus, one obtains well separated site A-emission spectra. In particular, this possibility provides clear proof for the assignment of sites. In the subsequent discussion we want to focus only on site A, since the properties of site B seem to be very similar.

Checking of fingerprints

With respect to the criteria presented in Sect. 4.2.10 (Fingerprints of a delocalized situation), it is an important result that also Pt(2-thpy-h_6)(2-thpy-d_6) exhibits only one set of three triplet sublevels (criterion (1)). The three electronic origins of the triplet of site A are equally blue shifted by 13 cm^{-1} relative to the energies of the perprotonated compound. (Fig. 26) This value for site A is somewhat smaller than one half of the total blue-shift of 36 cm^{-1} as found for the perdeuterated Pt(2-thpy)$_2$. (Site B exhibits a blue shift of 21 cm^{-1}. The mean value of the blue shift is $(13 + 21)/2 = 17$ cm^{-1}.) Thus, the intrinsic effect, which results from differences of the zero-point vibrational energies of the excited state and the ground state (Sect. 4.2.10) is superimposed by a slight shift due to the chromophore-matrix interaction. Nevertheless, criterion (2) of Sect. 4.2.10.2 is also fulfilled.

Criterion (3) of Sect. 4.2.10.2 represents the most important fingerprint for the occurrence of a delocalized situation. This criterion is based on the vibrational satellite structure of the emission spectrum. Therefore, in Fig. 27b, the 1.3 K emission spectrum of Pt(2-thpy-h_8)(2-thpy-d_8) is reproduced. The compound is excited selectively at the electronic origin II at 17,176 cm^{-1} of site A. For a better comparison of the vibrational satellite structures, the spectra of the two percompounds of Fig. 25 are also shown in Fig. 27. Further, the electronic origins I of all three compounds are set to zero on the wavenumber scale. Figure 27 demonstrates clearly that the partially deuterated compound exhibits a large number of vibrational satellites which have to be assigned to both ligands, the protonated **and** the deuterated one. (See also Table 8) According to criterion (3), this comparison is only carried out for the high-energy internal ligand modes with $\bar{\nu} > 550$ cm^{-1}. It is stressed that all these vibrational satellites belong to one single electronic origin I, which lies at 17,169 cm^{-1}. In particular, this result can only be explained in a delocalized model.

The results discussed above, in particular those concerning the vibrational satellite structures (shown in Fig. 27) allow us only to conclude on a delocalized situation for substate **I** of the triplet state $\mathbf{T_1}$. However, an equivalent conclusion can also be drawn from the 4.2 K emission spectra (not reproduced, but see Ref. [23]). In this case, one observes mainly the emission that results from state **II**. Again, vibrational satellites corresponding to both ligands are observed in the emission spectrum of Pt(2-thpy-h_6)(2-thpy-d_6), and they belong only to one single origin II at 17,176 cm^{-1} (site A). It follows that the triplet sublevel **II** is also delocalized over the two ligands.

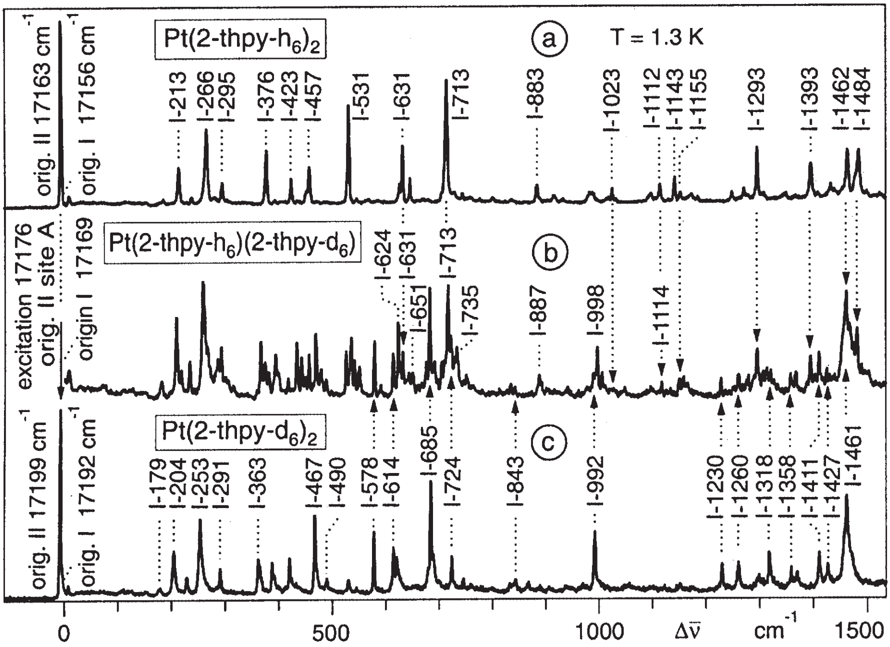

Fig. 27. Emission spectrum of (*b*) Pt(2-thpy-h_6)(2-thpy-d_6) at T=1.3 K of site A. For comparison, the spectra of (*a*) Pt(2-thpy-h_6)$_2$ and (*c*) Pt(2-thpy-d_6)$_2$ are also reproduced. (Compare Fig. 25.) The compounds are dissolved in an n-octane matrix (= Shpol'skii matrix) with a concentration of c ≈ 10^{-5} mol/l. The compounds (*a*) and (*c*) are excited at λ_{exc} = 457,9 nm (≙ 21,839 cm^{-1}), while the partially deuterated compound (*b*) is site-selectively excited at the electronic origin II (17,176 cm^{-1}) of site A. The wavenumber scales are set to zero with respect to the electronic origins I of all three compounds. The emission spectrum (*b*) of Pt(2-thpy-h_6)(2-thpy-d_6) exhibits many vibrational satellites in the high-energy range of internal ligand vibrations of the protonated and of the deuterated ligand (related by *arrows*). All satellites in this spectrum (*b*) belong to the same electronic origin I at 17,169 cm^{-1}. (Compare Ref. [23])

Interestingly, the information with respect to an involvement of the two ligands is manifested by different vibrational coupling mechanisms, i. e. by Herzberg-Teller activity and by Franck-Condon activity of an emission of state **I** and state **II**, respectively. Obviously, the coupling mechanisms are not significantly altered due to partial deuteration.

In an additional experiment it was also possible to demonstrate [143] that after application of a high magnetic field of B = 12 T the lowest excited state is still delocalized, as is evidenced again by the occurrence of vibrational satellites corresponding to both ligands in the emission of the magnetically strongly perturbed state $\mathbf{I_B}$. Since the radiative properties of state $\mathbf{I_B}$ are largely determined by those of state **III** due to the Zeeman interaction, one can conclude that sublevel **III** of Pt(2-thpy-h_6)(2-thpy-d_6) is also delocalized over the metal and the two ligands [23] (Compare also Refs. [22, 184]).

Table 8. Prominent satellites of high-frequency vibrational ligand modes found in the $T = 1.3$ K emission spectra of $Pt(2\text{-thpy-}h_6)_2$, $Pt(2\text{-thpy-}h_6)(2\text{-thpy-}d_6)$, and $Pt(2\text{-thpy-}d_6)$. All satellites belong to the respective electronic origin I[a]

$Pt(2\text{-thpy-}h_6)_2$ [cm^{-1}]	$Pt(2\text{-thpy-}h_6)(2\text{-thpy-}d_6)$ [cm^{-1}]	$Pt(2\text{-thpy-}d_6)_2$ [cm^{-1}]
	site A	
17156[b]	17169[b]	17192[b]
	578	578
	614	614
631	631	
	685	685
713	713	
	724	724
1112	1114	
	1230	1230
	1260	1260
1293	1293	
1393	1393	
	1411	1411
1462	1462(1)	1461
1484	1484	

[a] Experimental error ± 1 cm^{-1}.

[b] Electronic origin I corresponding to the lowest triplet substate I.

Emission decay time

Finally, we discuss briefly the emission decay behavior. At $T = 1.3$ K, the emission decay time is mainly determined by radiative and non-radiative processes of state **I**. For $Pt(2\text{-thpy-}h_6)(2\text{-thpy-}d_6)$ one finds a value of (120 ± 3) μs, which thus lies between (110 ± 3) μs and (140 ± 3) μs of the perprotonated and perdeuterated compounds, respectively (see also Fig. 26). Apart from the effects of spin-lattice relaxation occurring in the first microseconds, the decay is strictly monoexponential, at least over five lifetimes. It is important that the decay is exactly equal, when measured on a vibrational satellite, which is related to the protonated part of the molecule (e.g. 713 cm^{-1} satellite) and to the deuterated part (e.g. 685 cm^{-1} satellite), respectively. (Fig. 27b) This result also strongly supports the assignment to a delocalized excited state. A similar behavior has also been observed for $[Os(bpy)_3]^{2+}$, for which the lowest triplet states are also delocalized [47].

In summary, highly resolved emission spectra of compounds with isotopically labeled ligands reflect clear fingerprints with respect to the spatial extension of excited states. Using these relatively simple and distinct fingerprints, which are based mainly on comparisons of emission properties of perprotonated, perdeuterated, and partially deuterated compounds, one can decide whether an excited state is localized or not. This procedure is applied to $Pt(2\text{-thpy})_2$, and it could be shown that all criteria developed for a delocalized situation are fulfilled, while the fingerprints for the description of a localized situation do not fit to the experimental findings. Thus, it is concluded that the three substates of the lowest excited triplet of Pt(2-thpy-h_6)(2-thpy-d_6) being doped into an n-octane matrix cage are delocalized over the metal and the two different ligands [23]. Although, the partial deuteration induces a slight distortion, this effect is not large enough to induce a localization. From this result it also follows that the triplets of the homoleptic, more symmetric percompounds Pt(2-thpy-h_6)$_2$ and Pt(2-thpy-d_6)$_2$ are delocalized, too.

4.3
Higher Lying States of Pt(2-thpy)$_2$

The possibility of obtaining well-resolved spectra of higher lying electronic states is very often restricted due to overlapping absorptions of different states and due to the very short lifetimes of these states. (Compare also the discussion with respect to Pd(2-thpy)$_2$ in Sect. 3.2.) Still, it is achievable to monitor better resolved excitation spectra of (perprotonated) Pt(2-thpy)$_2$ for the energy range from $\approx$ 17 100 cm^{-1} to $\approx$ 26,000 cm^{-1}, than shown in Fig. 12.

$S_0 \rightarrow T_1$

The lowest triplet state $\mathbf{T_1}$ of Pt(2-thpy)$_2$ has been characterized thoroughly in the preceding sections. The three triplet substates are observed at 17,156, 17,163, and 17,172 cm^{-1}. At higher energies, one finds a large number of vibrational satellites that correspond to the substates **II** and **III** (Fig. 15). There is no indication of an occurrence of any other electronic transition between this $\mathbf{S_0} \rightarrow \mathbf{T_1}$ transition and the next higher lying electronic origin at 20,450 cm^{-1} [74].

$S_0 \rightarrow S_1$

Figure 28 shows some resolved structure in the energy range between $\approx$ 20,000 cm^{-1} and 22,000 cm^{-1}. This structure seems to correspond to the shoulder that is seen in the absorption spectrum reproduced in Fig. 12 near 21 700 cm^{-1} ($\approx$ 460 nm) with a molar extinction coefficient of $\approx$ 1900 l/mol cm [145]. The corresponding state has been assigned in Ref. [53] to a singlet of MLCT character ($\mathbf{S_1}$). This classification is confirmed by ab initio calculations in a CASPT2 study, in which the corresponding transition is found at 20,440 cm^{-1}. Grouptheoretically, this state is assigned in C_{2v} to $^1A_1$ [66].

The resolved excitation spectrum shows an electronic origin at 20,450 cm^{-1} and a number of vibrational satellites (see Fig. 28a and Refs. [74, 95]). The resolution is restricted to $\approx$ 100 cm^{-1}. Therefore, it is not reasonable to try to assign the satellites to vibrational modes that are known for the $\mathbf{T_1}$ state and the $\mathbf{S_0}$ state, respectively.

The inset of Fig. 28 reproduces the magnetic field dependence of the origin peak at 20,450 cm^{-1} up to B = 12 T (at $T = 1.5$ K). One does not observe any shift, splitting or change of the lineshape of this peak. Therefore, it is strongly indicated that the corresponding excited state is a singlet, thus confirming the assignment to the $\mathbf{S_1}$ state as discussed above.

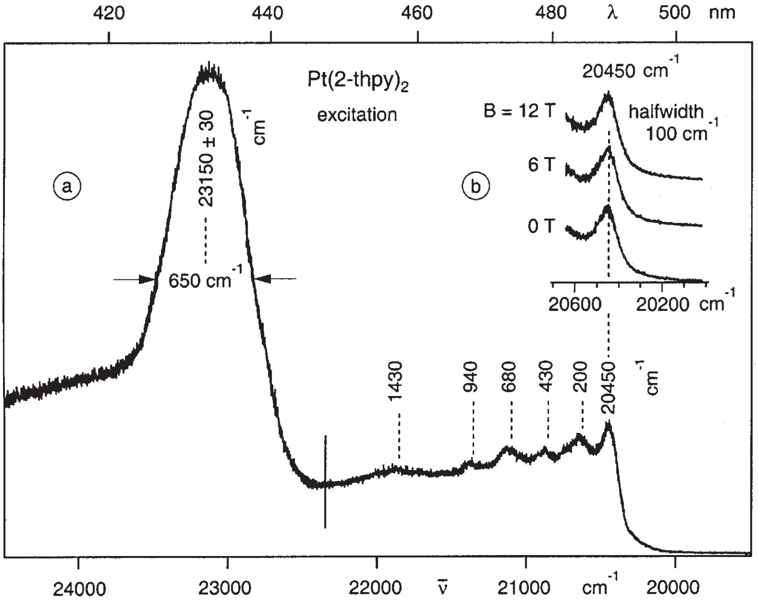

Fig. 28. Excitation spectra of Pt(2-thpy)$_2$ dissolved in n-octane (*a*) at zero magnetic field and $T = 4.2$ K and (*b*) for different magnetic fields at $T = 1.5$ K. Concentration $\approx 10^{-5}$ mol/l. For detection, the energy of 16,444 cm^{-1} with a band width of ≈ 5 cm^{-1} was used, in order to monitor simultaneously the 713 cm^{-1} and 718 cm^{-1} vibrational satellites that correspond to the emissions of the triplet substates **I** and **II**, respectively. Under magnetic fields (*b*), the detection energy is red-shifted according to the size of the field-induced red shift of these satellites. The total excitation spectrum is composed of different spectra. The spectral resolution of the equipment is ≈ 5 cm^{-1} and ≈ 160 cm^{-1} for energies below and above the vertical line near 22,300 cm^{-1}, respectively. Note, the halfwidth given in (*b*) refers to the fwhm of a Lorentzian line shape function which was fit to the red flank of the corresponding peak. (Compare also to the Refs. [74] and [95])

Interestingly, the low-energy flank of the electronic origin at 20,450 cm^{-1} can be sufficiently well approximated by a Lorentzian lineshape function, while a fit to a Gaussian lineshape is not successful, indicating that the transition is homogeneously broadened. (Compare Sect. 3.2 and the Refs. [103, 104].) From the Lorentzian fit, a halfwidth (fwhm) of ≈ 100 cm^{-1} is determined, which can be related by use of Eq. (2) to a lifetime of the $\mathbf{S}_1$ state to $\approx 5 \times 10^{-14}$ s. (Fig. 29) According to the relatively high quantum efficiency of the $\mathbf{T}_1$ emission of Pt(2-thpy)$_2$ of $\phi \approx 0.3$ [53] even at room temperature, it is reasonable to ascribe the shortness of this decay time mainly to an efficient intersystem crossing from $\mathbf{S}_1$ to $\mathbf{T}_1$ with a rate of $k_{isc} \approx 2 \times 10^{13}$ s^{-1}. This rate is more than one order of magnitude larger than found for Pd(2-thpy)$_2$ (Sect. 3.2). Presumably, the large rate in Pt(2-thpy)$_2$ is related to the higher spin-orbit coupling and the small energy separation between the states $\mathbf{S}_1$ and $\mathbf{T}_1$ of $\Delta E(\mathbf{S}_1 - \mathbf{T}_1) \approx 3280$ cm^{-1}. Thus, an intersystem crossing process in Pt(2-thpy)$_2$ from $\mathbf{S}_1$ to $\mathbf{T}_1$ requires only three vibrational quanta of $\approx 10^3$ cm^{-1} as compared to Pd(2-thpy)$_2$ for which five quanta of this

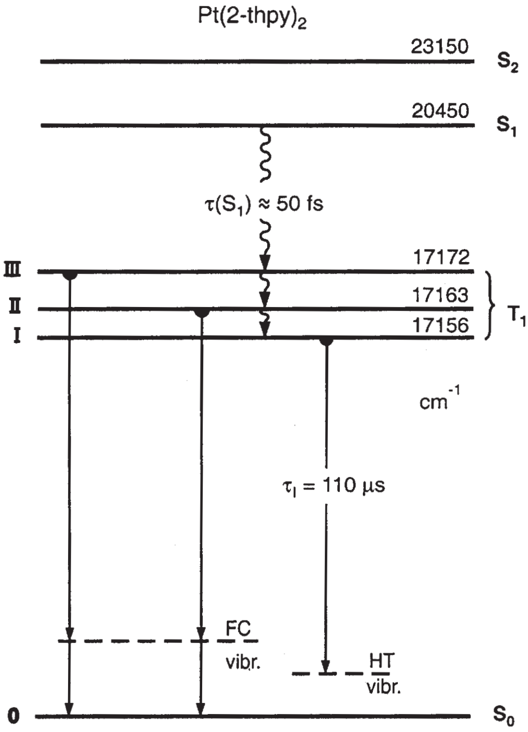

Fig. 29. Energy level diagram for Pt(2-thpy)$_2$ dissolved in n-octane. The electronic origin line I (0–0 transition) is not observed at zero magnetic field. The corresponding triplet substate **I** is radiatively deactivated via vibronic (HT = Herzberg-Teller) mechanisms. (Compare Fig. 13.) The emission lifetime given refers to T=1.3 K. The emissions from the triplet substates **II** and **III** are intense at the electronic origins and show vibrational Franck-Condon (FC) satellites. (Compare Fig. 14.) The lifetime of the S_1 state of 50 fs is determined from the homogeneous linewidth of the $S_0 \rightarrow S_1$ electronic transition at T = 1.3 K. (Compare Fig. 28)

energy are necessary for this relaxation process. Therefore, the differences in intersystem crossing efficiencies are not unexpected (e.g. see Refs. [98] and [99, p. 249]).

$S_0 \rightarrow S_2$

The dominating peak at 23,150 cm^{-1} with a halfwidth of ≈ 650 cm^{-1} (Figs. 28 and 29) corresponds obviously to the peak found in the absorption spectrum of Fig. 12 near 23,800 cm^{-1} (≈ 420 nm) with a molar extinction coefficient of ≈ 10,700 l/mol cm [145]. The corresponding electronic state has been classified in Ref. [53] as a ^{1}MLCT state. Due to the ab initio study of Ref. [66] the state is assigned to the second singlet that has also dominant MLCT character. The CASPT2 calculations place this state to ≈ 23,450 cm^{-1}. In a C_{2v} complex symmetry, this second singlet is classified as $^1B_2$ [66].

5
Assignments and Trends

In this review, we were mainly interested in studying photophysical properties of the lowest triplet states, although some information about higher lying states could also be worked out. Pd(2-thpy)$_2$ and Pt(2-thpy)$_2$ have been chosen as well suited representatives for detailed *case studies*, since the metal participation in the wavefunctions of the low-lying states increases strongly, when going from the Pd(II)- to the Pt(II)-compound. Although this tendency seems to be obvious one has, however, only rarely the opportunity to obtain a deeper insight into the consequences of this increase on photophysical properties. In this respect, Pd(2-thpy)$_2$ and Pt(2-thpy)$_2$ represent outstanding examples due to the possibility of obtaining detailed information from highly resolved optical spectra, from characteristic emission dynamics, and from ODMR and PMDR spectroscopic investigations.

In this section, photophysical properties of Pd(2-thpy)$_2$ and Pt(2-thpy)$_2$ are compared along two lines. In a first step, properties of these two compounds are contrasted in Table 9, and in a second step, a series of properties is related to those of other organometallic compounds or metal complexes with organic ligands in Table 10. In particular, this comparison elucidates a number of clear trends and points the interesting aspects of chemical tunability.

5.1
Comparison of Photophysical Properties and Assignments

Table 9 relates a number of photophysical properties of Pd(2-thpy)$_2$ to those of Pt(2-thpy)$_2$.

- The total zero-field splitting of the lowest triplet state $\mathbf{T}_1$ increases by a factor of ≈ 80 from about 0.2 cm^{-1} in Pd(2-thpy)$_2$ to 16 cm^{-1} in Pt(2-thpy)$_2$.
- The emission decay time of the long-living triplet sublevel **I** decreases by more than a factor of ten from 1200 µs in Pd(2-thpy)$_2$ to 110 µs in Pt(2-thpy)$_2$.
- The intensity of metal-ligand (M-L) vibrational satellites relative to the intensity of all vibrational satellites is by about 50% larger in Pt(2-thpy)$_2$ as compared to Pd(2-thpy)$_2$.
- The transition energies of the $\mathbf{T}_1$ state of Pd(2-thpy)$_2$ and of Pt(2-thpy)$_2$, respectively, lies by ≈ 2100 cm^{-1} and ≈ 3400 cm^{-1}, below the $\mathbf{T}_1$ energy of the free ligand (Not specified in Table 9, but see Ref. [18]).
- The lifetime of the lowest singlet state $\mathbf{S}_1$ is mainly determined by an intersystem crossing process from $\mathbf{S}_1$ to $\mathbf{T}_1$. This time decreases by a factor of 16 from 800 fs in Pd(2-thpy)$_2$ to 50 fs in Pt(2-thpy)$_2$.

All these properties clearly reflect the larger MLCT character in the lowest triplet state of Pt(2-thpy)$_2$ as compared to Pd(2-thpy)$_2$.

Interestingly, the increasing metal character has also important consequences on binding properties and on the spatial extension of the $\mathbf{T}_1$ state.

- With increasing MLCT character, the nuclear equilibrium positions of the excited $\mathbf{T}_1$ state become more similar to those of the electronic ground state. This is reflected in the vibrational satellite structures. In particular, the maxi-

Table 9. Photophysical data of $Pd(2\text{-thpy})_2$ and $Pt(2\text{-thpy})_2$ at T = 1.3 K in an n-octane matrix

Property	$Pd(2\text{-thpy})_2$	$Pt(2\text{-thpy})_2$	Sections, References, Remarks
$\mathbf{S_2}$	$\approx 26 \times 10^3\ cm^{-1}$	$23{,}150\ cm^{-1}$	3.2, 4.3, [54, 66]
$\mathbf{S_1}$	$23{,}836\ cm^{-1}$	$20{,}450\ cm^{-1}$	3.2, 4.3
$\tau(S_1)$	800 fs	50 fs	3.2, 4.3
$k_{isc}(S_1 \rightarrow T_1)$ [a]	$1.3 \times 10^{12}\ s^{-1}$	$20 \times 10^{12}\ s^{-1}$	3.2, 4.3
$\mathbf{T_1}$	$18{,}418\ cm^{-1}$	$17{,}156\ cm^{-1}$ (substate **I** of $\mathbf{T_1}$),	3.1.1, [56–58], and 4.2.1, [59, 60]
$\Delta E(S_1\text{–}T_1)$	$5{,}418\ cm^{-1}$	$3{,}278\ cm^{-1}$	ΔE refers to state **III**
zfs			
$\Delta E_{III,I}$	2E [c] = 2.886 GHz ($\triangleq 0.0962\ cm^{-1}$)	$16\ cm^{-1}$ [b]	3.1.5, [61], and 4.2.1, [59, 60, 62]
$\Delta E_{III,II}$	D [c] > 6.6 GHz ($\triangleq 0.22\ cm^{-1}$)	$9\ cm^{-1}$	
$\Delta E_{II,I}$		$7\ cm^{-1}$	
τ_I	1200 µs	110 µs	3.1.3, [58], and
τ_{II}	235 µs	3.6 µs	4.2.7, [59, 60, 62, 65, 95]
τ_{III}	130 µs	- [d]	
$\tau_{slr}(II \rightarrow I)$	τ_{slr} [d] $\gg \tau_I$	720 ns	3.1.3 and 4.2.7, [24, 60, 62, 64, 65]
τ_{ic} [e]	≈ 1 ps	– [d]	3.1.2.5
Anharmonicity x_e in $\mathbf{T_1}$	0.002	– [d]	3.1.2.4
S_{max} [f]	≈ 0.3	≈ 0.08	3.1.2.3 and 4.2.4.3
Int.(M-L vibr.)/ Int.(all vibr.) [g]	≈ 20%	≈ 30%	[18]
Assignment of $\mathbf{T_1}$	^{3}LC + small MLCT admixtures	^{3}LC + significant MLCT admixtures	5.1, [18, 56–60]
Spatial extension in $\mathbf{T_1}$	– [d]	delocalized	4.2.11, [23]

[a] Intersystem crossing rate $k_{isc}=1/\tau(S_1)$.

[b] Total zero-field splitting.

[c] D and E are the zero-field splitting parameters. 2 E corresponds to the energy difference between the substates **I** and **III**. [61].

[d] Not yet determined.

[e] Intrastate conversion time in a substate of $\mathbf{T_1}$ for an excited vibrational mode of $\approx 10^3\ cm^{-1}$.

[f] Maximal Huang-Rhys parameter for the $\mathbf{T_1} \leftrightarrow \mathbf{S_0}$ transition.

[g] Intensity ratio of vibrational satellites of metal-ligand (M-L) modes relative to all vibrational modes, determined for the $\mathbf{T_1} \rightarrow \mathbf{S_0}$ transition.

mum Huang-Rhys parameter S – that measures shifts along normal coordinates of different electronic states – is by a factor of about four smaller in $Pt(2\text{-thpy})_2$ than in $Pd(2\text{-thpy})_2$. (Table 9) A similar trend is also found for other compounds as is discussed below. (See also the Refs. [18, 22].)

- The MLCT admixture to the ligand centered (LC) wavefunctions leads to a metal-induced electronic ligand-ligand coupling. Obviously, in $Pt(2\text{-thpy})_2$

this coupling is large enough to delocalize the electronic wavefunctions of all three triplet substates over the metal and the two ligands, at least in the rigid n-octane matrix. For Pd(2-thpy)$_2$ the corresponding information is not available yet. However, according to the investigations carried out for [Ru(bpy)$_3$]$^{2+}$ and [Rh(bpy)$_3$]$^{3+}$ [21, 22, 33] and the discussion presented below, it is suggested that the metal participation in the **T$_1$** state of Pd(2-thpy)$_2$ is not sufficient to delocalize the excited state.

Table 9 summarizes also the energies of the low-lying singlets **S$_1$** and **S$_2$**. These are shifted by about 3×10^3 cm^{-1} to lower energy, when going from Pd(2-thpy)$_2$ to Pt(2-thpy)$_2$. This relatively large shift indicates an increasing metal participation also in the singlets. Indeed, the CASPT2 ab initio studies carried out by Pierloot and Ceulemans et al. [66] lead to the assignment of these states as being largely of ^{1}MLCT character.

Interestingly, the energy separation between the lowest singlet **S$_1$** and the triplet **T$_1$**, $\Delta E(S_1\text{-}T_1)$, follows also this trend. For Pd(2-thpy)$_2$ one finds $\Delta E(S_1\text{-}T_1)$ = 5418 cm^{-1} which is reduced to 3278 cm^{-1} in Pt(2-thpy)$_2$. Presumably, the relatively small $\Delta E(S_1\text{-}T_1)$ value of Pt(2-thpy)$_2$ is also connected to the larger spatial extension of the excited state wavefunctions in this latter compound as compared to Pd(2-thpy)$_2$.

In summary, the excited **T$_1$** state of Pd(2-thpy)$_2$ can be assigned as being dominantly of ^{3}LC($^3\pi\pi^*$) character. This is strongly supported by the value of zero-field splitting which is nearly as small as found for organic compounds. On the other hand, the emission decay time is by about three orders of magnitude smaller than in many organic molecules. Obviously, the small MLCT admixture to the ^{3}LC($^3\pi\pi^*$) state induces a higher radiative transition probability in Pd(2-thpy)$_2$, again as compared to organic compounds. Pt(2-thpy)$_2$ exhibits a significantly larger MLCT participation in the **T$_1$** state, as is demonstrated by all the results discussed above. However, a comparison of the photophysical properties of Pt(2-thpy)$_2$ to those of [Ru(bpy)$_3$]$^{2+}$and [Os(bpy)$_3$]$^{2+}$, for which the MLCT character of the lowest excited states is well established [3, 4, 21, 22, 33, 35–50], shows clearly that the lowest triplet state of Pt(2-thpy)$_2$ cannot be characterized as being mainly of ^{3}MLCT character. It is more adequate to classify it as ^{3}LC ($^3\pi\pi^*$) state with significant MLCT admixtures. These assignments will further be supported by ranking a larger number of compounds with respect to the importance of the metal participation in the lowest excited states. (See below.)

5.2
Chemically Tunable MLCT Character

In the preceding subsection an important trend is indicated. An increasing MLCT participation in the lowest **T$_1$** state is connected with a decreasing geometry change of this state as compared to the electronic ground state. This behavior has been observed by comparing the corresponding properties of Pd(2-thpy)$_2$ to those of Pt(2-thpy)$_2$. Interestingly, this trend is also observed, when the series of compounds is extended to other homoleptic complexes, namely to metal-bipyridine compounds, as summarized in Table 10.

Table 10. Spectroscopic trends with increasing metal character of the lowest excited triplet state. The compounds have an increasing metal character in the lowest $\mathbf{T}_1$ state going from top to bottom

Compound	Lowest triplet sublevel $\mathbf{I}$[d] [cm^{-1}]	Total zfs [cm^{-1}]	Blue-shift [cm^{-1}]	Blue-shift per proton[i] [cm^{-1}]	Huang-Rhys parameter S_{max}[j]	Assignments and references
bpy[a]	23,504	≈ 0.1[e]	86	10.8	0.3	$^3\pi\pi^*$, Refs. [22,133]
$[Rh(bpy)_3]^{3+}$[b]	22,757	≈ 0.1[f]	61	7.6	0.3	$^3LC(^3\pi\pi^*)$ +small dd* admixtures; $\mathbf{T}_1$ localized on one ligand; Refs. [19, 21, 22, 33]
$Pd(2\text{-thpy})_2$[c]	18,418	0.2[g]	–[h]	–[h]	0.3	$^3LC(^3\pi\pi^*)$ +small MLCT admixtures; Refs. [18, 56–58, 61, 90]
$Pt(2\text{-thpy})_2$[c]	17,156	16	36	3	0.08	$^3LC(^3\pi\pi^*)$ +significant MLCT admixtures; Refs. [18, 59, 60, 62–66], $\mathbf{T}_1$ delocalized [23]
$[Ru(bpy)_3]^{2+}$[b]	17,684	61	40	1.7	0.1	$^3MLCT(^3d\pi^*)$; delocalized [21, 22, 48]
$[Os(bpy)_3]^{2+}$[b]	14,223	211	32	1.3	0.08	$^3MLCT(^3d\pi^*)$; delocalized [22, 47]

[a] In n-heptane, bpy given for comparison.
[b] In $[Zn(bpy)_3](ClO_4)_2$.
[c] In n-octane.
[d] Protonated compounds.
[e] From Ref. [133].
[f] From Ref. [31].
[g] Estimated order, from Refs. [61, 90].
[h] Value not yet determined.
[i] Referring to the number of protons involved in the spatial region, where the electronic transition occurs.
[j] Maximum Huang-Rhys parameter for the $\mathbf{T}_1 \leftrightarrow \mathbf{S}_0$ transition (compare Fig. 18 and Eqs. (12), (13)).

For $[Rh(bpy)_3]^{3+}$, it is known that the lowest triplet has to be assigned as $^3LC(^3\pi\pi^*)$ state, which is only slightly metal-perturbed [19, 21, 22, 30–34]. On the other hand, the lowest states of $[Ru(bpy)_3]^{2+}$and $[Os(bpy)_3]^{2+}$represent ^{3}MLCT states [3, 4, 21, 22, 35–50]. In Table 10, these compounds including Pd(2-thpy)$_2$ and Pt(2-thpy)$_2$ are arranged in order of increasing zero-field splitting of the lowest triplet, i.e. according to increasing strength of metal/MLCT participation in this state. (Compare also the assignments given in Table 10.) Data for the free bpy-ligand are given for comparison. This series shows a clear trend:

1. The blue shift of the $\mathbf{S_0} \leftrightarrow \mathbf{T_1}$ transition induced by a deuteration of the ligands decreases clearly with increasing metal participation in the $\mathbf{T_1}$ state. This behavior becomes even more obvious, when the values of blue shifts per proton are related. For this comparison only those ligands (giving the number of protons) are taken into account that are involved in the electronic transition. In Sect. 4.2.10.1 and in Refs. [21, 22, 25, 172, 178, 185] it is shown that the size of deuteration-induced blue shift can be taken as a measure for the change of vibrational force constants (on average) of the involved electronic states. Thus, with increasing MLCT character, the vibrational force constants of the ground state $\mathbf{S_0}$ and the excited $\mathbf{T_1}$ state become on average more similar.
2. For the individual vibrational modes or force constants an equivalent trend is indicated. For example, the ground state $\mathbf{S_0}$ and the excited state $\mathbf{T_1}$ frequencies of Pt(2-thpy)$_2$ are still clearly different (see the Figs. 14 and 15 and Table 7). However, for $[Os(bpy)_3]^{2+}$ with a typical ^{3}MLCT state, ground state frequencies deviate from those of the excited state only by $\pm$ 2 cm^{-1}, as far as they have been determined (see Ref. [22, p. 228]).
3. A corresponding trend is also observed for the Huang-Rhys parameter S. According to Sect. 4.2.3, this parameter reflects the shift of the equilibrium position of a specific normal coordinate between the electronic ground state and the excited state. For the series given in Table 10, it is seen that an increasing MLCT character leads to a smaller Huang-Rhys parameter. This implies smaller changes of the equilibrium positions of the potential hypersurfaces. Probably, the reduction of the S value by a factor of three to four represents also an indication for a chemically tuned transition from a localized to a delocalized situation. (Compare Sects. 4.2.3, 4.2.10, and 4.2.11.)

In summary, a growing MLCT admixture induces an increasing covalency. Thus, beyond a certain MLCT admixture, the charge distribution is smeared out over the whole complex. It follows that the simple picture of a transfer of one electron charge from the metal to one ligand is not adequate to describe the states of the compounds discussed here. Presumably, the net amount of charge transfer from the metal to the ligands in the course of the excitation process is relatively small. Therefore, the term "MLCT state" might be misleading, if applied uncritically.

6
Summary

The detailed spectroscopic investigation of the two representative organometallic compounds, Pd(2-thpy)$_2$ and Pt(2-thpy)$_2$, allowed us to obtain a deep insight into a series of photophysical properties. In particular this was possible, since we could measure and interpret highly energy-resolved emission and excitation spectra of the regions of electronic origins and vibrational satellites, time-resolved excitation and emission spectra, the detailed emission rise and decay behavior, and for $Pd(2\text{-thpy})_2$ also ODMR and PMDR spectra. It seems to be useful, to summarize several interesting results and highlights:

6.1
Orbital Character

The orbital character of the lowest triplet state of both compounds is classified to be mainly ligand centered of $^3\pi\pi^*$ character, though perturbed by a small MLCT admixture in $Pd(2\text{-thpy})_2$, but by a significant MLCT participation in $Pt(2\text{-thpy})_2$. (Table 9, Sect. 5, and Refs. [18, 56, 59]) The importance of this MLCT admixture is most clearly reflected in the size of the total zero-field splitting (Fig. 1, Refs. [18–24]).

6.2
Delocalized T_1 State in $Pt(2\text{-thpy})_2$

$Pt(2\text{-thpy})_2$ represents a compound with a significantly smaller MLCT contribution in the lowest excited triplet than found for $[Ru(bpy)_3]^{2+}$or $[Os(bpy)_3]^{2+}$. (Compare also Fig. 1.) For example, the amount of zero-field splitting of the triplet, being characteristic for the MLCT or d-orbital admixture, is smaller by a factor of about four for $Pt(2\text{-thpy})_2$ than for $[Ru(bpy)_3]^{2+}$. Nevertheless, for $Pt(2\text{-thpy})_2$ (doped into a rigid n-octane matrix), one still finds an electronically delocalized state, as mainly shown by fingerprints reflected by partially deuterated compounds. From this behavior, we come to the conclusion that for homoleptic compounds with symmetry related ligands even a moderate metal character couples the ligands sufficiently and thus induces a delocalized situation in the triplet state. For $Pd(2\text{-thpy})_2$, the corresponding information is not yet available. However, it is suggested that the metal-mediated ligand-ligand coupling is too small to induce a delocalization. (See also Sects. 4.2.10, 4.2.11, Table 10, and Refs. [22, 23].)

6.3
Binding Situation in the Excited State T_1 Compared to the Ground State S_0

From the vibrational satellite structures, one can infer differences of the binding situation in the electronic ground state $\mathbf{S_0}$ as compared to the excited state $\mathbf{T_1}$. In particular, it is shown that the nuclear equilibrium positions and the vibrational force constants of these two states differ only slightly, whereby the binding properties in $Pt(2\text{-thpy})_2$ are even more similar than in $Pd(2\text{-thpy})_2$. This effect is ascribed to the larger MLCT admixture in the $\mathbf{T_1}$ state of the Pt(II) compound. (Tables 9, 10 and Refs. [18, 56, 59, 60].)

6.4
Relaxation Times

The internal conversion time within a potential surface of an individual triplet substate has been determined for Pd(2-thpy)$_2$ to $\tau_{ic} \approx 1$ ps from the homogeneous linewidth of a vibrational satellite in the $\mathbf{T}_1$ excitation spectrum. Intersystem crossing times could be evaluated for Pd(2-thpy)$_2$ and for Pt(2-thpy)$_2$ to $\tau_{isc} \approx 0.8$ ps and to ≈ 50 fs, respectively. (Figs. 5 and 29) These times have been determined from the homogeneous linewidths of the corresponding $\mathbf{S}_0 \rightarrow \mathbf{S}_1$ transitions. On the other hand, the relaxation time from one triplet sublevel to another one, the spin-lattice relaxation (slr) time, is orders of magnitude longer and can, in part, be measured directly. For Pt(2-thpy)$_2$, the slr time between the two lowest triplet sublevels amounts to $\tau_{slr} = 720$ ns at $T = 1.3$ K. (Fig. 20 and Refs. [24, 60, 62, 64, 65]) For Pd(2-thpy)$_2$, the slr times are much longer than the longest emission decay time at $T = 1.3$ K ($\tau_{slr} \gg 1$ ms) and may be of the order of one second.

6.5
Processes of Spin-Lattice Relaxation

At low temperature, the processes of spin-lattice relaxation between the triplet substates are slow. With temperature increase, the slr rates increase strongly. For Pt(2-thpy)$_2$, three different processes govern the slr. At a temperature below T ≈ 3 K, the slr rate is exclusively determined by the *direct process*. Above T ≈ 3 K, the *Orbach process* and above T ≈ 6 K, the *T^5 Raman process*, become additionally important. For Pd(2-thpy)$_2$, the processes that govern the slr have not been determined yet, but it is suggested that the *Raman process* is of main importance, since no real electronic state lies in the energy vicinity of the $\mathbf{T}_1$ state. (Figs. 19, 21, and Refs. [24, 60, 62, 64, 65].)

6.6
Time-Resolved Emission

Due to the slow processes of spin-lattice relaxation, an emission of a higher lying triplet substate cannot be frozen out even at very low temperature. Thus, emissions of different substates are often superimposed in the usually monitored time-integrated spectra. This fact can strongly complicate an interpretation. However, by use of the method of time-resolved emission spectroscopy, separated triplet sublevel spectra are obtained for Pd(2-thpy)$_2$ (Fig. 8) and for Pt(2-thpy)$_2$ (Fig. 22). Thus, a more reliable assignment of the spectra, particularly in the regions of the vibrational satellites is achieved [58, 60].

6.7
Vibrational Satellites Induced by Herzberg-Teller and Franck-Condon Activities

Pd(2-thpy)$_2$ and Pt(2-thpy)$_2$ are very suitable compounds for studying different radiative deactivation processes that involve vibrational modes. The long-lived triplet substates of both compounds are nearly exclusively deactivated by vibronic coupling mechanisms according to Herzberg-Teller processes. This is particularly pronounced for Pt(2-thpy)$_2$. As the corresponding transition at the electronic origin is spin- and symmetry-forbidden, spin-vibronic coupling and the combined effect of spin-orbit coupling together with vibronic coupling seem to be important. (Fig. 17) On the other hand, the shorter-lived triplet substates with significantly allowed transitions at the electronic origins are vibrationally deactivated mainly by Franck-Condon satellites, though with very weakly appearing progressions. The maximum Huang-Rhys parameter is determined to $S \approx 0.3$ and ≈ 0.08 for Pd(2-thpy)$_2$ and Pt(2-thpy)$_2$, respectively (Fig. 18).

6.8
PMDR Spectroscopy and Time-Resolved Emission

Pd(2-thpy)$_2$ was investigated by applying the methods of time-resolved emission (Fig. 8) and phosphorescence-microwave double resonance (PMDR) spectroscopy (Fig. 10). By both methods, the vibrational satellite structures are resolved and reveal spin selectivity in these satellites. Thus, vibrational satellites can be assigned to the respective triplet substates. The complementary character of these two methods is demonstrated for the first time for transition metal compounds [58, 61] (Compare Sects. 3.1.4 and 3.1.5.).

6.9
Determination of Relaxation Paths

By monitoring excitation spectra with a time-resolved detection of the emission, briefly called "time-resolved excitation spectroscopy", it is possible, to identify specific relaxation paths. Although, these occur on a ps time scale, only measurements with a µs time resolution are required. It is shown that the relaxation from an excited vibrational state of an individual triplet sublevel takes place by a fast process of intra-system relaxation (on the order of 1 ps) within the same potential surface to its zero-point vibrational level. Only subsequently, a relatively slow crossing to a different sublevel is possible. This latter process is determined by the slow spin-lattice relaxation. A crossing at the energy of an excited vibrational/phonon level from this potential hypersurface to the one of a different substate does not occur (Fig. 24, Ref. [60]). This method of time-resolved excitation spectroscopy, applied for the first time to transition metal complexes, can also be utilized to resolve spectrally overlapping excited state vibrational satellites and to assign these to their triplet substates.

7
Outlook

It is our interest to extend the concept [18–24] of correlating the size of zero-field splitting with photophysical properties also to other organometallic and related compounds. This is of special interest, since the zfs reflects the importance of metal and/or MLCT participation in the wavefunctions of the lowest

Table 11. Energies of electronic states [cm^{-1}], emission decay and spin-lattice relaxation times of triplet sublevels (**I**, **II**, and **III**) at $T \leq 1.3$ K. The compounds are arranged according to an increasing value of the total zero-field splitting $\Delta E_{III,I}$

Compound	Lowest electronic origin I	Zero-field splittings		Emission decay times [μs]			slr time	Assignments[d]	Remarks, References
		$\mathbf{\Delta E_{III,I}}$	$\Delta E_{II,I}$	τ_I	τ_{II}	τ_{III}	τ_{slr} [ns]		
$[Rh(bpy\text{-}h_8)_3]^{3+\,a,b}$	22,757	$0.04\ \mathrm{cm}^{-1}$ $0.077\ \mathrm{cm}^{-1}$ $0.116\ \mathrm{cm}^{-1}$	$(1.18\ \mathrm{GHz})^c$ $(2.32\ \mathrm{GHz})^c$ $(3.49\ \mathrm{GHz})^c$	4.5×10^3	1.35×10^3	0.65×10^3	$\gg \tau_I$	^{3}LC +small dd* admixtures	[19, 21, 22, 30–33, 90]
$[Rh(bpy\text{-}d_8)_3]^{3+\,a,b}$	22,818	$-^e$	$-^e$	13.6×10^3	1.55×10^3	0.7×10^3	$\gg \tau_I$	^{3}LC +small dd* admixtures	[19, 21, 22, 33]
$Pd(qol)_2{}^{b,f}$	16,090	$0.0785\ \mathrm{cm}^{-1}$ $0.175\ \mathrm{cm}^{-1}$	$(2.356\ \mathrm{GHz})^c$ $(5.241\ \mathrm{GHz})^c$	90×10^3	180	80	$\gg \tau_I$	^{3}ILCT	[72–75]
$Pd(2\text{-}thpy)_2{}^{b,f}$	18,418	$0.0962\ \mathrm{cm}^{-1}$	$(2.886\ \mathrm{GHz})^c$	1.2×10^3	235	130	$\gg \tau_I$	^{3}LC +small MLCT admixtures	[18, 56–58, 61], this work
$[Pt(bpy)_2]^{2+\,b,g}$	21,237	$\mathbf{0.2}^h$	0.2^h	50^i	8^i	3^i	$\gg \tau_I$	^{3}LC +small MLCT admixtures	[34, 21, 22, 24]
$Pt(qol)_2{}^{b,f}$	15,426	**<1**	<1	60	13	4.5	$-^e$	^{3}ILCT	[72–74]
$Pt(qtl)_2{}^{b,f,j}$	13,158	**<1**	<1	7	2.8	0.55	$-^e$	^{3}ILCT	[73, 74]
$Pt(2\text{-}thpy)_2(CO)(Cl)$	18,012.5	**3.8**	0.055^c	120	45	35	$3.0 \times 10^{3\,k}$	^{3}LC + MLCT admixtures	[24, 62, 74, 148, 186]
$Pt(phpy)(CO)(Cl)^{b,f,l}$	20,916	**6.4**	$\approx 0.1^h$	$-^e$	$-^e$	$-^e$	$-^e$	^{3}LC +MLCT admixtures	[62, 74]

Table 11. *(Continued)*

Compound	Lowest electronic origin I	Zero-field splittings		Emission decay times [μs]			slr time	Assignments[d]	Remarks, References
		$\Delta E_{III,I}$	$\Delta E_{II,I}$	τ_I	τ_{II}	τ_{III}	τ_{slr} [ns]		
$[Pt(mnt)_2]^{2-}$ [b,m]	14,128	**7**	–[e]	13	–[e]	–[e]	–[e]	^{3}LC +MLCT admixtures	[187]
$Pt(2\text{-}thpy\text{-}h_6)_2$ [b,f]	17,156	**16**	7	110	3.6	–[e]	720	^{3}LC +MLCT admixtures	[18, 23, 24, 59, 60, 62–65], this work
$Pt(2\text{-}thpy\text{-}d_6)_2$ [b,f]	17,192	**16**	7	140	4.3	–[e]	710	^{3}LC +MLCT admixtures	[23, 143], this work
$Pt(3\text{-}thpy)_2$ [b,f]	18,020	**22**	13	105	2.7	≈5	≈25	^{3}LC +MLCT admixtures	[95, 188]
$Pt(phpy)_2$ [b,f]	19,571	**32**	6.9	70	2.4	–[e]	390	^{3}LC – MLCT	[62, 65, 95, 148], site of lowest energy
$Pt(bhq)_2$ [b,n]	19,814	**39**	11	–[e]	–[e]	–[e]	–[e]	^{3}LC – MLCT	[189], site of lowest energy
$[Ru(bpz)_3]^{2+}$ [a,o]	18,226	**54**	8.5	400	–[e]	–[e]	180	^{3}MLCT	[22, 62, 143]
$[Ru(bpdz)_3]^{2+}$ [a,p]	17,346	**61**	8	195	–[e]	–[e]	410	^{3}MLCT	[22, 62, 143]
$[Ru(bpy\text{-}d_8)_3]^{2+}$ [a,b]	17,724	**60**	8.3	310	11	1.1	200 ± 30	^{3}MLCT	[21–23, 25, 33, 48, 190]
$[Ru(bpy\text{-}h_8)_3]^{2+}$ [a,b]	17,684	**61**	8.7	230	8	0.9	220	^{3}MLCT	[18, 20–25, 33, 48, 60, 155]

Table 11. *(Continued)*

Compound	Lowest electronic origin I	Zero-field splittings $\mathbf{\Delta E_{III,I}}$	$\Delta E_{II,I}$	Emission decay times [µs] τ_I	τ_{II}	τ_{III}	slr time τ_{slr} [ns]	Assignments[d]	Remarks, References
$[Os(phen)_3]^{2+}$ [a,b]	14,475	**186**	66	46	– [e]	– [e]	– [e]	^{3}MLCT	[191]
$[Os(bpy\text{-}h_8)_3]^{2+}$ [a,b]	14,223	**221**	63	22	– [e]	– [e]	– [e]	^{3}MLCT	[17, 18, 22, 47, 155, 169]
$[Os(bpy\text{-}d_8)_3]^{2+}$ [a,b]	14,256	**223**	64	46	– [e]	– [e]	– [e]	^{3}MLCT	[22, 47, 155, 169]

[a] In $[Zn(bpy)_3](ClO_4)_2$.

[b] Compare structure formulae in Fig. 1.

[c] ODMR transition.

[d] LC: ligand centered; MLCT: metal-to-ligand charge transfer; ILCT: intra-ligand charge transfer.

[e] Not yet determined.

[f] In n-octane.

[g] Trap in neat $[Pt(bpy\text{-}h_8)_2](ClO_4)_2$.

[h] Estimated order of magnitude.

[i] Value probably reduced by matrix effects.

[j] $(qtl)^-$ = 8-quinolinethiolate.

[k] The spin-lattice relaxation time τ_{slr} is given for the process from state **III** to states **I** and **II**. In all other cases τ_{slr} refers to the process from state **II** to state **I**.

[l] $(phpy)^-$ = phenylpyridinate.

[m] Investigated as $[Bu_4N]_2[Pt(mnt)_2]$ salt, $[Bu_4N]^+$ = tetra-n-butyl-ammonium.

[n] In n-decane.

[o] (bpz) = 2,2-bipyrazine.

[p] (bpdz) 3,3′-bipyridazine.

triplet state. Obviously, such a correlation that comprises compounds with different types of electronic transitions, i.e. different involved orbitals, should not be carried out too rigorously. Nevertheless, a classification of a large number of compounds according to the size of total zero-field splitting ($\Delta E_{III,I}$) seems to be attractive, since such a series implies aspects of a chemical tunability. The corresponding ordering is given in Table 11. (Compare also Fig. 1.) Pd(2-thpy)$_2$ and Pt(2-thpy)$_2$ are included in this series, and it is seen that Pd(2-thpy)$_2$ belongs to the group of small metal character in the low-lying triplet state, while Pt(2-thpy)$_2$ is placed at an intermediate position.

It is not intended in this outlook to discuss properties of the given compounds individually. However, the large number of photophysical data presented in Table 11 is well-suited to point to some potentialities and trends:

- From the information concerning the size of zero-field splitting, transition energy, emission decay times, and messages that are reflected in the vibrational satellite structures (not included in Table 11, but see the references given) one can identify molecular orbitals of dominant importance for the excited triplet states.
- The values of zero-field splittings $\Delta E_{II,I}$ and $\Delta E_{III,I}$ vary over a large range. This property has already been applied to select different situations, i.e. compounds for which specific processes of spin-lattice relaxation become effective. These processes largely control the population dynamics of a triplet system and thus significantly determine the emission properties at low-temperature. (Compare Sects. 3.1.3 to 3.1.6, 4.2.6, and 4.2.7 and the Refs. [22, 24, 60–62, 64, 65, 72–75, 90].)
- With increasing metal d and/or MLCT character, the metal mediated electronic ligand-ligand coupling becomes larger. This stabilizes increasingly a delocalized excited state in homoleptic compounds with symmetry related ligands as compared to a localization tendency that might be induced by unsymmetric distortions. Thus, it is indicated that in homoleptic compounds with small MLCT character (small zfs splittings) the excited triplets are localized, while in compounds with a larger MLCT character (larger values of zfs) the lowest excited states are delocalized. This aspect has been addressed in Sect. 5 (Table 10) and in Sects. 4.2.10 and 4.2.11. (Compare also the Refs. [18, 21, 23, 33, 47, 48].)

In summary, Table 11 provides information concerning the very large ranges of photophysical properties of organometallic or related compounds. In particular, transition energies, zero-field splittings, transition probabilities, emission decay times, spin-lattice relaxation times, etc. cover ranges that are not found in purely organic molecules. Thus, the classes of transition metal compounds discussed here, represent interesting sources for new materials or applications as mentioned in Sect. 1.

Acknowledgements. We thank Dr. Werner Humbs and Professor Dr. A. von Zelewsky for preparation of Pt(2-thpy)$_2$ and Pd(2-thpy)$_2$, respectively. Dr. Harald Wiedenhofer is acknowledged for some results concerning the excitation spectrum shown in Fig. 28. This investigation was financially supported by the Fonds der Chemischen Industrie, the Deutsche Forschungsgemeinschaft, and the Volkswagen-Stiftung.

8
References

1. Conolly JS (ed) (1981) Photochemical Conversion and Storage of Solar Energy. Academic Press, New York
2. Harriman A, West MA (ed) (1982) Photogeneration of Hydrogen. Academic Pess, London
3. Juris A, Balzani V, Barigelletti F, Campagna S, Belser P, von Zelewsky A (1988) Coord Chem Rev 84:85
4. Kalyanasundaram K (1992) Photochemistry of Polypyridine and Porphyrin Complexes. Academic Press, London
5. Calzaferri G (ed) (1994) Proceedings of the 10th International Conference on Photochemical Transformation and Storage of Solar Energy. Vol 38 of Solar Energy Materials and Solar Cells, Interlaken
6. O'Regan B, Grätzel M (1991) Nature 353:737
7. Nazeeruddin MK, Kay A, Rodicio I, Humphry-Baker R, Müller E, Liska P, Vlachopoulos N, Grätzel M (1993) J Am Chem Soc 115:6382
8. Heimer TA, Bignozzi CA, Meyer GJ (1993) J Phys Chem 97:11987
9. Leitner W (1995) Angew Chem 107:2391
10. Maede TJ, Kayyem JF (1995) Angew Chem 107:358
11. Terpetschnik E, Szmacinski H, Malak H, Lakowicz JR (1995) Biophys 68:342
12. Kosch U, Klimant I, Werner T, Wolfbeis OS (1998) Anal Chem 70:3892
13. Holmlin RE, Barton JK (1995) Inorg Chem 34:7
14. Baldo MA, Lamansky S, Burrows PE, Thompson ME, Forrest SR (1999) Appl Phys Lett 75:4
15. Wilson GJ, Sasse WHF, Mau AW-H (1996) Chem Phys Lett 250:583
16. Tyson DS, Castellano FN (1999) Inorg Chem 38:4382
17. Breu J, Kratzer C, Yersin H (2000) J Am Chem Soc 122:2548
18. Yersin H, Huber P, Wiedenhofer H (1994) Coord Chem Rev 132:35
19. Humbs W, Yersin H (1996) Inorg Chem 35:2220
20. Yersin H, Strasser J (1997) J Luminescence 72–74:462
21. Yersin H, Humbs W, Strasser J (1997) Coord Chem Rev 159:325
22. Yersin H, Humbs W, Strasser J (1997) In: Electronic and Vibronic Spectra of Transition Metal Complexes. Vol II. Yersin H (ed) Vol 191 of Topics in Current Chemistry. Springer, Berlin p 153
23. Yersin H, Humbs W (1999) Inorg Chem 38:5820
24. Yersin H, Strasser J (2000) Coord Chem Rev 208:331
25. Yersin H, Braun D (1991) Chem Phys Lett 179:85
26. Vogler A, Kunkely H (2001) In: Transition Metal and Rare Earth Compounds. Excited States, Transitions, Interactions. Yersin H (ed) Topics in Current Chemistry. Vol. 213 Springer, Berlin, p 143–182
27. Crosby GA, Elfring WH jr (1976) J Phys Chem 97:2206
28. Nishizawa M, Suzuki TM, Sprouse S, Watts RJ, Ford PC (1984) Inorg Chem 23:1837
29. Komada Y, Yamauchi S, Hirota N (1986) J Phys Chem 90:6425
30. Westra J, Glasbeek M (1990) Chem Phys Lett 166:535
31. Westra J, Glasbeek M (1991) Chem Phys Lett 180:41
32. Kamyshny AL, Suisalu AP, Aslanov LA (1992) Coord Chem Rev 117:1
33. Humbs W, Strasser J, Yersin H (1997) J Luminescence 72–74:677
34. Humbs W, Yersin H (1997) Inorg Chim Acta 265:139
35. Orgel LE (1961) J Chem Soc 3683
36. a) Crosby GA (1975) Acc Chem Res 8:231 b) Baker DC, Hipps KW, Crosby GA (1978) Chem Phys Lett 53:333
37. Felix F, Ferguson J, Güdel HU, Ludi A (1980) J Am Chem Soc 102:4096
38. Elfring WH jr, Crosby GA (1981) J Am Chem Soc 103:2683
39. Ceulemans A, Vanquickenborne LG (1981) J Am Chem Soc 103:2238
40. Kober EM, Meyer TJ (1982) Inorg Chem 21:3967

41. Meyer TJ (1986) Pure and Appl Chem 58:1193
42. Krause RA (1987) Structure and Bonding (Berlin) 67:2
43. Krausz E (1988) Comments Inorg Chem 7:139
44. Meyer TJ (1989) Acc Chem Res 22:163
45. Yersin H, Braun D, Hensler G, Gallhuber E (1989) In: Vibronic Processes in Inorganic Chemistry. Flint CD (ed) Vol 288 Series C Nato ASI, Mathematical and Physical Sciences. Kluwer Acad Publishers, Dordrecht p 195
46. Belser P (1990) Chemica 44:226
47. Huber P, Yersin H (1993) J Phys Chem 97:12705
48. Braun D, Huber P, Wudy J, Schmidt J, Yersin H (1994) J Phys Chem 98:8044
49. Roundhill DM (1994) Photochemistry and Photophysics of Metal Complexes. Plenum Press, New York p 165
50. Riesen H, Krausz E (1995) Comments Inorg Chem 18:27
51. Maestri M, Sandrini D, Balzani V, Chassot L, Jolliet P, von Zelewsky A (1985) Chem Phys Lett 122:375
52. Balzani V, Maestri M, Melandri A, Sandrini D, Chassot L, Cornioley-Deuschel C, Jolliet P, Maeder U, von Zelewsky A (1987) In: Photochemistry and Photophysics of Coordination Compounds. Yersin H, Vogler A (ed) Springer, Berlin Heidelberg New York, p 71
53. Sandrini D, Maestri M, Ciano M, Balzani V, Lueoend R, Deuschel-Cornioley C, Chassot L, von Zelewsky A (1988) Gazzetta Chimica Italiana 118:661
54. Maestri M, Sandrini D, Balzani V, von Zelewsky A, Jolliet P (1988) Helvetica Chimica Acta 71:134
55. Maestri M, Balzani V, Deuschel-Cornioley C, von Zelewsky A (1992) Adv Photochem 17:1
56. Yersin H, Schützenmeier S, Wiedenhofer H, von Zelewsky A (1993) J Phys Chem 97:13496
57. Becker-Donges D, Yersin H, von Zelewsky A (1995) Chem Phys Lett 235:490
58. Schmidt J, Wiedenhofer H, von Zelewsky A, Yersin H (1995) J Phys Chem 99:226
59. Wiedenhofer H, Schützenmeier S, von Zelewsky A, Yersin H (1995) J Phys Chem 99:13385
60. Schmidt J, Strasser J, Yersin H (1997) Inorg Chem 36:3957
61. Glasbeek M, Sitters R, van Veldhoven E, von Zelewsky A, Humbs W, Yersin H (1998) Inorg Chem 37:5159
62. Strasser J, Donges D, Humbs W, Kulikova MV, Balashev KP, Yersin H (1998) J Luminescence 76–77:611
63. Yersin H, Trümbach D, Wiedenhofer H (1999) Inorg Chem 38:1411
64. Homeier HHH, Strasser J, Yersin H (2000) Chem Phys Lett 316:280
65. Strasser J, Homeier HHH, Yersin H (2000) Chem Phys 255:301
66. Pierloot K, Ceulemans A, Merchán M, Serrano-Andrés L (2000) J Phys Chem A 104:4374
67. Vogler A, Kunkely H (1981) Inorg Chim Acta 54:L273
68. Ballardini R, Indelli MT, Varani G, Bignozzi CA, Scandola F (1978) Inorg Chim Acta 31:L423
69. Scandola F, Ballardini R, Indelli MT (1982) In: Photochemical and Photoelectrochemical and Photobiological Processes, Solar Energy R. and D. Eur Com Ser D, Hall DO (ed) Kluwer, Dordrecht, The Netherlands p 66
70. Borgarello E, Pelizzetti E, Ballardini R, Scandola F (1984) Nouv J Chim 8:567
71. Ballardini R, Varani G, Indelli MT, Scandola F (1986) Inorg Chem 25:3858
72. Donges D, Nagle JK, Yersin H (1997) Inorg Chem 36:3040
73. Donges D, Nagle JK, Yersin H (1997) J Luminescence 72–74:658
74. Donges D (1997) PhD thesis, Universität Regensburg
75. Yersin H, Donges D, Nagle JK, Sitters R, Glasbeek M (2000) Inorg Chem 39:770
76. Nurmukhametow RN (1969) Russian Chem Rev. 38:180
77. Lamotte M, Merle AM, Joussot-Dubien J, Dupuy F (1975) Chem Phys Lett 35:410
78. Pitts WM, Merle AM, El-Sayed MA (1979) Chem Phys 36:437
79. Murao T, Azumi T (1979) J. Chem. Phys 70:4460
80. Shpol'skii EV (1960) Sov Phys Usp (engl translation) 3:372
81. Canters GW, van der Waals JH (1978) In: The Porphyrins, Vol III. Dolphin D (ed) Acad Press, New York p 531

82. Jansen G, Noort M, van Dijk N, van der Waals JH (1980) Mol Phys 39:865
83. Huang T-H, Rieckhoff KE, Voigt E-M (1979) Chem Phys 36:423
84. Chen W-H, Rieckhoff KR, Voigt E-M (1986) Chem Phys 102:193
85. a) Mathisen H, Norman N, Pedersen BF (1967) Acta Chem Scand 21:127. b) Norman N, Mathisen H (1972) Acta Chem Scand 26:3913
86. a) Nakhimovsky LA, Lamotte M, Joussot-Dubien J (1989) Physical Sciences Data 40, Handbook of Low Temperature Electronic Spectra of Polycyclic Aromatic Hydrocarbons. Elsevier, Amsterdam b) Boese R, Weiss H-C, Bläser D (1999) Angew Chem Int Ed 38:988 (German edition 111:1042)
87. Imbusch GF, Kopelman R (1981) In: Laser Spectroscopy of Solids. Yen WM, Selzer PM (ed) Topic in Applied Physics. Springer, Berlin 49:1
88. Jolliet P, Gianini M, von Zelewsky A, Bernardinelli G, Stoeckli-Evans H (1996) Inorg Chem 35:4883
89. Andersson K, Malmqvist P-Å, Roos BO, Sadlej AJ, Wolinski K (1990) J Phys Chem 94:5483
90. Glasbeek M (2001) In: Transition Metal and Rare Earth Compounds. Excited States, Transitions, Interactions. Yersin H (ed) Topics in Current Chemistry. Vol. 213 Springer, Berlin, p 95 – 142
91. Konzelmann U, Klipper D, Schwoerer M (1975) Z Naturforsch 30a:754
92. Flint CD, Matthews AD (1976) J Chem Soc Faraday. Transactions II. 72:579
93. Zilian A, Güdel HU (1992) Inorg Chem 31:830
94. Nakamoto K (1978) Infrared and Raman Spectra of Inorganic and Coordination Compounds. Wiley-Interscience Publ, New York
95. Wiedenhofer H (1994) PhD thesis, Universität Regensburg
96. Denning RG (1989) In: Vibronic Processes in Inorganic Chemistry. Flint CD (ed) Kluwer, Dordrecht, p111
97. Wilson RB, Solomon EI (1980) J Am Chem Soc 102:4085
98. Brunold TC, Güdel HU (1999) In: Inorganic Electronic Structure and Spectroscopy. Solomon EI, Lever ABP (ed) Wiley, Vol 1, p 259
99. Henderson B, Imbusch GF (1989) Optical Spectroscopy of Inorganic Solids. Carendon, Oxford, UK
100. Solomon EI (1984) Comments Inorg Chem 3:225
101. Yersin H, Otto H, Zink JI, Gliemann G (1980) J Am Chem Soc 102:951
102. Banwell CN (1972) Fundamentals of Molecular Spectroscopy. McGraw-Hill. London (UK), p 73
103. Demtröder W (1991) Laser-Spektroskopie. Springer, Berlin, p 42ff
104. Dick B, Nickel B (1986) Chem Phys 110:131
105. Azumi T, O'Donnell CM, McGlynn SP (1966) J Chem Phys 45:2735
106. El-Sayed MA (1971) Acc Chem Res 4:23
107. Tinti DS, El-Sayed MA (1971) J Chem Phys 54:2529
108. Yamauchi S, Azumi T (1973) Chem Phys Lett 21:603
109. Hall LH, El-Sayed MA (1975) Chem Phys 8:272
110. Yamauchi S, Azumi T (1977) J Chem Phys 67:7
111. Azumi T, Miki H (1997) In: Electronic and Vibronic Spectra of Transition Metal Complexes, Vol. II Yersin H (ed) Topics in Current Chemistry 191. Springer, Berlin, p. 1
112. El-Sayed MA (1974) In: Excited States, Vol I. Lim EC (ed) Academic Press, New York, p 35
113. Waller I (1932) Z f Physik 79:370
114. de Kronig RL (1939) Physica 6:33
115. van Vleck JH (1940) Phys Rev 57:426
116. Scott PL, Jeffries CD (1962) Phys Rev 127:32
117. Manenkov AA, Orbach R (1966) Spin-Lattice-Relaxation in Ionic Solids. Haper & Row, New York
118. Abragam A, Bleaney B (1970) Electron Paramagnetic Resonance of Transition Ions. Clarendon Press, Oxford
119. Walker MB (1968) Can J Phys 46:1347
120. Walker MB (1967) Phys Rev Lett 162:199

121. Orbach R, Blume M (1962) Phys Rev Lett 8:478
122. Andreev VA, Prilutskii YI (1993) Phys Solid State 35:1624
123. Andreev VA, Prilutskii YI (1992) Sov Phys Solid State (engl translation) 34:1178
124. Albrecht AC (1963) J Chem Phys 38:354
125. Fischer G (1984) Vibronic Coupling. Academic Press, London (UK)
126. Flint CD (ed) (1989) Vibronic Processes in Inorganic Chemistry. NATO ASI Series C, Vol. 288. Kluwer Academic Publishers, Dordrecht
127. Hochstrasser RM (1966) Molecular Aspects of Symmetry. Benjamin Inc WA, New York Amsterdam
128. Mataga N, Kubota T (1970) Molecular Interactions and Electronic Spectra. Marcel Dekker Inc., New York
129. Braun D, Hensler G, Gallhuber E, Yersin H (1991) J Phys Chem 95:1067
130. Clarke RH (ed) (1982) Triplet State ODMR Spectroscopy. Wiley, New York
131. Tinti DS, El-Sayed MA, Maki AH, Harris CB (1969) Chem Phys Lett 3:343
132. Schweitzer D, Hausser KH, Vogler H, Diederich F, Staab HA (1982) Mol Physics 46:1141
133. Okabe N, Ikeyama T, Azumi T (1990) Chem Phys Lett 165:24
134. Yersin H, Gallhuber E, Hensler G, Schweitzer D (1989) Chem Phys Lett 161:315
135. Ikeda S, Yamamoto S, Nozaki K, Ikeyama I, Azumi T, Burt JA, Crosby GA (1991) J Phys Chem 95:8538
136. Giesbergen CPM, Terletski C, Frei G, Güdel HU, Glasbeek M (1993) Chem Phys Lett 213:597
137. Giesbergen CPM, Glasbeek M (1993) J Phys Chem 97:9942
138. Miki H, Shimada M, Azumi T, Brozik JA, Crosby GA (1993) J Phys Chem 97:11175
139. Miki H, Azumi T (1994) J Phys Chem 98:6059
140. Kimachi S, Satomi R, Miki H, Maeda K, Azumi T, Onishi M (1997) J Phys Chem A 101:345
141. Bartell LS, Higginbotham HK (1965) J Chem Phys 42:851
142. Ewbank JD, Kirsch G, Schäfer L (1976) J Mol Structure 31:39
143. Humbs W (1997) PhD thesis, Universität Regensburg
144. Menzel ER, Rieckhoff KE, Voigt EM (1973) J Chem Phys 58:5726
145. Chassot L, von Zelewsky A (1987) Inorg Chem 26:2814
146. Vijayakumar M, Gopinathan MS (1996) J Molecular Structure (Theochem) 361:15
147. McClure DS (1959) Solid State Phys 9:399
148. Strasser J (1999) PhD thesis, Universität Regensburg
149. Lifshitz E, Kaplan A, Ehrenfreund E, Meissner D (1999) Chem Phys Lett 300:626
150. Bray KL (2001) In: Transition Metal and Rare Earth Compounds. Excited States, Transitions, Interactions. Yersin H (ed) Topics in Current Chemistry. Vol. 213 Springer, Berlin, p 1–94
151. Breu J, Range K-J, von Zelewsky A, Yersin H (1997) Acta Crystallogr C53:562
152. Koehler TR (1980) J Chem Phys 72:3389
153. Salthouse JA, Ware MJ (1972) Point group character tables and related data. Cambridge University Press, London (UK)
154. Ballhausen CJ (1979) Molecular Electronic Structures of Transition Metal Complexes. McGrawHill, New York
155. Yersin H, Braun D (1991) Coord Chem Rev 111:39
156. Harrigan RW, Crosby GA (1973) J Chem Phys 59:3468
157. Yersin H, Otto H, Gliemann G (1974) Theoret Chim Acta (Berlin) 33:63
158. Green JR, Scheie CE (1967) J Phys Chem Solids 28:383
159. Hellwege KH (1976) Einführung in die Festkörperphysik. Springer, Berlin
160. Holstein T (1959) Annals of Phys 8:325 and 343
161. Emin D (1976) In: Linear and Nonlinear Electron Transport in Solids. Devreese JT, van Doren VE (ed). Plenum Press, New York, p 409
162. Toyozawa Y (1983) In: Organic Molecular Aggregates. Reinecker P, Haken H, Wolf HC (ed) Springer Series in Solid State Sciences 49:90
163. Rössler U, Pertzsch B, Yersin H (1981) J Luminescence 24/25:437
164. Rössler U, Yersin H (1982) Phys Rev B26:3187

165. Gliemann G, Yersin H (1985) Structure and Bonding 62:87
166. Poizat O, Sourisseau C (1984) J Phys Chem 88:3007
167. Maruszewski K, Bajdor K, Strommen DP, Kincaid JR (1995) J Phys Chem 99:6286
168. Strommen DP, Mallick PK, Danzer GD, Lumpkin RS, Kincaid JR (1990) J Phys Chem 94:1357
169. Yersin H, Huber P, Braun D (1990) J Phys Chem 94:3560
170. Herzberg G (1945) Molecular Spectra and Molecular Structure. Van Nostrant Reinhold, New York Vol II p 282, Vol III (1966) p 181
171. Watman-Grajcar (1969) J Chim Phys 66:1023
172. King GW, So SP (1971) J Mol Spectry 37:543
173. Lipert RJ, Colson SD (1989) J Phys Chem 93:135
174. Yanagida S, Hasegawa Y, Murakoshi K, Wada Y, Nakashima N, Yamanaka T (1998) Coord Chem Rev 171:461
175. Johnson PM, Ziegler L (1972) J Chem Phys 56:2169
176. Ochs FW, Prasad PN, Kopelman R (1974) Chem Phys 6:253
177. Khalil OS, Hankin SW, Goodman L (1977) Chem Phys Lett 52:187
178. Callomon JH, Dunn TM, Mills IM (1966) Phil Trans Roy Soc (London) A259:499
179. McCarthy PK, Blanchard GJ (1996) J Phys Chem 100:14592
180. Weidlein J, Müller U, Dehnicke K (1982) Schwingungsspektroskopie. Georg Thieme Verlag, Stuttgart, p 52
181. Nakamoto K (1978) Infrared and Raman Spectra of Inorganic and Coordination Compounds. Wiley J, New York, p 197
182. Mohan N, Cyvin SJ, Müller A (1976) Coord Chem Rev 21:221
183. Gastilovich EA (1991) Sov Phys Usp (engl Transl) 34:592
184. Gallhuber E, Hensler G, Yersin H (1987) J Am Chem Soc 109:4818
185. Yersin H, Huber P, Gietl G, Trümbach D (1992) Chem Phys Lett 199:1
186. Humbs W, Glasbeek M, Sitters R, Yersin H submitted
187. Güntner W, Gliemann G (1990) J Phys Chem 94:618
188. Eichenseer M (1999) Diplomarbeit, Universität Regensburg
189. Backert H, Yersin H, von Zelewsky A (1999) 13th Intern Symp on Photochem and Photophys of Coordination Compounds. Book of Abstracts, Lipari. p 90
190. Strasser J (1995) Diplomarbeit, Universität Regensburg
191. Backert H (1996) Diplomarbeit, Universität Regensburg

Author Index Volume 201-214

Author Index Vols. 26-50 see Vol. 50
Author Index Vols. 51-100 see Vol. 100
Author Index Vols. 101-150 see Vol. 150
Author Index Vols. 151-200 see Vol. 200

The volume numbers are printed in italics

Printing (Computer to Film): Saladruck, Berlin
Binding: Lüderitz & Bauer, Berlin